

Physical Description of Centrosomes as Active Droplets

DISSERTATION

zur Erlangung des akademischen Grades

Doctor rerum naturalium
(Dr. rer. nat.)

vorgelegt

der Fakultät Mathematik und Naturwissenschaften
der Technischen Universität Dresden

von

Dipl.-Phys. David Zwicker

geboren am 7. Januar 1984 in Karl-Marx-Stadt



MAX-PLANCK-INSTITUT FÜR PHYSIK KOMPLEXER SYSTEME

Dresden, 2013

Eingereicht am 14. Mai 2013
Verteidigt am 30. Oktober 2013

1. Gutachter: Prof. Dr. Frank Jülicher
2. Gutachter: Prof. Dr. Jens-Uwe Sommer

Acknowledgments

Foremost, I thank my supervisor Frank Jülicher for proposing the project and guiding me all the way to the end of my doctorate. He infected me with his enthusiasm for science. I also thank the students Coleman Broaddus and Franz-Richard Kunze who collaborated with me during their stay at our institute. They helped me asking the right questions, solving problems, and understanding the results through invaluable discussions. Furthermore, I thank Jens-Uwe Sommer for accepting to review this thesis.

I am also grateful to the fruitful experimental collaboration with the group of Anthony A. Hyman of the Max Planck Institute of Molecular Cell Biology. Not only did he encourage me to interpret theoretical results in the light of experiments, but he also made it especially easy for me to interact with his group members. Here, I thank in particular Markus Decker, Steffen Jaensch, Oliver Wüseke, Jeff Woodruff, and Garret Greenan, who openly shared their experimental data with me. Furthermore, they were very patient and answered my uncountable questions regarding basic biology. Additionally, they also helped me to focus on the fundamental aspects of the theoretical description and directed my research by asking invaluable questions.

Likewise, I thank in alphabetical order Justin Bois, Clifford P. Brangwynne, Benjamin Friedrich, Sebastian Fürthhauer, Jöbin Gharakhani, Nate Goehring, Michael Kuhn, Chiu Fan Lee, Simone Reber, Pablo Sartori Velasco, Steffen Werner, and all aforementioned people for stimulating discussions, which helped me to understand the physics discussed in this thesis. On this note, I thank Mario Mulansky, Sebastian Fürthhauer, Coleman Broaddus, and Oliver Wüseke, who critically read the draft of this thesis and surely increased its quality by their constructive feedback. Generally, I thank all members of the Biological Physics Division at the MPI-PKS and the whole Hyman lab at MPI-CBG for making my work a lot of fun and for always being available to answer my questions or giving me advice. Finally, I thank my parents, my friends, Eva Bösche, and Daniela Engelmann for personal support and making life so enjoyable.

Abstract

Biological cells consist of many subunits that form distinct compartments and work together to allow for life. These compartments are clearly separated from each other and their sizes are often strongly correlated with cell size. Examples for those structures are centrosomes, which we consider in this thesis. Centrosomes are essential for many processes inside cells, most importantly for organizing cell division, and they provide an interesting example of cellular compartments without a membrane. Experiments suggest that such compartments can be described as liquid-like droplets.

In this thesis, we suggest a theoretical description of the growth phase of centrosomes. We identify a possible mechanism based on phase separation by which the centrosome may be organized. Specifically, we propose that the centrosome material exists in a soluble and in a phase separating form. Chemical reactions controlling the transitions between these forms then determine the temporal evolution of the system. We investigate various possible reaction schemes and generally find that droplet sizes and nucleation properties deviate from the known equilibrium results. Additionally, the non-equilibrium effects of the chemical reactions can stabilize multiple droplets and thus counteract the destabilizing effect of surface tension. Interestingly, only a reaction scheme with autocatalytic growth can account for the experimental data of centrosomes. Here, it is important that the centrioles found at the center of all centrosomes also catalyze the production of droplet material. This catalytic activity allows the centrioles to control the onset of centrosome growth, to stabilize multiple centrosomes, and to center themselves inside the centrosome. We also investigate a stochastic version of the model, where we find that the autocatalytic growth amplifies noise.

Our theory explains the growth dynamics of the centrosomes of the round worm *Caenorhabditis elegans* for all embryonic cells down to the eight-cell stage. It also accounts for data acquired in experiments with aberrant numbers of centrosomes and altered cell volumes. Furthermore, the model can describe unequal centrosome sizes observed in cells with disturbed centrioles. Our example thus suggests a general picture of the organization of membrane-less organelles.

Zusammenfassung

Biologische Zellen bestehen aus vielen Unterstrukturen, die zusammen arbeiten um Leben zu ermöglichen. Die Größe dieser meist klar voneinander abgegrenzten Strukturen korreliert oft mit der Zellgröße. In der vorliegenden Arbeit werden als Beispiel für solche Strukturen Zentrosomen untersucht. Zentrosomen sind für viele Prozesse innerhalb der Zelle, insbesondere für die Zellteilung, unverzichtbar und sie besitzen keine Membran, welche ihnen eine feste Struktur verleihen könnte. Experimentelle Untersuchungen legen nahe, dass solche membranlose Strukturen als Flüssigkeitstropfen beschrieben werden können.

In dieser Arbeit wird eine theoretische Beschreibung der Wachstumsphase von Zentrosomen hergeleitet, welche auf Phasenseparation beruht. Im Modell wird angenommen, dass das Zentrosomenmaterial in einer löslichen und einer phasenseparierenden Form existiert, wobei der Übergang zwischen diesen Formen durch chemische Reaktionen gesteuert wird. Die drei verschiedenen in dieser Arbeit untersuchten Reaktionen führen unter anderem zu Tropfengrößen und Nukleationseigenschaften, welche von den bekannten Ergebnissen im thermodynamischen Gleichgewicht abweichen. Insbesondere verursachen die chemischen Reaktionen ein thermisches Nichtgleichgewicht, in dem mehrere Tropfen stabil sein können und der destabilisierende Effekt der Oberflächenspannung unterdrückt wird. Konkret kann die Wachstumsdynamik der Zentrosomen nur durch eine selbstverstärkende Produktion der phasenseparierenden Form des Zentrosomenmaterials erklärt werden. Hierbei ist zusätzlich wichtig, dass die Zentriolen, die im Inneren jedes Zentrosoms vorhanden sind, ebenfalls diese Produktion katalysieren. Dadurch können die Zentriolen den Beginn des Zentrosomwachstums kontrollieren, mehrere Zentrosomen stabilisieren und sich selbst im Zentrosom zentrieren. Des Weiteren führt das selbstverstärkende Wachstum zu einer Verstärkung von Fluktuationen der Zentrosomgröße.

Unsere Theorie erklärt die Wachstumsdynamik der Zentrosomen des Fadenwurms *Caenorhabditis elegans* für alle Embryonalzellen bis zum Achtzellstadium und deckt dabei auch Fälle mit anormaler Zentrosomenanzahl und veränderter Zellgröße ab. Das Modell kann auch Situationen mit unterschiedlich großen Zentrosomen erklären, welche auftreten, wenn die Struktur der Zentriolen verändert wird. Unser Beispiel beschreibt damit eine generelle Möglichkeit, wie membranlose Zellstrukturen organisiert sein können.

Contents

1	Introduction	1
1.1	Organization of the cell interior	1
1.2	Biology of centrosomes	3
1.2.1	The model organism <i>Caenorhabditis elegans</i>	3
1.2.2	Cellular functions of centrosomes	4
1.2.3	The centriole pair is the core structure of a centrosome	6
1.2.4	Pericentriolar material accumulates around the centrioles	7
1.3	Other membrane-less organelles and their organization	9
1.4	Phase separation as an organization principle	10
1.5	Equilibrium physics of liquid-liquid phase separation	11
1.5.1	Spinodal decomposition and droplet formation	12
1.5.2	Formation of a single droplet	14
1.5.3	Ostwald ripening destabilizes multiple droplets	20
1.6	Non-equilibrium phase separation caused by chemical reactions	22
1.7	Overview of this thesis	25
2	Physical Description of Centrosomes as Active Droplets	27
2.1	Physical description of centrosomes as liquid-like droplets	27
2.1.1	Pericentriolar material as a complex fluid	27
2.1.2	Reaction-diffusion kinetics of the components	29
2.1.3	Centrioles described as catalytic active cores	31
2.1.4	Droplet formation and growth kinetics	31
2.1.5	Complete set of the dynamical equations	34
2.2	Three simple growth scenarios	35
2.2.1	Scenario A: First-order kinetics	36
2.2.2	Scenario B: Autocatalytic growth	38
2.2.3	Scenario C: Incorporation at the centrioles	39
2.3	Diffusion-limited droplet growth	41
2.4	Discussion	42
3	Isolated Active Droplets	45
3.1	Compositional fluxes in the stationary state	45
3.2	Critical droplet size: Instability of small droplets	48
3.3	Droplet nucleation facilitated by the active core	52
3.4	Interplay of critical droplet size and nucleation	53

3.5	Perturbations of the spherical droplet shape	57
3.5.1	Linear stability analysis of the spherical droplet shape	58
3.5.2	Active cores can center themselves in droplets	59
3.5.3	Surface tension stabilizes the spherical shape	62
3.5.4	First-order kinetics destabilize large droplets	62
3.6	Discussion	64
4	Multiple Interacting Active Droplets	67
4.1	Approximate description of multiple droplets	67
4.2	Linear stability analysis of the symmetric state	70
4.3	Late stage droplet dynamics and Ostwald ripening	71
4.4	Active droplets can suppress Ostwald ripening	72
4.4.1	Perturbation growth rate in the simple growth scenarios	74
4.4.2	Parameter dependence of the stability of multiple droplets	80
4.4.3	Stability of more than two droplets	84
4.5	Discussion	86
5	Active Droplets with Fluctuations	89
5.1	Stochastic version of the active droplet model	90
5.1.1	Comparison with the deterministic model	92
5.1.2	Ensemble statistics and ergodicity	93
5.1.3	Quantification of fluctuations by the standard deviation	94
5.2	Noise amplification by the autocatalytic reaction	94
5.3	Transient growth regime of multiple droplets	99
5.4	Influence of the system geometry on the droplet growth	101
5.5	Discussion	102
6	Comparison Between Theory and Experiment	103
6.1	Summary of the experimental observations	103
6.2	Estimation of key model parameters	105
6.3	Fits to experimental data	107
6.4	Dependence of centrosome size on cell volume and centrosome count	111
6.5	Nucleation and stability of centrosomes	113
6.6	Multiple centrosomes with unequal sizes	115
6.7	Disintegration phase of centrosomes	118
7	Summary and Outlook	121
	Appendix	127
A	Coexistence conditions in a ternary fluid	127
B	Instability of multiple equilibrium droplets	129
C	Numerical solution of the droplet growth	130
D	Diffusion-limited growth of a single droplet	131

E	Approximate efflux of droplet material	133
F	Determining stationary states of single droplets	134
G	Droplet size including surface tension effects	137
H	Distortions of the spherical droplet shape	140
	H.1 Harmonic distortions of a sphere	140
	H.2 Physical description of the perturbed droplet	142
	H.3 Volume fraction profiles in the perturbed droplet	142
	H.4 Perturbation growth rates	147
I	Multiple droplets with gradients inside droplets	149
J	Numerical stability analysis of multiple droplets	151
K	Numerical implementation of the stochastic model	153
Nomenclature		156
List of Figures		158
Bibliography		161

Chapter 1

Introduction

ALL organisms are made of cells, the basic building blocks of nature [1]. Cells are complex machineries that contain many different substructures and their interior is highly organized, see Fig. 1.1. This organization of the interior of cells has excited scientists since centuries, but it is still not understood [2–4].

In this thesis, we investigate the formation of centrosomes, which are cellular substructures important for cell division. We assume that the proteins these centrosomes are made of attract each other and thus form assemblies, which we describe as liquid-like droplets. Additionally, we introduce chemical reactions to control this phase separation process. With such a model, we are able to account for the major experimental observations of the dynamics of centrosomes. We try to keep the description general enough to be able to learn something about phase separation as a possible organization principle in cells.

1.1 Organization of the cell interior

The cell is not just a homogeneous container of proteins and associated molecules, but exhibits a pronounced spatiotemporal order. To achieve order, any physical system has to work against reaching the thermodynamic equilibrium [3]. In biological systems, this is accomplished by a complex process known as metabolism that alters the material of the surrounding. In general, the food taken up by an organism has lower entropy than the material it excretes. Consequently, living systems are able to expel entropy and thus stay away from the entropy maximum associated with the thermodynamic equilibrium [6]. Biological organisms are thus open, non-equilibrium systems that can lower their own entropy without violating the second law of thermodynamics.

This ejection of entropy is the reason that biological systems can stay away from equilibrium. Although this argument explains *why* an organism can obtain spatiotemporal order, it still does not clarify *how* such an order comes about. It is thus still puzzling how proteins arrange in patterns on scales orders of magnitude larger than themselves, e.g. at the scale of a cell or the whole organism itself. One of the main questions in biology therefore is how the cell achieves the spatial organization of its proteins and maintains it over time despite the large separation of

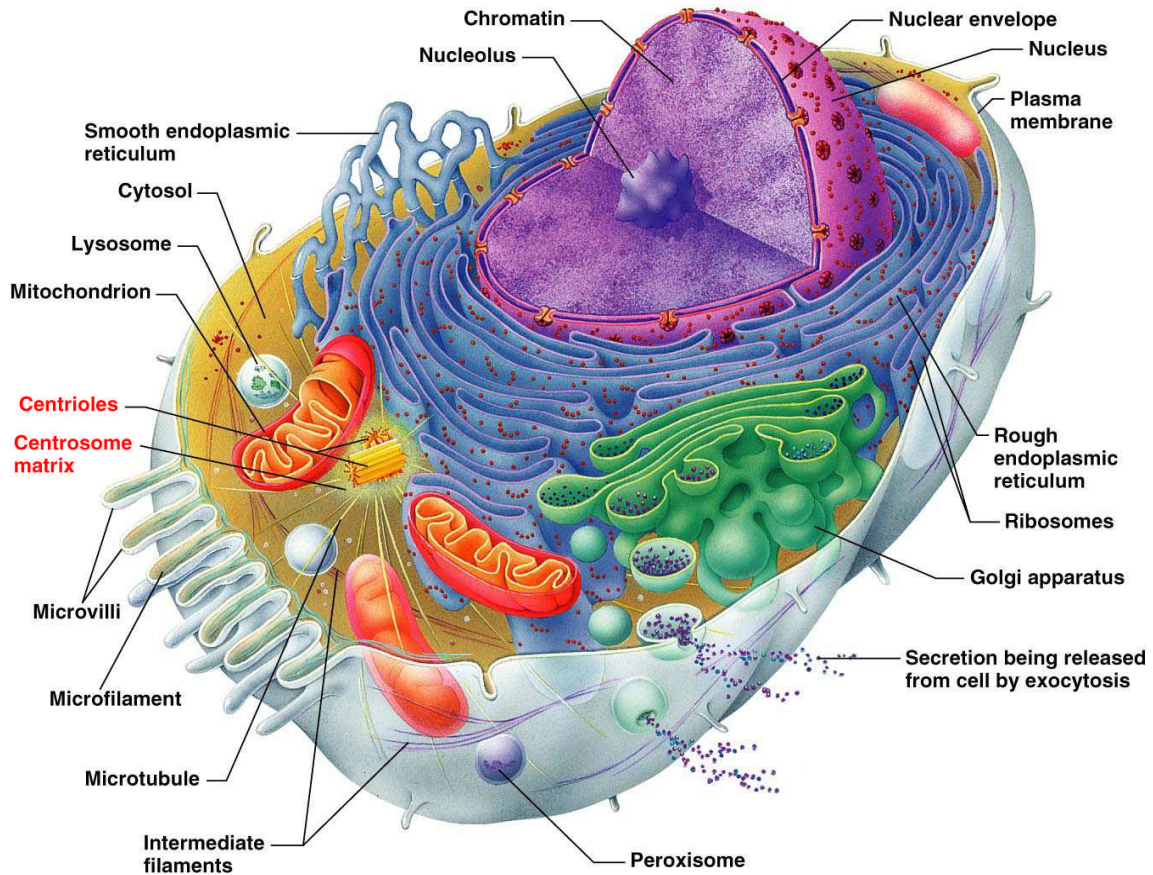


Figure 1.1: Internal organization of a cell in an artistic representation. The most important organelles are shown. Centrioles and the surrounding matrix forming centrosomes are highlighted. Image reprinted by permission of Pearson Education, Inc., Upper Saddle River, NJ [5].

length-scales [7]. Most notably, this spatial organization of proteins is also required to form substructures in cells, which are often called organelles.[†] There are many different, indispensable types of these organelles in a typical cell, see Fig. 1.1, and it is crucial that their size, their count, and their position is controlled to guarantee their function. Indeed, the size of many cell organelles is correlated with cell size [10–12]. This brings up the question of how cells both measure and adjust the size of their organelles [13–15]. We try to answer this question using the example of centrosomes, which we introduce in the next section.

[†] The term «organelle» refers to “any of the specialized structures within a cell that perform a specific function” [8]. Often times, the term is restricted to cellular substructures enclosed by a membrane [9]. In this thesis, we argue that such a membrane is not necessary to form large, stable, and well-defined substructures in a controlled manner and we therefore use the term «organelle» in its broader sense.

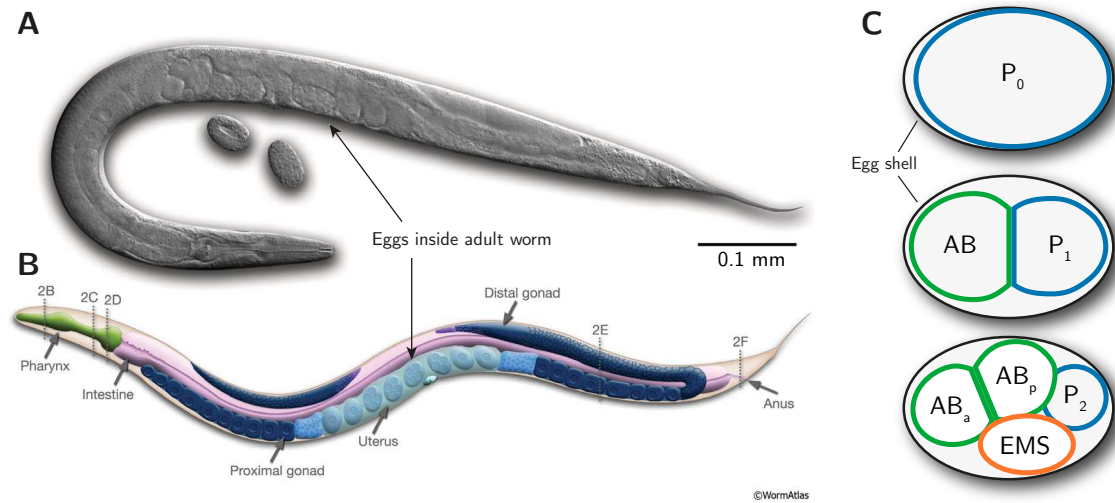


Figure 1.2: Anatomy of the model organism *Caenorhabditis elegans*. **(A)** Image of an adult hermaphrodite worm obtained by differential interference contrast microscopy. Eggs inside the body are highlighted and two laid eggs are shown next to the adult. **(B)** Schematic drawing of anatomical structures. **(C)** Schematic drawing of the first cell generations. The development of the egg is shown from top to bottom until the four-cell stage and the cell names are indicated. Panels A and B were modified from Ref. [17] and Panel C was inspired by Ref. [18].

1.2 Biology of centrosomes

Centrosomes are examples of organelles that can occur in varying sizes. However, the mechanisms regulating their size and their growth kinetics are not understood [16]. In this thesis, we present a model of centrosome growth, which we compare to quantitative experimental data.

1.2.1 The model organism *Caenorhabditis elegans*

Many of the basic principles of cellular functions are the same in all organisms, since they evolved a long time ago. It is thus conceivable that important processes, like the division of a human cell, can be understood by studying simpler organisms, which are easier to handle in the lab and are ethically less delicate than their human counterpart.

The majority of the experimental data used in this thesis has been obtained from experiments on the nematode *Caenorhabditis elegans*. This small roundworm was first used in experiments by Sydney Brenner in 1974 [19]. The adult worm is transparent and about 1 mm long, see Fig. 1.2A. It occurs in two sexes, although the hermaphrodites are usually much more abundant than the males. All experiments on

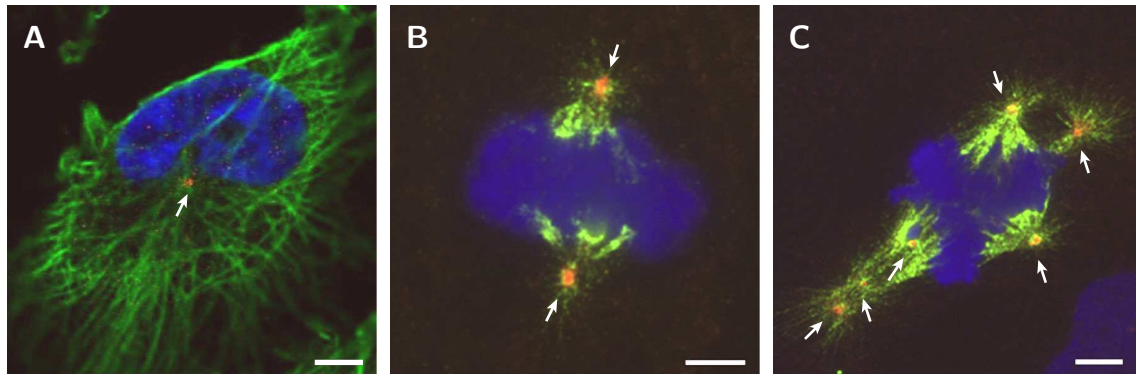


Figure 1.3: Immunofluorescence stainings showing important structures in the cell: centrosomes (red spots, highlighted by white arrows) are located near the DNA (blue region) and organize the microtubules (green filaments). **(A)** Picture of a cell of the human cell line U-251 MG in interphase. Image modified from the Human Protein Atlas [25]. **(B–C)** Pictures of cells of the human prostate cancer cell line DU-145 in mitosis. Two situations are shown: (B) a normal, bipolar mitotic spindle with two centrosomes and (C) a multipolar mitotic spindle with an increased number of centrosomes. Panels B and C were modified from Ref. [26]. Scale bars indicate 5 μm .

C. elegans mentioned in this thesis were carried out with hermaphrodites, which each have exactly 959 cells in the adult stage [20]. Interestingly, *C. elegans* was the first multicellular organism whose genome was complete sequenced [21]. This enabled the development of the powerful technique of RNA interference (RNAi), which can be used to reduce the amount of specific proteins in the living organism [22]. Controlling the concentration of single proteins allows to probe their function and the discoverers of RNAi were therefore awarded the Noble Prize in 2006 [23]. All these properties make *C. elegans* a popular model organism in molecular and developmental biology.

The life of a *C. elegans* worm starts inside its mother where the egg cell is fertilized and the resulting embryo is protected by an egg shell. This initial phase is dominated by rapid cell divisions, which lead to a highly stereotypical development, such that the location and the structure of cells can be used to identify and name them, see Fig. 1.2C. These cell divisions inside the embryo can be studied under the microscope by dissecting the mother and isolating the eggs. In particular, this system has been used to study centrosomes by our collaborators [24].

1.2.2 Cellular functions of centrosomes

The material properties and the shape of a cell are largely determined by its cytoskeleton [27]. The cytoskeleton is a scaffolding structure in cells, which consist of various different kinds of filaments. Among these, microtubules are probably the stiffest objects, which span the complete cell, see Fig. 1.3. They are involved in

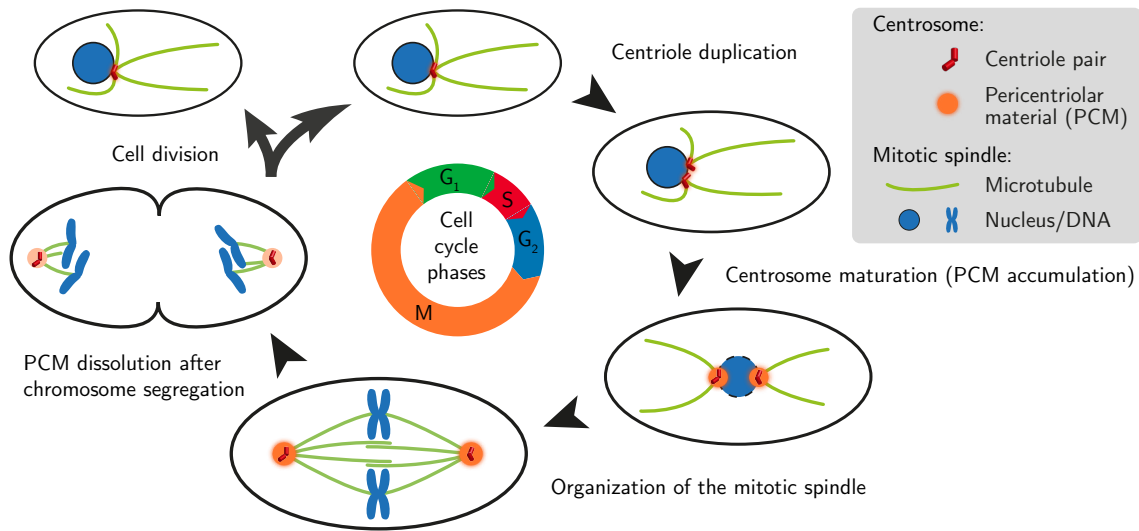


Figure 1.4: Schematic lifecycle of centrosomes. One centrosome organizes the microtubule network in the G₁ phase [1]. After centriole duplication in the synthesis phase (S phase), two centrosomes grow by accumulating pericentriolar material (PCM) in preparation of mitosis (M phase). They organize the mitotic spindle and disintegrate prior to cell division. The two daughter cells each inherit one pair of centrioles and the cycle starts again.

intracellular transport, positioning of the nucleus, and cell division [1]. In order to control all these processes, the cell thus has to organize its microtubules in space and time.

Centrosomes are the main microtubule organizing centers and therefore influence most processes dependent on microtubules [28]. Generally, centrosomes regulate the number of microtubules and their spatial structure [1]. They are important both for dividing cells as well as for cells in interphase, i.e. the phase in-between cell divisions. In interphase cells, microtubules emanate from a single centrosome and span the entire cell volume, see Fig. 1.3A. Conversely, in dividing cells, two centrosomes organize a bipolar, spindle-like structure, see Fig. 1.3B. This mitotic spindle is responsible for the segregation of the duplicated chromosomes into the daughter cells, see Fig. 1.4. Centrosomes are thus important for orchestrating cell division [29]. In particular, it has been shown that in the nematode *C. elegans*, centrosome size directly sets the length of the mitotic spindle [30]. The position of the centrosome also determines the position of the cell division plane, which is important for asymmetric cell divisions [31]. Although centrosomes are not strictly needed for cell division in higher organisms, they still might increase the robustness of cell division [32]. However, there is also the possibility that centrosomes localize to the poles of the mitotic spindle to ensure the proper segregation of centrioles to the two daughter cells [33].

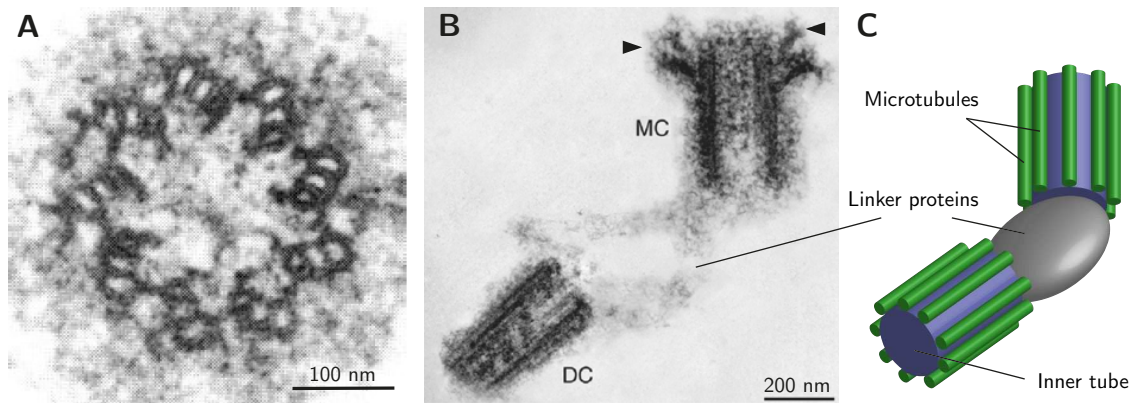


Figure 1.5: Electron micrographs of centrioles from human cells. **(A)** The cross-section of a single centriole shows a nine-fold symmetry created by the regular configuration of nine triplets of microtubules. Panel modified from Ref. [52]. **(B)** The side view shows a pair of centrioles connected by linker proteins. The mother centriole (MC) has appendages (arrowheads) consisting of additional proteins which are not present at the daughter centriole (DC). Panel modified from Ref. [53]. **(C)** Schematic view of the pair of centrioles.

Cell division is arguably the most important event in the cell cycle and its failure can lead to missegregation of the genetic information, thus yielding two compromised cells. Abnormal cell division is a key aspect of all cancers and the role of centrosomes in these diseases has been heavily discussed [34–38]. Often times, more than two centrosomes are found in cancer cells, a phenomenon termed «centrosome amplification» [39–44]. The multipolar spindles originating from the elevated centrosome count are thought of being the cause for chromosomal missegregation, see Fig. 1.3C.

Besides organizing the microtubule network, centrosomes also have other functions in the cell [45]: they play an important role in controlling the cell-cycle progression [46, 47], they are thought of interacting with endosomes [48], and they might possibly have additional regulating functions, i.e. as a signaling hub [49]. Yet, it is still debated whether centrosomes are strictly needed in these processes [50]. Generally, the role of centrioles and centrosomes may depend on the type of the cell that contains them. Therefore, it is crucial to investigate the assembly and the structure of centrosomes to understand their functions and eventually develop therapies targeted at centrosomes, e.g. for curing cancer or diseases of brain development [50, 51].

1.2.3 The centriole pair is the core structure of a centrosome

Centrosomes consist of a pair of centrioles surrounded by a cloud of proteins, the pericentriolar material (PCM), from which the microtubules emanate. The centrosome count is set by the number of centriole pairs, since centrosomes can only form around centrioles.

Centrioles have an interesting structure, which is not completely understood [54]. The two barrel-shaped centrioles of a centrosome are typically linked by special proteins, see Fig. 1.5. A single centriole consists of a cylindrical inner tube surrounded by microtubules arranged in a nine-fold symmetry [55]. In higher animals, there are nine triples of microtubules, see Fig. 1.5A, whereas other organisms may have centrioles with nine single microtubules. This is for instance the case in *C. elegans*, where a single centriole has a length of about 150 nm and a diameter of 100 nm [56].

The number of centrioles is regulated by the centriole duplication cycle, which happens once every cell cycle, see Fig. 1.4. This duplication ensures that a cell has two centrosomes at cell division, since it typically contains exactly one centrosome before it starts to divide. After cell division of the mother cell, each daughter cell inherits exactly one pair of centrioles and the cycle starts again. The duplication of a centriole occurs in multiple steps and is not completely understood [53, 56–60]. New centrioles usually grow perpendicular at the proximal end of preexisting centrioles, which gives rise to the observed L-shaped arrangement, see Fig. 1.5B. Apart from this duplication process, centrioles can also form *de novo* in cells lacking centrioles [61]. Apparently, the usual centriole duplication cycle suppresses the *de novo* formation, such that always two centrosomes are present at cell division [62]. It is not yet known how this complex regulation of the centriole formation arose from an evolutionary perspective [63]. Centrioles must have appeared at an early stage of life, though, since centrosomes are present in all major eukaryotic animals [64].

Interestingly, centrioles also fulfill other roles apart from organizing centrosomes. For instance, centrioles are found at the cell membrane, where they are called basal bodies and are important for organizing cilia, which are cell appendages important for motility and sensing. Because of their requirement for multiple basic processes in cells, it is not surprising that centrioles are thought of being involved in many diseases [49].

The role of the centrioles is difficult to disentangle from the function of the PCM surrounding them [65]. In this thesis, we focus on the accumulation of the PCM and are therefore less concerned with possible downstream effects onto the cell. The interaction between centrioles and the surrounding PCM is important, though. Centrioles evidently influence centrosomes size [66–68]. It has been hypothesized that SAS-4, a protein localizing to the region of the centrioles, tethers PCM components to the centriole [67–70]. Later in this thesis, we will show that the interaction between centrioles and the PCM can supply a suitable mechanism to control the formation of the PCM.

1.2.4 Pericentriolar material accumulates around the centrioles

The structure and material properties of the PCM are not known and it is usually described as an amorphous cloud of proteins [16]. Although electron microscopy studies and structural analysis were successfully used to examine the small centrioles, see Fig. 1.5, the same techniques are less effective in gathering detailed information

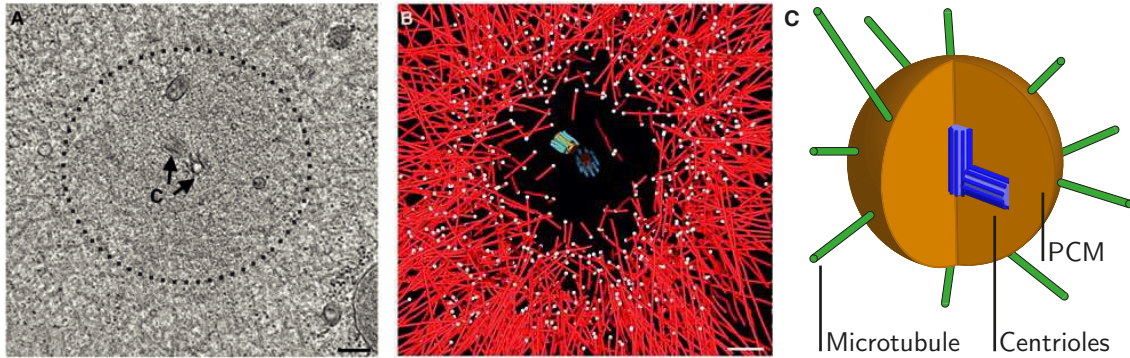


Figure 1.6: Structure of a centrosome. **(A)** Electron microscopy image of a centrosome of *C. elegans*. The centrioles located at the center of the centrosome are marked with arrows. The dashed circle indicates the approximate region of the pericentriolar material (PCM). **(B)** 3D reconstruction of the same data. The centrioles each consist of a inner tube (orange cylinder) surrounded by nine microtubules (light blue cylinders). Microtubules (red lines) emanate from the centrosome with their ends (white dots) apparently anchored at the PCM surface (black void region). **(C)** Schematic picture of the centrosome, where the pericentriolar material (PCM) is depicted as an orange sphere. Panels A and B were modified from Ref. [71]. Scale bars indicate 200 nm.

about the surrounding PCM, see Fig. 1.6. However, new high-resolution microscopy technologies begin to reveal substructures within the PCM [72, 73]. These studies predict a hierarchical ordering of proteins, at least in interphase centrosomes of humans and *Drosophila melanogaster*. Conversely, the PCM of the large centrosomes in metaphase is still thought of being amorphous [74]. We thus adopt the view that the PCM has no apparent structure to describe large centrosomes in this thesis.

The organization of centrosomes is regulated over the cell cycle, see Fig. 1.4 [1]. Initially, interphase cells have only one centrosome with little PCM surrounding a single pair of centrioles. Either this pair is inherited from the mother cell at cell division or the fertilizing sperm donates it to the egg cell, which lacks centrioles. Before a cell divides, it first duplicates its DNA. Around the same time, the pair of centrioles also duplicates as described above. Subsequently, these two pairs of centrioles accumulate PCM in metaphase, a process termed «centrosome maturation» [75]. The microtubule nucleating capacity increases accordingly and leads to the formation of the bipolar mitotic spindle. The two centrosomes lose most of their PCM after chromosome segregation, but before the cell divides physically. Finally, the two daughter cells each inherit one pair of centrioles and the cell cycle starts again. Centrosomes therefore have a dynamic life cycle, where they grow and dissolve in synchrony with the cell cycle.

We want to describe how PCM accumulates around centrioles. To this end, we have to know the structure of the PCM. There are hundreds of different kinds of

proteins localizing to the centrosome [76–78]. They can be broadly categorized into three classes: (i) proteins, that are necessary for the formation of centrioles without which centrosomes would not form; (ii) proteins that are indispensable for the accumulation of PCM around the centrioles; (iii) proteins that use the centrosome to fulfill other functions, e.g. to regulate microtubule dynamics. Since, we consider PCM accumulation, we focus on the second class, although some proteins may fall into several classes. In the case of *C. elegans*, many of the centrosome proteins are known and categorized. In a genetic screen, three proteins have been identified that play a dominant role in PCM formation [79]: SPD-2, a coiled-coil protein which is additionally involved in centriole duplication [80], SPD-5 another coiled-coil protein [81], and AIR-1, a kinase which also has other roles, e.g. in spindle assembly [82–85]. Additionally, the protein PLK-1 has been identified as another kinase indispensable for centrosome growth [24, 86–89]. These four proteins seem to be the core constituents of the PCM, although it is possible that additional proteins not yet found are required to form PCM. The function of the proteins that are not strictly required for PCM accumulation is less well understood, although some of them have been investigated in more detail: γ -tubulin for instance plays a role in anchoring and possibly nucleating microtubules [71, 90–96]; other proteins, like TAC-1, ZYG-9, or KLP-7, control microtubule dynamics in *C. elegans* [79].

Apparently, many proteins associate only loosely with the centrosome, which thus forms a dynamic structure [16]. Additionally, RNA has been found inside the PCM [97], although its role is not yet known [98, 99]. Generally, RNA can mediate attractive interactions between proteins and thereby play an important role in organizing membrane-less organelles [100].

1.3 Other membrane-less organelles and their organization

In addition to centrosomes, the cell contains other membrane-less organelles, e.g. germ granules, Cajal bodies, and nucleoli, which are all spherical and usually exist in multiple copies, see Fig. 1.7. They consist of many different kinds of proteins exchanging quickly with the surrounding cytosol [101]. This dynamic organization implies fast relaxation of mechanical stresses, a property that is reminiscent of fluid droplets. Indeed, germ-granules are liquid droplets and their segregation dynamics can be described by the interplay of droplet formation and a chemical gradient over the complete cell [102, 103]. In fact, even non-spherical organelles without membranes may have liquid-like properties. For instance, metaphase spindles were described by a theory based on liquid crystal properties [?]. This led to a successful prediction of metaphase spindle size in dependence on kinematic parameters, which was also confirmed experimentally [?]. In summary, many membrane-less organelles appear to behave like liquid droplets.

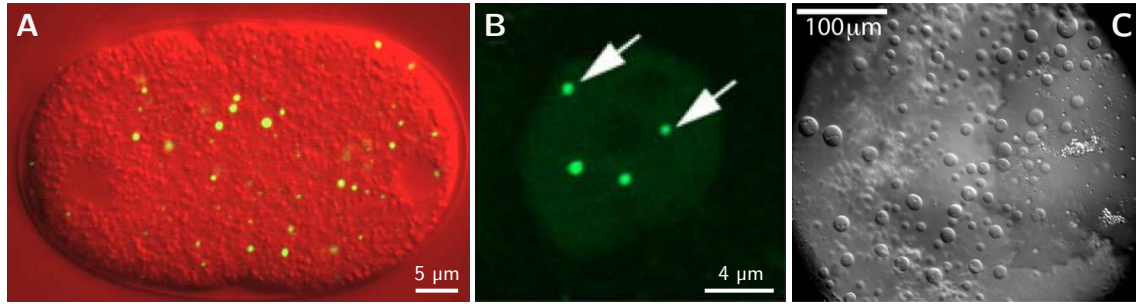


Figure 1.7: Examples of organelles without membrane in cells. **(A)** Germ-granules (green) in *Caenorhabditis elegans* visualized using a GFP-tagged version of the protein PGL-1. Panel modified from Ref. [102]. **(B)** Cajal-bodies (green) in human HeLa cells marked by GFP-tagged coilin proteins. Panel modified from Ref. [104]. **(C)** Nucleoli imaged by differential interference contrast microscopy of a *Xenopus laevis* germinal vesicle. Panel modified from Ref. [105].

Liquid droplets form due to attractive interactions between their constituents. Attractive interactions between the involved proteins are presumably also the reason for the formation of the membrane-less organelles [101, 106]. Similar systems have already been studied in biology. For instance, attractive interactions can lead to protein assemblies in various contexts: they may localize chemical reactions [107], act as storage compartments [108], or function as waste disposal systems [109]. Aggregations of misfolded proteins are also involved in aging and various diseases [110]. As an example, amyloid formation is hypothesized to cause Alzheimer’s and Parkinson’s disease, amongst others [111]. It is therefore important to investigate the formation of protein assemblies in the cell for both understanding the healthy cell as well as for curing diseases. At the current point, the mechanical properties of these assemblies are difficult to measure and it remains to be seen if they have liquid-like properties, which is a likely possibility [112].

The formation of liquid droplets can be described as a *liquid-liquid phase separation* process, where proteins segregate from the cytosol into the liquid droplets. These liquid droplets thus have a distinct composition and could form the aggregates or organelles mentioned above.

1.4 Phase separation as an organization principle

Phase separation is a general physical phenomenon that appears in many different fields [113]. It describes how a mixture of components segregates and forms compartments. Here, the components could be anything ranging from chemical molecules to protein complexes, or even individual animals, depending on the scale at which the phase separation occurs. In this context, compartments are homogeneous regions

in the system with distinct composition, i.e. they are enriched in the respective components. The compartments are separated by interface regions, which are small compared to the size of the compartments themselves. Consequently, the process of phase separation describes how a single-phase system becomes a multi-phase system. In the context of liquids, this could be the process of separating a miscible solution into two immiscible liquids.

Theories based on phase separation have been used successfully to describe structures in soft matter [114, 115], in particular in living systems [116, 117]. In the biological science, the theory of phase separation has been applied to problems at many different scales: at the sub-cellular level, it describes Cajal bodies inside the nucleus [118] or lipid rafts found in the cell membrane [119–121]. Other protein assemblies with liquid-like properties are found in the cytosol, e.g. the protein Dishevelled forms puncta, which seem to be functionally relevant [122, 123]. They have been analyzed theoretically using a model based on phase separation [124, 125]. Furthermore, the concept also proved to be useful on the tissue level, e.g. for investigating pattern formation in bird wings [126]. In general, phase separation is a generic physical mechanism for morphogenesis, i.e. it may explain how the shape of tissues is controlled [127]. Interestingly, the range of applications extends to problems at the population level: phase separation appears in the organization of bacterial colonies [128, 129] and flocks of birds [130].

The theory of phase separation is therefore a widely used concept, which can explain spatial inhomogeneities. We will also use it in this thesis to explain the organization and formation of centrosomes. Before we introduce and analyze our model, we summarize the basic theory of equilibrium phase separation in the next section.

1.5 Equilibrium physics of liquid-liquid phase separation

We develop the theory of phase separation in the minimal framework of a binary fluid, where we distinguish two components that can segregate from each other. To be consistent with the terminology used later in this thesis, we already call these two components droplet material and solvent material. For simplicity, we consider an incompressible fluid with constant and equal molecular volume ν for the two components. We can then characterize the state of the system by the volume fraction ϕ of the droplet material, which is proportional to its number density $n = \phi/\nu$. Note that the volume fraction of the solvent material is given by $1 - \phi$, since the solvent material together with the droplet material must occupy the entire volume.

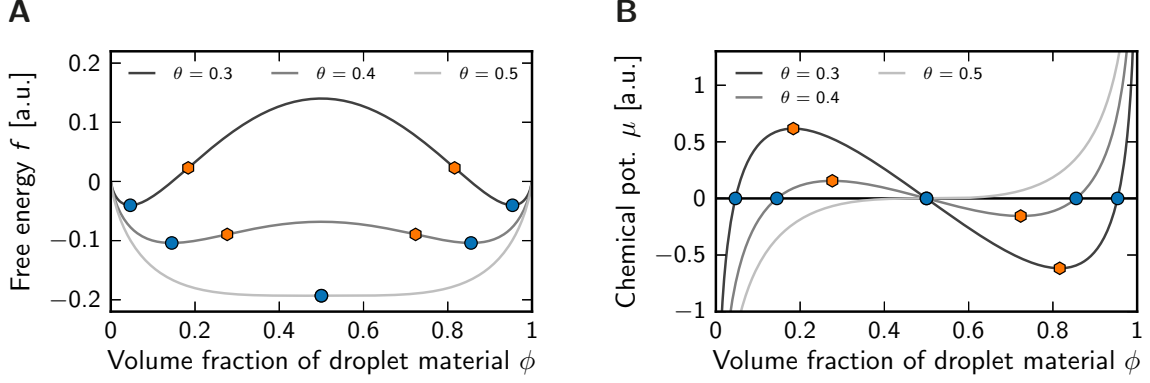


Figure 1.8: Free energy density f of a binary fluid as a function of the volume fraction ϕ of droplet material for different normalized temperatures $\theta = k_B T / (\nu \chi)$. **(A)** The free energy density $f(\phi)$ is shown. **(B)** The chemical potential $\mu(\phi) \propto \partial_\phi f(\phi)$ is shown. The minima (blue dots) and inflection points (orange hexagons) of $f(\phi)$ are indicated in both panels.

1.5.1 Spinodal decomposition and droplet formation

Phase separation is generally driven by the interactions between the components of the binary mixture [113]. If concentrating components of the same kind lowers the free energy, the system tends to phase separate. This ordering process is opposed by entropy, which tends to mix the system. These two antagonistic processes are captured by a simple choice of the free energy density

$$f(\phi) = \frac{k_B T}{\nu} [\phi \ln \phi + (1 - \phi) \ln(1 - \phi)] + \chi \phi \cdot (1 - \phi), \quad (1.1)$$

which stems from a simplified Flory-Huggins theory [131, 132]. The first term, proportional to the temperature T and Boltzmann's constant k_B , describes the entropy of mixing, which increases if components are concentrated. Conversely, the second term accounts for the interaction energy, which is large if the system is mixed.

The ratio of entropic to enthalpic effects, quantified by the normalized temperature $\theta = k_B T / (\nu \chi)$, determines whether the system can undergo phase separation [113]. For large θ entropic effects dominate, $f(\phi)$ has only a single minimum, and the system is therefore always mixed, see Fig. 1.8A. Conversely, for small θ the free energy has two minima and the system can separate into two phases, where the volume fraction in these phases are given by the positions of the minima. Note that two phases only form if the average fraction $\bar{\phi}$ of droplet material lies between the two minima. Furthermore, spontaneous demixing of a homogeneous system, known as *spinodal decomposition*, is only possible if $f(\phi)$ is concave at $\phi = \bar{\phi}$ [113]. Otherwise, the homogeneous state is metastable and fluctuations are necessary to initiate demixing. The unstable and metastable regions are separated by the inflection points

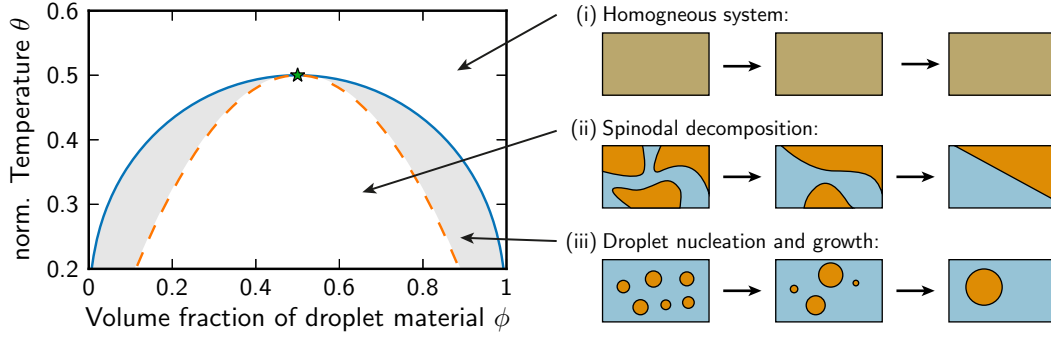


Figure 1.9: Phase diagram of a binary mixture as a function of the normalized temperature $\theta = k_B T / (\nu \chi)$ and the composition $\bar{\phi}$ of the system. Regions with qualitatively different behavior are separated by the binodal line (blue solid line) and the spinodal line (orange dashed line), which touch each other in the critical point (green star). The schematics on the right illustrate the time-evolution of the system in the three different regions: (i) homogenous, mixed system at large enough temperature, (ii) spontaneous spinodal decomposition, and (iii) nucleation and growth of droplets of the minority phase. The rightmost illustrations indicate possible equilibrium states.

of $f(\phi)$. Consequently, the minima and inflection points of $f(\phi)$ mark transition points between qualitative different dynamics and they are therefore respectively known as the binodal point and spinodal point [113]. They are shown as a function of θ in the phase diagram in Fig. 1.9, which highlights the three possible regions:

- (i) The system is homogeneous and well-mixed at high temperatures.
- (ii) For low temperatures, a system prepared in the homogeneous state is unstable and will undergo spontaneous, global demixing to lower its free energy. This spinodal decomposition at least transiently yields bicontinuous structures instead of droplets [133–135].
- (iii) In between these two extremes lies a case, where the homogenous system does not have the lowest energy, but is locally stable. Small perturbations are not enough to drive the system from this metastable state toward the equilibrium state. Instead, large fluctuations, which typically only occur rarely, can nucleate droplets which then grow subsequently.

We consider phase separation in the context of centrosome formation within cells in this thesis. The total volume of the centrosomes is typically much smaller than the volume of the entire cell [24]. Consequently, we do not observe spontaneous spinodal decomposition and bicontinuous structures, but the system is rather in the droplet nucleation and growth regime. We thus focus on the case, where a small number of droplets form within the system. This common situation can also be observed

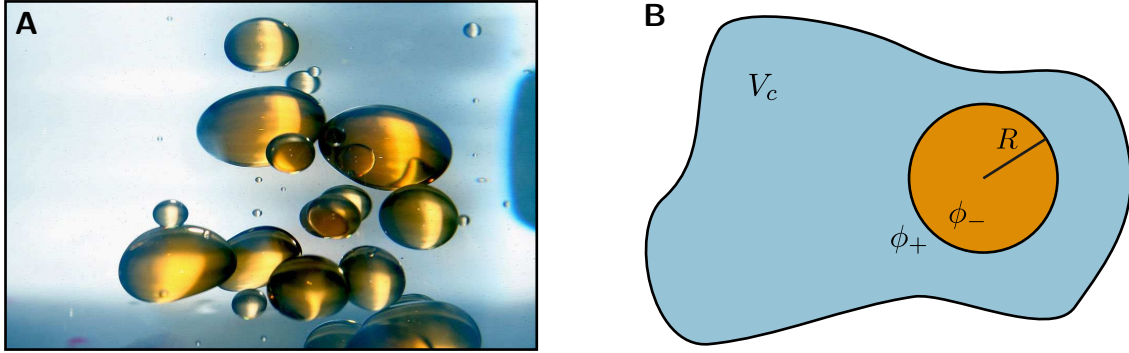


Figure 1.10: General droplet formation by phase separation. **(A)** Oil droplets in water. Photography courtesy of T  tine [141]. **(B)** Schematic drawing of a spherical droplet of radius R embedded in a system of volume V_c . The volume fraction of droplet material inside and outside the droplet is ϕ_- and ϕ_+ , respectively.

in daily life, e.g. when mixing oil and water, see Fig. 1.10A. Generally, droplet formation by phase separation is well understood [115, 136, 137]. For instance, the size distribution of droplets over time can be predicted theoretically [138–140]. It is still a challenge to control the nucleation and therefore the count and position of droplets, though.

1.5.2 Formation of a single droplet

We first consider a single droplet of volume V located in a closed system of volume V_c , see Fig. 1.10B. If the respective volume fractions within the droplet and in the solvent are homogeneous, the free energy F of the system is given by

$$F = Vf(\phi_-) + (V_c - V)f(\phi_+) + \gamma A, \quad (1.2)$$

where $f(\phi)$ is a suitable free energy density capturing the interactions of the material with itself and the solvent, e.g. the one given in Eq. (1.1). Here, ϕ_- and ϕ_+ are the homogeneous volume fractions inside and outside the droplet, respectively. The last term in Eq. (1.2) accounts for the interface between the droplet and the solvent. The associated surface free energy is given by the product of the surface area A of the droplet and the surface tension γ , which is a material property [142].

In the thermodynamic equilibrium, the free energy given in Eq. (1.2) is minimal. We calculate the droplet volume later in this section, but we can already state that the equilibrium shape will be a sphere, since this geometry minimizes the surface energy γA for a given droplet volume. The spherical droplet shape can be parameterized by the droplet radius R . The volume V and the surface area A of the droplet are then related by $V = 4\pi R^3/3$ and $A = 4\pi R^2$, respectively. Consequently,

the two volume fractions, ϕ_- and ϕ_+ , and any value quantifying the droplet size describe the system completely.

We assume a closed system, such that the total amount of material is conserved. The variables that the free energy depends on are therefore related by

$$\bar{\phi}V_c = V\phi_- + (V_c - V)\phi_+ . \quad (1.3)$$

Here, $\bar{\phi}$ is the volume fraction of droplet material in the corresponding homogeneous, mixed system. The conserved total volume of droplet material is thus given by $\bar{\phi}V_c$. It is distributed between the droplet phase, described by the first term on the right hand side of Eq. (1.3), and the solvent captured by the last term.

Nucleation of a single droplet

We first discuss the free energy given in Eq. (1.2) for a small droplet. In the simple case investigated here, we consider a fixed volume fraction ϕ_- inside the droplet. The volume fraction ϕ_+ outside the droplet can then be determined from the conservation equation (1.3) and the droplet size becomes the only state variable. Since we consider small droplets, ϕ_+ will hardly deviate from the volume fraction $\bar{\phi}$ of the homogeneous system. We thus expand the free energy density, $f(\phi_+) \approx f(\bar{\phi}) + \tilde{\mu}(\bar{\phi})(\phi_+ - \bar{\phi})$, and eliminate ϕ_+ using the material conservation given by Eq. (1.3). Here, we introduced the abbreviation $\tilde{\mu}(\phi) = \partial f(\phi)/\partial \phi$, which is proportional to the chemical potential, $\mu = \nu\tilde{\mu}$, with the molecular volume ν . Using these approximations, the free energy F given in Eq. (1.2) simplifies to

$$F \approx f(\bar{\phi})V_c - \Delta f \cdot V + \gamma A , \quad (1.4)$$

where $\Delta f = f(\bar{\phi}) - f(\phi_-) + \tilde{\mu}(\bar{\phi})(\phi_- - \bar{\phi})$. The first term is the free energy of the homogeneous reference system. Conversely, the other terms respectively describe the bulk and surface contributions to the free energy that are caused by the formation of a small droplet. This droplet can only be stable if the total free energy F is lower than that of the homogeneous system. The surface tension γ is typically positive, such that only the bulk term can reduce F . We thus consider the case $\Delta f > 0$ in the following.

The simplified free energy given in Eq. (1.4) only depends on the droplet size. It exhibits an interesting scaling with the droplet radius R : while the bulk term proportional to Δf scales with $V \propto R^3$, the surface term proportional to γ only scales with $A \propto R^2$. Consequently, the surface term dominates for small radii and the free energy increases with growing droplets, see Fig. 1.11. Conversely, for large radii, the bulk term typically lowers the free energy. If the droplet is larger than a critical size, it can thus lower the free energy by growing further. Taken together, droplets larger than a certain critical size grow spontaneously, while smaller droplets dissolve.

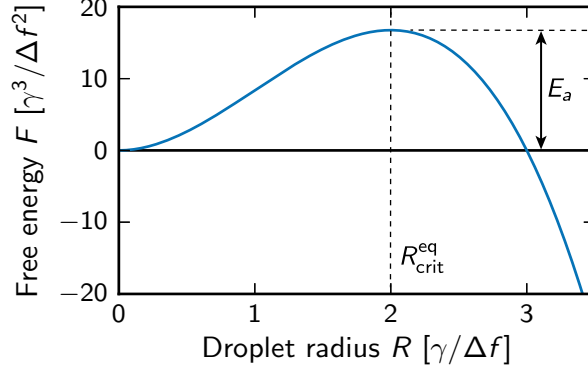


Figure 1.11: Free energy of a small droplet as a function of its radius R as given by Eq. (1.4) without the constant term. The activation energy E_a is given by the maximum at the critical droplet radius $R_{\text{crit}}^{\text{eq}}$, see Eq. (1.5).

The critical droplet size is given by the local maximum of $F(R)$, where the derivative with respect to R vanishes, see Fig. 1.11. Using Eq. (1.4), we can solve for the critical droplet radius,

$$R_{\text{crit}}^{\text{eq}} \approx \frac{2\gamma}{f(\bar{\phi}) - f(\phi_-) + \tilde{\mu}(\bar{\phi})(\phi_- - \bar{\phi})} . \quad (1.5)$$

We thus find the typical relation that the critical droplet radius is proportional to the surface tension γ and vanishes in the limit $\gamma \rightarrow 0$ [143]. Growth of small droplets can therefore be understood as a competition between the attractive interactions in the bulk and the thermodynamically unfavorable creation of interface. Consequently, the spontaneous nucleation of a droplet that is larger than the critical size and can thus overcome the energy barrier is a stochastic process driven by thermal fluctuations in the system. The associated probability P_{nuc} is typically given by $P_{\text{nuc}} \propto \exp(-E_a/k_B T)$ [144], where $E_a = F(R_{\text{crit}}^{\text{eq}}) - F(0)$ is the height of the energy barrier. Because of this exponential relationship, nucleation processes are typically erratic and thus difficult to control.

Coexistence conditions at the droplet interface

Once a droplet is formed, it can be described as a dense phase of droplet material immersed in the solvent, where different volume fractions ϕ of the droplet material coexist inside and outside of the droplet surface. Local thermodynamic equilibrium at the interface between the droplet and the solvent governs the conditions of this coexistence. In order to derive general conditions, we will now lift the constraint that the volume fraction ϕ_- inside the droplet is constant. Still, the free energy given in Eq. (1.2) is minimal if the system is in equilibrium and the partial derivatives of F with respect to the state variables, ϕ_- and V , must vanish. Note that ϕ_+ is not a

state variable, since we eliminate it using Eq. (1.3). The two necessary conditions for the minimum of the free energy can thus be formulated as

$$0 = \tilde{\mu}(\phi_-) - \tilde{\mu}(\phi_+) \quad (1.6a)$$

$$0 = (\phi_+ - \phi_-)\tilde{\mu}(\phi_-) + f(\phi_-) - f(\phi_+) + \frac{2\gamma}{R}, \quad (1.6b)$$

where again $\tilde{\mu}(\phi) = \partial_\phi f(\phi)$. These two equations are the coexistence conditions for the volume fractions inside and outside of the interface. Eq. (1.6a) states that the chemical potentials $\mu = \nu\tilde{\mu}$ on both sides of the interface must match. This is nothing else but the chemical equilibrium between the two phases. Similarly, the second condition can be interpreted as the mechanical equilibrium of the pressures inside and outside the droplet. This can be seen by considering the grand-canonical Helmholtz free energy, $F = N\mu - pV$, where $N = nV$ is the total number of molecules. Dividing this expression by V , we get $f = \phi\tilde{\mu} - p$, which we use to eliminate f in Eq. (1.6b). This yields

$$p(\phi_-) - p(\phi_+) = \Pi, \quad (1.7)$$

where $\Pi = 2\gamma/R$ denotes the Laplace pressure caused by the surface tension of the curved interface [113]. Both surface tension γ and the droplet radius R enter the Eqs. (1.6) only via the Laplace pressure. We can thus discuss their influence on the coexisting volume fractions together. Note that the limit $R \rightarrow \infty$ corresponds to a flat interface without any Laplace pressure. Taken together, the coexistence conditions are that the chemical potentials on both sides of the interface match and that the pressure difference across the interface is equal to the Laplace pressure.

We now determine the coexisting volume fractions ϕ_- and ϕ_+ inside and outside of the droplet, respectively. These two values are given by solving the Eqs. (1.6) for ϕ_- and ϕ_+ , where the functional form of $f(\phi)$ enters. Given a graph of $f(\phi)$, the solutions can be determined geometrically using the so called Maxwell construction [145]: Two tangents to the graph of $f(\phi)$ have to be constructed that have the same slope and are separated by a distance equal to the Laplace pressure Π . The points where these two tangents touch the curve of $f(\phi)$ are the solutions ϕ_- and ϕ_+ of Eqs. (1.6). For a finite Laplace pressure, $\Pi > 0$, this procedure is visualized by the green lines in Fig. 1.12. In the special case of vanishing surface tension or a flat interface, $\Pi = 0$, the two tangents are identical, see solid orange line. Note that in this case the droplet radius does not enter the Eqs. (1.6) and the solutions are thus uniquely defined by $f(\phi)$, i.e. the material properties of the phase separating fluid. We denote these special solutions for vanishing Laplace pressure by ψ_- and ψ_+ , see the dashed orange lines in Fig. 1.12. ψ_- and ψ_+ are the volume fractions that coexist at equilibrium at a flat interfaces.

The Maxwell construction introduced above can be used to justify an analytical approximation to the solution of Eqs. (1.6). Fig. 1.12 shows that the Laplace pres-

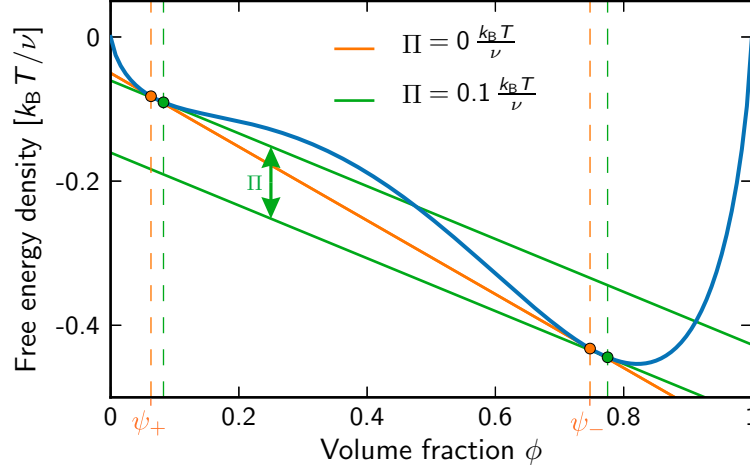


Figure 1.12: The free energy density of a binary fluid (blue) is shown as a function of the volume fraction ϕ of the phase separating material. The equilibrium solutions given by the coexistence conditions of Eq. (1.6) at the interface are indicated by dashed lines. They are obtained from the Maxwell construction (solid lines) described in the main text for vanishing (orange) and finite (green) Laplace pressure Π .

sure Π raises the equilibrium volume fractions slightly above the solutions for $\Pi = 0$. To derive an expression for this correction, we expand the free energy density around the reference solutions for vanishing surface tension, see Appendix A. Truncating the expansion at the quadratic order and solving for ϕ_- and ϕ_+ , we get

$$\phi_- \approx \psi_- + \frac{\gamma\beta_-}{R} \quad (1.8a)$$

$$\phi_+ \approx \psi_+ + \frac{\gamma\beta_+}{R}, \quad (1.8b)$$

where we introduced the coefficients β_- and β_+ . They quantify the influence of the surface tension onto the coexisting volume fractions and are related to the curvature of the free energy density function, $\beta_{\pm} = 2/[f''(\psi_{\pm})(\psi_- - \psi_+)]$, see Eq. (A.8) in the appendix. The coefficients β_- and β_+ are positive, since the free energy density usually has a convex shape close to the basal solutions, $f''(\psi_{\pm}) > 0$. The approximation leading to the Eqs. (1.8) is valid if the influence of Laplace pressure is small, $\Pi \ll \beta_{\pm}^{-1}$. These equations are known as the Gibbs-Thompson equations and the combined parameters $\gamma\beta_-$ and $\gamma\beta_+$ are sometimes called «capillary length» [146]. In general, ψ_- , ψ_+ , β_- and β_+ are material parameters, which can be derived from the free energy density describing the phase separation. However, the full functional form of the free energy density is often not known and we therefore use these four parameters as a parameterization of the phase separation physics in this thesis.

The coexisting volume fractions on both sides of the interface given by Eqs. (1.8) increase with the Laplace pressure Π . This can be interpreted in a physical picture: Eq. (1.7) states that the pressure p_- inside the droplet rises by Π compared to the situation of a flat interface. Using the Gibbs-Duhem relation, $Nd\mu = -SdT + Vdp$, at constant temperature, this can be translated into an increase $\Delta\mu = \nu\Pi/\psi_-$ of the chemical potential inside the droplet [147]. Since the interface is in thermodynamic equilibrium, the chemical potential right outside of the interface has to rise by the same amount, see Eq. (1.6a). The effect of this change in the chemical potential onto the volume fraction ϕ can be calculated by considering an ideal mixture for simplicity, which is described by the free energy density given in Eq. (1.1) with $\chi = 0$. Differentiating the resulting expression twice with respect to the fraction ϕ and assuming $\phi \ll 1$ results in $\partial_\phi\mu \approx k_B T/\psi_\pm$, where ψ_\pm denotes the values of the coexisting volume fraction at a flat interface. Consequently, we arrive at the change in volume fraction $\Delta\phi_\pm \approx \psi_\pm \Delta\mu/(k_B T)$, caused by a small increase $\Delta\mu$ of the chemical potential. Taken together, we can thus estimate $\Delta\phi_\pm \approx 2\nu\psi_\pm\gamma/(k_B T R \psi_-)$ [147]. Comparing this expression to the second term in Eq. (1.8), the series coefficients β_- and β_+ associated with the influence of surface tension can thus be given as

$$\beta_- \approx \frac{2\nu}{k_B T} \quad \text{and} \quad \beta_+ \approx \frac{2\nu\psi_+}{k_B T \psi_-} \quad (1.9)$$

and are indeed positive. Using a typical molecular volume $\nu \approx 120 \text{ nm}^3$ of globular proteins [27] and $k_B T \approx 4 \text{ pN nm}$, we thus get $\beta_+ \ll \beta_- \approx 6 \times 10^{-5} \text{ } \mu\text{m}^2/\text{pN}$.

The order of magnitude of the surface tension γ can also be estimated. For soft, biological matter, thermal fluctuations play a significant role, since the interaction energies of molecules are usually of the order of $k_B T$ [148, 149]. Consequently, the surface energy can be estimated as $\gamma \sim k_B T/l^2$, where l is the size of the molecules. Typical surface energies determined from this approximation are $\gamma \approx 1 \text{ pN}/\mu\text{m}$ [101].

Equilibrium configurations of a single droplet

The minimum of the free energy allowed us to derive the coexistence conditions given in Eqs. (1.8). The droplet volume V is then set by the total amount of material, see Eq. (1.3). Combining these equations yields

$$\bar{\phi}V_c \approx V\psi_- + (V_c - V) \left(\psi_+ + \frac{\gamma\beta_+}{R} \right), \quad (1.10)$$

where we neglected the small effect of surface tension γ onto the volume fraction inside the droplet by considering $\phi_- \approx \psi_-$. For large droplets, surface tension is also negligible in the last term and we can solve for V , which yields

$$V \approx V_c \cdot \frac{\bar{\phi} - \psi_+}{\psi_- - \psi_+}, \quad (1.11)$$

This relation explains how phase separation leads to an automatic adjustment of the droplet size to the system volume V_c . The critical size above which droplets grow spontaneously can also be estimated. Typically, the critical size is small and we thus consider Eq. (1.10) in the limit of small R . In this limit, the surface tension effects are important, but the terms proportional to V are negligible. We can thus solve for the critical radius, which reads

$$R_{\text{crit}}^{\text{eq}} \approx \frac{\gamma\beta_+}{\phi - \psi_+} . \quad (1.12)$$

As expected, the critical radius scales with the surface tension, compare to Eq. (1.5). Similarly, we can use Eq. (1.10) to determine the minimal fraction $\bar{\phi}_{\text{min}}^{\text{eq}}$ above which droplets can grow. For small droplets compared to the system size, $V \ll V_c$, it reads

$$\bar{\phi}_{\text{min}}^{\text{eq}} \approx \psi_+ + \frac{4}{3} \left(\frac{4\pi(\gamma\beta_+)^3\psi_-}{V_c} \right)^{\frac{1}{4}} . \quad (1.13)$$

The second term is a correction factor, which can be omitted for very large systems.

The qualitative results summarized here already show that phase separation can concentrate material in a compartment whose size scales with the system size. This mechanism can potentially be used by cells to scale their organelles. In such a picture, the stable size is set by the available pool of material [150]. The size of centrosomes is also limited by the amount of one of the constituents [24], which is one motivation to base our theory of centrosome growth on phase separation.

1.5.3 Ostwald ripening destabilizes multiple droplets

So far, we considered single droplets, but centrosomes and other membrane-less organelles often occur in multiple copies in a single cell. We thus next investigate the equilibrium thermodynamics of multiple droplets. The state of m droplets is characterized by the volume fractions ϕ_i of droplet material inside of the droplets, their volume V_i , and their surface area A_i , where the index $i = 1, \dots, m$ enumerates the droplets. The free energy F associated with such a configuration is analogous to the one given in Eq. (1.2) and again consists of the bulk energies given by the free energy density times the compartment volumes and the surface energies calculated from the surface tension times the surface areas. The free energy thus reads

$$F = V_c f(\phi_0) + \sum_{i=1}^m [f(\phi_i) - f(\phi_0)] V_i + \gamma \sum_{i=1}^m A_i , \quad (1.14)$$

where ϕ_0 denotes the volume fraction in the solvent, i.e. outside droplets. The minimum of F is again attained for spherical droplets, since this geometry minimizes the surface area for a given volume. The droplets can thus be characterized by

their radii R_i , from which the volume and the surface area follow. This allows us to generalize the local equilibrium conditions given in Eq. (1.6) to

$$0 = \tilde{\mu}(\phi_i) - \tilde{\mu}(\phi_0) \quad (1.15a)$$

$$0 = (\phi_0 - \phi_i)\tilde{\mu}(\phi_0) + f(\phi_i) - f(\phi_0) + \frac{2\gamma}{R_i}, \quad (1.15b)$$

for $i = 1, \dots, m$. These are the conditions for a stationary point of the free energy F given in Eq. (1.14). Such a stationary point is only a minimum of F and thus a stable equilibrium state if the associated Hessian matrix is positive definite. In fact, it can be proven that this is never the case if $m \geq 2$, see Appendix B. Consequently, all stationary points with multiple droplets are unstable and at most one droplet exists in an equilibrium system described by Eq. (1.14).

This result can be understood intuitively by noting that the total volume of all droplets and therefore the bulk energy depends only weakly on the droplet count, since the total amount of droplet material is conserved. Conversely, the surface area of all droplets is typically reduced if there are fewer droplets, since larger spheres have a smaller surface to volume ratio than smaller spheres. The minimal total surface area for a given total droplet volume is thus achieved for a single spherical compartment. This effect is dependent on the surface tension γ , since otherwise the surface areas A_i would not matter in Eq. (1.14).

Surface tension γ causes a Laplace pressure $\Pi = 2\gamma/R$, which is smaller for droplet with larger radius R and thus leads to a smaller chemical potential in the surrounding solvent. This causes a gradient of the chemical potential between droplets of different sizes, which leads to a flux of droplet material from smaller droplets to larger ones, thus amplifying the mismatch in size. Consequently, large droplets grow at the expense of smaller ones, thus reducing the total number of droplets while increasing their mean size [138–140]. This process is known as *Ostwald ripening* [146].

The coarsening induced by Ostwald ripening is often undesirable, e.g. for making emulsions, which are mixtures of many droplets in a solvent [151]. The macroscopic physical properties of these emulsions are determined by the size and count of the droplets, which is important in various applications, e.g. in controlling the properties of foods, cosmetics, and technological processes [147, 152]. In order to preserve emulsions for a long period, both droplet coalescence and Ostwald ripening has to be suppressed. The effect of coalescence can be reduced by surfactants at the droplet surface or by simply keeping the droplets spatially separated [147]. Ostwald ripening on the other hand is more difficult to suppress. It can be delayed by surfactants [153] and completely suppressed by a constant shear of the fluid [154]. Additionally, adding extra components that are trapped inside the droplet can also prevent the coarsening [155, 156]. These components modify the chemical potential and thereby inhibit the diffusive flux of material. However, the size of such droplets is difficult to control, since it depends on the amount of trapped species in each droplet [147]. Taken

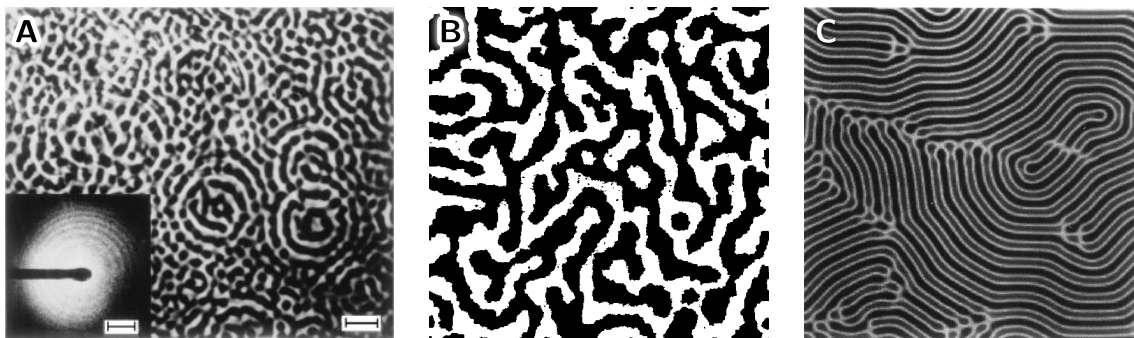


Figure 1.13: Pattern formation in phase separating systems augmented with chemical reactions. The grey scale in the three panels corresponds to the value of the order parameter Ψ . **(A)** Phase-contrast optical micrograph of a phase separating polymer mixture where chemical reactions have been triggered by ultraviolet light. The inset shows the light scattering pattern. The scale bars indicate $10\ \mu\text{m}$ and $10^4\ \text{cm}^{-1}$ for the panel and the inset, respectively. Panel modified from Ref. [159]. **(B)** Monte Carlo simulation of a binary mixture. Panel modified from Ref. [160]. **(C)** Numerical simulation of Eq. (1.16). Panel modified from Ref. [173].

together, controlling the size and count of droplets is a technological challenge, which is still not solved.

Biological systems face the same difficulties, since there are often multiple organelles of the same type in cells, see Fig. 1.7. If we describe these organelles using the theory of phase separation, it is thus puzzling how they can be stable for a long time. We will resolve this apparent contradiction in Chapter 4 for the model discussed in this thesis. There, it will turn out that non-equilibrium features of the model become important and the equilibrium considerations of this section are thus not applicable.

1.6 Non-equilibrium phase separation caused by chemical reactions

The Ostwald ripening of phase separating systems can generally be suppressed by chemical reactions, which typically leads to regular patterns like the ones shown in Fig. 1.13. Such systems have already been examined experimentally [157–159], numerically [160–168], and analytically [167–174]. These works can be summarized in a general theoretical framework, where the composition of the system is described by an order parameter $\Psi(\mathbf{r}, t)$ as a function of position \mathbf{r} and time t . For instance, Ψ could be the difference of the volume fractions of two species A and B , which phase separate from each other. The chemical reactions are then often implemented

as an interconversion of these two species, which in the simplest case is described by the reaction $A \rightleftharpoons B$ with the same rate constant k for both reaction directions. The dynamical equation for Ψ is typically given as a generalized reaction-diffusion equation of the form

$$\partial_t \Psi(\mathbf{r}, t) = M \nabla^2 \frac{\delta \mathcal{F}[\Psi(\mathbf{r}, t)]}{\delta \Psi(\mathbf{r}, t)} - k \Psi(\mathbf{r}, t), \quad (1.16)$$

where M is a mobility parameter. Here, the first term on the right hand side describes the phase separation dynamics, which tends to relax the system to an equilibrium configuration set by the free energy functional $\mathcal{F}[\Psi]$. A typical choice for $\mathcal{F}[\Psi]$ is

$$\mathcal{F}[\Psi(\mathbf{r})] = \int \left\{ f(\Psi(\mathbf{r})) + \frac{\kappa}{2} (\nabla \Psi(\mathbf{r}))^2 \right\} d^3 r, \quad (1.17)$$

which has been proposed by Cahn and Hilliard [175]. Here, $f(\Psi)$ is a free energy density containing the bulk entropic and enthalpic effects as described in Section 1.5.1. The term proportional to the parameter κ penalizes large gradients in $\Psi(\mathbf{r})$, which leads to interfaces of finite width between different phases [175]. The energy associated with κ induces a surface tension comparable to the one we introduced in Eq. (1.2). Generally, a system described by the free energy $\mathcal{F}[\Psi]$ behaves similarly to the one considered in the previous section. In particular, the relaxation toward equilibrium can be deduced from $\mathcal{F}[\Psi]$ by assuming that gradients in the chemical potential $\mu = \delta \mathcal{F}[\Psi] / \delta \Psi$ drive fluxes of the order parameter field Ψ , which explains the first term of Eq. (1.16).

The chemical reactions captured by the second term in Eq. (1.16) are not derived from equilibrium physics, but put in by hand. This artificial incorporation “pushes aside the thermodynamics underlying the reaction-diffusion problem studied” [176]. However, this can be reconciled by assuming that the “reactions were triggered and sustained by an external source [...], and were thus, in general, far from equilibrium” [177]. In fact, Eq. (1.16) dictates a chemical rate law instead of deriving the reaction rates from chemical potentials. Consequently, the chemical reactions described in this way “do not take into account the nonideality of the systems considered” [174]. On the other side, a thermodynamically consistent treatment complicates the equations significantly, and Eq. (1.16) can therefore be considered as a useful toy model for studying general reaction effects onto phase separation [174].

In this simple formulation, the chemical reactions tend to mix the system, i.e. any deviation from the homogeneous state $\Psi = 0$ will decay with rate k if the equilibrium dynamics are negligible. The chemical reactions thus oppose the phase separation physics and may introduce additional, non-equilibrium effects. Interestingly, the problem can be turned into an equilibrium one by rewriting Eq. (1.16) as

$$\partial_t \Psi(\mathbf{r}, t) = M \nabla^2 \mu'(\mathbf{r}, t), \quad (1.18)$$

where fluxes in the order parameter Ψ are driven by gradients in the new chemical potential $\mu' = \delta\mathcal{F}'[\Psi]/\delta\Psi$ [175]. The dynamics of Ψ close to equilibrium are thus solely derived from the new free energy functional [167]

$$\mathcal{F}'[\Psi(\mathbf{r})] = \mathcal{F}[\Psi(\mathbf{r})] + \frac{k}{M} \iint \Psi(\mathbf{r}) G(\mathbf{r}, \mathbf{r}') \Psi(\mathbf{r}') d^3r d^3r', \quad (1.19)$$

where $G(\mathbf{r}, \mathbf{r}')$ is a Green's function defined by $\nabla_{\mathbf{r}}^2 G(\mathbf{r}, \mathbf{r}') = -\delta(\mathbf{r} - \mathbf{r}')$. Both Eq. (1.16) and Eq. (1.18) yield the same dynamic equation for the order parameter field $\Psi(\mathbf{r}, t)$, but the final state is only at equilibrium with respect to $\mathcal{F}'[\Psi(\mathbf{r})]$. This equilibrium state can thus be determined by minimizing $\mathcal{F}'[\Psi(\mathbf{r})]$. For suitable boundary conditions, the Green's function in three dimensions is the Coulomb potential, $G(\mathbf{r}, \mathbf{r}') = (4\pi|\mathbf{r} - \mathbf{r}'|)^{-1}$. In this case, the last term in Eq. (1.19) therefore describes a long-ranged interaction, which is repulsive [167]. Conversely, the attractive interactions causing the phase separation are short-ranged. This competition of interactions can cause pattern formation [178]. Instead of coarsening indefinitely, these systems typically favor a pattern with a finite wavelength [179]. The typical wavelength Λ of such patterns depends on the reaction rate constant k . Christensen et al. found two different regimes with typical dependencies $\Lambda \propto k^{-1/3}$ and $\Lambda \propto k^{-1/4}$ for low and high reaction rates, respectively [167]. The equilibrium situation is recovered in the limit of vanishing k where Λ diverges and the system thus coarsens indefinitely. Generally, chemical reactions can therefore modify the equilibrium picture of phase separation and lead to pattern formation.

Apart from this basic mechanism of pattern formation, multiple extensions of the model given in Eq. (1.16) have been considered: In the case of unequal first-order rate constants in the reaction $A \rightleftharpoons B$, the order parameter Ψ will not be zero on average and droplets of the minority phase are typically observed [162, 168]. Similarly, considering the autocatalytic reaction $A + B \rightarrow 2B$ can also produce multiple stable droplets of the B -phase [163]. Furthermore, considering a ternary mixture can produce more complex patterns, including droplets [164]. Therefore, extending the model typically breaks the symmetric state where the order parameter Ψ is zero on average. This typically leads to a minority phase that forms droplets, which are stable due to the non-equilibrium conditions caused by the chemical reactions. Generally, a thermodynamically consistent treatment predicts that the system has to have autocatalytic reactions that are sufficiently far away from equilibrium in order to show pattern formation [174].

In this section, we showed briefly, that adding chemical reactions to a phase separating system can produce stable patterns. If we use the theory of phase separation to describe biological structures, we could thus expect similar phenomena. This is because chemical reactions, e.g. phosphorylation, acylation, and methylation, are very common in biological systems and drive them away from the thermodynamic equilibrium. In this thesis, we will show that centrosomes can be described as active droplets, i.e. the combination of phase separation and chemical reactions.

1.7 Overview of this thesis

Although centrosomes have been studied for more than a century [180], their formation is not understood. Several models have been proposed [16], but none of these provides a comprehensive picture of centrosome assembly.

In this thesis, we propose a theoretical model of centrosome growth that explains key experimental facts. We derive this model in Chapter 2 based on experimental facts and general assumptions. Here, centrosomes are described as active droplets, where chemical reactions influence the phase separation process. We discuss different properties of this model in the remaining chapters.

We start by considering isolated active droplets in Chapter 3. Here, we find critical droplet sizes that suppresses spontaneous droplet formation. We propose that catalytic active centrioles at the core of the centrosome control the droplet nucleation and thereby determine the count of the centrosomes. Furthermore, we find that surface tension causes the droplet to assume a spherical shape, as expected from the equilibrium theory. Interestingly, we also find that the centrioles can actively center themselves in the centrosome. In summary, the critical radius and the spherical shape are qualitatively similar to the equilibrium phase separation discussed in Section 1.5.

We find a striking difference to the equilibrium picture, when we investigate multiple droplets in Chapter 4. Here, multiple droplets can be stable due to non-equilibrium properties of the model. Ostwald ripening is suppressed and we can thus explain how both centrosomes are stable inside the cell, despite the considerable amount of thermal fluctuations due to the small system size. We consider the effect of fluctuations in Chapter 5. There, we develop a stochastic simulation of the active droplet model. Using these numerical simulations and some analytical models, we find that the nonlinearities in the model can enhance fluctuations. Furthermore, we vary the geometry of the system and find that this aspect only plays a minor role.

In Chapter 6, we compare the model to experimental data obtained from embryonic cells of *C. elegans*. We first determine the model parameters by taking them from the literature, estimating their order of magnitude, or determining them using a fit to the experimental data. We then discuss how the model can explain the quantitative experimental finding that the total volume of all centrosomes in a cell always adds up to a value that is proportional to the cell volume. Our model also accounts for some mutant data, where the cell size or the centrosome count has been disturbed. Here, the most interesting experiment results in two centrosomes of different size in the same cell. We can explain the full growth dynamics in this case and thus speculate about the origin of the size mismatch. Finally, we conclude this thesis with a summary and an outlook in Chapter 7.

Chapter 2

Physical Description of Centrosomes as Active Droplets

THE material properties of centrosomes are difficult to measure and are therefore not known at present [16]. In this chapter, we propose a physical picture of the centrosome material based on indirect experimental observations. We first introduce a detailed model describing the dynamics of the centrosome material and then consider three simple scenarios with distinct growth dynamics.

2.1 Physical description of centrosomes as liquid-like droplets

Centrosome growth is an assembly process by which pericentriolar material (PCM) accumulates around the centrioles. We describe this accumulation process as a phase separation. In order to account for the cyclic growth of the centrosomes, we will additionally add chemical reactions that control the phase separation process. In this section, we first discuss the physical properties of the PCM and then give the mathematical formulation of the model in the subsequent sections.

2.1.1 Pericentriolar material as a complex fluid

The PCM has no obvious structure if it is visualized by electron micrographs, see Fig. 1.6A. Our model is thus based on the description of the PCM as a homogeneous material. We assume that the PCM is visco-elastic and effectively behaves like a liquid on long time scales. We propose that interactions between PCM constituents cause the PCM to segregate from the cytosol in a phase separation process. In this picture, the centrosome is a dense phase of PCM, which can be described as a droplet in coexistence with the cytosol.

The lifecycle of centrosomes implies that droplet formation is regulated in time, see Fig. 1.4. This could be achieved either by controlling the amount of PCM proteins or by changing the interactions between the components during the cell cycle. If we consider the first cell divisions of the *C. elegans* embryo, division is fast and protein

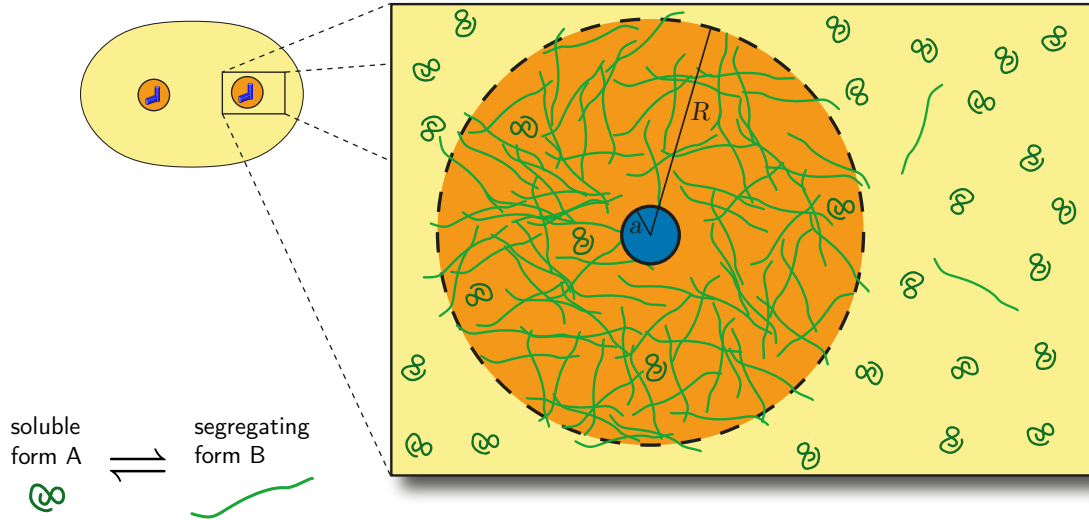


Figure 2.1: Schematic representation of a centrosome consisting of centrioles (blue) surrounded by a dense phase of pericentriolar material (PCM). In our model, the building blocks of the PCM (green) exist in two conformations: a form A that dissolves in the cytosol and a form B that segregates from the cytosol into a droplet phase (orange). The dynamics of the system is governed by diffusion of the components in the cytosol and transitions between the A and the B form. Furthermore, the centrioles and the droplet can catalyze the transition from A to B . The centrosome thus is described as a liquid droplet of PCM, which is nucleated by the centrioles and grows autocatalytically. Upper left: schematic representation of a cell with two centrosomes.

production and degradation can be neglected [181]. Consequently, the total amount of PCM components in the cell is approximately constant. This argument suggests that molecular properties of PCM components vary during the cell cycle to achieve centrosome assembly and subsequent disassembly. It is known that kinases such as PLK-1 are essential in regulating centrosome assembly [77, 86]. This raises the possibility that kinase activity changes the molecular properties of PCM components such that e.g. their solubility in cytosol is modified. In the following, we propose a simplified model of centrosome assembly based on the idea that PCM is made of subunits that can exist in two different forms: (i) building blocks that dissolve in the cytosol. We call this form A . (ii) Droplet material that phase separates from the cytosol and produces centrosomes. We call this form B . Chemical reactions such as a phosphorylation are assumed to switch between forms A and B and thereby regulate centrosome growth and disassembly, see Fig. 2.1.

The dynamics of these forms are given by three different processes: (i) the diffusion of PCM components, (ii) the chemical reactions converting the two forms into each other, and (iii) the phase separation causing the segregation of the droplet material of form B into the droplet phase. We will now describe these processes in detail.

2.1.2 Reaction-diffusion kinetics of the components

Centrosomes are embedded in the cytosol, which we describe as a simple fluid. The local composition of the system in the cytosol and also inside the centrosomes is characterized by the volume fractions ϕ^A of soluble building blocks and ϕ^B of droplet material. The components can diffuse and undergo chemical reactions in the cytosol and in the centrosome. The diffusion constants D_A and D_B of the two forms may in general differ inside and outside the centrosomes. The chemical reactions $A \rightleftharpoons B$, which switch the material between form A and form B , are described by the reaction rate s , which depends on the local composition. These processes can be described by reaction-diffusion equations,

$$\partial_t \phi^A = D_A \nabla^2 \phi^A - s(\phi^A, \phi^B) \quad (2.1a)$$

$$\partial_t \phi^B = D_B \nabla^2 \phi^B + s(\phi^A, \phi^B) . \quad (2.1b)$$

These equations are valid both inside and outside the centrosomes, however, not at the interface between the centrosome and the cytosol (see below). The reaction rate s enters as a sink in Eq. (2.1a) and as a source in Eq. (2.1b), but its dependence on the composition is not known experimentally. Generally, chemical reactions in biological systems are often driven by enzymes [1]. In its simplest form, the enzymatic catalysis of creating droplet material can be captured by the chemical reaction $A + E \rightarrow B + E$, where E denotes the enzyme. The rate of this reaction obviously depends on the concentration of E and therefore on its spatio-temporal dynamics. In the case of centrosomes, the enzyme driving the droplet formation is not known and we thus cannot write down a detailed model for it. In particular, we do not know the spatial distribution of E . As a consequence, we will examine two simple, generic cases in the following: (i) the enzyme is distributed homogeneously in the cell and the enzymatic reaction therefore reduces to the first-order reaction $A \rightarrow B$, and (ii) the enzyme preferably segregates into the PCM phase or, alternatively, is only active within the PCM phase. The latter possibility can be described by the autocatalytic reaction $A + B \rightarrow 2B$, where the presence of droplet material B catalyzes its own production from form A . Considering these two contributions, we propose the simple form of the bulk reaction rate

$$s(\phi^A, \phi^B) = k_{AB} \phi^A - k_{BA} \phi^B + k_c \phi^B \phi^A , \quad (2.2)$$

where k_{AB} and k_{BA} are the rate constants for the first-order reactions $A \rightarrow B$ and $B \rightarrow A$, respectively. The coefficient k_c in the last term describes the bimolecular, autocatalytic reaction $A + B \rightarrow 2B$. Note that this autocatalytic reaction will typically dominate inside the centrosome, where the form B is enriched. We only consider the case $k_c > 0$ in this thesis. Negative k_c would account for the reaction $A + B \rightarrow 2A$, which describes dissolving droplets.

The reaction rate given in Eq. (2.2) relies on simple rate laws proportional to the volume fractions of the reactants. Generally, chemical reaction rates are given by the chemical potentials and the simple form used here thus neglects the non-ideality of the system, as discussed in Section 1.6 and Ref. [174]. However, Eq. (2.2) can also be considered as a Taylor expansion of s for small ϕ^A and ϕ^B . In general, there are two additional terms quadratic in the volume fractions that are proportional to the square of ϕ^A and ϕ^B , respectively. They also describe cooperative transitions. We neglect those, since they do not yield the desired behavior: if the transition of the building blocks to droplet material was cooperative, $2A \rightarrow A + B$, the droplet material would be predominately produced in regions of high concentrations of building blocks, i.e. away from droplets. Conversely, cooperativity in the transition of droplet material to the soluble form, $2B \rightarrow A + B$, would destabilize droplets. In the bulk, we thus only consider reactions captured by the flux given in Eq. (2.2). This form allows us to discuss the effect of generic chemical transitions without the complications of a thermodynamically correct treatment [174].

Conservation of material in the complete system

The eggshell, which encloses the *C. elegans* embryo and therefore our volume of interest, is impermeable even to small molecules [182]. At the system boundary, we thus impose no-flux conditions for the volume fractions, which read

$$\mathbf{n} \nabla \phi^A = 0 \quad \text{and} \quad \mathbf{n} \nabla \phi^B = 0, \quad (2.3)$$

where \mathbf{n} is the surface normal vector at the boundary. Here, we assume no-flux conditions at the interface between different cells of the same embryo. This restriction is not significant, since all cells will have a similar concentration of PCM components and diffusive fluxes between cells should thus cancel.

We already assumed in the previous section that the total amount of PCM components in the cell is constant. This is obeyed by the reaction-diffusion system introduced in this section. The material conservation law can be formulated as a volume integral over the complete system volume,

$$\bar{\phi} V_c = \int_{\text{cell}} \{\phi^A + \phi^B\} d^3x, \quad (2.4)$$

where V_c is the total volume of the system and $\bar{\phi}$ denotes the average fraction of the PCM components in the system. The total volume of PCM components is thus given by $\bar{\phi} V_c$.

So far, we introduced a reaction-diffusion system describing how the PCM components behave in the bulk. It remains to discuss the centrosomes themselves. In general there are multiple centrosomes in the cell. For notational simplicity, we consider the case of spherical symmetry for each centrosome, where the volume fractions

depend on the distance r from the center of the centrosome. In this case, the total volume fraction flux passing a spherical shell at distance r is given by

$$J^A(r) = -4\pi r^2 D_A \partial_r \phi^A(r) \quad \text{and} \quad (2.5a)$$

$$J^B(r) = -4\pi r^2 D_B \partial_r \phi^B(r) \quad (2.5b)$$

for the two forms of the PCM components. Here, J has units of volume per time.

2.1.3 Centrioles described as catalytic active cores

At the core of each centrosome are two centrioles, which we represent by a small sphere of radius a . If centrioles only play a passive role, we would impose no-flux boundary conditions on their surface. However, motivated by the fact that centrioles can influence centrosome assembly [68], we propose that centrioles can catalyze the chemical reaction $A \rightarrow B$. This reaction induced by the centrioles is quantified by the total volume per unit time J of PCM components that is converted from form A to form B . We write $J = Q\phi^A(a)$, which implies a first order reaction at the centrioles, where the coefficient Q describes the centriolar enzymatic activity. The amount of PCM components is conserved, i.e. all soluble building blocks undergoing this reaction must appear as form B . This yields

$$-J^A(a) = J^B(a) = Q\phi^A(a), \quad (2.6)$$

which is a boundary condition for the Eq. (2.1) at the core of each centrosome. Note that $Q = 0$ corresponds to passive centrioles. In this case, the above equations reduces to no-flux conditions at the centrioles.

2.1.4 Droplet formation and growth kinetics

The reaction-diffusion system given in Eq. (2.1) together with the activity at the centrioles create a locally increased concentration of form B that gradually decreases at larger distances from the centrioles. However, so far there is no interface which separates the PCM phase from the cytosol. Formation of a PCM phase can be accounted for by phase separation of form B from the cytosol.

Coexistence condition at the interface

Considering the centrosome as a droplet phase implies that there exists an interface that separates the droplet from the cytosol. We consider an infinitesimal thin interface region, since the typically width of such interfaces is of the order of the size of the molecules [183]. At the interface, different volume fractions of PCM components coexist inside and outside the centrosome, see Section 1.5.2. The conditions of coexistence are governed by the local thermodynamic equilibrium at the interface between the droplet and the cytosol, see Fig. 2.2A. If the interface equilibrates

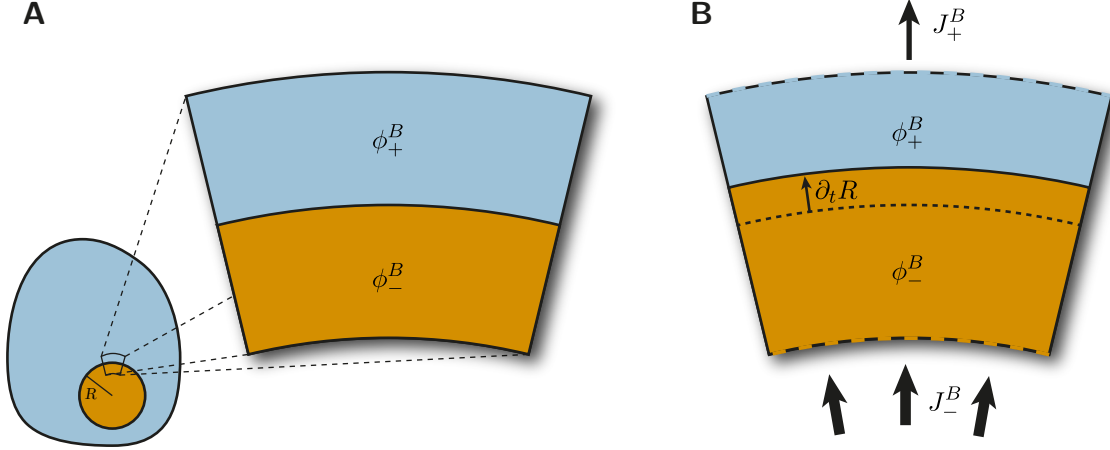


Figure 2.2: Schematic representation of the conditions at the interface between the droplet (orange) and the cytosol (blue). **(A)** A sketch of a test volume containing part of the interface is shown for the situation at short timescales. Here, the volume fractions ϕ_-^B and ϕ_+^B equilibrate as if the test volume was isolated. **(B)** A sketch of the same test volume is shown for the situation at longer time scales, where fluxes J^B of droplet material into and out of the test volume lead to a displacement $\partial_t R$ of the interface.

fast compared to changes in the composition induced by diffusive fluxes, these conditions can be taken from Eqs. (1.6). Consequently, the chemical potentials of each component must be equal on both sides of the interface. Additionally, the pressure difference between the inside and the outside is given by the Laplace pressure that is generated by the surface tension γ of the curved interface. The curvature of the interface is $1/R$, where R is the radius of the spherical droplet representing the centrosome. Using these thermodynamic principles, we obtain conditions for the equilibrium volume fractions of form B inside and outside the droplet, which we call ϕ_-^B and ϕ_+^B , respectively. These volume fractions have the form

$$\phi_-^B(R) \approx \psi_- + \frac{\gamma\beta_-}{R} \quad (2.7a)$$

$$\phi_+^B(R) \approx \psi_+ + \frac{\gamma\beta_+}{R}, \quad (2.7b)$$

for small surface tension, $\gamma \ll R\beta_{\pm}^{-1}$, and are equivalent to the equilibrium case given in Eqs. (1.8). Here, ψ_- and ψ_+ are the volume fractions that coexist at equilibrium at a flat interface. The coefficients β_- and β_+ describe the effects of surface tension, see Appendix A. The five parameters ψ_- , ψ_+ , β_- , β_+ , and γ are material properties of the PCM components and the cytosol. Note that we generally use the indices “−” and “+” to denote values at the inside and the outside of the droplet surface, respectively.

Similar arguments also yield a coexistence condition for the soluble building blocks of form A . Assuming that form A is well mixed with the cytosol and does not contribute to phase separation, it passively follows the phase separation and exhibits different solubilities in the two phases. This is described by

$$\frac{\phi_+^A(R)}{1 - \phi_+^B(R)} = \frac{\phi_-^A(R)}{1 - \phi_-^B(R)}, \quad (2.8)$$

where $1 - \phi^B$ is the volume fraction of the mixture of cytosol and soluble components A . This relation states that the building blocks occupy the same fraction of the available volume, $1 - \phi^B$, on both sides of the interface.

Rate of change of the droplet volume

The volume of a droplet is set by the number of its components together with their molecular volumes. Droplet growth is driven by the addition of droplet material to the droplet. Changes in volume can thus be related to compositional fluxes in and out of the droplet, see Fig. 2.2B. The volume fraction flux at the droplet surface can be derived from the fluxes passing a spherical shell defined in Eq. (2.5) and read

$$J_+^B(R) = \lim_{\varepsilon \rightarrow 0^+} J^B(R + \varepsilon) \quad (2.9a)$$

$$J_-^B(R) = \lim_{\varepsilon \rightarrow 0^+} J^B(R - \varepsilon), \quad (2.9b)$$

where $J_+^B(R)$ is the total flux of droplet material away from the droplet surface. Conversely, $J_-^B(R)$ denotes the total flux from the inside of the droplet toward its surface. The net flux of droplet material at the surface, $\Delta J^B = J_-^B(R) - J_+^B(R)$, thus drives droplet growth. This flux has to compensate for the difference $\phi_-^B(R) - \phi_+^B(R)$ in the volume fractions between the inside and the outside of the droplet surface, see Fig. 2.2B. In particular, the droplet material in a small shell around the droplet surface obeys a balance equation, $\Delta J^B = [\phi_-^B(R) - \phi_+^B(R)] \partial_t V$. The rate of change $\partial_t V$ of the droplet volume thus follows as

$$\partial_t V = \frac{J_-^B(R) - J_+^B(R)}{\phi_-^B(R) - \phi_+^B(R)}. \quad (2.10)$$

This equation captures the conservation of droplet material at the interface. The conservation of soluble building blocks at the interface yields a similar condition for ϕ^A at the interface, which reads

$$\frac{J_-^A(R) - J_+^A(R)}{\phi_-^A(R) - \phi_+^A(R)} = \frac{J_-^B(R) - J_+^B(R)}{\phi_-^B(R) - \phi_+^B(R)}, \quad (2.11)$$

where the J_-^A and J_+^A are defined analogously to Eq. (2.9).

2.1.5 Complete set of the dynamical equations

We thus arrive at a description of droplet growth that combines phase separation with chemical reactions. The state variables are the droplet volumes $V_i(t)$ together with the volume fractions $\phi^A(\mathbf{r}, t)$ and $\phi^B(\mathbf{r}, t)$, respectively describing the distribution of soluble building blocks and droplet material. They depend on the position $\mathbf{r} \in \mathbb{R}^3$ in space and on time $t \in \mathbb{R}$. The time evolution of the state variables is given by a reaction-diffusion system reading

$$\partial_t \phi^A = D_A \nabla^2 \phi^A - k_{AB} \phi^A + k_{BA} \phi^B - k_c \phi^B \phi^A \quad \text{and} \quad (2.12a)$$

$$\partial_t \phi^B = D_B \nabla^2 \phi^B + k_{AB} \phi^A - k_{BA} \phi^B + k_c \phi^B \phi^A \quad (2.12b)$$

with no-flux conditions at the system boundary,

$$\mathbf{n}(\mathbf{r}) \cdot \nabla \phi^{A/B}(\mathbf{r}, t) = 0, \quad (2.13)$$

where \mathbf{n} is the normal vector at the system boundary. We describe the i -th centrosome by a sphere with radius R_i . Assuming spherical symmetry, we express the volume fractions as functions of time t and the distance r to the center of the centrosome. The rate of change of the volume $V_i = (R_i^3 - a^3)4\pi/3$ then reads

$$\partial_t V_i(t) = \frac{J_-^B(R_i, t) - J_+^B(R_i, t)}{\phi_-^B(R_i) - \phi_+^B(R_i)}, \quad (2.14)$$

where $J_\pm^x(R) = -4\pi R^2 D_x \cdot \lim_{\varepsilon \rightarrow 0} [\partial_r \phi^x(r, t)]_{r=R \pm \varepsilon}$ and $\phi_\pm^x(R) = \lim_{\varepsilon \rightarrow 0} \phi^x(R \pm \varepsilon)$ for $x = A, B$. The droplet growth is thus coupled to the reaction-diffusion system of Eqs. (2.12). The description is completed by boundary conditions at the surface of the centrioles at $r = a$,

$$-D_A \partial_r \phi^A(r, t)|_{r=a} = D_B \partial_r \phi^B(r, t)|_{r=a} = \frac{Q \phi^A(a, t)}{4\pi a^2}. \quad (2.15)$$

Furthermore, the local equilibrium of the droplet interface imposes the conditions

$$\phi_\pm^B(R_i) = \psi_\pm + \frac{\gamma \beta_\pm}{R_i}, \quad (2.16a)$$

$$\frac{\phi_+^A(R_i, t)}{1 - \phi_+^B(R_i)} = \frac{\phi_-^A(R_i, t)}{1 - \phi_-^B(R_i)}, \text{ and} \quad (2.16b)$$

$$\frac{J_-^A(R_i, t) - J_+^A(R_i, t)}{\phi_-^A(R_i, t) - \phi_+^A(R_i, t)} = \frac{J_-^B(R_i, t) - J_+^B(R_i, t)}{\phi_-^B(R_i) - \phi_+^B(R_i)}. \quad (2.16c)$$

The dynamics of droplet growth are thus given by coupled partial differential equations. Important in this description are the moving boundary conditions summarized

in Eqs. (2.16). In the following, we will analyze both the transient dynamics and the long-term behavior of these equations. Here, we first introduce simplified scenarios based on limiting cases and then discuss more complex behaviors in the subsequent chapters.

2.2 Three simple growth scenarios

The droplet growth rate is determined both by the rate of the chemical reactions producing droplet material B and the rate at which material diffuses to the droplet. In this section, we consider the case of fast diffusion, $D_A, D_B \rightarrow \infty$, where the droplet growth is limited by the rate of the chemical reactions and the volume fractions are homogeneous in each compartment. For simplicity, we first consider vanishing surface tension, $\gamma = 0$, and the strong segregation regime, $\psi_+ = 0$, such that there is no droplet material right outside of the droplet surface, $\phi_+^B = 0$. We investigate m growing droplets of equal volume V placed in a system of volume V_c and we denote by ϕ_1^A and ϕ_0^A the volume fraction of soluble building blocks inside and outside of the droplets, respectively. They are linked by Eq. (2.8), which leads to $\phi_1^A = (1 - \psi_-)\phi_0^A$. With the assumptions from above, the volume fraction ϕ_1^B of droplet material inside of droplets is given by ψ_- , see Eq. (2.7a). Since we consider strong phase separation and fast diffusion, the droplet material is confined to the droplets in the simple scenarios discussed here. The material conservation equation (2.4) then reads $\bar{\phi}V_c = (\psi_- + \phi_1^A)mV + (V_c - mV)\phi_0^A$. It can be solved for the volume fraction ϕ_0^A of building blocks in the cytosol,

$$\phi_0^A \approx \bar{\phi} - \frac{\psi_- mV}{V_c}, \quad (2.17)$$

where we assumed that droplets only occupy a small fraction of the total volume, $mV \ll V_c$. The rate of change of the droplet volumes is given by the change in the amount of droplet material,

$$\psi_- m \partial_t V = J^S, \quad (2.18)$$

i.e. the temporal change of the total volume of droplet material is given by the total reaction flux J^S in the system. J^S can be determined by integrating the reaction rate s given in Eq. (2.2) over the entire system volume and adding the effects of the catalytic centrioles, see Eq. (2.6). In summary, this yields

$$J^S \approx k_{AB}V_c\phi_0^A - k_{BA}mV\psi_- + k_c mV\phi_1^A\psi_- + mQ\phi_1^A. \quad (2.19)$$

Inserting J^S into Eq. (2.18), we arrive at an ordinary differential equation for the droplet volume $V(t)$, which we can solve.

We now investigate several limiting cases of the model to test whether a single scenario can account for the dynamics of centrosomes observed in experiments. The most important parameters of our model will be the reaction rates. There are three different ways of producing droplet material of form B :

- (i) by the first-order chemical reaction with rate constant k_{AB} ,
- (ii) by the autocatalytic mechanism with rate constant k_c , and
- (iii) by the catalytic activity of the centrioles, parameterized by Q .

We start by individually examining the effects of these rates on the growth of droplets. For this purpose, we will set the value of the other two parameters to zero and examine what happens to droplet growth when only one of the parameters is active.

2.2.1 Scenario A: First-order kinetics

We first examine the case where droplet material of form B is generated by first-order kinetics from form A ($k_{AB} > 0$, $k_c = 0$, $Q = 0$). The droplet material is produced in the complete system and can segregate in a preexisting droplet leading to droplet growth. The time it takes for the material produced in the cytosol to diffuse to the preexisting droplet is negligible in the reaction-limited case. The differential equation for the droplet volume reads

$$\partial_t V \approx \frac{\bar{\phi} k_{AB}}{m \psi_-} V_c - (k_{AB} + k_{BA}) V. \quad (2.20)$$

This linear equation can be solved for the droplet volume as a function of time,

$$V(t) \approx \frac{\bar{\phi} V_c k_{AB}}{m \lambda_A \psi_-} (1 - e^{-t \lambda_A}), \quad (2.21)$$

where the growth rate is given by $\lambda_A = k_{AB} + k_{BA}$. The growth slows down due to the depletion of the soluble building blocks of form A and the system reaches a steady state after a characteristic time λ_A^{-1} , see the blue lines in Fig. 2.3. In panel B of this figure, we additionally show numerical solutions of the full model. The details of the implementation are given in Appendix C. We compare the reaction-limited case (blue line) with one where we include the effects of diffusion and surface tension (green line). These additions slow down the growth of the droplet slightly. The major deviation happens in the initial phase where the growth of the model with diffusion accelerates. This is caused by the sudden activation of the chemical reaction producing droplet material in the cytosol which then diffuses to the droplet. The diffusive influx increases with growing droplets creating a positive feedback which explains the initial acceleration of the droplet growth. Nonetheless, the growth of

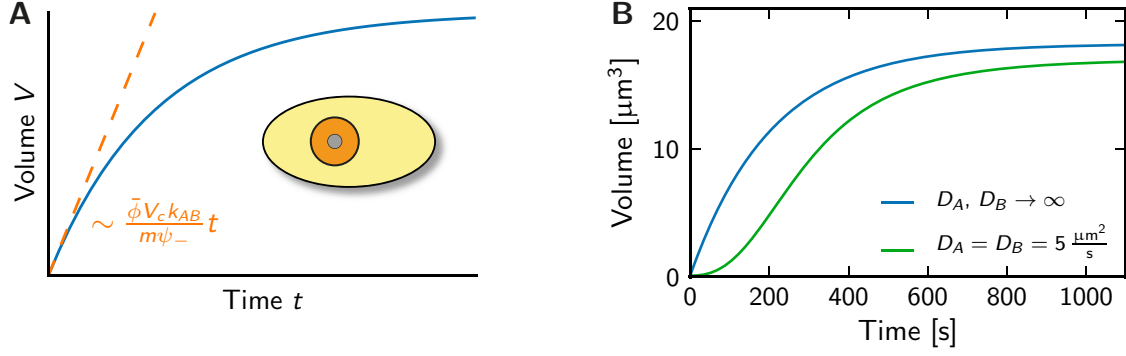


Figure 2.3: Droplet volume V as a function of time in scenario A, where the form B is generated by first-order kinetics from form A . **(A)** Schematic growth curve (blue line). The orange dashed line indicates the maximal volume growth and the corresponding time dependence is given. The droplet material is produced in the entire system, which is indicated by the bright colors in the schematic inset. **(B)** Numerical simulations of the reaction-limited case (blue) and the droplet growth including diffusion and surface tension (green). The parameter values of scenario A are: $V_c = 10^4 \mu\text{m}^3$, $a = 0.075 \mu\text{m}$, $\psi_- = 0.1$, $\psi_+ = 0$, $D_{A/B} = 5 \mu\text{m}^2/\text{s}$, $k_{BA} = 10^{-3} \text{s}^{-1}$, $k_{AB} = 0.016 \text{s}^{-1}$, $k_c = 0$, $Q = 0$, $\gamma = 1 \text{ pN}/\mu\text{m}$, and $\beta_{\pm} = 10^{-6} \mu\text{m}^2/\text{pN}$.

the droplet in scenario A is qualitatively captured by Eq. (2.21) even if the effects of a finite diffusivity and surface tension alter the initial phase.

Furthermore, we can also study the long time behavior of the model. The stationary state droplet volume,

$$V^A \approx \frac{\bar{\phi} V_c k_{AB}}{(k_{AB} + k_{BA}) m \psi_-}, \quad (2.22)$$

is derived from the long time limit of Eq. (2.21). This expression can be understood by comparing it to the droplet volume in an equilibrium system given in Eq. (1.11). In the scenario discussed here, the droplet components can be either in their soluble form A or in the phase separating form B . Only the latter form segregates into droplets and its fraction ϕ^B in the system thus determines the final droplet size. Consequently, ϕ^B can be used in Eq. (1.11) instead of the fraction $\bar{\phi}$ of droplet material in the equilibrium system. We get the fraction ϕ^B of the B form by assuming that the chemical reactions $A \rightleftharpoons B$ are in equilibrium. This leads to the simple solution $\phi^B = k_{AB} \bar{\phi} / (k_{AB} + k_{BA})$, which we use instead of $\bar{\phi}$ in Eq. (1.11). The resulting expression is identical to Eq. (2.22). Consequently, the chemical equilibrium between the two forms determines the amount of droplet material and therefore the droplet size in scenario A.

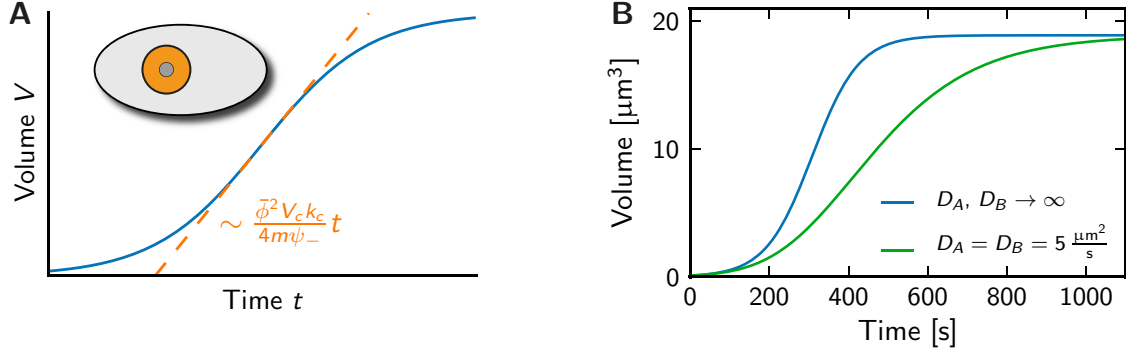


Figure 2.4: Droplet volume V as a function of time in scenario B, where the form B is generated by the autocatalytic reaction. **(A)** Schematic growth curve (blue line). The orange dashed line indicates the maximal volume growth and the corresponding time dependence is given. The droplet material is produced inside the droplets themselves (orange region in schematic inset). **(B)** Numerical simulations of the reaction-limited case (blue) and the droplet growth including diffusion and surface tension (green). The parameter values of scenario B are: $V_c = 10^4 \mu\text{m}^3$, $a = 0.075 \mu\text{m}$, $\psi_- = 0.1$, $\psi_+ = 0$, $D_{A/B} = 5 \mu\text{m}^2/\text{s}$, $k_{BA} = 10^{-3} \text{s}^{-1}$, $k_{AB} = 0$, $k_c = 100 \text{s}^{-1}$, $Q = 0$, $\gamma = 1 \text{ pN}/\mu\text{m}$, and $\beta_{\pm} = 10^{-8} \mu\text{m}^2/\text{pN}$.

2.2.2 Scenario B: Autocatalytic growth

Here, we consider the case where droplet material of form B is generated by a second-order reaction that depends on the concentration of preexisting B ($k_{AB} = 0$, $k_c > 0$, $Q = 0$). The droplet material of form B is thus predominately produced inside the preexisting droplet itself. Because growth is autocatalytic, larger droplets recruit material at a higher rate than smaller ones. The differential equation describing droplet growth reads

$$\partial_t V \approx [(1 - \psi_-)\bar{\phi}k_c - k_{BA}] V - \frac{(1 - \psi_-)\psi_- m k_c}{V_c} V^2, \quad (2.23)$$

see Eqs. (2.17)–(2.19). The resulting growth,

$$V(t) \approx \frac{V_c \lambda_B}{(1 - \psi_-) m k_c \psi_-} \left(1 + \tanh[(t - t_0)\lambda_B] \right), \quad (2.24)$$

exhibits a sigmoidal shape, see Fig. 2.4. Here, the characteristic growth rate is given by $\lambda_B = \frac{1}{2}[(1 - \psi_-)\bar{\phi}k_c - k_{BA}]$ and t_0 is a parameter set by the initial volume. The sigmoidal shape is caused by the autocatalytic reaction: initially, there is sufficient material in the cell and the growth rate is limited by the droplet size and therefore proportional to the droplet volume. This leads to self-reinforcing growth and thus a

droplet volume that increases exponentially with time. Conversely, if droplets are large enough at later times, they have depleted their surrounding and the amount of available building blocks becomes limiting. They then experience the same relaxation to the stationary state that was also observed in scenario A.

Note that if only the autocatalytic reaction would produced droplet material of form B , droplets could not form spontaneously: if there was no droplet material, the autocatalytic reaction would be halted. It is thus plausible that droplets can only grow in the autocatalytic scenario if enough material is present to overcome the inevitable loss by the reaction $B \rightarrow A$. This can also be observed in the stationary state droplet volume,

$$V^B \approx \frac{V_c}{m\psi_-} \left(\bar{\phi} - \frac{k_{BA}}{(1-\psi_-)k_c} \right), \quad (2.25)$$

which is derived from the long-time limit of Eq. (2.24). This expression predicts unphysical negative volumes for small volume fractions $\bar{\phi}$ of PCM components. Proper droplets can thus only form if there is enough material in the system. The threshold value

$$\bar{\phi}_{\min}^B = \frac{k_{BA}}{(1-\psi_-)k_c} \quad (2.26)$$

is calculated from the point where the right hand side of Eq. (2.25) vanishes. In the autocatalytic scenario, droplet formation is thus only possible if $\bar{\phi} > \bar{\phi}_{\min}^B$. This is in contrast to the case of first-order kinetics, where droplets may also form for very small amounts of material.

2.2.3 Scenario C: Incorporation at the centrioles

In this case, we consider that droplet material of form B is produced by a reaction that happens at the surface of the centrioles ($k_{AB} = 0$, $k_c = 0$, $Q > 0$). Here, the material naturally accumulates around the centrioles. Consequently, the number of droplets and their position is dictated by the centrioles. The droplet growth rate is given by the amount of material produced at the centrioles, which is proportional to the concentration of the soluble building blocks. The differential equation for the droplet volume is given by

$$\partial_t V \approx \frac{(1-\psi_-)\bar{\phi}Q}{\psi_-} - \frac{(1-\psi_-)mQ + k_{BA}V_c}{V_c} V, \quad (2.27)$$

see Eqs. (2.17)–(2.19). The resulting droplet volume in dependence on time reads

$$V(t) \approx \frac{1-\psi_-}{\psi_-} \cdot \frac{\bar{\phi}Q}{k_{BA} + (\lambda_C - k_{BA})m} (1 - e^{-t\lambda_C}), \quad (2.28)$$

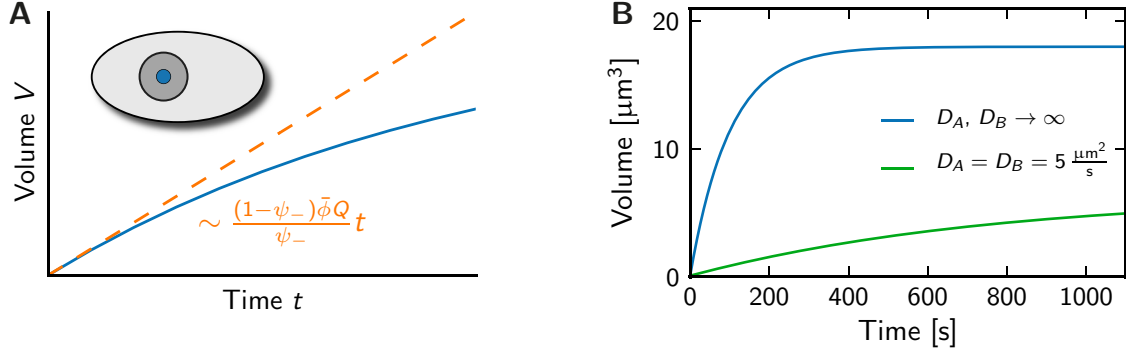


Figure 2.5: Droplet volume V as a function of time in scenario C, where the droplet material B is generated at the centrioles. **(A)** Schematic growth curve (blue line). The orange dashed line indicates the maximal volume growth and the corresponding time dependence is given. The droplet material is produced at the centrioles (blue region in schematic inset). **(B)** Numerical simulations of the reaction-limited case (blue) and the droplet growth including diffusion and surface tension effects (green). The parameter values of scenario C are: $V_c = 10^4 \mu\text{m}^3$, $a = 0.075 \mu\text{m}$, $\psi_- = 0.1$, $\psi_+ = 0$, $D_{A/B} = 5 \mu\text{m}^2/\text{s}$, $k_{BA} = 10^{-3} \text{s}^{-1}$, $k_{AB} = 0$, $k_c = 0$, $Q = 100 \mu\text{m}^3/\text{s}$, $\gamma = 1 \text{pN}/\mu\text{m}$, and $\beta_{\pm} = 10^{-7} \mu\text{m}^2/\text{pN}$.

i. e. growth slows down and the system reaches a steady state after a characteristic time λ_C^{-1} , with $\lambda_C \approx k_{BA} + (1 - \psi_-)mQ/V_c$, see Fig. 2.5. The stationary state volume,

$$V^C \approx \frac{1 - \psi_-}{\psi_-} \cdot \frac{\bar{\phi} Q V_c}{V_c k_{BA} + (1 - \psi_-) m Q}, \quad (2.29)$$

is again derived from the long-time limit of the growth curve. It is proportional to the activity Q of the cores in the limit of a large system. Since Q can be interpreted as a reaction rate constant times the volume of the centrioles, the maximal growth rate of the droplet, $(\partial_t V)_{\max} \approx (1 - \psi_-)\bar{\phi}Q/\psi_-$, is proportional to the volume of the centrioles. This raises the question whether the pictured scenario is sufficiently efficient to produce droplets fast enough. For a very high rate of conversion of PCM components, however, we can no longer assume that diffusion is fast. Fig. 2.5B shows that the diffusion of PCM components can slow down the growth significantly. In scenario C, it is therefore instructive to also consider the diffusion-limited case, where the incorporation reaction at the core is fast and droplet growth is limited by the diffusive influx.

2.3 Diffusion-limited droplet growth

We now consider the diffusion-limited growth of a droplet, where the droplet material is incorporated at the centrioles. To simplify the calculation, we consider a single droplet located at the origin of a spherical cell of radius R_c . We also neglect the reaction $B \rightarrow A$ for simplicity, $k_{BA} = 0$. With these approximations, the model becomes a diffusion problem in spherical coordinates with a reflective boundary condition at $r = R_c$ and an absorbing boundary condition at the centrioles, at $r = a$. It can be solved analytically using a modified Fourier method, see Appendix D. Considering an initially homogeneous system, $\phi(r, t = 0) = \bar{\phi}$, the droplet volume as a function of time reads

$$V(t) = \frac{\bar{\phi}}{\psi_-} \left[V_c - \sum_{k=1}^{\infty} \frac{(2 + 2R_c^2\alpha_k^2)4\pi a^2}{(R_c - a)R_c^2\alpha_k^4 - a\alpha_k^2} e^{-D_A\alpha_k^2 t} \right]. \quad (2.30)$$

The admissible inverse length scales α_k are given by the positive solutions of the equation $\alpha_k R_c = \tan[(R_c - a)\alpha_k]$. The α_k have associated time scales $\tau_k = D_A^{-1}\alpha_k^{-2}$ that give the decay time of the modes in Eq. (2.30). The two longest time scales are

$$\tau_1 \approx \frac{V_c}{4\pi a D_A} \quad \text{and} \quad \tau_2 \approx \frac{V_c}{3\pi^2 R_c D_A}, \quad (2.31)$$

where we used that the centrioles are much smaller than the complete system, $a \ll R_c$. The longer time scale τ_1 is dominant, since $\tau_1/\tau_2 \approx R_c/a \approx 100$, where we used $R_c \approx 10 \mu\text{m}$ [24] and $a \approx 100 \text{ nm}$ [56]. We thus simplify the solution given in Eq. (2.30) by only considering the slowest mode, which yields

$$V(t) \approx \frac{\bar{\phi} V_c}{\psi_-} (1 - e^{-t/\tau_1}). \quad (2.32)$$

Hence, τ_1 is the characteristic time after which the stationary state is reached, i.e. it is an estimate of how long it takes to deplete the complete system by taking away soluble building blocks at the centrioles. As we show later, because of the small size of the centrioles, the time scale τ_1 is typically long, and diffusion thus significantly limits the rate of droplet growth in scenario C, see also Fig. 2.5B.

In scenarios A and B, we neglected diffusion completely, although it might also influence the growth dynamics there, see Fig. 2.3B and Fig. 2.4B. We will thus now estimate the time scales of growth in these scenarios, assuming that the growth was diffusion-limited. To this end, we can use the results of the previous paragraph, i.e. the slowest growth time given in Eq. (2.31). This expression was derived for a situation, where the centrioles deplete the cytosol of soluble building blocks in a diffusion-limited manner. In scenario B, the soluble building blocks are converted inside droplet. It is thus the entire droplet, which takes away soluble building blocks from the system. In order to estimate the time scale of diffusion-limited growth, it

is therefore sufficient to replace the radius a by a typical droplet radius in Eq. (2.31). Strictly spoken, this is only true if the droplet would not change its size. However, since we are only interested in a rough estimation of the droplet growth time, we for simplicity neglect the complications that arise from the increasing droplet radius. The time scale of growth in a diffusion-limited variant of scenario B can then be estimated as $\tau_1^B \approx V_c/(4\pi\tilde{R}D_A)$, where \tilde{R} is a typical droplet size. The diffusion-limited variant of scenario A is similar: here, droplet material is produced in the cytosol and has to diffuse to the droplet subsequently. If diffusion is limiting, the time scale of droplet growth is thus determined by the diffusion of the droplet material to the droplet. Since the incorporation of material still happens in the entire droplet, we again replace a by \tilde{R} and can thus estimate the growth time scale as $\tau_1^A \approx V_c/(4\pi\tilde{R}D_B)$. Here, we replaced the diffusion constant of the building blocks by that of the droplet material. In summary, droplet growth in scenarios A and B is quicker than in scenario C by a factor \tilde{R}/a , assuming that the diffusion constants D_A and D_B are comparable.

2.4 Discussion

We derived a theoretical model describing the accumulation of PCM and thus the growth of centrosomes in this chapter. It is based on the idea that the PCM has the inherent tendency to aggregate and therefore segregates from the cytosol in a phase separation process. We proposed that the material has two conformations with different segregation properties. The kinetics of the transitions between these states regulate the droplet formation. Control over the transition rates could then be used to steer the cyclic growth observed in experiments. In general, we thus investigate a phase separation process augmented by chemical reactions.

Our model is based on a reaction-diffusion system, where we neglect directed transport. This directed transport could happen along specific tracks, e.g. microtubules [1], or by flows in the cytosol, which advects components. It has been shown experimentally that microtubules do not influence centrosome growth in *C. elegans* [82]. This is also seen from the fact that the size of centrosomes does not change if the amount of the protein TAC-1 is reduced in *C. elegans* [184], although TAC-1 strongly influences the length of microtubules [185]. Microtubules therefore do not seem to play a significant role in centrosome growth. Conversely, cytosolic flows have been reported for *C. elegans* [186]. Taking typical values for the cytosolic flow speed of $v \approx 5 \mu\text{m}/\text{min}$ [186], a droplet radius of $R \approx 1 \mu\text{m}$ [24], and a diffusion constant of the PCM components of $D \approx 5 \mu\text{m}^2/\text{s}$ [86], the associated Péclet number is $vR/D \approx 1/60$. The centrosomes themselves also move inside the cytoplasm [187]. A typical speed is $15 \mu\text{m}/\text{min}$, which then leads to a Péclet number of $1/20$. We will therefore consider stationary centrosomes, which only change their size, but not their position. In summary, diffusion of monomers is dominant over advection, which justifies our approximation.

Table 2.1: Conversion table for terms used in this thesis.

Biological context		Physical context
Cytosol	\leftrightarrow	Solvent
Centrosome/PCM	\leftrightarrow	Droplet
PCM components	\leftrightarrow	Droplet components
(Enzymatically active) centrioles	\leftrightarrow	(Active) core

We assume that the diffusive flux of PCM components is driven by gradients in their volume fractions, which is a valid description for simple diffusion. However, cytosol is generally expected to show subdiffusive behavior [188, 189], which would modify the reaction-diffusion equation (2.1). Simple diffusion has been observed in *C. elegans* embryos, though [190]. Additionally, diffusion will not be the major factor determining the growth behavior in our model and we will often discuss the limit of infinite diffusivity anyway. Taken together, approximating the generally complex behavior of proteins in cells by a reaction-diffusion equation for the PCM components seems justified in our case.

We describe the chemical reactions, which switch the PCM components between the phase separating and the soluble form, by a generic reaction flux s that includes reactions of first and second order. We used this general approach since the precise biochemistry of the centrosome proteins is not known. We will discuss this issue in some more detail when we compare the model to experimental data in Chapter 6. The idea that post-translational modifications can influence the physical properties of proteins is not completely new, though. The properties of many proteins can be modified by a chemical reaction called phosphorylation where a phosphate group is added to the protein [1]. Interestingly, phosphorylation has already been observed to influence phase separation dynamics of proteins in cells [191, 192].

The key feature of our model is the interplay of phase separation and chemical reactions. The model describes a non-equilibrium system, where energy can be exchanged with the surrounding, thus allowing the system to stay away from the thermodynamic equilibrium. We showed briefly that the chemical reactions can be identified with a long-ranged repulsive interaction, while the phase separation is driven by short-ranged attractive forces, see Section 1.6. Such systems may generally lead to pattern formation [178]. We will investigate this point further in Chapter 4, where we consider the stability of multiple droplets growing in the same system.

Generally, our model might apply to other system where droplets are formed by phase separation and the droplet material is influenced by chemical reactions. We thus use a neutral language, where we speak of (active) droplets that are immersed in a solvent and have an (active) core at their center. In the context of the biological example, these droplets are the centrosomes immersed in the cytosol with their

centrioles at the center. The term «active» in this context describes the non-equilibrium chemical reactions producing the droplet material, either in the droplet or at the core. The relations of these terms are summarized in Table 2.1. After we discussed the physical properties in the next three chapters, we compare the model to experimental data in Chapter 6. There, we again focus on the case of centrosomes.

Chapter 3

Isolated Active Droplets

THE active droplets we consider in this thesis form by phase separation of droplet material. This droplet material is produced by chemical reactions from soluble building blocks. We also allow for the possibility that an active core located at the center of a droplet catalyzes the production of droplet material. The chemical reactions in the bulk and at the core make the model non-equilibrium. This explains the notation of «active droplets» and «active cores» that we use throughout the chapter to distinguish our model from equilibrium systems.

We now examine the introduced model in more detail. In this chapter, we investigate the behavior of individual droplets. We will first consider the initial phase of droplet growth, where droplets are small. Later in the chapter, we investigate large droplets and the stability of the spherical shape, which droplets typically exhibit because of surface tension effects. The more complicated case of multiple droplets will then be discussed in the subsequent chapter.

3.1 Compositional fluxes in the stationary state

We discussed three reaction-limited scenarios of the model in Section 2.2 and we found that diffusion had only a significant impact on droplet growth in scenario C, see Section 2.3. In this scenario, where the incorporation of droplet material is driven by the active core, the diffusion of soluble building blocks limits the rate at which the droplet can grow. Conversely, the droplet growth was not limited by diffusion in the other two scenarios. However, diffusion also becomes relevant in scenarios A and B when surface tension γ is considered. In this case, the coexisting volume fractions at the droplet surface depend on the droplet radius R , see Eq. (2.7). Due to this dependence, the droplet radius and the volume fractions at the surface influence each other. It is thus difficult to look at surface tension in time-dependent droplet growth and we first discuss the stationary states and their stability only.

Concentration profiles in the stationary state

We consider the model in the stationary state, where time derivatives vanish. The reaction-diffusion system given in the Eqs. (2.1) then reduces to simpler equations

where only spatial derivatives appear. We reduce the complexity further by considering a single droplet growing in a spherical geometry. In this geometry, the complete system becomes spherical symmetric and the fractions $\phi^A(r)$ and $\phi^B(r)$ of the two components only depend on the distance r to the center of the droplet. This approximation simplifies notation and calculations greatly and changes the results only slightly as we will show later in Section 5.4.

We next simplify the expression for the reaction rate s given in Eq. (2.2). Here, the first-order reactions depend linearly on the volume fractions. However, the bimolecular reaction $A + B \rightarrow 2B$ yields a non-linear term, since it depends on the product of the volume fractions of form A and form B . Form B drives the phase separation and the associated volume fraction ϕ^B thus assumes vastly different values inside and outside of the droplet. Surface tension effects and spatial inhomogeneities within compartments are negligible compared to this difference and we thus approximate ϕ^B by ψ_- and ψ_+ inside and outside of the droplet, respectively. This substitution linearizes the non-linear term in the reaction rate of Eq. (2.2), which then reads

$$s \approx k_{AB}\phi^A - k_{BA}\phi^B + \begin{cases} k_c\psi_-\phi^A & r < R \\ k_c\psi_+\phi^A & r \geq R \end{cases}. \quad (3.1)$$

This approximation is good if the gradients in ϕ^B are weak. Note that we only use this approximation to simplify the reaction rate, but we keep track of the full volume fraction profile of the droplet material otherwise.

We use the approximations introduced in this section to determine the stationary state of the model, see Appendix F. The first result of this analysis are the profiles of the volume fractions as a function of the distance r to the droplet center. The volume fractions of the different forms vary by orders of magnitudes, which makes the respective plots difficult to read, see Fig. F.1 in Appendix F. This is mainly caused by the phase separation process, which concentrates droplet material of form B inside the droplet leading to much higher volume fractions there. To simplify the discussion in the following, we thus focus on a schematic representation of the stationary state profiles given in Fig. 3.1. Here, the general shapes of the profiles are preserved, but their values are not drawn to scale.

Fig. 3.1 reveals gradients in the volume fraction profiles, which are related to compositional fluxes, see Eq. (2.5). These fluxes are caused by the chemical reactions and can only exist in non-equilibrium systems. In fact, these non-equilibrium effects are responsible for most results that we will describe in the following and we thus start by quantifying the compositional fluxes further.

Compositional fluxes in the stationary state

The schematic picture in Fig. 3.1 shows the stationary state fluxes for the two growth scenarios A and B. There is a qualitative difference in the direction of the fluxes: for the case of first-order kinetics, droplet material of form B is mainly produced in

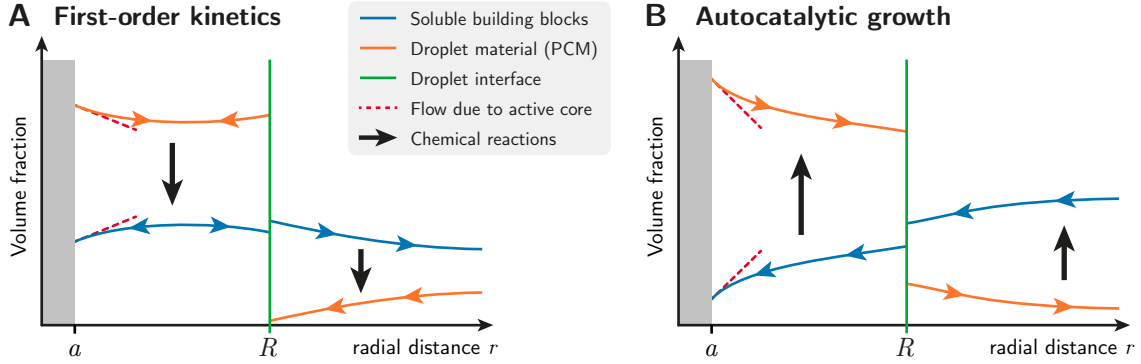


Figure 3.1: Schematic representation of the stationary volume fraction profiles as a function of the distance r to the droplet center. The droplet extends to the interface at $r = R$ (green line). Chemical reactions cause a conversion of the droplet components (black arrows) and the activity of the core (grey area) sets the slope at $r = a$ (red line). Note that fluxes across the interface are opposite in the two scenarios: **(A)** First-order kinetics, where droplet material is produced in the whole system. **(B)** Autocatalytic growth, where droplet material is produced inside droplets.

the solvent and then diffuses toward the droplet, where it concentrates due to the phase separation; it then gets converted back to the soluble form A inside the droplet and diffuses away from the droplet, closing the cycle, see Fig. 3.1A. Conversely, in the autocatalytic scenario, droplet material of form B is predominately produced inside the droplet and then partly diffuses away from the droplet; it gets turned back to its soluble form A in the solvent and subsequently diffuses back to the droplet, closing the cycle, see Fig. 3.1B. The material thus flows in opposite directions in the two scenarios. In particular, the directions of the net flux induced by the chemical reactions are opposite in the two scenario, see the black arrows in Fig. 3.1.

We are left to discuss the influence of the active cores, which impose a flux at the inner boundary at $r = a$, see Eq. (2.6) and the red dashed lines in Fig. 3.1. We can determine their importance in the stationary state by quantifying the material flux induced by the reaction $A \rightarrow B$ in three important compartments: at the core, in the droplet, and in the solvent. Using the concentration profiles in stationary state, we plot the three associated integrated reaction fluxes versus the droplet radius in Fig. 3.2. It is evident from this plot that the cores only contribute little to the production of droplet material of form B for typical droplet sizes. Note that the reaction fluxes are comparable for small droplets in the autocatalytic scenario.

Fig. 3.2 furthermore shows the magnitude of flux J^B across the surface of the droplet, which can be quantified using Eq. (2.9). Comparing the two scenarios, $|J^B|$ is much larger in scenario A, since droplet material is predominately produced in the solvent and flows toward the droplet there. In scenario B, the droplet material is produced in the droplet and thus flows in the opposite direction.

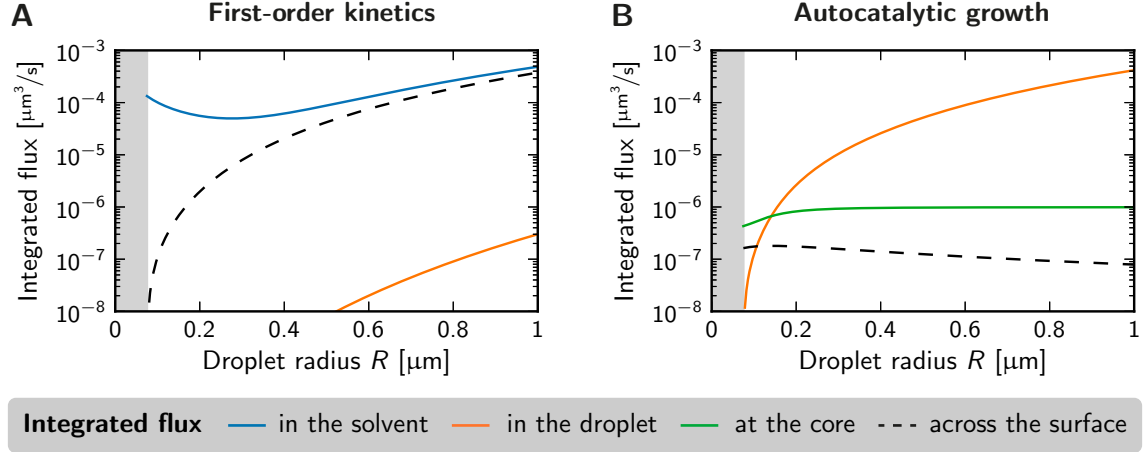


Figure 3.2: Integrated fluxes of material in the stationary state as a function of the droplet radius R . The magnitude of the fluxes caused by the reaction $A \rightarrow B$ in the solvent (blue), in the bulk of the droplet (orange), and at the active cores (green) are shown. The magnitude of the flux of droplet material across the droplet surface is shown for comparison (black dashed line). R is varied by changing the fraction $\bar{\phi}$ of droplet components. **(A)** First-order kinetics with parameters given in Fig. 2.3. **(B)** Autocatalytic growth with a catalytic activity $Q = 0.1 \mu\text{m}^3/\text{s}$ and remaining parameters given in Fig. 2.4.

Generally, the flux J^B across the droplet surface can be estimated by looking at a stationary concentration profile around the droplet and quantifying J^B from the definition given in Eq. (2.9), see Appendix E. This procedure has also been used in the seminal paper by Lifshitz and Slyozov [138] and leads to

$$J^B(R, \phi_0^B) \approx 4\pi D_B R \cdot (\phi_+^B(R) - \phi_0^B) , \quad (3.2)$$

see Eq. (E.4) in the appendix. J^B is thus driven by the difference in the volume fraction $\phi_+^B(R)$ at the interface and the volume fraction ϕ_0^B far away from the droplet. This flux destabilizes small droplets, which we investigate in the next section.

3.2 Critical droplet size: Instability of small droplets

Fig. 3.3 shows the droplet radius in the stationary state as a function of the fraction $\bar{\phi}$ of droplet components. Additionally, we indicate the stability of all states, which is determined by a linear stability analysis, see Appendix F. In the strong segregation regime, $\psi_+ = 0$, and without surface tension effects, $\gamma = 0$, we only find stable droplets in scenarios A and B, see the green lines in Fig. 3.3. These lines are consistent with the analytical estimates given in Eqs. (2.22) and (2.25). In scenario A, droplets exist for all values of $\bar{\phi}$, while $\bar{\phi}$ has to be above a threshold $\bar{\phi}_{\min}^B$ in scenario B. We

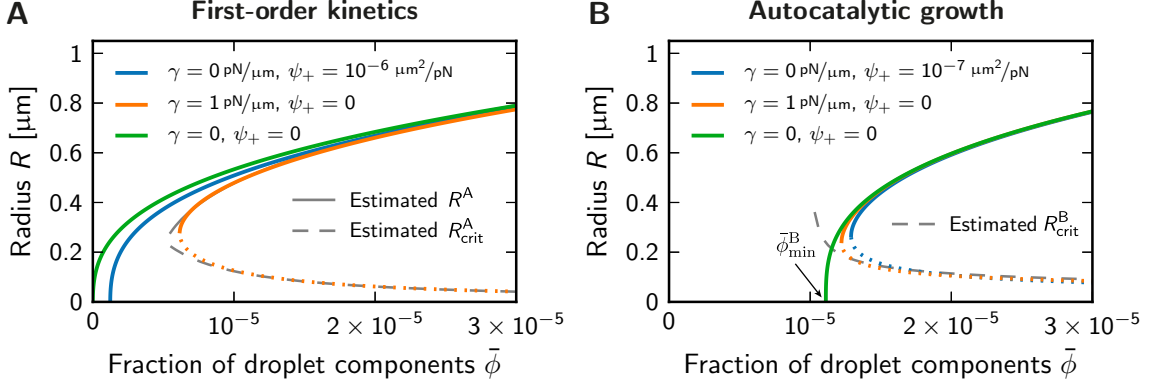


Figure 3.3: Radii of stationary droplets as a function of the overall volume fraction $\bar{\phi}$ of droplet components for different values of surface tension γ and basal volume fraction ψ_+ . **(A)** First-order kinetics with parameters given in Fig. 2.3. **(B)** Autocatalytic growth with parameters given in Fig. 2.4. The dotted parts of the curves indicate unstable stationary states and the grey dashed lines are estimates thereof, see Eq. (3.5) and Eq. (3.6).

already calculated this threshold earlier, see Eq. (2.26). Taken together, droplets are thus always stable and their size increases if there are more droplet components if we consider the strong segregation regime and neglect surface tension effects.

With surface tension, the stable droplet size is only slightly reduced, see the solid orange lines in Fig. 3.3. The reduction is most dominant in scenario A and we derive an analytical expression for the droplet size in Appendix G. The volume of droplets in the stationary state in scenario A reads

$$V^A = \frac{V_c}{m\psi_-} \left[\frac{k_{AB}}{k_{AB} + k_{BA}} \bar{\phi} - \left(\frac{9(\gamma\beta_+)^2 k_{BA}\psi_-}{4D_B} \right)^{1/3} - \psi_+ \right], \quad (3.3)$$

see Eq. (G.4) and the solid grey line in Fig. 3.3A. This expression reduces to the familiar form given in Eq. (2.22) if $\gamma = 0$ and $\psi_+ = 0$. The expression given in Eq. (3.3) clearly shows that surface tension effects reduce the stationary state size. Interestingly, the reduction due to surface tension is also dependent on the chemical reactions.

Surface tension can furthermore induce a critical droplet size, which corresponds to a second, unstable stationary state, see the dotted orange lines in Fig. 3.3. Droplets smaller than this threshold dissolve spontaneously, while larger droplets grow until they reach the size of the stable stationary state. This is reminiscent of droplet formation in equilibrium systems, see Section 1.5.2, where the associated critical radius is given in Eq. (1.12). We next derive analytical estimates of the critical radius for active droplets to discuss their parameter dependencies and compare it with the equilibrium result.

Analytical estimates of the critical droplet size for scenarios A and B

In scenario A, the droplet material is predominately produced in the solvent. Droplets reach a stationary state size if the influx of droplet material ceases. This is the case if $\phi_+^B(R)$ equals ϕ_0^B , see Eq. (3.2). While ϕ_+^B is directly given by Eq. (2.7b), we estimate the fraction ϕ_0^B of droplet material in the solvent by assuming that the chemical reactions are in equilibrium in the solvent. This leads to $k_{BA}\phi_0^B \approx k_{AB}\phi_0^A$, where ϕ_0^A is the fraction of soluble building blocks in the solvent. We can then use the material conservation, $\bar{\phi}V_c \approx m\psi_-V + (\phi_0^A + \phi_0^B)V_c$ to derive a value for ϕ_0^B . Using the equality $\phi_+^B = \phi_0^B$, we can thus derive the stationary state condition

$$\psi_+ + \frac{\gamma\beta_+}{R} \approx \frac{k_{AB}}{k_{AB} + k_{BA}} \left(\bar{\phi} - \frac{mV\psi_-}{V_c} \right). \quad (3.4)$$

In the case of the small droplets associated with the critical size, the amount of droplet material they contain is negligible, $mV\psi_- \ll V_c\bar{\phi}$. With this approximation, we get an estimate for the critical droplet size that reads

$$R_{\text{crit}}^A \approx \frac{(k_{AB} + k_{BA})\gamma\beta_+}{k_{AB}\bar{\phi} - (k_{AB} + k_{BA})\psi_+}. \quad (3.5)$$

This value approximates the critical radius well, see the grey dashed line in Fig. 3.3A. Note that the critical radius is proportional to the surface tension parameter $\gamma\beta_+$ and depends on the rate constants of the chemical reaction.

In scenario B, the droplet material is predominately produced by the droplet itself. We can again consider the case where the chemical reactions are in equilibrium in the solvent, which now leads to $\phi_0^A \approx \bar{\phi}$. The droplet components are thus almost entirely in their soluble form A. Inside the small droplet there is a reaction flux J^S producing droplet material driven by both the activity of the core and the autocatalytic reaction. This reaction flux is given by $J^S \approx (Q + k_c\psi_-V)(1 - \psi_-)\phi_0^A - k_{BA}\psi_-V$, see Eq. (2.19). In the stationary state, J^S must compensate the flux J_+^B of droplet material away from the droplet. For small droplets, this efflux can be estimated by $J_+^B \approx 4\pi D_B\gamma\beta_+$, see Eq. (3.2). This approximation assumes the strong segregation regime, $\psi_+ = 0$, such that there is hardly any droplet material in the solvent, $\phi_0^B \approx 0$. The critical droplet size is then given by the balance of the two fluxes and reads

$$V_{\text{crit}}^B \approx \frac{4\pi D_B\gamma\beta_+ - (1 - \psi_-)Q\bar{\phi}}{(1 - \psi_-)k_c\bar{\phi}\psi_- - k_{BA}\psi_-}. \quad (3.6)$$

We also present a more detailed calculation of the critical droplet size in Appendix G. We deduce from that calculation that Eq. (3.6) is a good estimate for the critical size if surface tension effects are small and if the catalytic activity does not dominate the droplet growth. The critical radius calculated from V_{crit}^B is shown as a function of $\bar{\phi}$ as a grey dashed line in Fig. 3.3B. If the core is passive, $Q = 0$, the critical

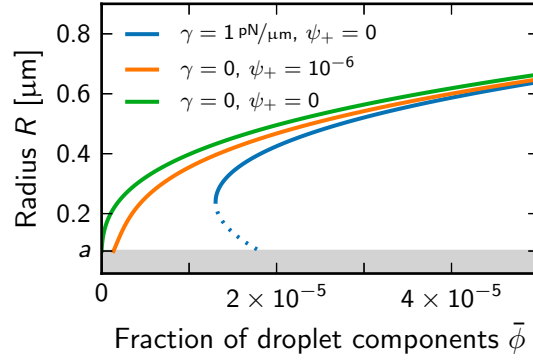


Figure 3.4: Radii of stationary droplets as a function of the overall volume fraction $\bar{\phi}$ of droplet components in scenario C, where the incorporation is driven by the catalytic activity $Q = 10 \mu\text{m}^3/\text{s}$ of the core. The figure shows curves for different values of surface tension γ and basal volume fraction ψ_+ .

size of an active droplet scales with the surface tension γ in scenario A and B. This is reminiscent of equilibrium droplets where this scaling is also observed, see Eq. (1.5). Note that while in the equilibrium case and in scenario A the radius of the droplet scales with γ , in scenario B it is the droplet volume. This already hints at a fundamental difference in the origin of the critical size.

Fig. 3.3 also shows the stationary states in the case where the phase separation is weaker, i. e. where $\psi_+ > 0$ (blue lines). Here, the stable droplet size found in the case $\psi_+ = 0$ is only slightly reduced (compare green and blue solid lines), much like in the case of surface tension discussed in the preceding paragraph. However, the emergence of a critical size due to ψ_+ is only observed in scenario B, see the dotted blue line in Fig. 3.3B. In scenario A, ψ_+ reduces the droplet size in stationary state, but it does not introduce a critical droplet size. This is also captured in the approximate equation (3.5), where surface tension is required for a critical size. Additionally, ψ_+ causes a threshold for the fraction of droplet components, below which droplet formation is impossible. The effect of ψ_+ is thus more difficult to discuss and we ignore it in the following for simplicity. The interesting phenomenon of a critical size can be created using surface tension in both scenarios and we therefore concentrate on this parameter.

Influence of surface tension in scenario C

So far, we focused on scenarios A and B and discussed the stationary states therein, where we found that surface tension typically causes a critical size. Conversely, in scenario C, surface tension has a minor effect and a critical size only appears in a small parameter regime, see Fig. 3.4. This is because the droplet material of form B is directly produced at the active core and incorporated in the droplet there. In scenario C, droplets therefore form spontaneously if the activity Q at the core is

strong enough. Otherwise, if surface tension is large, droplet formation is typically suppressed completely. The threshold value Q_{\min}^C that is necessary to overcome these surface tension effects reads

$$Q_{\min}^C = \frac{4\pi D_B k_{BA} V_c \gamma \beta_+}{(1 - \psi_-)(k_{BA} V_c \bar{\phi} - 4\pi m D_B \gamma \beta_+)} , \quad (3.7)$$

see Eq. (G.9b) in Appendix G.

In summary, surface tension causes a critical droplet size in scenario A and B, similar to the equilibrium situation sketched in Section 1.5. It is important that this property carries over to the non-equilibrium model discussed in this chapter, since it makes spontaneous droplet nucleation unlikely. This allows for controlled droplet growth at nucleation sites, which we discuss subsequently. In scenario C, droplets form spontaneously around the core, however in a diffusion-limited process, which leads to slow droplet growth and thus small droplets in a given time span, see Section 2.3.

3.3 Droplet nucleation facilitated by the active core

In order to be able to create large droplets quickly, we now consider scenarios A and B with an additional enzymatic activity at the core, $Q > 0$. This combines the advantage of scenarios A and B to produce droplet material efficiently with scenario C to trigger droplet formation around the core.

In scenario A, where droplet material is produced in the entire system, there exists a critical radius even for $Q > 0$, see Fig. 3.5A. Consequently, spontaneous nucleation can still be suppressed. Although the activity Q does not have a great influence, the presence of the core may still facilitate nucleation: if the core is wetted by the droplet material of form B , a small surface layer will form around it. In this case, the core acts as a classical nucleation site. Considering this surface layer as a small droplet, we can estimate its size by the radius a of the core. If this radius is larger than the critical radius R_{crit}^A given by Eq. (3.5), droplet growth proceeds spontaneously. The critical value $\bar{\phi}_{\text{crit}}^A$ for the fraction of droplet components above which droplets grow spontaneously can then be given as

$$\bar{\phi}_{\text{crit}}^A \approx \frac{k_{AB} + k_{BA}}{k_{AB}} \left(\psi_+ + \frac{\gamma \beta_+}{a} \right) . \quad (3.8)$$

Fig. 3.5A shows that this expression predicts the observed threshold very well. In summary, a passive core can act as a nucleation seed in scenario A if it is wetted by droplet material of form B . The catalytic activity at its surface does not play a significant role in this process.

In scenario B, where the droplet material is produced inside the droplet by the autocatalytic reaction, the influence of the active core is dramatically different. Here,

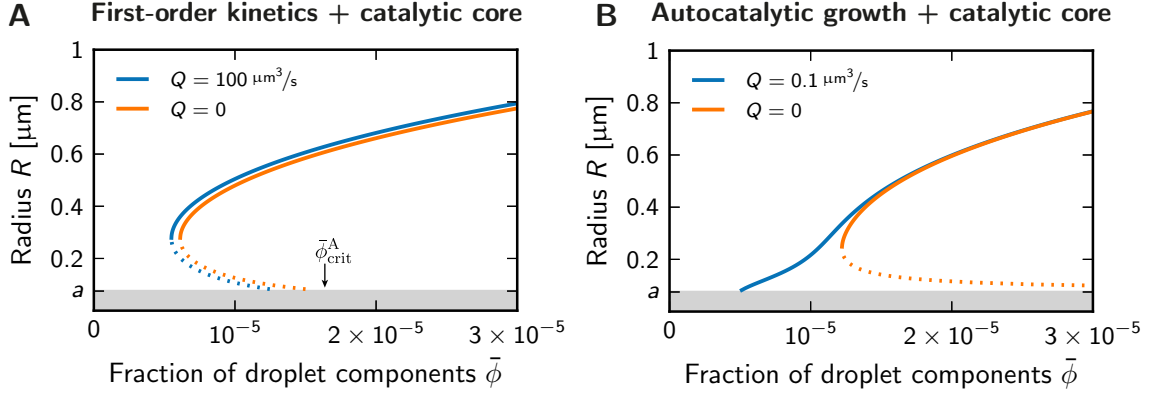


Figure 3.5: Radii of stationary droplets as a function of the overall volume fraction $\bar{\phi}$ of droplet components for different values of the catalytic activity Q at the core. **(A)** First-order kinetics with parameters given in Fig. 2.3. **(B)** Autocatalytic growth with parameters given in Fig. 2.4. The grey area marks the size of the core and the dotted curves indicate unstable stationary states.

the critical radius disappears for $Q > Q_{\text{crit}}^{\text{B}}$ (see blue line in Fig. 3.5B), implying that beyond a critical enzymatic activity $Q_{\text{crit}}^{\text{B}}$, nucleation of a droplet at the core is guaranteed. Note that spontaneous nucleation is still suppressed in the cytosol, see the orange dotted line in Fig. 3.5B. This mechanism therefore ensures that the droplet grows reliably around the active core and not anywhere else in the system. The critical activity $Q_{\text{crit}}^{\text{B}}$ can be estimate from the expression for the critical droplet volume given in Eq. (3.6) and reads

$$Q_{\text{crit}}^{\text{B}} \approx \frac{4\pi D_B \gamma \beta_+}{\bar{\phi}}. \quad (3.9)$$

We will show in the next section that this expression gives a good estimate of the critical catalytic activity.

In summary, while both growth scenarios A and B suppress spontaneous droplet formation away from active cores, only the autocatalytic case provides a way to control nucleation. In this scenario, droplets grow around the active cores if $Q > Q_{\text{crit}}^{\text{B}}$. Conversely, in scenario A, the catalytic activity at the cores has no significant influence, but the cores may still act as classical, passive nucleation seeds.

3.4 Interplay of critical droplet size and nucleation

In the previous sections, we found that surface tension γ induces a critical droplet size that suppresses spontaneous droplet nucleation. We also studied the effect of a catalytic activity Q at the core, which can remove the critical size and thereby

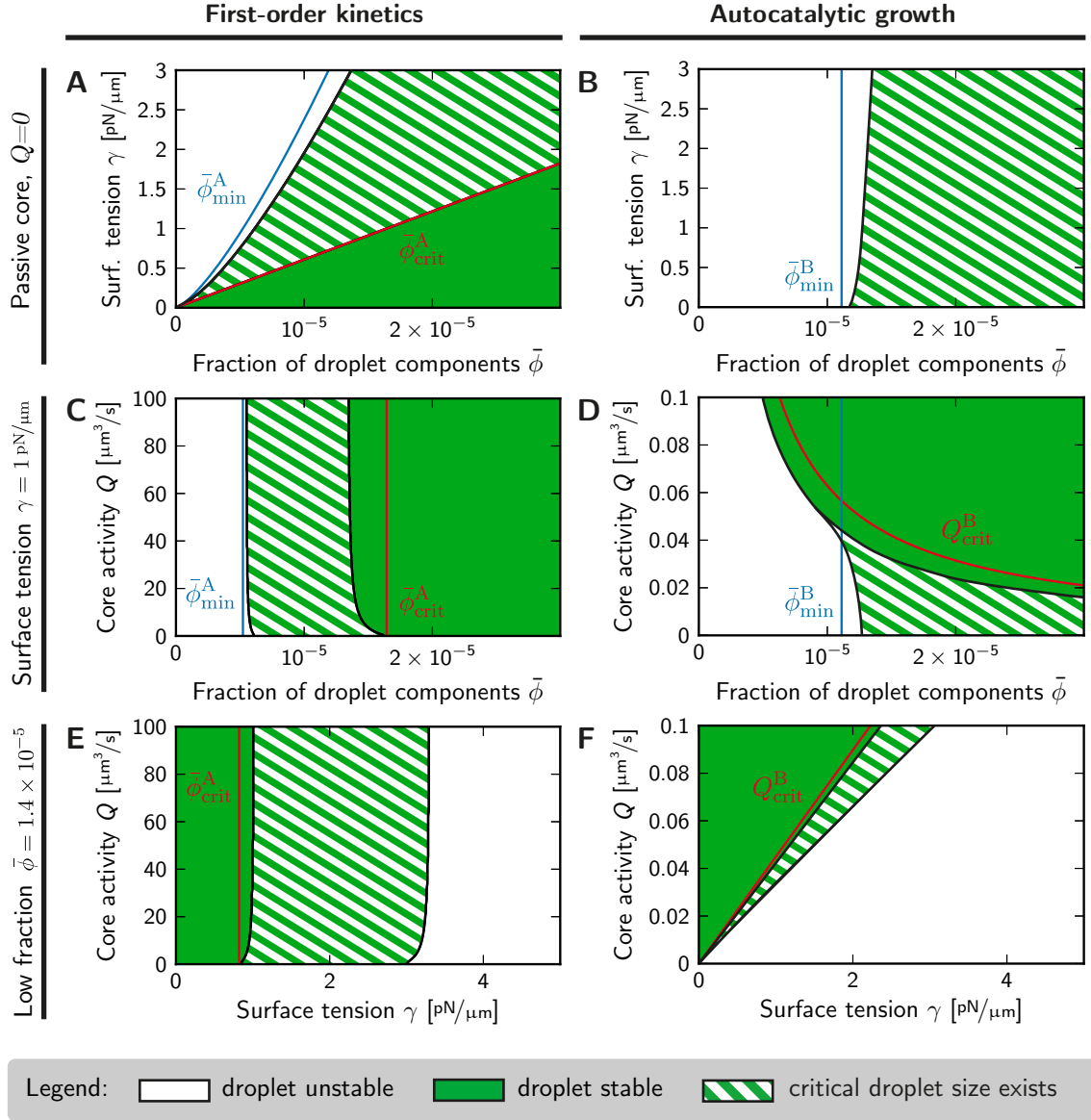


Figure 3.6: Stationary state configurations of a single droplet for different parameter sets: **(A, B)** passive core, $Q = 0$, **(C, D)** active core with $\gamma = 1 \text{ pN}/\mu\text{m}$, and **(E, F)** low fraction of material, $\bar{\phi} = \bar{\phi}_{\text{crit}}^B = 1.4 \times 10^{-5}$. Two scenarios are considered: **(A, C, E)** first-order kinetics with parameters given in Fig. 2.3 and **(B, D, F)** autocatalytic growth with parameters given in Fig. 2.4. Shaded areas indicate the different possible states: no droplet (white regions), one stable droplet (green filled region), or a stable droplet with a critical size (green hatched regions). The red lines indicate the critical thresholds given in Eqs. (3.8) and (3.9) and the blue lines mark the minimal fraction $\bar{\phi}$ necessary to grow droplets, see Eqs. (3.11) and (2.26).

guarantee the droplet nucleation. During these investigations, we found three possible stationary state configurations, see Figs. 3.3 and 3.5:

- (i) No droplets, i.e. all initial conditions lead to a homogeneous system.
- (ii) One stable stationary state, where all initial conditions yield a single droplet of defined size.
- (iii) An unstable stationary state that separates initial conditions for which the droplet dissolves from those for which it grows to a defined size.

These three possible stationary state configurations therefore describe the regimes in which droplet growth can happen. It is thus sufficient to determine into which of these categories the system falls to get a qualitative idea about the dynamics of the system. Using these ideas, we now investigate the interplay of the critical droplet size and nucleation in dependence on γ and Q . We show the different possible stationary state configurations for the growth scenarios A and B in Fig. 3.6. In these diagrams, each point corresponds to a different set of parameters where the color indicates the stationary state category.

For the case of first-order kinetics, scenario A, we again find that a critical fraction $\bar{\phi}_{\text{crit}}^A$ of material is necessary to trigger droplet formation, see Fig. 3.6A. $\bar{\phi}_{\text{crit}}^A$ increases with the surface tension γ , which is in agreement with Eq. (3.8). Figs. 3.6C and 3.6E show that the catalytic activity Q at the core only has a minor effect on the dynamics of droplet formation. Here, we also observe a minimal fraction $\bar{\phi}_{\text{min}}^A$ that is necessary for droplets to form. We can estimate its value using the stationary state condition given in Eq. (3.4). Solving this equation for $\bar{\phi}$, we get $\bar{\phi} \approx \psi_+ \kappa^{-1} + (\kappa R)^{-1} \gamma \beta_+ + m V \psi_- V_c^{-1}$, where $\kappa = k_{AB}/(k_{AB} + k_{BA})$. The right hand side of this expression attains its minimal value for $R = R_{\text{min}}^A$, where

$$R_{\text{min}}^A \approx \left(\frac{(k_{AB} + k_{BA}) V_c \gamma \beta_+}{4\pi m k_{AB} \psi_-} \right)^{\frac{1}{4}}. \quad (3.10)$$

The minimal fraction of droplet components necessary to build droplets thus reads

$$\bar{\phi}_{\text{min}}^A = \frac{k_{AB} + k_{BA}}{k_{AB}} \left[\frac{4}{3} \left(\frac{4\pi (\gamma \beta_+)^3 m k_{AB} \psi_-}{(k_{AB} + k_{BA}) V_c} \right)^{\frac{1}{4}} + \psi_+ \right]. \quad (3.11)$$

We show this solution as the blue line in panel A and C of Fig. 3.6. In summary, in scenario A the overall fraction $\bar{\phi}$ must exceed threshold values $\bar{\phi}_{\text{min}}^A$ and $\bar{\phi}_{\text{crit}}^A$ in order to support and nucleate stable droplets, respectively. These threshold values dependent only weakly on Q .

Conversely, in scenario B, the catalytic activity Q has a dramatic effect. If the core was passive, $Q = 0$, the critical size would persist independent of the amount of material in the system, see Fig. 3.6B. This can be easily explained by noting that the

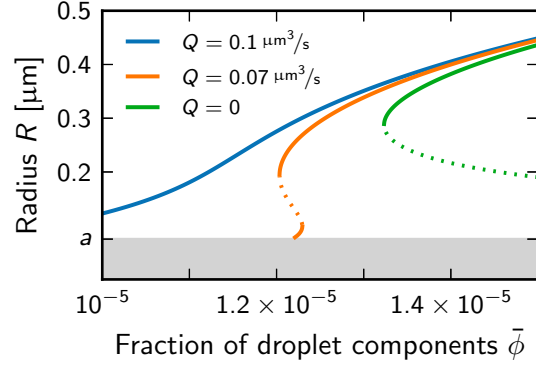


Figure 3.7: Radii of stationary droplets as a function of the overall volume fraction $\bar{\phi}$ of droplet components for different values of the catalytic activity Q at the core in the autocatalytic scenario with a basal volume fraction $\psi_+ = 10^{-7}$ of droplet material in the solvent. The grey area marks the size of the core and the dotted parts of the curves indicate unstable stationary states. The model parameters are given in Fig. 2.4.

autocatalytic reaction ceases if there is no droplet material, $\phi^B = 0$. Consequently, there is no way of producing droplet material in this case and the homogeneous system, where only soluble building blocks exist, must be stable. If there is enough material in the system, $\bar{\phi} > \bar{\phi}_{\min}^B$, a stable droplet can exist, but it only forms, if the initial droplet size is above the critical size. Evidently, the minimal amount $\bar{\phi}_{\min}^B$ depends only weakly on the surface tension and the catalytic activity at the core, see Figs. 3.6B and 3.6D. The minimal value derived for $Q = 0$, see Eq. (2.26), is therefore a good approximation to $\bar{\phi}_{\min}^B$ in general. Fig. 3.6D additionally shows that a small catalytic activity Q can trigger droplet formation. If Q is above Q_{crit}^B , a droplet of finite size is the only stationary state and all initial conditions must therefore lead to this configuration. The boundary of the stable region is well approximated by the analytical expression of Eq. (3.9) derived in the previous section. The critical catalytic activity not only depends on the fraction $\bar{\phi}$ of droplet components, but also on the strength of the surface tension, see Fig. 3.6F. This functional dependence is also captured by Eq. (3.9).

In this section, we only considered single droplets. Of course, more complicated situations could arise in the case of multiple droplets. We investigate this problem later in Chapter 4. Nonetheless, also in the case of a single droplet additional effects can be observed for certain choices of the parameters. For instance, Fig. 3.7 shows that bistable systems can occur in scenario B if additionally a basal volume fraction ψ_+ of the droplet material outside of the droplet is added (see orange line). Here, the two stable stationary states correspond to two different ways of organizing the droplet material: the larger state resembles the situation discussed above, where the droplet material is mainly produced by the autocatalytic reaction in the droplet volume. Conversely, the smaller stable stationary state corresponds to a situation,

where the droplet material is predominately produced at the core. Here the activity at the core is not quite strong enough to push the droplet size above the critical size, where the droplet would then grow further to reach the larger stable size. This behavior only occurs in a narrow parameter regime and is therefore most likely irrelevant for the biological case.

In summary, surface tension typically causes a critical droplet size, both in equilibrium thermodynamics, see Section 1.5, and in the non-equilibrium system discussed in this thesis, see Section 3.2. Interestingly, the nucleation barrier associated with this critical size can be removed by chemical reactions, at least in the autocatalytic growth scenario. Here, a catalytic core facilitates the formation of an initial droplet and thereby controls the nucleation properties. The interplay of phase separation and chemical reactions can thus cause a behavior that is qualitatively different from the associated equilibrium system without chemical reactions. In the next section, we investigate whether qualitative differences between the growth scenarios are also observed for droplets at their maximal size. Here, we expect stable droplets, which are spherical in equilibriums systems.

3.5 Perturbations of the spherical droplet shape

Droplets are typically spherical, since this configuration has the lowest surface area for a given volume and thereby minimizes the total free energy [183]. If a droplet is perturbed from its spherical shape, it typically returns to the preferred shape in an oscillating manner [193]. The time scale associated with this behavior can be measured experimentally and compared to theoretical predictions to extract information about material parameters [194–196]. These theoretical models typically consider small deviations from the spherical shape and employ a linear stability analysis to deduce the oscillation time scale [193, 197, 198]. The theory is well established for passive droplets, but we are not aware of any comparable studies of droplet formation under the influence of chemical reactions.

In this section, we investigate whether droplets are always spherical in the model discussed in this thesis. This model neglects inertial effects of the fluid, owing to the typical small Reynolds number inside biological cells. The droplet shape can therefore only change by the chemical reactions that rebuild the droplet. This is in contrast to examples discussed above, where the observed droplet oscillations are caused by inertial effects [193], and we will thus not be able to compare the results directly. However, we can still investigate whether surface tension stabilizes the spherical shape or if thermal fluctuations destroy this symmetric state. Furthermore, we will consider the effect of chemical reactions to see whether they again revoke the expectations from the equilibrium theory. Both questions can be answered by investigating small perturbations of the spherical droplet shape in a linear stability analysis. Interestingly, this approach also allows us to investigate the centering of the core inside the droplet.

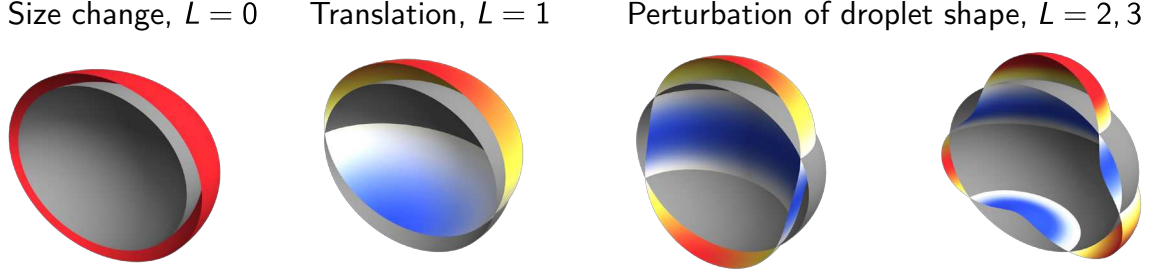


Figure 3.8: Perturbation modes of the spherical droplet shape. Axisymmetric perturbations (colored surface) of degree L and order $M = 0$ are shown in comparison to the spherical symmetric state (grey).

3.5.1 Linear stability analysis of the spherical droplet shape

It is convenient to describe the perturbations of the droplet shape using spherical harmonic functions, since this allows us to consider changes in volume, displacement of the droplet, and shape changes within the same formalism, see Fig. 3.8. We describe the system in a convenient spherical coordinate system (r, θ, φ) with its origin at the center of the unperturbed droplet. The droplet surface is given by its distance R to the origin,

$$R(\theta, \varphi, t) = \bar{R} + \sum_{L=0}^{\infty} \sum_{M=-L}^L \varepsilon_{L,M}(t) Y_{L,M}(\theta, \varphi), \quad (3.12)$$

for all angles θ and φ . Here, \bar{R} is the radius of the undisturbed, spherical droplet, $\varepsilon_{L,M}$ are the magnitudes of the small perturbations, $|\varepsilon_{L,M}| \ll \bar{R}$, and the functions $Y_{L,M}(\theta, \varphi)$ are the real spherical harmonics, see Appendix H.1. The perturbation mode is defined by the degree L and order M of the spherical harmonics, see Fig. 3.8. Similar descriptions of droplet perturbations have been used since a long time [199].

The shape of the droplet is defined by the magnitude of the perturbations $\varepsilon_{L,M}$ at any time. The temporal evolution of $\varepsilon_{L,M}$ is readily generalized from Eq. (2.10), see Appendix H.2. For simplicity, we consider the case where the perturbations $\varepsilon_{L,M}$ are the only slow variables in the system. That is, the volume fraction profiles ϕ^A and ϕ^B of the soluble building blocks and droplet material are assumed to equilibrate quickly, i.e. on timescales shorter than the dynamics of the perturbation. We furthermore consider fast diffusion of the soluble building blocks, which should not influence the result much since ϕ^A does not directly enter Eq. (2.10), which describes the droplet growth. Using these approximations, we can determine the functions $\phi^A(\mathbf{r})$ and $\phi^B(\mathbf{r})$ analytically, see Appendix H.3. Assuming that the perturbations are small,

we linearize the dynamical equations and the volume fraction profiles with respect to $\varepsilon_{L,M}$ and arrive at the solution

$$\varepsilon_{L,M}(t) = \varepsilon_{L,M}(0) e^{\lambda_L t}, \quad (3.13)$$

see Appendix H.4. The perturbation growth rates λ_L are given by the implicit equation (H.40). Interestingly, these growth rates only depend on the degree L of the spherical harmonics while their order M does not influence the associated growth rate. Note also that all perturbation modes decouple, i.e. the dynamics of the mode (L, M) does not depend on the amplitude of other modes. This allows us to discuss all perturbation modes separately. In the following, it is therefore sufficient to consider only the axisymmetric perturbations with $M = 0$, keeping in mind that other orders only change the spatial configuration but not the dynamics of the perturbation. The special mode $L = 0$ is the only one where the droplet volume changes. Since it simultaneously is also the only isotropic perturbation, we already calculated the perturbation growth rate in Section 3.1. We use these results to test the derivation presented here in the case of isotropic perturbation with $L = 0$, see Fig. H.2 in the Appendix H.4.

The perturbation growth rates λ_L derived here are real numbers. This is because they are directly calculated from the volume fraction profiles and their gradients, see Eq. (H.40) in the Appendix H.4. Consequently, the droplet does not return to the spherical shape in an oscillating manner, an effect that would be described by the imaginary part of λ_L .

3.5.2 Active cores can center themselves in droplets

We now use the analysis given in the previous section to investigate the stability of the spherical shape of active droplets. We first investigate perturbations with $L = 1$, which are translations of the droplet, see Fig. 3.8. To remove the effect of the system boundary, we consider the limit of an infinite system, $V_c \rightarrow \infty$, while keeping the droplet volume finite. In this limit, the only object that breaks translational symmetry is the core at the origin. The translation of the droplet can therefore also be interpreted as the core moving relative to the droplet. We will adapt this view in the following discussion.

In the first-order kinetics case, scenario A, the core always has the tendency to be centered within the droplet, see the left column in Fig. 3.9. This effect is quite small for the standard set of parameters, but can be enhanced by a catalytic activity $Q > 0$ at the core. In the case of autocatalytic growth, scenario B, the effect of such a catalytic activity is even more pronounced. Here, the growth rate is even larger than in the first-order kinetics case, see the bottom row of Fig. 3.9. This is surprising because in the autocatalytic case, a passive core exhibits a weak tendency to move away from the center, $\lambda_1 > 0$, see the upper right panel of the figure. The opposite behavior of passive cores in the two scenarios is likely due to the differences

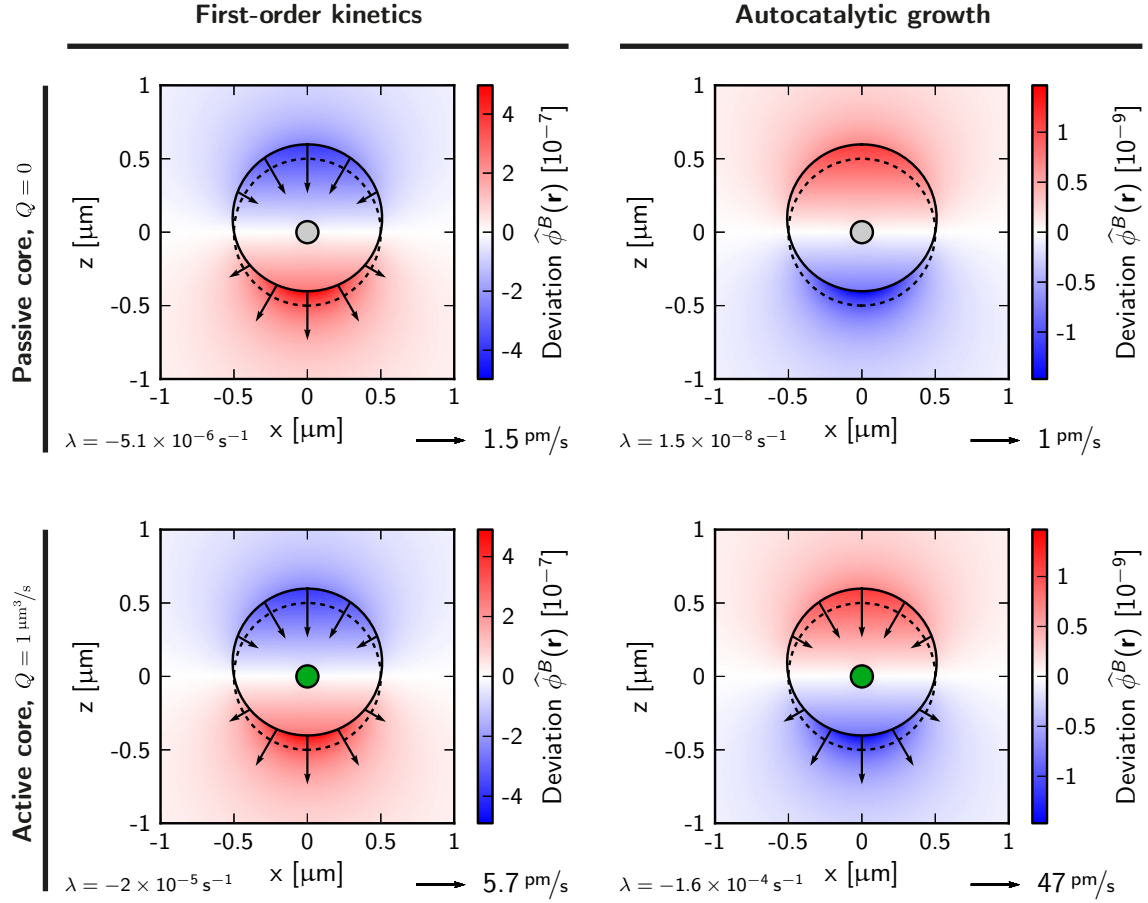


Figure 3.9: Response of an active droplet to translational perturbations (degree $L = 1$). The droplet surface (black solid line) has been distorted with respect to the symmetric case (black dotted line). Arrows indicate in which direction the surface moves according to Eq. (H.41) and the speed is given by the length of the arrow. The perturbation growth rate λ is indicated in the bottom left of each panel and the distortion $\hat{\phi}^B$ of the volume fraction of droplet material is shown as a heat map in the background. We consider passive cores ($Q = 0$, grey disc) and active cores ($Q = 1 \text{ } \mu\text{m}^3/\text{s}$, green disc) for the two growth scenarios, first-order kinetics and autocatalytic growth, where the parameters values are given in Fig. 2.3 and Fig. 2.4, respectively.

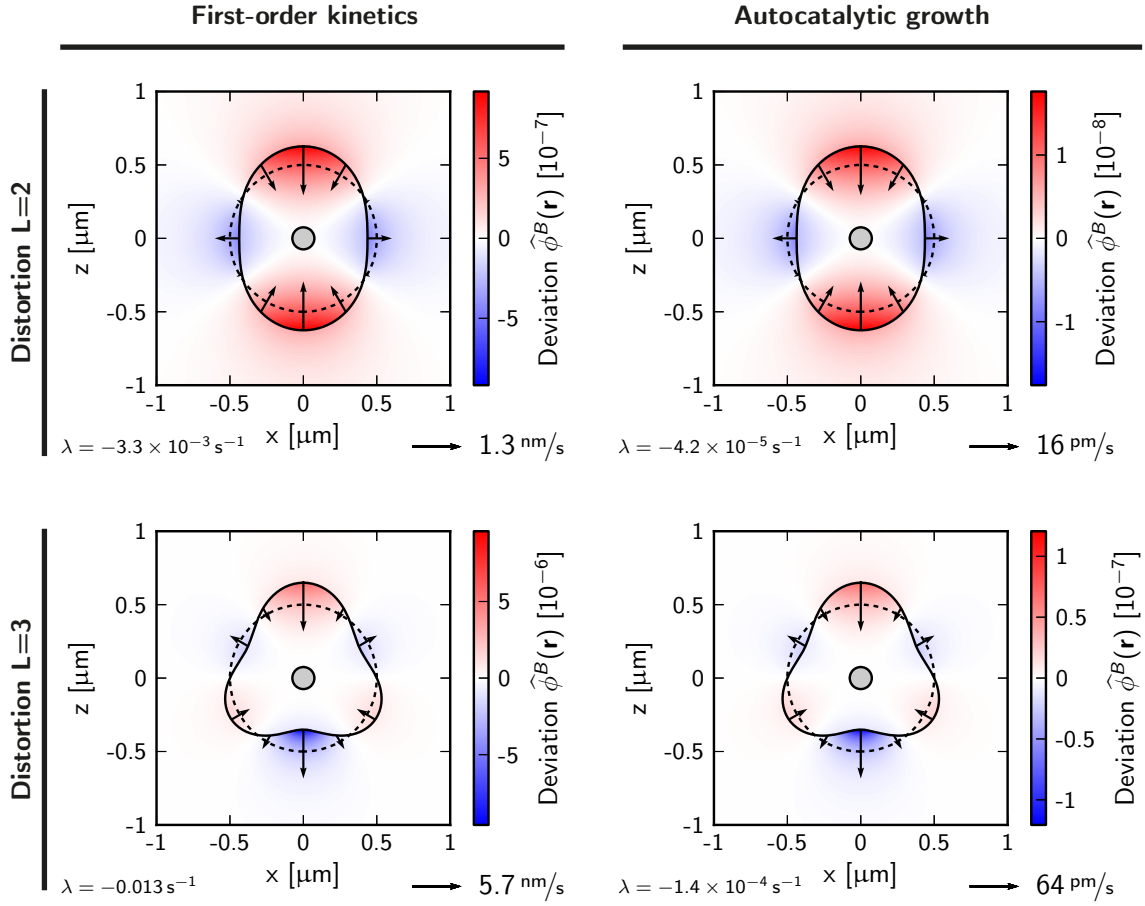


Figure 3.10: Response of an active droplet to shape perturbations. The droplet surface (black solid line) has been distorted with respect to the spherical case (black dotted line). Arrows indicate in which direction the surface moves according to Eq. (H.41) and the speed is given by the length of the arrow. The perturbation growth rate λ is indicated in the bottom left of each panel and the distortion $\hat{\phi}^B$ of the fraction of the droplet material is shown as a heat map in the background. The small grey circle in the center indicates the passive core with $Q = 0$. Two growth scenarios, first-order kinetics and autocatalytic growth, are considered with parameters given in Fig. 2.3 and Fig. 2.4, respectively.

in the stationary state fluxes, which we discussed in Section 3.1 and which is also apparent in the reversed background colors between the two cases visible in Fig. 3.9. Although these observations are dependent on the choice of parameters, they are also in line with our earlier observation that the activity at the core has a stronger influence in the autocatalytic scenario, see Section 3.3.

The centering of the core in the autocatalytic scenario can be explained intuitively: Soluble building blocks entering the droplet may diffuse toward the core, but there is a chance that they get incorporated into the droplet by the autocatalytic reaction. The propensity of conversion is larger if the building blocks stay inside the droplet longer. In a droplet where the core is off-center, the concentration of building blocks is larger on the site of the core that is located closer to the droplet surface since the diffusion of the building blocks toward the core takes time. A larger concentration of building blocks leads to a higher conversion rate and thus to more incorporation of droplet material at this site of the core. If the core is located away from the center, this mechanism leads to a stronger growth on the side of the core that is closer to the droplet surface. The droplet thus grows quicker on that side and the core experiences an effective centering force. This mechanism also works in the stationary state, where it relies on the material turnover since the overall droplet size does not change.

3.5.3 Surface tension stabilizes the spherical shape

We next consider shape fluctuations, where the droplet volume stays constant and the droplet center is not moved, i. e. modes with $L \geq 2$, see Fig. 3.8. We consider both the scenario A with first-order kinetics as well as the scenario B with autocatalytic droplet growth and plot the results in Fig. 3.10. In both scenarios, perturbations with degree $L \geq 2$ decay and the droplet returns to its spherical shape. This effect is in general stronger for perturbations with higher degree, i. e. the perturbation growth rate λ_L has a larger absolute value for higher L . The direction of the movement of the droplet interface is correlated with the correction $\hat{\phi}^B$ to the stationary state volume fraction in its vicinity. The interface expands if there is less droplet material, presumably because the efflux of droplet material is reduced. Conversely, the interface retracts if the volume fraction of droplet material is above the stationary state value. In scenario A, we observe a quicker relaxation to the stationary state than in the autocatalytic scenario B, although this behavior again depends on the specific choice of parameters.

3.5.4 First-order kinetics destabilize large droplets

The stability of a spherical droplet with respect to perturbations of its shape is given by the sign of the perturbation growth rates. Here, we can distinguish several different scenarios, depending on whether the size of the droplet, its shape, or only the position of the core becomes unstable, see Fig. 3.11. These diagrams confirm

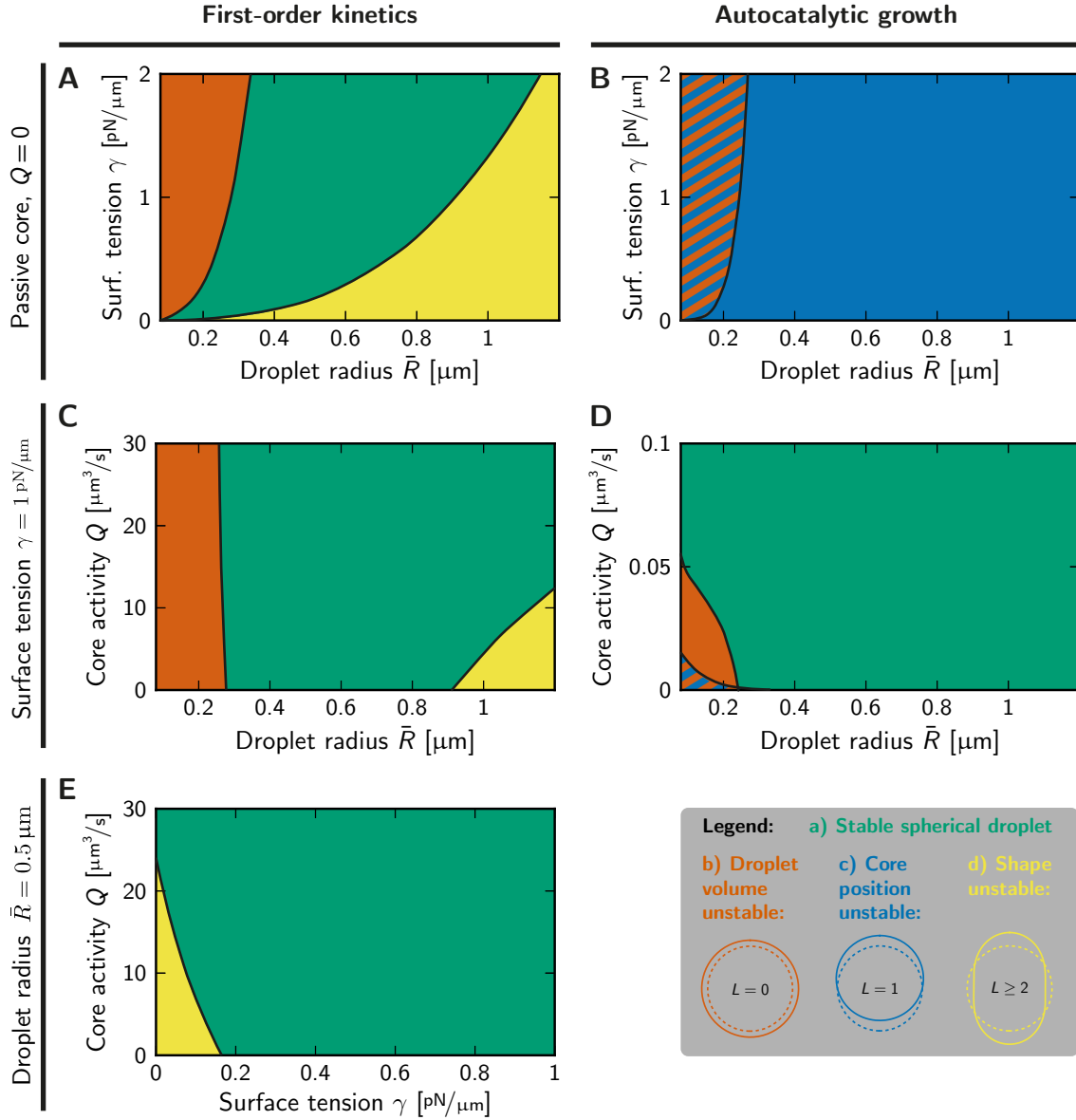


Figure 3.11: Stability diagrams of a spherical droplet. Droplets are either stable (green) or unstable with respect to the droplet size (orange), the droplet shape (yellow), or the position of the core (blue). Mixture of these instabilities can also occur (hatched regions). Various parameters are varied: **(A, B)** surface tension γ and droplet radius \bar{R} at $Q = 0$; **(C, D)** activity Q at the core and \bar{R} at $\gamma = 1 \text{ pN}/\mu\text{m}$; **(E)** Q and γ at $\bar{R} = 0.5 \mu\text{m}$. The droplet size is varied by adjusting $\bar{\phi}$ and two scenarios are considered: (A, C, E) first-order kinetics with parameters given in Fig. 2.3 and (B, D) autocatalytic growth with parameters given in Fig. 2.4. A droplet with radius $\bar{R} = 0.5 \mu\text{m}$ and finite Q is always stable in the autocatalytic case and the associated panel is thus omitted.

the earlier result that small droplets are unstable in the autocatalytic scenario if the core activity is too low, see Fig. 3.11D. In the first-order kinetics scenario, small droplets are also unstable, but the activity at the core cannot compensate for this. Interestingly, there is another regime for large droplets, where the shape becomes unstable, i.e. perturbations with $L \geq 2$ grow spontaneously, see Fig. 3.11A. Consequently, there are lower and upper bounds for the droplet size in the case of first-order kinetics. Taking together the results from both scenarios A and B, active cores center themselves within a droplet and surface tension stabilizes the spherical shape, which is reminiscent of the equilibrium situation [183]. Furthermore, the stability of the droplet in the autocatalytic case is assured if the catalytic activity at the core is strong enough. Interestingly, droplets are always spherical in this case, while large droplets tend to be non-spherical in the case of first-order kinetics.

3.6 Discussion

In this chapter, we analyzed active, isolated droplets. We found that all aspects of the droplet physics are influenced by the additional chemical reactions. Most notably, active cores that catalyze the production of droplet material can influence the nucleation behavior and the morphology of the droplet.

In accordance with the equilibrium situation, we found that surface tension can cause a critical size that droplets have to overcome in order to grow spontaneously. This critical size is larger if droplets are built by the autocatalytic mechanism since a large enough droplet is required to produce sufficient droplet material. Generally, such a critical size acts as a nucleation barrier and makes spontaneous droplet formation unlikely. However, this nucleation barrier can be overcome by a core that acts as a suitable nucleation site. If such a core additionally catalyzes the production of droplet material at the surface, its nucleation capacity can be enhanced drastically, at least in the autocatalytic scenario. Taken together, the influence of the active cores depends on the reactions that produce the droplet material from soluble building blocks, see Fig. 3.12.

The active cores also have the interesting property that they can center themselves within the droplet and they also tend to make droplets spherical, see Fig. 3.12. This spherical shape is also stabilized by surface tension effects, comparable to the equilibrium picture, where the surface energy is minimized by the spherical shape. Conversely, the first-order kinetics can destabilize large droplets and it is tempting to speculate that these droplets break up into many smaller ones which would then be stable. To investigate such a behavior, it is thus necessary to examine states with multiple active droplets, which we do in the next chapter.

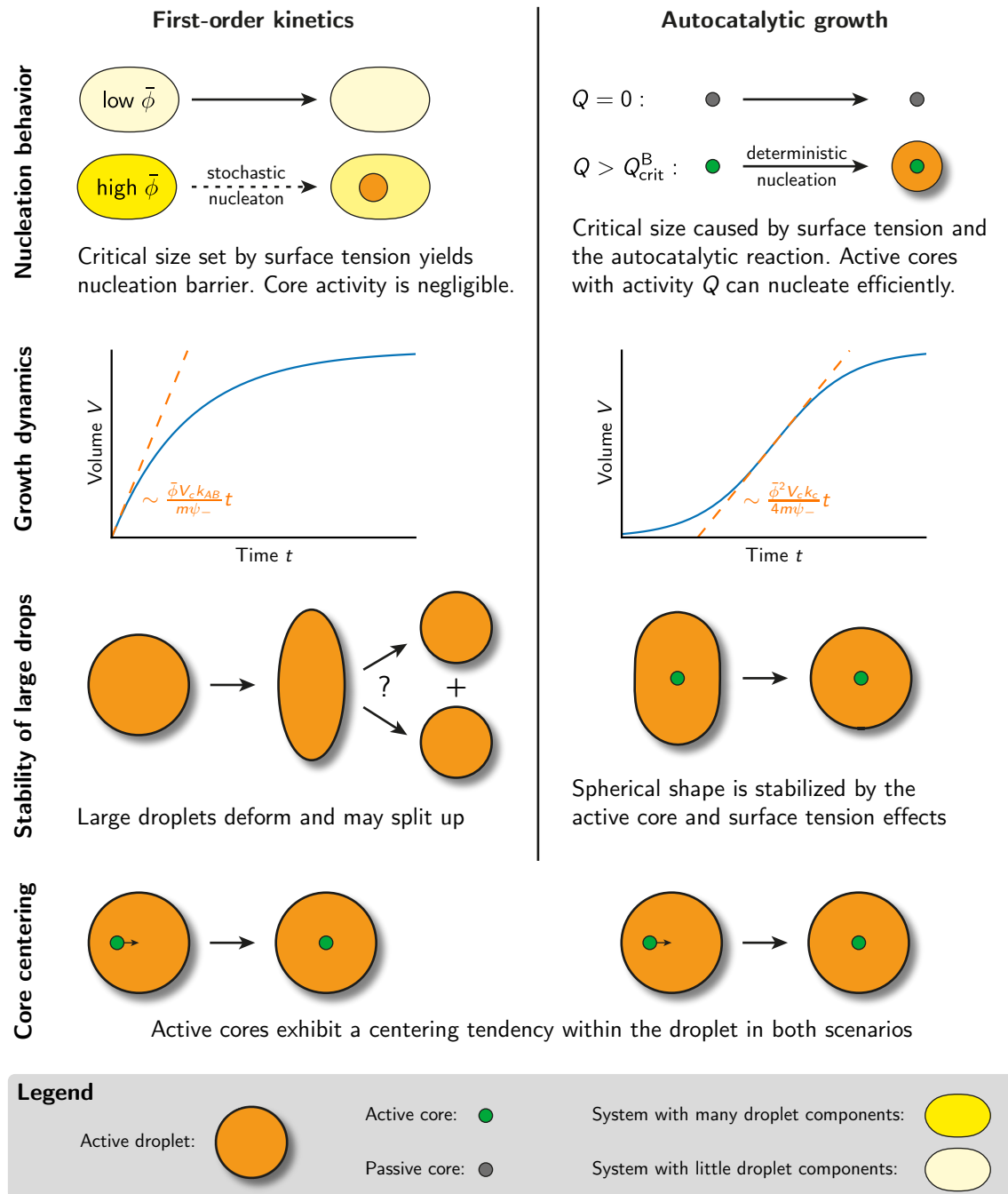


Figure 3.12: Summarized behavior of isolated active droplets. The droplet material (orange) is either produced by first-order kinetics in the whole system (left column) or by an autocatalytic reaction inside the droplet (right column). Additionally, an active core (green disc) may catalyze the production of droplet material and thereby for instance center itself within a droplet. Typically, droplets grow after their nucleation until they reach their final size, where they are either stable or break up into smaller droplets.

Chapter 4

Multiple Interacting Active Droplets

WE now consider systems of multiple droplets, which can exchange material through a common solvent. In a passive system, which reaches equilibrium after a long time, this exchange of droplet material leads to Ostwald ripening, see Section 1.5.3. Ostwald ripening is the phenomenon by which emulsions of many small droplets coarse into a system with fewer and larger droplets. In equilibrium, only the state with a single droplet is stable. We will now show that Ostwald ripening can be suppressed in the system of active droplets we discuss in this thesis.

4.1 Approximate description of multiple droplets

The model defined in Section 2.1 readily accounts for the case of multiple droplets. We describe droplets as stable cores surrounded by droplet material that is produced from soluble building blocks. The cores may also catalyze the production of droplet material and thereby support droplet growth. For simplicity, we consider the case where the droplets are homogeneous, i.e. the droplet components diffuse quick enough such that gradients in the volume fractions can be neglected. The differential equation describing the growth of droplet i given by Eq. (2.10) then reads

$$\partial_t V_i = \frac{J_i^S(\mathbf{V}) - J_i^B(\mathbf{V})}{\psi_-}, \quad (4.1)$$

where $i = 1, \dots, m$ enumerates the droplets and we approximated the difference of the fraction of droplet material between the inside and the outside of the droplet by ψ_- , thus neglecting the small surface tension effects. Here, J_i^S is the reaction flux inside the droplet and J_i^B denotes the flux of droplet material away from the droplet. Both these quantities generally depend on all droplet volumes $\mathbf{V} = \{V_1, V_2, \dots, V_m\}$. The reaction flux inside the droplet reads

$$J_i^S(\mathbf{V}) \approx (k_c \psi_- V_i + Q) (1 - \psi_-) \phi_0^A(\mathbf{V}) - k_{BA} V_i \psi_-, \quad (4.2)$$

which contains both the bulk reactions, see Eq. (2.2), and the catalytic activity of the cores, parameterized by Q , see Eq. (2.6). Here, ϕ_0^A is the fraction of building blocks in the solvent and we approximate the respective fraction inside the droplet

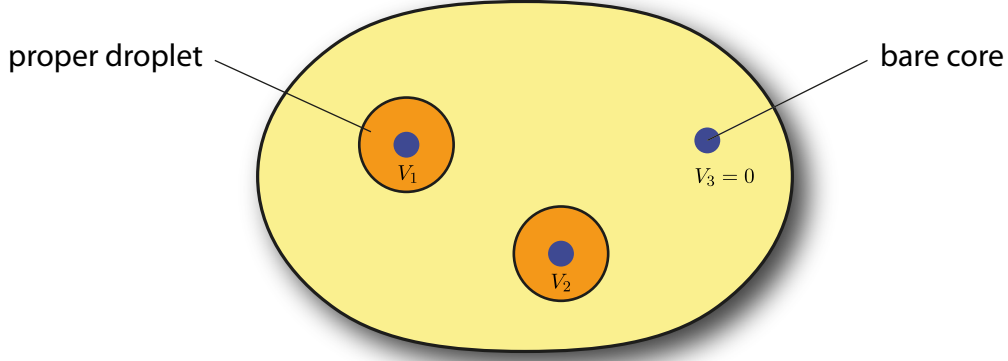


Figure 4.1: Schematic drawing of a system where active cores (blue dots) are possibly surrounded by droplet material (orange). Two proper droplets and a bare core are shown. This example configuration is described by the state vector $\mathbf{V} = \{V, V, 0\}$ of the droplet volumes, assuming that $V_1 = V_2 = V$.

by $(1 - \psi_-)\phi_0^A$, which works well in the strong segregation regime, see Eq. (2.8). Additionally, we neglect the first-order reaction $A \rightarrow B$ inside the droplet, since it has only a minor influence.

In the description of the dynamics of the droplet volume, we have to employ a constraint, $V_i \geq 0$, to ensure that the volumes do not become negative. In fact, there are situations in which the production of droplet material is not strong enough to overcome the critical radius created by surface tension effects, see Section 3.3. In these cases, the droplet volume is zero. The associated cores are not surrounded by droplet material and we thus call them «bare cores», see Fig. 4.1. Note that the droplet material created by the catalytic activity of such cores immediately ends up in the solvent and diffuses away from the core without forming a droplet. We have to consider this special case in the expression for the flux J_i^B of droplet material away from the droplet surface, which consequently reads

$$J_i^B(V_i, \phi_0^A, \phi_0^B) \approx \begin{cases} 4\pi D_B R_i \cdot (\phi_+^B(R_i) - \phi_0^B) & V_i > 0 \\ Q\phi_0^A & V_i = 0 \end{cases}, \quad (4.3)$$

where the two branches follows from Eq. (3.2) and Eq. (2.6), respectively. Here, ϕ_0^A is the fraction of building blocks in the solvent and ϕ_0^B is the fraction of droplet material far away from droplets. Note that Eq. (4.3) assumes that the flux away from a droplet is driven by the difference of the fraction ϕ_+^B right at its surface and the mean fraction ϕ_0^B in the solvent. The direct influence of other droplets is thus neglected and we only consider a mean-field model of multiple droplets. It remains

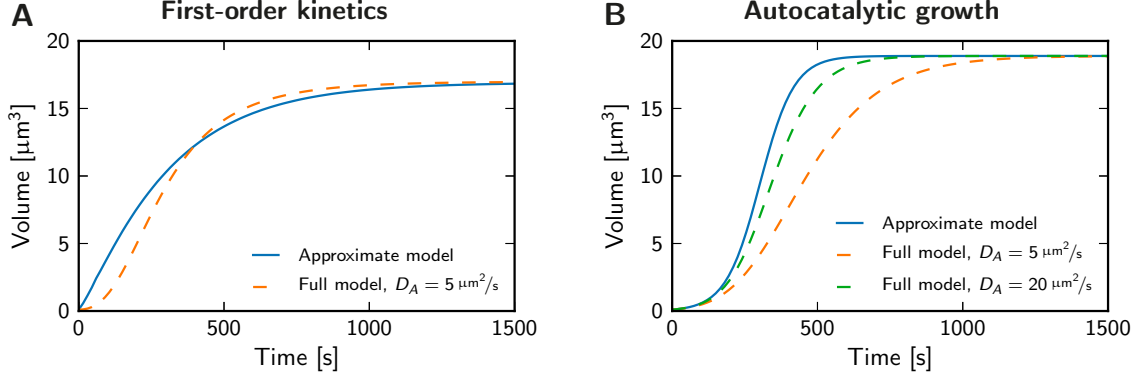


Figure 4.2: Droplet volume as a function of time for a single droplet in the approximate model (blue line) in comparison to numerical solutions of the full equations (dashed lines). **(A)** First-order kinetics with parameters given in Fig. 2.3. **(B)** Autocatalytic growth with parameters given in Fig. 2.4. Different diffusivities D_A of the building blocks A are compared.

to consider the fractions ϕ_0^A and ϕ_0^B in the solvent. The fraction ϕ_0^A of building blocks can be derived from the conservation equation (2.4) and reads

$$\phi_0^A(\mathbf{V}, \phi_0^B) \approx \bar{\phi} - \phi_0^B - \frac{\psi_-}{V_c} \sum_{i=1}^{m_1} V_i. \quad (4.4)$$

The fraction ϕ_0^B can be determined by considering its dynamics in the solvent: The amount of droplet material in the solvent changes by the compositional fluxes given in Eq. (4.3) and by the chemical flux $j_0^S \approx k_{AB}\phi_0^A - k_{BA}\phi_0^B$ in the solvent. Taken together, ϕ_0^B changes according to

$$\partial_t \phi_0^B = j_0^S + \frac{1}{V_c} \sum_{i=1}^m J_i^B, \quad (4.5)$$

where we approximated the solvent volume by V_c . For simplicity, we consider the case, where ϕ_0^B is in the stationary state, $\partial_t \phi_0^B = 0$. This approximation allows us to combine Eqs. (4.3)–(4.5) and solve for ϕ_0^B , which yields

$$\phi_0^B(\mathbf{V}) = \frac{4\pi D_B \sum_{i=1}^{m_1} R_i \phi_+^B(R_i) + (k_{AB}V_c + m_0Q) (\bar{\phi} - \psi_- V_c^{-1} \sum_{i=1}^{m_1} V_i)}{m_0Q + (k_{AB} + k_{BA})V_c + 4\pi D_B \sum_{i=1}^{m_1} R_i}. \quad (4.6)$$

Here, we assumed without loss of generality that \mathbf{V} is arranged such that m_1 proper droplets with $V_i > 0$ are in front of the m_0 bare cores with $V_i = 0$. Note that the total number of cores is conserved, $m_0 + m_1 = m$.

Taken together, the droplet volumes \mathbf{V} are the only state variables and the dynamics of the system are given by the m coupled differential equations of Eq. (4.1).

We solve these equations numerically employing a simple Euler-scheme, which allows for a straight-forward implementation of the constraint $V_i \geq 0$ [200]. The growth dynamics of single droplets are not affected significantly, despite the multiple simplifications introduced in this section, see Fig. 4.2. The figure shows that the stationary state volumes are unchanged and that the shapes of the curves agree qualitatively. Furthermore, the deviations found in the autocatalytic scenario decrease if the diffusivity of the building blocks is increased beyond the standard value, see Fig. 4.2B. This is to be expected, since we assumed an infinite diffusivity D_A to derive the approximate model. The approximate model thus agrees well with the full model in the case of a single droplet. We take this observation as a justification to study the approximate model in the case of multiple droplets in the system.[†]

4.2 Linear stability analysis of the symmetric state

The stability of a stationary state with multiple droplets can be assessed by considering small perturbations of their volumes. The linear part of the temporal evolution of these perturbations are captured by the Jacobian $\mathcal{J}_{ij} = \partial f_i(\mathbf{V})/\partial V_j$, where $f_i(\mathbf{V}) = \partial_t V_i(\mathbf{V})$ is the growth rate of the i -th droplet, see Eq. (4.1). Using these definitions, the Jacobian can be decomposed as $\mathcal{J}_{ij} = \mathcal{A}_{ij} + \mathcal{B}_i \delta_{ij}$ with

$$\mathcal{A}_{ij} = -(k_c \psi_- V_i + k_{AB} V_i + Q) \frac{1 - \psi_-}{\psi_-} \left(\frac{\partial \phi_0^B}{\partial V_j} + \frac{\psi_-}{V_c} \right) + \frac{4\pi D_B R_i}{\psi_-} \cdot \frac{\partial \phi_0^B}{\partial V_j} \quad (4.7a)$$

$$\mathcal{B}_i = (k_c \psi_- + k_{AB}) \frac{1 - \psi_-}{\psi_-} \phi_0^A - k_{BA} + \frac{D_B}{R_i^2 \psi_-} (\phi_0^B - \psi_+) , \quad (4.7b)$$

where ϕ_0^A and ϕ_0^B are given in Eqs. (4.4) and (4.6). The eigenvalues of the matrix \mathcal{J}_{ij} are the rates with which the perturbations evolve in time [201]. If all these rates are negative, perturbations decay and the associated stationary state is stable. Here, we have to treat the special case of bare cores with vanishing volume separately. They must have a negative growth rate, $\partial_t V_i \leq 0$, in the stationary state, since otherwise proper droplet would grow around them. Because of this negative growth rate, bare cores are always stable and for the stability analysis it is thus sufficient to consider proper droplets, i.e. the submatrix of \mathcal{J}_{ij} with $0 \leq i, j \leq m_1$.

We next consider the symmetric case, where all proper droplets have the same volume, $V_i = \bar{V}$ for $i = 1, 2, \dots, m_1$. Later, it will turn out that this state is anyway the only relevant one. The Jacobian of this state is particularly simple and its eigenvalues read

$$\lambda_0 = m_1 \mathcal{A} + \mathcal{B} \quad \text{and} \quad \lambda_m = \mathcal{B} , \quad (4.8)$$

[†] The reader is invited to follow the arguments given here using the publicly available webpage <http://www.david-zwicker.de/centrosomes>, where the solution of Eq. (4.1) are shown and all model parameters can be varied interactively.

where λ_m has the multiplicity $m_1 - 1$ and is only present if there are multiple proper droplets. Consequently, the stability of a single droplet is given by the sign of $\mathcal{A} + \mathcal{B}$, which can be either positive or negative as discussed in Chapter 3. In the case of multiple droplets, the first mode given by the eigenvalue λ_0 has an associated eigenvector $\boldsymbol{\xi}_1 = (1, 1, \dots, 1)^\top$ and thus describes the dynamics of the total droplet volume V_{tot} . If λ_0 is positive, V_{tot} and therefore also the droplets are unstable. This case is related to the instability of single droplets and we thus do not discuss it further in this chapter. Conversely, if λ_0 is negative, the stability of the droplets depends on $\lambda_m = \mathcal{B}$. This case is interesting, since here V_{tot} is stable and therefore stays constant, but droplets may exchange material and thereby change their individual volumes.

In summary, the dynamics of the perturbations can be decomposed in the dynamics of the total droplet volume, which evolves with a rate λ_0 , and the dynamics of the volume differences of droplets. The latter are described by vectors of the eigenspace associated with the eigenvalue λ_m , which spans all possible configurations where the total droplet volume is fixed. Differences in the droplet volumes thus all evolve with the rate λ_m .

4.3 Late stage droplet dynamics and Ostwald ripening

In order to understand the behavior of multiple droplets, we start by considering the simple case of two droplets. We express their volumes V_1 and V_2 using the total volume $V_{\text{tot}} = V_1 + V_2$ and the difference $\delta V = V_1 - V_2$. The volume fraction ϕ_0^B of droplet material in the solvent developed in terms of these variables reads

$$\phi_0^B = \frac{4\pi D_B m_1 \bar{R} \phi_+^B(\bar{R}) + (k_{AB} V_c + m_0 Q) (\bar{\phi} - \psi_- V_{\text{tot}} V_c^{-1})}{m_0 Q + (k_{AB} + k_{BA}) V_c + 4\pi D_B m_1 \bar{R}} + \mathcal{O}(\delta V^2) , \quad (4.9)$$

see Eq. (4.6). Here, \bar{R} is the radius of the droplets of volume $V_1 = V_2 = \bar{V}$ in the symmetric stationary state. Note that ϕ_0^B only depends on quadratic and higher-order terms of δV and we may thus neglect this dependence in our linear stability analysis. Equivalently, ϕ_0^A also only depends on δV^2 and higher powers, see Eq. (4.4).

In the case where V_{tot} is stable, i.e. $\lambda_0 < 0$, we can discuss the dynamics of two droplets by considering only their volume difference $\delta V(t)$. This is the late stage of droplet coarsening, where the solvent is depleted of droplet components and their volume fractions ϕ_0^A and ϕ_0^B are constant. Consequently, the total volume V_{tot} of all droplets has reached its stationary state. However, the distribution of this volume among the droplets might still change by compositional fluxes between the droplets. In fact, the volume fraction $\phi_+^B(R_i)$ right outside of droplet i depends on its radius R_i because of surface tension effects, see Eq. (2.7b). Droplets of different size thus impose different volume fractions in the solvent, which leads to the compositional fluxes between the droplets, see Fig. 4.3. In an equilibrium system, these fluxes are

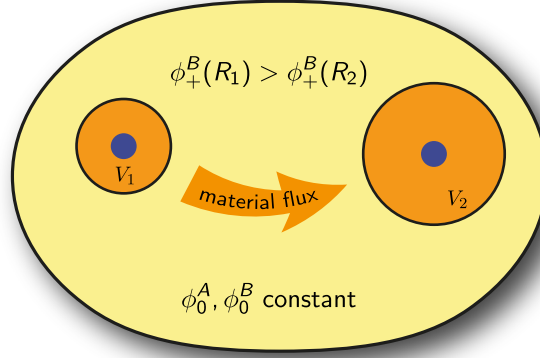


Figure 4.3: Schematic explanation of Ostwald ripening in the late stage of droplet growth, where the solvent (yellow) has been depleted. Consequently, the fraction ϕ_0^A , the fraction ϕ_0^B , and the total droplet volume have reached their stationary state value. Conversely, droplets (orange discs) may have different volumes V_i , which lead to different volume fractions ϕ_+^B right outside their interfaces and thus compositional fluxes (orange arrow) from the smaller toward the larger droplet.

oriented from smaller to larger droplets and thus cause larger droplets to grow at the expense of smaller ones, which is known as Ostwald ripening, see Section 1.5.3.

The flux of droplet material between droplets ceases only if they have the same size. This qualitative argument presented here thus already suggests that all droplets are of the same size if the stationary state is stable.

4.4 Active droplets can suppress Ostwald ripening

We analyze the situation of multiple droplets using the approximate model introduced in Section 4.1. Its numerical solution shows that the passive system without chemical reactions indeed shows Ostwald ripening, see Fig. 4.4A. However, in the case of active droplets, Ostwald ripening can be suppressed, see Fig. 4.4B. Here, droplets with different volumes exchange material until they reach the same size. In the following, we analyze the reasons and determine the required model parameters for this qualitatively different behavior.

The stationary states of the dynamical system are defined by Eq. (4.1) with a vanishing time derivative. The resulting system of algebraic equations can be solved for the droplet volume assuming that all droplets have the same size. The analysis presented in Section 4.2 is then used to determine the stability of these stationary states. Fig. 4.5 shows the droplet sizes in stationary state for the scenarios of first-order kinetics and autocatalytic growth. The case of droplets without surface tension effects discussed in Section 2.2 is shown as a reference (orange lines). All the other

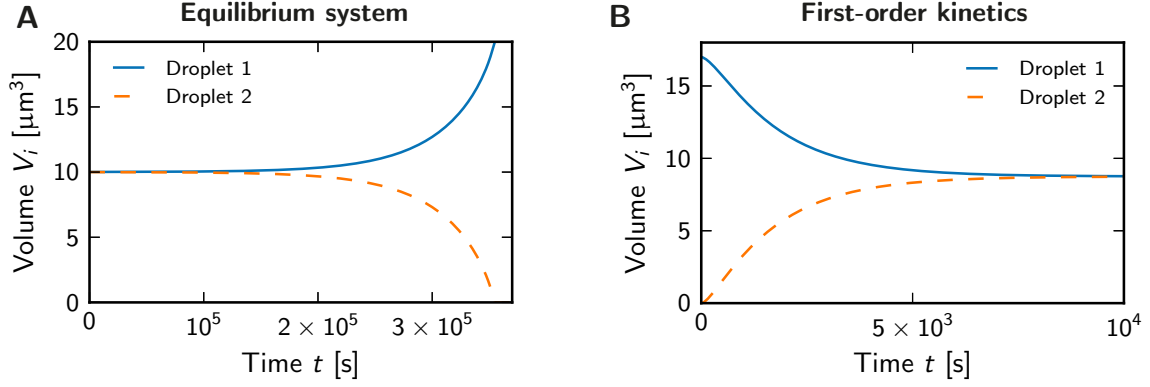


Figure 4.4: Volumes V_i of two droplets $i = 1, 2$ as a function of time t . **(A)** Data of an equilibrium system with initial conditions $V_1(0) = 10.01 \mu\text{m}^3$ and $V_2(0) = 10 \mu\text{m}^3$ are shown. The model parameters are that of Fig. 2.3, but without chemical reactions, $k_{AB} = k_{BA} = 0$, $k_c = 0$, and $Q = 0$. **(B)** Data of active droplets with first-order kinetics and initial conditions $V_1(0) = 17 \mu\text{m}^3$ and $V_2(0) = 0$ are shown. Model parameters have been taken from Fig. 2.3.

lines cover cases where surface tension effects are included. Analogously to the case of a single droplet, which we discussed in Section 3.2, surface tension does not change the stable droplet size much if there are multiple droplets.

If droplets are large, their volumes are thus well approximated by Eq. (2.22) and Eq. (2.25) derived for the respective scenarios A and B without surface tension. These expressions assume that the amount of droplet material in the system is independent of the droplet count m and is equally distributed between all droplets. The volume of a single droplet is thus proportional to m^{-1} . This argument explains why in Fig. 4.5 the stable branch for the case $m = 1$ (solid gray lines) is at significantly larger radii than that for $m = 2$ (blue lines).

The unstable branch of the curve describing the stationary state of a single droplet (dotted gray lines) can be attributed to a critical size, see Section 3.2. We find a similar behavior in the case of multiple droplets, compare the lower branch of the gray and blue lines in Fig. 4.5. Apparently, the critical size a droplet has to overcome in order to grow spontaneously does not depend strongly on the number m of droplets in the system. This is in contrast to the size of the stable stationary state discussed in the previous paragraph. Consequently, the nucleation properties discussed in Section 3.3 are retained: in the case of first-order kinetics, a critical size is observed below a critical fraction $\bar{\phi}$ of droplet components. The threshold value is only weakly dependent on the catalytic activity Q of the core. Conversely, in the autocatalytic scenario, a critical size exists for all values of $\bar{\phi}$ but the critical size vanishes completely for sufficiently large Q . The nucleation of droplets can therefore

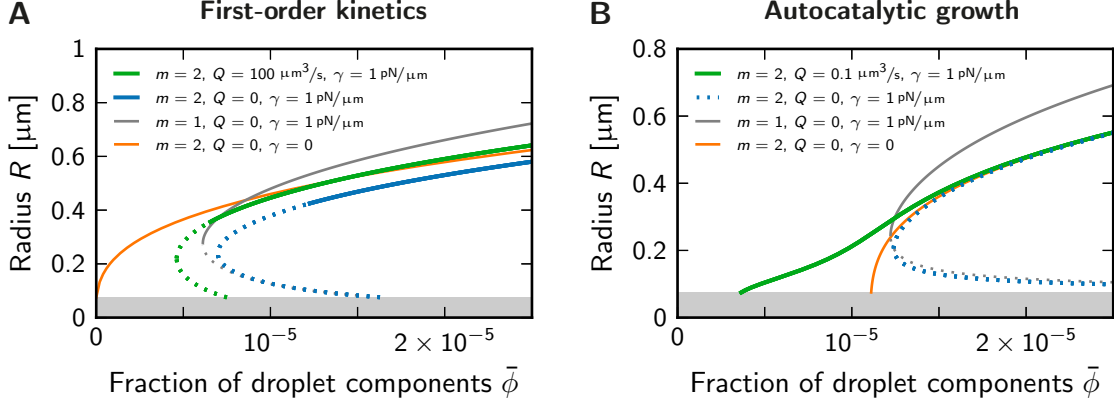


Figure 4.5: Radii of stationary droplets as a function of the overall volume fraction $\bar{\phi}$ of droplet components for different values of the droplet count m , the catalytic activity Q at the cores, and surface tension γ . **(A)** First-order kinetics with parameters given in Fig. 2.3. **(B)** Autocatalytic growth with parameters given in Fig. 2.4. The grey area marks the core and the dotted parts of the curves indicate unstable stationary states.

be seen as a local phenomenon, which is only weakly influenced by the presence of other droplets.

A major difference between the case of multiple and single droplets is the stability of large droplets, compare the upper branch of the red and blue lines in Fig. 4.5. For first-order kinetics, multiple droplets are only stable if there is a sufficient fraction $\bar{\phi}$ of droplet components in the system. The threshold value of $\bar{\phi}$ for this stability depends weakly on the catalytic activity Q of the cores, compare the blue and the green line in Fig. 4.5A. Conversely, in the case of autocatalytic growth, multiple droplets are always unstable if the cores are passive, $Q = 0$. Multiple droplets can be stable if Q exceeds a threshold value, compare the blue and the green line in Fig. 4.5B. In both scenarios, multiple droplets can thus be stable or unstable. We next determine conditions for the parameter values, where this stability can be observed.

4.4.1 Perturbation growth rate in the simple growth scenarios

We consider the late stage of droplet growth, where the volume fractions in the solvent and the total droplet volume have reached their stationary state value and are stable with respect to perturbations. For this typical case, the linear stability analysis presented in Section 4.2 yields the rate $\lambda_m = \mathcal{B}$ with which the difference of volumes of multiple droplets evolves. It reads

$$\lambda_m = (k_c \psi_- + k_{AB}) \frac{1 - \psi_-}{\psi_-} \phi_0^A(V_{\text{tot}}) - k_{BA} + \frac{D_B}{\bar{R}^2 \psi_-} [\phi_0^B(V_{\text{tot}}) - \psi_+] , \quad (4.10)$$

see Eq. (4.7b). Note that the volume fractions ϕ_0^A and ϕ_0^B only depend on the total droplet volume V_{tot} , see Section 4.3, and we can thus solve for the growth rate λ_m without knowing the exact distribution of droplet volumes. Additionally, the growth rate $\partial_t V_i$ vanishes at the stationary state $V_i = \bar{V}$, which leads to the condition

$$0 = (k_c \phi_i^A - k_{BA}) \bar{V} + \frac{Q \phi_i^A}{\psi_-} + \frac{4\pi D_B}{\psi_-} [(\phi_0^B - \psi_+) \bar{R} - \gamma \beta_+] , \quad (4.11)$$

see Eq. (4.1), where $\phi_i^A = (1 - \psi_-) \phi_0^A$. Using the expressions for ϕ_0^A and ϕ_0^B in the stationary state, see Eqs. (4.4) and (4.6), we can thus determine λ_m for different parameter sets.

Scenario A: First-order kinetics

In scenario A, we have $k_c = 0$ and $Q = 0$, which we use together with Eq. (4.11) to solve for ϕ_0^B . With this result, the growth rate λ_m becomes

$$\lambda_m^A(\bar{V}) \approx \frac{4\pi D_B \gamma \beta_+}{3\bar{V} \psi_-} - \frac{2k_{BA}}{3} . \quad (4.12)$$

This expression still contains the droplet volume \bar{V} , which is well approximated by neglecting surface tension effects, see Fig. 4.5. We thus use Eq. (2.22) to arrive at

$$\lambda_m^A \approx \frac{(k_{AB} + k_{BA}) m 4\pi D_B \gamma \beta_+}{3\bar{\phi} V_c k_{AB}} - \frac{2k_{BA}}{3} , \quad (4.13)$$

which only depends on model parameters. Fig. 4.6A shows that this expression captures the behavior of the approximate model of Section 4.1 very well. The analytical expression of λ_m^A can be used to determine the parameter values, where the associated stationary state is stable, i.e. where $\lambda_m^A < 0$. We use the equality $\lambda_m^A = 0$ to derive the minimal fraction of material

$$\bar{\phi}_{\text{stab}}^A \approx \frac{k_{AB} + k_{BA}}{k_{AB} k_{BA}} \cdot \frac{2\pi m D_B \gamma \beta_+}{V_c} \quad (4.14)$$

above which m droplets are stable in scenario A.

According to Eq. (4.14), the stability of multiple droplets depends on the strength of the chemical reaction: if either reaction rate constant, k_{AB} or k_{BA} , vanishes, the threshold fraction $\bar{\phi}_{\text{stab}}^A$ diverges and multiple droplets cannot be stable. One important consequence of the chemical reactions are the induced fluxes of material in the stationary state. These fluxes allow us to explain the stability qualitatively: the chemical reactions convert droplet material of form B into its soluble form A predominately inside the droplet. The associated integrated reaction flux scales with the droplet volume, i.e. with R^3 . The droplet material lost in this way must be compensated for by the influx across the droplet surface. This flux typically scales

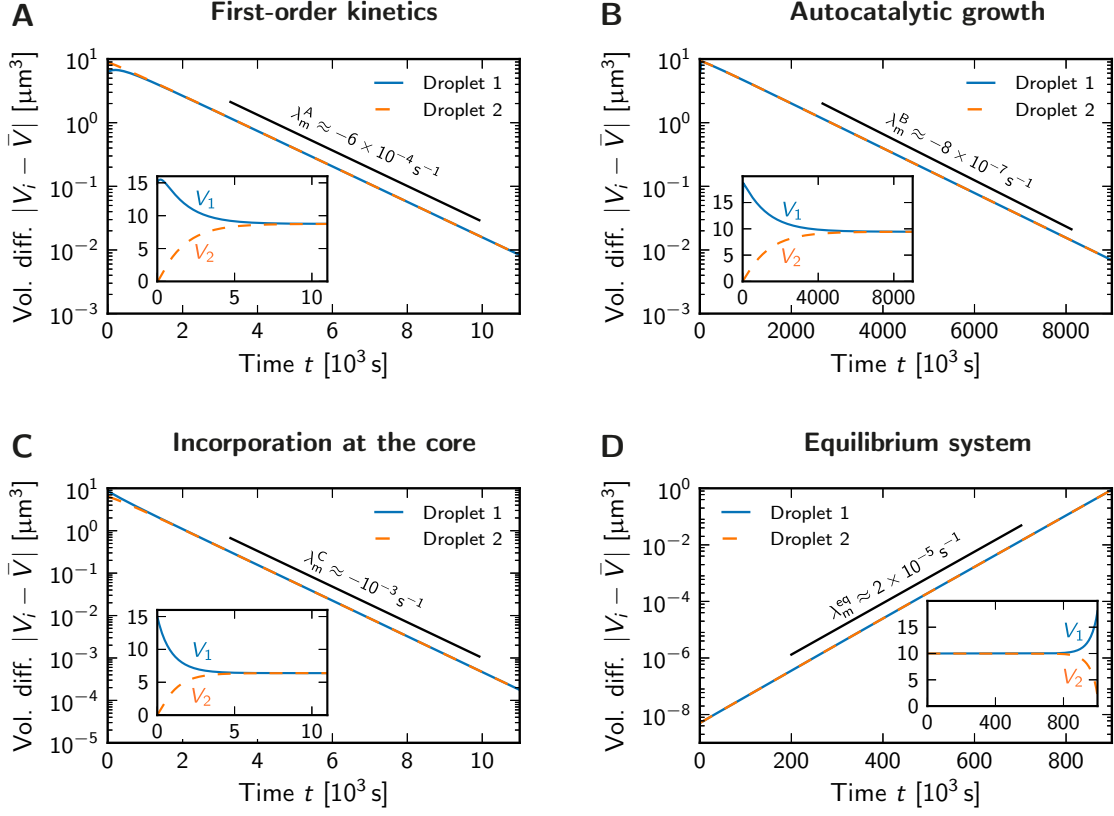


Figure 4.6: The volumes $V_1(t)$ and $V_2(t)$ of two droplets are shown as a function of time t . The semi-logarithmic plots show the difference to the stationary state volume \bar{V} and the associated analytical rates λ_m are indicated by black lines. The insets show the trajectories $V_1(t)$ and $V_2(t)$. **(A–C)** Two unequal droplets ($V_1(0) = 0$, $V_2(0) = 15 \mu\text{m}^3$) approach the same size in the three non-equilibrium scenarios: (A) first-order kinetics, (B) autocatalytic growth, and (C) incorporation at the cores. The model parameters are taken from Figs. 2.3, 2.4, and 2.5, respectively, and the rates λ_m are respectively given in Eqs. (4.13), (4.16), and (4.20). **(D)** Ostwald ripening of an equilibrium system is shown. Two droplets of similar volume ($V_1(0) - V_2(0) = 10^{-8} \mu\text{m}^3$) are simulated in a passive system without chemical reactions, $k_{AB} = k_{BA} = 0$, $k_c = 0$, and $Q = 0$, but including surface tension effects, $\gamma_{\beta+} = 10^{-6} \mu\text{m}$. Their volumes diverge with a rate λ_m^{eq} given in Eq. (4.21).

with R^n , where $n \leq 1$. Because of these different scalings, the droplet loses more material than it gains if it grows beyond its stationary state size where the two fluxes are balanced. Consequently, larger droplets will shrink back to the stationary state size. This explains intuitively why multiple droplets can be stable in the non-equilibrium model with first-order reaction kinetics.

Scenario B: Autocatalytic growth

In scenario B, the droplet material is predominately produced inside the droplet by the autocatalytic reaction. The flux of droplet material is thus opposite to the one in scenario A, see Fig. 3.1. Additionally, the fraction of droplet material outside of droplets can be estimated by $\phi_0^B \approx \phi_+^B$, which is a good approximation for small systems, where the length scale $\alpha^{-1} = \sqrt{D_B/k_{BA}}$ of the droplet material distribution is large compared to the system size. Using Eq. (4.11), we can then express the growth rate as

$$\lambda_m^B(\bar{V}) \approx \frac{4\pi D_B \gamma \beta_+}{3\bar{V}\psi_-} - \frac{Q k_{BA}}{Q + k_c \bar{V}\psi_-}. \quad (4.15)$$

In the following, we consider the case of a small catalytic activity, $Q \ll k_c \bar{V}\psi_-$, for scenario B. Here, the stationary state droplet volume \bar{V} is well approximated by Eq. (2.25), see Fig. 4.5. Using these approximations, we arrive at

$$\lambda_m^B \approx \frac{m}{V_c} \left(\bar{\phi} - \frac{k_{BA}}{(1 - \psi_-)k_c} \right)^{-1} \left[\frac{4\pi D_B \gamma \beta_+}{3} - \frac{k_{BA} Q}{k_c} \right]. \quad (4.16)$$

This expression for the perturbation growth rate agrees very well with numerical simulations, see Fig. 4.6B. These simulations show that the associated stationary state with multiple droplets can be stable, i. e. λ_m^B can take negative values. Generally, the sign of λ_m^B is determined by the sign of the square bracket, since $\bar{\phi}$ must be larger than $\bar{\phi}_{\min}^B$ given in Eq. (2.26) and the round bracket is thus positive. We can use the equality $\lambda_m^B = 0$ to determine the minimal catalytic activity Q_{stab}^B above which multiple droplets are stable in the autocatalytic scenario. This threshold reads

$$Q_{\text{stab}}^B \approx \frac{4\pi D_B k_c \gamma \beta_+}{3k_{BA}}. \quad (4.17)$$

In scenario B, multiple droplets are thus only stable if the catalytic activity Q at their cores is strong enough to overcome the destabilizing effects of both surface tension γ and the autocatalytic reaction quantified by the rate constant k_c .

Moreover, Eq. (4.17) can be used to discuss the influence of the chemical reactions on the stability of multiple droplets. Comparable to scenario A, the stability threshold diverges if the rate constant k_{BA} of the reaction $B \rightarrow A$ vanishes. Consequently, multiple droplets can only be stable if the chemical reactions are present.

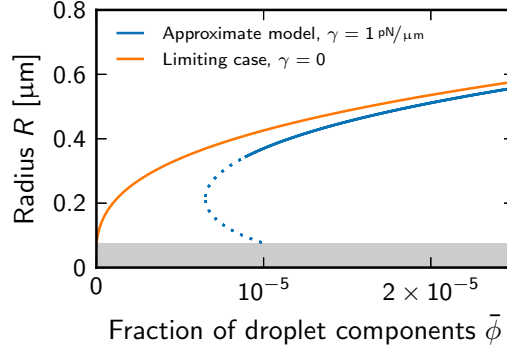


Figure 4.7: Radius of droplets built by active cores in scenario C as a function of the fraction $\bar{\phi}$ of droplet components. The stationary state size is shown with (blue line) and without (orange line) surface tension effects. The model parameters have been taken from Fig. 2.5.

Interestingly, the stability threshold Q_{stab}^B increases for larger rate constants k_c of the autocatalytic reaction. The autocatalytic reaction thus has a destabilizing effect. This can be explained qualitatively by noting that the reaction flux of the autocatalytic reaction scales with the droplet volume. Larger droplets gain more droplet material and grow quicker than smaller ones because of this scaling. If fluctuations increase the droplet volume beyond its stationary state size, these fluctuations will be enhanced at the expense of the volumes of other droplets and the associated stationary state is therefore not stable.

We showed that the autocatalytic reaction destabilizes multiple droplets and that the reaction flux at the core can counteract this behavior. Here, it is important to note that the reaction flux at the core does not only depend on the quantity Q , which describes the strength of the catalytic reaction, but also on the fraction $\phi^A(a)$ of soluble building blocks at the core. Since soluble building blocks are turned into droplet material in the whole volume of the droplet by the autocatalytic reaction, their fraction is typically lower close to the core. This effect thus weakens the stabilizing effect of the core. The magnitude of the decrease depends on the details of the reaction-diffusion system. We investigate this problem in more detail in Appendix I. Accounting for this depletion effect alters the results quantitatively and shift the calculated stability thresholds, see Fig. I.1. More importantly, the qualitative, general stability criteria are conserved, i. e. multiple droplets are stable in the case of first-order kinetics if there is enough material in the system. Conversely, a strong enough catalytic activity at the cores is required to stabilize multiplied droplets in the autocatalytic growth scenario.

Scenario C: Incorporation by the active cores

The size and stability of multiple droplets built by active cores can also be investigated using the stationary state analysis presented in Section 4.1. Fig. 4.7 shows that the

droplet size is not much modified from the analytical value given in Eq. (2.29), where surface tension γ is ignored. However, surface tension introduces a minimal amount of material necessary to grow droplets. This threshold value can be estimated from Eq. (4.11). For simplicity, we consider the strong segregation regime, $\psi_+ = 0$, and neglect droplet material outside of droplets, $\phi_0^B \approx 0$. We additionally assume that the fraction of soluble building blocks is roughly given by $\phi_0^A \approx \bar{\phi}$, which is a good approximation for small droplets. Taken together, we solve Eq. (4.11) for the fraction $\bar{\phi}$ of droplet components, which yields the threshold value

$$\bar{\phi}_{\min}^C \approx \frac{4\pi D_B \gamma \beta_+}{(1 - \psi_-)Q}. \quad (4.18)$$

Equivalently, we get the minimal catalytic activity Q required to form droplets at a given fraction $\bar{\phi}$, which reads

$$Q_{\text{stab}}^C \approx \frac{4\pi D_B \gamma \beta_+}{(1 - \psi_-)\bar{\phi}}. \quad (4.19)$$

Furthermore, we get the rate λ_m at which perturbations of the stationary state decay by setting $k_c = 0$ in Eq. (4.15). This yields

$$\lambda_m^C \approx \frac{4\pi D_B \gamma \beta_+}{3\psi_- V^C} - k_{BA}. \quad (4.20)$$

We can recover Eq. (4.19) from the condition $\lambda_m^C > 0$ if we approximate the droplet volume V^C by Eq. (2.29) and assume that surface tension effects are small. Interestingly, the second term of Eq. (4.20) is dominant and the perturbation growth rate is thus very well captured by $\lambda_m^C \approx -k_{BA}$, see Fig. 4.6C. Interestingly, we find that droplets are almost always stable, which underlines the stabilizing effect of the active cores found in the previous section.

Ostwald ripening of an equilibrium system

The main result of this chapter is the existence of multiple stable droplets in several non-equilibrium scenarios. Interestingly, the perturbation growth rates of Eqs. (4.13), (4.16), and (4.20) all converge to the same expression in the limit of vanishing reaction rates, $k_{BA} \rightarrow 0$. The perturbation growth rate then becomes

$$\lambda_m^{\text{eq}} \approx \frac{4\pi D_B m \gamma \beta_+}{3\bar{\phi} V_c}. \quad (4.21)$$

This rate is positive and multiple droplets are thus unstable. The value of λ_m^{eq} also agrees very well with the numerical simulations, see Fig. 4.6D. In the limit $k_{BA} \rightarrow 0$, all droplet components are turned into their phase separating form B . Consequently,

λ_m^{eq} is the rate at which droplets exchange material in an equilibrium system of multiple droplets.

The perturbation growth rate λ_m^{eq} has been derived for the late stage of Ostwald ripening, where the total droplet volumes stays constant. Additionally, the theory only considers cases where the droplets are far apart from each other such that the mean field description is valid. Similar considerations have been used earlier to derive the coarsening rate of precipitates [202]. λ_m^{eq} describes how individual droplets evolve in time in the presence of other droplets. Small droplets will eventually disappear from the solution, which leads to a decrease of the droplet count and thus to an increase of the average volume over time. For large systems, this process typically leads to an average droplet volume that increases linearly with time [138].

4.4.2 Parameter dependence of the stability of multiple droplets

We found that the stability of multiple droplets depends on the choice of model parameters. In this section, we explore the conditions under which multiple droplets can coexist in the scenarios A and B. Here, we use numerical simulations of the dynamical system introduced in Section 4.1 and compare these to the approximate, analytical results of the previous section.

For simplicity, we first consider the situation of at most two droplets forming. Assuming that there are two cores in the system, there are three different stationary state configurations: two bare cores ($m_0 = 2, m_1 = 0$), a single droplet and a bare core ($m_0 = m_1 = 1$), or two droplets of the same size ($m_0 = 0, m_1 = 2$). The analysis of the stationary states works as follows: we first determine the droplet volumes associated with the three possible stationary states mentioned above. Using these results, we then determine their stability by numerically calculating the eigenvalues of the Jacobian given in Eq. (4.1). This allows us to identify the set of stable stationary states for each parameter configuration. The procedure is explained in more detail in Appendix J and is also illustrated in Fig. J.1. With this method, we can analyze the stability as a function of two model parameters using different colors for the different states, see Fig. 4.8.

We show the possible stationary states for both the first-order kinetics and the autocatalytic growth scenario in Fig. 4.8. A first observation is that all three droplet configurations can be stable in both scenarios. Typically, no droplets form and only bare cores exist if there is not enough material in the system. Panels A and B highlight that the reaction rate constant k_{BA} must be sufficiently large for multiple droplets to be stable. If k_{BA} is small, almost all the droplet components are in form B and we recover the equilibrium situation in the limit $k_{BA} \rightarrow 0$.

The stability of multiple droplets also depends on the strength of the surface tension, see panels C and D of Fig. 4.8. Typically, configurations of one or two droplets are only stable if the surface tension is low enough. Furthermore, the stability of the droplets is influenced by the catalytic activity Q at the cores, see panels E and F. In the case of first-order kinetics, Q only has a minor effect and

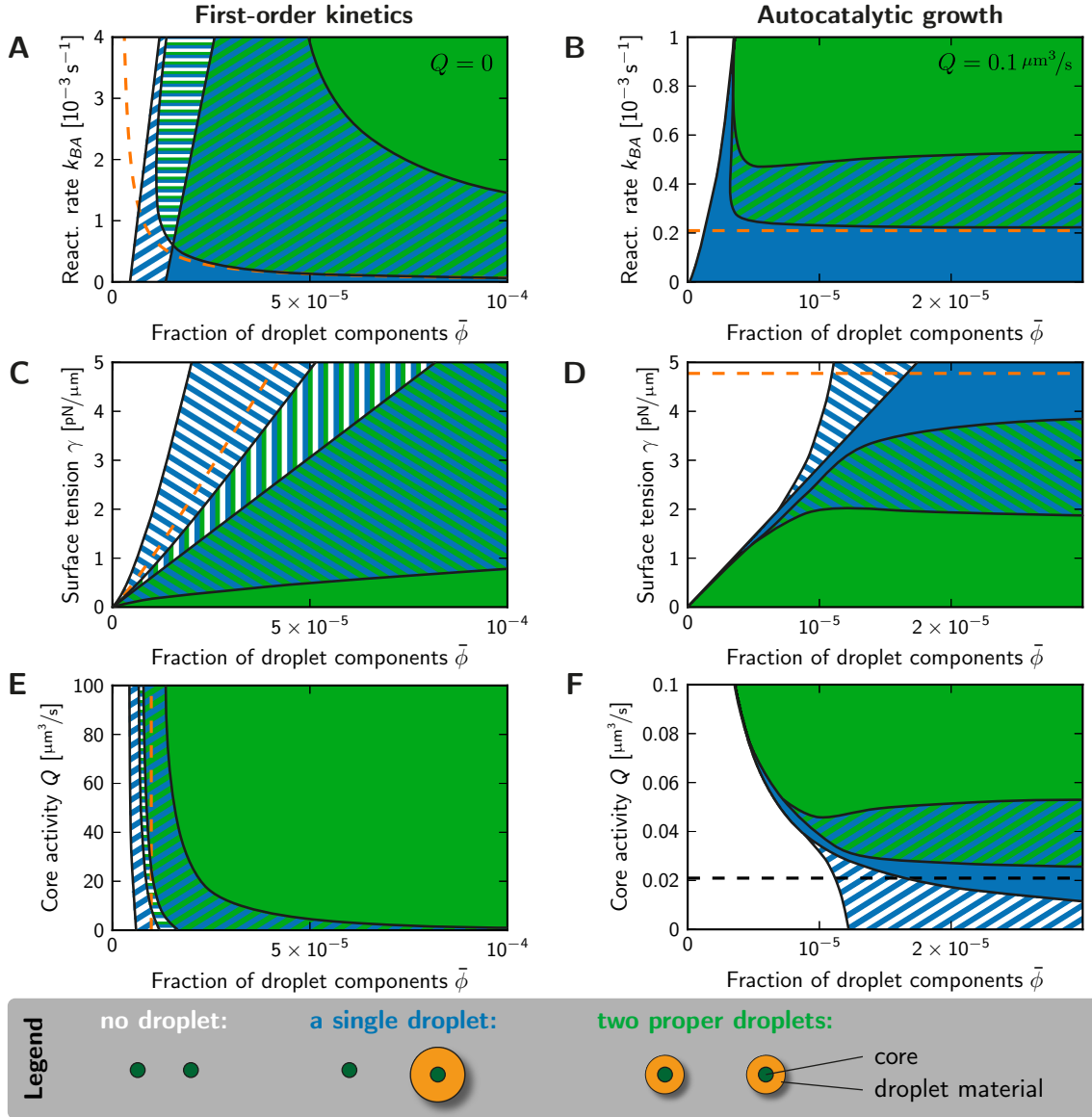


Figure 4.8: Stable stationary states of droplets growing around two cores. We distinguish configurations with no droplets (white region), one stable droplet (blue region), and two stable droplets (green region). Regions with multistability are drawn in a hatched style with colors corresponding to the states mentioned before. The fraction $\bar{\phi}$ of droplet components is varied in addition to (A, B) the reaction rate constant k_{BA} , (C, D) the surface tension γ , and (E, F) the catalytic activity Q at the core at $\gamma = 1 \text{ pN}/\mu\text{m}$. The remaining parameters depend on the scenario: **(A, C, E)** First-order kinetics with parameters given in Fig. 2.3. The dashed orange lines mark stability thresholds derived from Eq. (4.14) for $m = 2$. **(B, D, F)** Autocatalytic growth with $Q = 0.1 \mu\text{m}^3/\text{s}$ and other parameters given in Fig. 2.4. The dashed orange lines mark stability thresholds derived from Eq. (4.17).

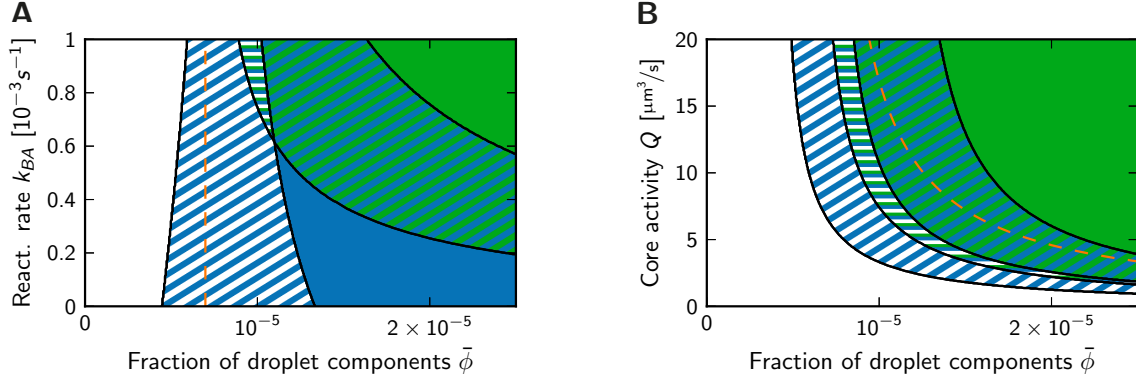


Figure 4.9: Stability diagrams of two droplets built by active cores in scenario C. We distinguish configurations with no droplets (white region), one stable droplet (blue region), and two stable droplets (green region). Regions with multi-stability are drawn in a hatched style with colors corresponding to the states mentioned before. **(A)** Stability diagram as a function of the fraction $\bar{\phi}$ of droplet components and the reaction rate constant k_{BA} . The dashed orange line marks the threshold given in Eq. (4.18). **(B)** Stability diagram as a function of the fraction $\bar{\phi}$ of droplet components and catalytic activity Q . The dashed orange line marks the threshold given in Eq. (4.19). The model parameters have been taken from Fig. 2.5 in both panels.

the stability is mainly determined by the fraction $\bar{\phi}$ of droplet components in the system. Conversely, Q has a dominating role in the autocatalytic scenario. Here, multiple droplets can only be stable, if Q is sufficiently large.

The orange dashed lines in Fig. 4.8 additionally indicate the approximate, analytical stability thresholds of Eqs. (4.14) and (4.17) calculated in the previous section. Both values predict the onset of stability of two droplets with reasonable accuracy. There are notable deviations, especially for small volume fractions in the autocatalytic growth scenario. We attribute these differences to the approximation of the volume fraction ϕ_0^B of droplet material in the solvent.

Remarkably, the state of a single droplet becomes unstable in scenario A if the fraction $\bar{\phi}$ is sufficiently large, see the left column of Fig. 4.8. This is surprising because it means that a single large droplet becomes unstable and spontaneously split up into smaller droplets in this case. In fact, this observation is in accordance with the shape instability of large droplets that we discussed earlier, see Fig. 3.11 in Section 3.5.4. That is, the system favors a certain finite droplet size, which is reminiscent of the pattern formation discussed in Section 1.6. In the autocatalytic scenario, a similar effect is observed, see the right column of Fig. 4.8. Here, the effect is introduced by catalytic cores, which may nucleate droplets if Q is sufficiently large. Generally, a catalytic activity at the cores stabilizes multiple droplets. This is especially apparent in scenario C, where it is the only way of creating droplet

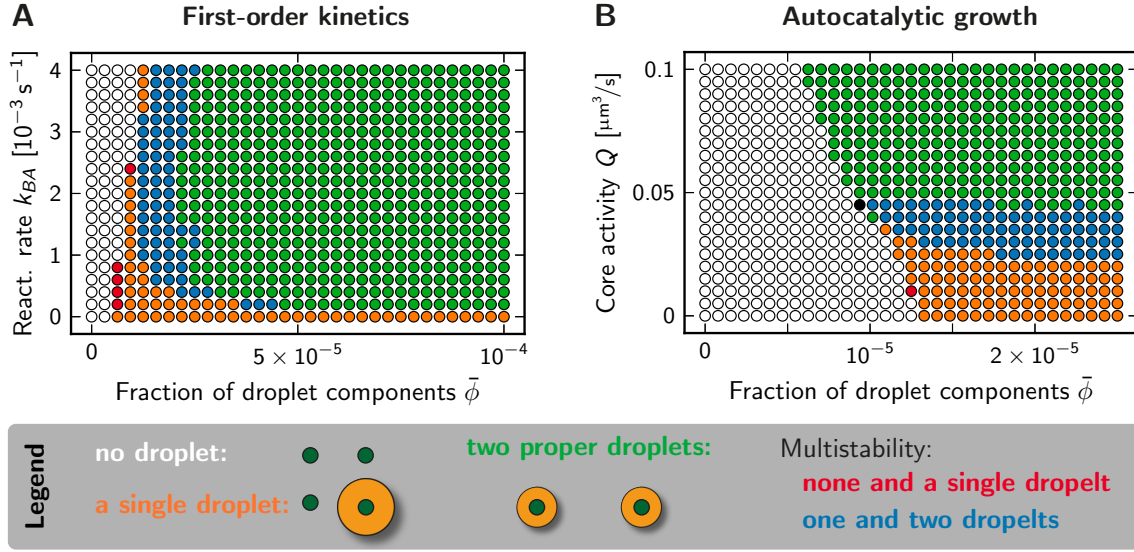


Figure 4.10: Quantification of the final state of an ensemble of numerical simulations of the evolution equation (4.1) with random initial conditions. Each dot indicates one set of tested parameters, where the color corresponds to the observed result: no stable droplets (white), no droplets or a single one (red), only a single droplet (orange), a single or two droplets (blue), only a pair of droplets (green). Regions where the numerical method was not conclusive are marked in black. **(A)** First-order kinetics with parameters given in Fig. 2.3. **(B)** Autocatalytic growth with parameters given in Fig. 2.4.

material. The stability thresholds in this case were calculated in Eqs. (4.18) and (4.19) and are compared to the associated stability diagrams in Fig. 4.9.

Figs. 4.8 and 4.9 furthermore identify regions in parameter space, where multiple stationary states can be stable. Here, the attained stationary state configuration depends on the initial condition. In order to determine the importance of these multistable regions, we now simulate the dynamical system given in Eq. (4.1) numerically. In this way, we can test the stability diagrams obtained above and we also get a better insight into the dynamics of the system. We start each individual simulation with a random initial configuration of two droplet volumes, each chosen uniformly from the interval $[0, V_{\max}]$, with $V_{\max} = \bar{\phi}V_c/(m\psi_-)$. For each parameter point investigated, we simulate 10^3 trajectories for $t = 10^7$ s and record the two final droplet volumes, V_1 and V_2 . We then compile a histogram of the frequency of the pairs (V_1, V_2) . We locate clusters in this distribution of the final droplet volumes to judge which configuration has been reached, see Appendix J and Fig. J.2. From this analysis we determine the stability diagram in an alternative way, see Fig. 4.10. This procedure is a Monte Carlo method to sample phase space and detect the stationary states.

The two ways of determining the stability diagram show a similar structure of the possible stationary states, compare the panels *A* and *F* of Fig. 4.8 with Fig. 4.10. One difference between the two methods becomes apparent when the stability boundaries of multistable regions are considered. The regions of multistability predicted by the linear stability analysis are much larger than the corresponding ones in the stability diagram obtained with the Monte Carlo method. This is to be expected, since multistability can only be observed with the right choice of initial conditions in the Monte Carlo method. When the stability boundary is approached, the number of initial conditions leading to the less likely configuration reduces until it vanishes at the boundary. In the Monte Carlo method, we only consider a finite number of different initial conditions, thus possibly missing initial conditions leading to other final configurations. On the other hand, this numerical investigation provides an estimate of the size of the basin of attraction of stationary state configurations: a given stationary state configuration that does not appear in the Monte Carlo method is unlikely to be relevant in experiments, since it is only reached from a small number of initial conditions. All in all, the Monte Carlo method therefore should give a better picture of what to expect in experiments, while the stability diagram obtained from the analytical analysis is a more accurate representation of the possible solutions of the dynamical system.

4.4.3 Stability of more than two droplets

So far, we only showed results of the situation of at most two droplets. We found that the non-equilibrium system sometimes favors the situation of multiple droplets over those containing only a single droplet, which can be unstable. In this section, we investigate whether this is a general trend and whether such phase separating systems typically favor a certain number of droplets or a specific droplet size. To examine these questions, we investigate the stability of configurations with more than two droplets.

For simplicity, we only consider configurations with up to four droplets. We thus have to investigate five different configurations containing anything from zero to four droplets. For each parameter point, we assess the stability of these states numerically. The analysis is the same as the one for two droplets, see Section 4.4.2. Fig. 4.11 shows the stability regions of configurations with up to four droplets. In both scenarios A and B, we again find that all possible configurations are only stable in a limited parameter range and that multistable regions exist. Note that any state with multiple droplets is only stable between a minimal and a maximal reaction rate constant k_{BA} . The stability thresholds depend both on the fraction $\bar{\phi}$ of droplet components and on the number m of droplets that we investigate. Generally, we find that both the minimal and the maximal threshold of $\bar{\phi}$ increase with larger values of m . For a given set of parameters, there thus exist lower and upper bounds for the droplet count m of possible stable configurations. Alternatively, we can interpret these bounds as upper and lower limits for the associated droplet volume. This is because

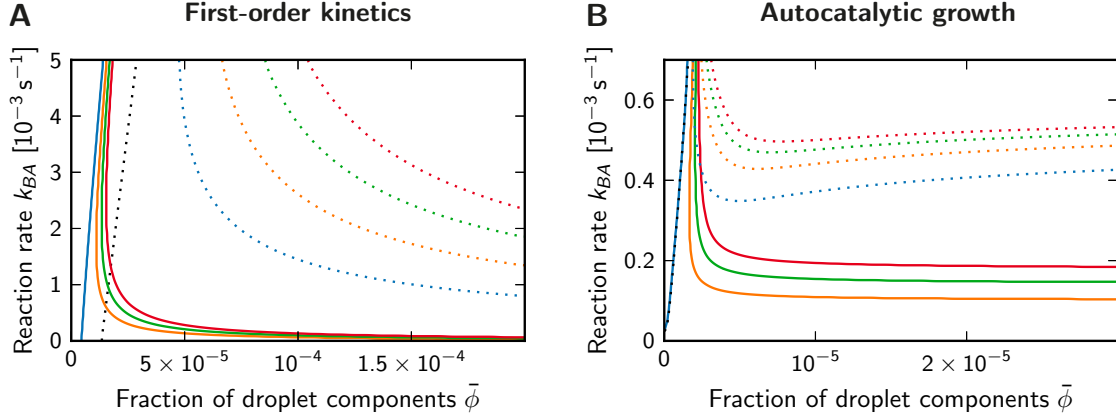


Figure 4.11: Stability diagrams of the possible stationary states of up to four droplets. The state with m droplets is stable in the regions enclosed by the solid and the dotted line of the respective color: blue, orange, green, and red for $m = 1, 2, 3, 4$. The state without droplets is only stable for values of $\bar{\phi}$ below the threshold indicated by the dotted black line. **(A)** First-order kinetics with parameters given in Fig. 2.3. **(B)** Autocatalytic growth with parameters given in Fig. 2.4.

the droplet volume is roughly inversely related to m , see Eqs. (2.22) and (2.25). The non-equilibrium model discussed in this thesis thus has the interesting property that it selects for a certain droplet size.

We next examine analytical expressions approximating the stability bounds that we observe numerically. Here, we focus on the first-order kinetics of scenario A, where the number of droplets that can coexist increases with both the reaction rate constant k_{BA} and the fraction $\bar{\phi}$ of droplet components, see Fig. 4.11A. The associated lower and upper bounds on the droplet volume can be derived analytically. The minimal droplet radius,

$$R_{\min}^A \approx \left(\frac{(k_{AB} + k_{BA})V_c\gamma\beta_+}{4\pi m k_{AB}\psi_-} \right)^{\frac{1}{4}}, \quad (4.22)$$

has already been calculated in Eq. (3.10). Conversely, the maximal volume V_{\max}^A of droplets is related to the minimal value for $\bar{\phi}$ at which m droplets are stable, see Eq. (4.14). Solving this equation for m and inserting it into the expression for the droplet volume, Eq. (2.22), we retrieve the maximal volume V_{\max}^A of a droplet such that it is stable in scenario A. The approximate expression reads

$$V_{\max}^A \approx \frac{4\pi D_B \gamma \beta_+}{k_{BA} \psi_-}. \quad (4.23)$$

We can thus analyze how the chemical reactions influence the minimal and maximal droplet size. Using the expressions from above, we find that $R_{\min}^A \propto \kappa^{-1/4}$ and $R_{\max}^A \propto k_{BA}^{-1/3}$, where $\kappa = k_{AB}/(k_{AB} + k_{BA})$. The minimal droplet size thus depends on the chemical equilibrium constant k_{AB}/k_{BA} . Conversely, the maximal droplet size is determined by the rate constant k_{BA} . The scaling of R_{\max}^A with the reaction rate constant is reminiscent of the result obtained in other system combining phase separation with chemical reactions [167]. The typical length scales of patterns that form in these systems also scales with $k_{BA}^{-1/3}$ in the strong segregation regime where the interface between droplet phase and solvent is sharp [167]. In our model, the droplet radius can be interpreted as a typical length scale characterizing the system. The analogous scaling behavior with the chemical reaction rate constant thus suggests that our scenario A is very similar to the systems studied earlier.

4.5 Discussion

Multiple droplets can be stable in the non-equilibrium model discussed in this thesis. This is in contrast to the equilibrium case, where only the state with a single droplet can be stable because of Ostwald ripening, see Section 1.5.3. We can recover this result as a limiting case of our non-equilibrium model by letting $k_{BA} \rightarrow 0$. In this limit, all the material would end up in the phase separating form B and all the chemical reactions would cease. In accordance with the equilibrium results, the perturbation growth rate λ_m^{eq} of a state with multiple droplets is positive, indicating that multiple droplets can never be stable in this limit. This emphasizes the importance of the stationary state fluxes driven by chemical reactions.

The analysis of the stationary states showed that surface tension tends to destabilize the situation of multiple droplets in all scenarios considered here. This is again in agreement with the equilibrium situation, where the configuration with a single droplet minimizes the surface energy. Interestingly, the chemical reactions of the non-equilibrium model can either be stabilizing or destabilizing: if first-order kinetics dominate droplet growth, multiple droplets are stable. Conversely, an autocatalytic mechanism producing droplet material tends to destabilize the state of multiple droplets. These differences are related to the different directions of the compositional fluxes in the stationary state. The overall stability of multiple droplets depends on the combination of stabilizing and destabilizing effects. In the case of the autocatalytic scenario, which is inherently unstable, the catalytic activity at the cores can provide a stabilizing mechanism. This is also the reason why multiple droplets are typically stable if they are solely built by active cores.

The growth of multiple small droplets occurs in two stages until they reach the stable stationary states discussed in this chapter. Initially, all the droplets grow until their total volume approaches the stationary state value that we discussed in Section 2.2. Droplet material is then exchanged between the droplets until they reach a state where all droplets have the same size. This second phase happens with a

different time scale and is driven by the stabilizing factors discussed in the paragraph above. The time scales of these two processes can be markedly different. For instance, in the autocatalytic scenario with parameter values given in Fig. 2.4, the growth rate $\lambda_B = \frac{1}{2}[(1 - \psi_-)\bar{\phi}k_c - k_{BA}]$ of the first stage is about four orders of magnitude faster than the rate λ_m^B associated with the tendency to get droplets of the same size, see Eq. (4.16). Consequently, these autocatalytic droplets quickly reach their final total size, but initial mismatches decay comparatively slowly. For all examples considered here, these two growth regimes are well separated as indicated by the excellent agreement between the numerical results and the theoretical predication of the transient dynamics, see Fig. 4.6. This separation of time scales allows us to discuss the two growth regimes independently to arrive at simple analytical results.

All results of this chapter are based on the approximate model that we introduced in Section 4.1. The model is based on a mean-field description of the droplet interaction, where the position of droplets is unimportant. This is an approximation, since droplets could in general be close together and the active behavior might facility coalescences or repel the droplets from each other.

In a more general view, the interplay of phase separation and chemical reactions causes new behavior that is not present in the equilibrium case where chemical reactions are absent. These systems for instance favor a certain number of droplets and thus provide a mechanism for controlling droplet size and count. This is reminiscent of the system discussed in Section 1.6, where pattern formation caused by the non-equilibrium nature of the chemical reactions has been observed. The configuration of multiple droplets investigated here can also be seen as a kind of pattern and the results are therefore related. In summary, it seems to be a general feature of non-equilibrium phase separating systems that they can support states with multiple structures of a defined size.

Chapter 5

Active Droplets with Fluctuations

PROTEINS are produced by translating mRNA transcribed from the respective genes [1]. This gene expression is a stochastic process that leads to randomness in the copy number of proteins [203–205]. These fluctuations are significant for many processes inside cells since each type of protein only exists in a low number of copies, where a typically order of magnitude is 10^4 [206]. Estimating the size of the fluctuations by the square root of the copy number [207], the relative uncertainty of the protein copy number is thus about 1%. This number seems low enough to allow for a robust function of the proteins. However, signaling molecules and enzymes often exist at much lower copy numbers and many proteins only function in a sub-volume of the cell. Consequently, the effective copy number of the proteins taking part in chemical reactions can be much lower than the total number in the cell. Moreover, the explicit formation and translation of mRNA [208], as well as slow promoter-state fluctuations [209, 210], could lead to bursts in protein synthesis. Here, several proteins are produced within a short time and fluctuations in mRNA copy number would thus amplify fluctuations in protein copy numbers. Under these situations, the relative fluctuations are much higher and may contribute significantly to randomness in the protein function. Taken together, noise is an important aspect each cell has to deal with. This motivates us to investigate the effect of finite copy numbers in our model.

The small copy number of proteins influences chemical reactions happening in the cell. Here, the copy number of the product of a chemical reaction fluctuates both due to the randomness in the number of reactants as well as due to the stochastic nature of the chemical reaction itself. If non-linear processes are involved, fluctuations in copy numbers may be amplified [207] or they may trigger qualitatively different behaviors, e.g. oscillations in an otherwise non-oscillatory system [211]. Investigating the effect of fluctuations is thus even more important if non-linearities dominate the deterministic situation. Such systems of chemical reactions are often discussed in the context of a well-stirred mixture at constant temperature in a fixed volume [212]. For this special case, efficient simulation algorithms for solving the chemical master equation, for instance the Gillespie algorithm [213], have been developed. These algorithms cannot be used in our case, since a key feature of our model is the droplet formation causing spatial inhomogeneities. We therefore have to develop an

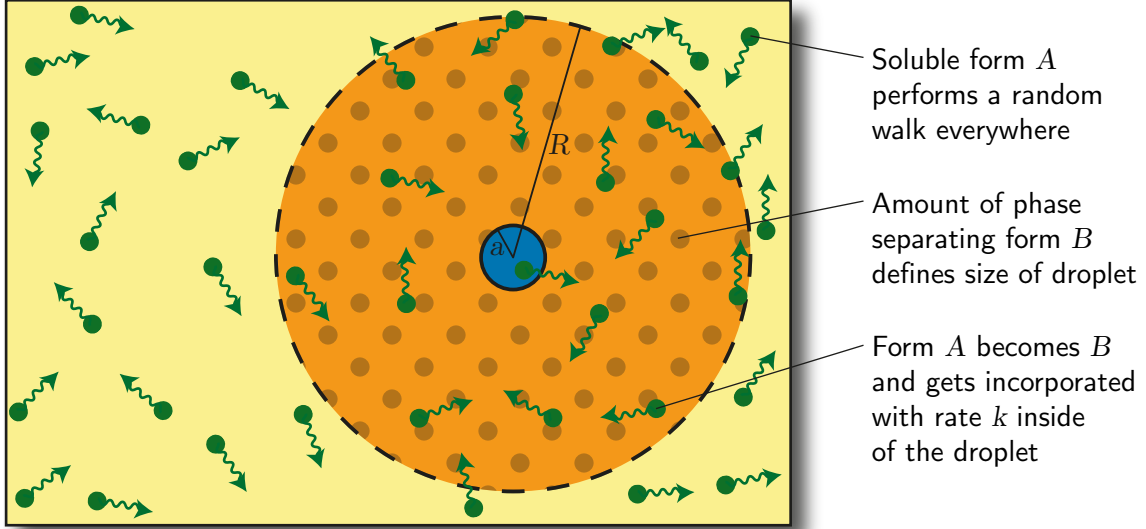


Figure 5.1: Schematic representation of an active droplet in the stochastic model. Particles in the soluble form A (green dots) diffuse freely and become form B with a rate k inside the droplet (orange). Individual B particles are not considered, but their amount defines the droplet radius R . The blue circle of radius a represents the active core, where A particles are turned into form B with a rate k_Q .

algorithm that also accounts for this spatial structure. This will allow us to examine how noise influences the interplay of chemical reactions and phase separation.

In the next section, we introduce a stochastic version of our model. The algorithm itself and its implementation as a computer program were developed with the help of a Master student, Coleman Broaddus. After describing the stochastic simulations briefly, we compare them to a numerical solution of the deterministic model. We focus on scenario B, since the autocatalytic growth discussed there results in multiplicative noise. In the remaining sections, we then analyze this stochastic model and find that the autocatalytic term amplifies fluctuations and accelerates droplet growth.

5.1 Stochastic version of the active droplet model

In this section, we define a stochastic version of the model that we introduced in Section 2.1. Here, we consider the droplet components of form A and B as individual particles that diffuse in the system and undergo chemical reactions $A \rightleftharpoons B$ as introduced in Section 2.1.2. The B particles accumulate into droplets and thereby define distinct compartments within the system. At any point in time, the system is fully described by the positions and types of these particles.

Table 5.1: Standard values of the parameters of the stochastic simulations.

Quantity	Symbol	Value	Remark
Model parameters:			
Cell volume	V_c	$10^4 \mu\text{m}^3$	Parameters of the autocatalytic scenario, see Fig. 2.4 or Table 6.2
Radius of the core	a	75 nm	
Rate constant of $B \rightarrow A$	k_{BA}	10^{-3} 1/s	
Fraction of B in droplets	ψ_-	0.1	
Diffusion constant	D_A	$5 \mu\text{m}^2/\text{s}$	
Droplet component fraction	$\bar{\phi}$	2×10^{-4}	
Autocatalytic rate constant	k_c	100 1/s	
Activity of the core	Q	$0.1 \mu\text{m}^3/\text{s}$	
Simulation parameters:			
Time step	Δt	10^{-3} s	Estimated, see Appendix K
Number of particles	N	10^4	Low fluctuations, see Section 5.3
Initial droplet volume	V_0	$0.1 \mu\text{m}^3$	Arbitrary small volume

In order to arrive at a simple description, we focus on the autocatalytic scenario and therefore set $k_{AB} = 0$. We furthermore consider the strong segregation regime, $\psi_+ = 0$, and neglect surface tension, $\gamma = 0$. Consequently, droplet material of form B only exists within droplets. The fraction ψ_- of form B in the droplet is typically large compared to the volume fraction of form A anywhere in the system. We take this as a justification to neglect the individual particle positions of B and only keep track of their number N_i^B within each droplet $i = 1, \dots, m$. The volume of droplet i is then given by

$$V_i = \frac{\tilde{\nu} N_i^B}{\psi_-}, \quad (5.1)$$

where $\tilde{\nu} = \bar{\phi} V_c / N$ is the particle volume and N denotes the total number of particles. Spatial fluctuations of the volume fraction of form B inside the droplets are thus ignored. In contrast, the soluble building blocks of form A are subjected to microscopic dynamics. Here, we keep track of the individual positions \mathbf{x}_j for $j = 1, \dots, N_A$, where N_A is the number of A particles. We thus consider a simplified version of the deterministic model, where we focus on the effects of introducing stochasticity in the number of droplet components and concentration of building blocks, see Fig. 5.1. We will also account for the stochastic nature of the chemical reactions, although we neglect the effect of catalyzing enzymes, whose spatial distribution is an additional source of noise.

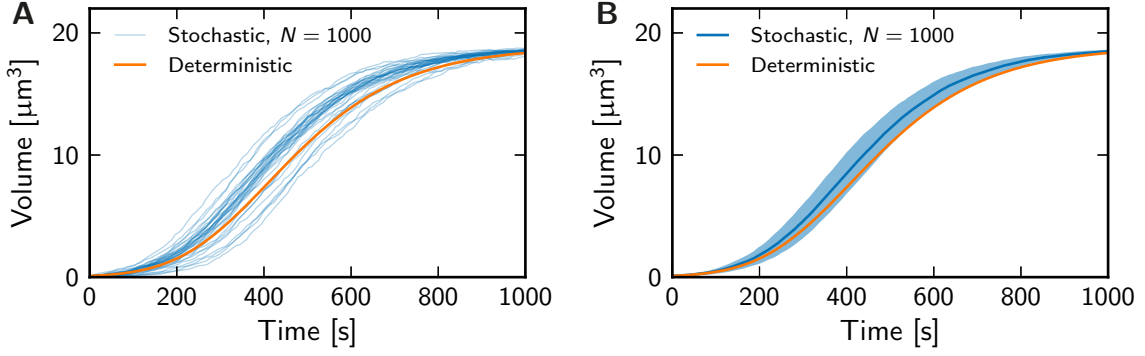


Figure 5.2: Droplet volume as a function of time in both the stochastic model (blue, $N = 1000$) and the deterministic one (orange lines). **(A)** All 32 individual trajectories of an ensemble of stochastic simulations are shown. **(B)** The ensemble average of the data from panel (A) is shown. The blue solid line denotes the mean droplet volume while the width of the blue shaded area indicates the associated standard deviation. Model parameters are given in Table 5.1.

The numerical implementation of this stochastic model is essentially a Monte Carlo simulation, where we update the position \mathbf{x}_j of the A particles by performing a step of a random walk during each time step of duration Δt . The chemical transitions are implemented by switching the identity of a particle with probability $k\Delta t$, where k is the associated reaction rate. Here, we also update the count N_i^B of B particles in all droplets and calculate the associated volumes using Eq. (5.1). The catalytic active cores are implemented similarly, i.e. A particles can diffuse into the region occupied by the cores and have a large rate $k_Q = 3Q/(4\pi a^3)$ of becoming form B there. More details on the numerical implementation are given in the Appendix K. With such an algorithm, we are able to simulate the stochastic growth dynamics of active droplets, which we analyze in the following.

5.1.1 Comparison with the deterministic model

We first compare the stochastic simulations to the deterministic results to validate the numerical implementation of the stochastic model. Fig. 5.2 shows the droplet volume as a function of time for both cases. The curves converge to the same stationary state value at large times and the qualitative shape of the growth curves is similar. The curve of the deterministic model lies within one standard deviation of the results of the stochastic simulations. However, the mean droplet volume is consistently higher in the stochastic simulations. We now introduced suitable quantifications of the fluctuating droplet volumes to investigate this interesting feature later.

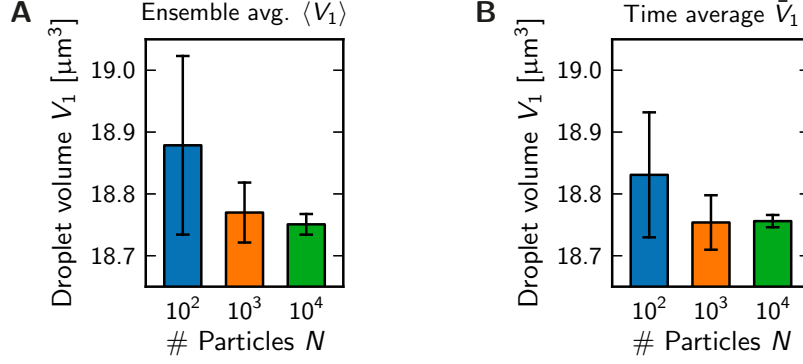


Figure 5.3: Average droplet volume in stationary state for different number of particles N in the stochastic simulation. **(A)** The ensemble average $\langle V \rangle$ of $n = 32$ independent simulations is shown. **(B)** The time average \bar{V} of a single simulation is shown. The error bars indicate the standard error of the mean given by σ_1^V / \sqrt{n} . The model parameters used in the simulations are given in Table 5.1.

5.1.2 Ensemble statistics and ergodicity

We investigate the fluctuating droplet volumes $V_i(t)$ determined from multiple simulations with the same parameters but different realizations j of the random numbers. The volumes $V_i^{(j)}(t)$ are thus stochastic quantities both with respect to time t and the realization j . This is in contrast to the deterministic model, where droplets reach a certain stationary state volume after a typical growth time. To compare the stochastic and the deterministic results, we define the *mean* stationary droplet volume $\langle V_i \rangle$ in the stochastic model according to

$$\langle V_i \rangle = \lim_{t \rightarrow \infty} \frac{1}{n} \sum_{j=1}^n V_i^{(j)}(t), \quad (5.2)$$

where n denotes the number of realizations. If the stochastic version of our model is ergodic, $\langle V_i \rangle$ is identical to the volume \bar{V}_i of a single droplet averaged over time [201], which we define as

$$\bar{V}_i = \lim_{t \rightarrow \infty} \frac{1}{t} \int_0^t V_i(t') dt' \quad (5.3)$$

for a single realization. The ensemble and time average defined above are similar for various different numbers N of particles in our stochastic simulation, see Fig. 5.3. Consequently, we conclude that the system is ergodic and we will only investigate the ensemble average in the following [201].

5.1.3 Quantification of fluctuations by the standard deviation

Fig. 5.3 also indicates the uncertainty of the volume average. This uncertainty stems from the finite sample set and is quantified by the standard error of the mean σ_i^V/\sqrt{n} [214]. Here, σ_i^V is the standard deviation of the volume of droplet i reading

$$\sigma_i^V = \sqrt{\frac{n}{n-1}} \cdot \sqrt{\langle V_i^2 \rangle - \langle V_i \rangle^2}, \quad (5.4)$$

where $\langle \cdot \rangle$ denotes the ensemble average defined in Eq. (5.2). Here, the prefactor in the definition of σ_i^V corrects for a possibly small number n of realizations [215].

The value σ_i^V quantifies the typical deviation of the droplet volumes from their mean value. It can thus additionally be used to quantify the magnitude of the fluctuations of these volumes. Fig. 5.3 shows that the fluctuations decrease if the number N of particles in the system increase. This is to be expected, since the system should recover the deterministic limit without fluctuations in the limit of large N .

In order to compare the fluctuations of different systems, we also need to quantify the error of estimating the standard deviation σ_i^V from an ensemble of n values. Assuming that the original random quantities are normally distributed with a standard deviation σ , the probability of measuring a certain standard deviation x is given by the Chi distribution $P_\chi(x; \sigma, n)$ with the probability density function

$$P_\chi(x; \sigma, n) = \frac{\sqrt{n} 2^{1-\frac{n}{2}}}{\sigma \Gamma(\frac{n}{2})} \left(\frac{x\sqrt{n}}{\sigma} \right)^{n-1} \cdot \exp\left(-\frac{nx^2}{2\sigma^2}\right), \quad (5.5)$$

where $\Gamma(x)$ denotes the gamma function [214]. Using this probability distribution, we can estimate the confidence interval $[\sigma_i^V - \Delta\sigma, \sigma_i^V + \Delta\sigma]$ that contains the true standard deviation σ with 95 % certainty. We determine $\Delta\sigma$ by solving

$$\int_{-\Delta\sigma}^{\Delta\sigma} P_\chi(\sigma_i^V + y; \sigma_i^V, n) dy = 0.95 \quad (5.6)$$

for the measurement error $\Delta\sigma$.

5.2 Noise amplification by the autocatalytic reaction

We next develop a simple stochastic model, which we can analyze analytically and then use to understand the effects seen in the previous section. The main ingredient of this model is the autocatalytic growth. This term is non-linear and could therefore explain the amplification of noise [207]. We focus on the early growth regime, where droplets are still small, since this part shows the amplification of fluctuations, see Fig. 5.2. For simplicity, we neglect the depletion of the building blocks, i.e. we

assume that their amount stays constant. Additionally, we consider a homogeneous distribution of the building blocks. The rate of droplet growth is then given by

$$\partial_t V(t) = \lambda(t)V(t) , \quad (5.7)$$

where λ is the instantaneous growth rate at time t . This growth rate is determined by both the incorporation of droplet material due to the autocatalytic reaction and the loss of droplet material caused by the reaction $B \rightarrow A$. The rate of the first process is given by the product of the volume fraction of building blocks ϕ^A and the reaction rate constant k_c . The second process is quantified by the reaction rate constant k_{BA} . With the approximations introduced above, the instantaneous growth rate reads $\lambda(t) \approx k_c \phi^A(t) - k_{BA}$.

In the deterministic model, the assumption that the amount of building blocks in the system is conserved would lead to a constant volume fraction of building blocks inside the droplet. However, in the stochastic version of the model discussed here, the volume fraction of building blocks inside the droplet fluctuates. Combining all terms without fluctuations in a constant quantity λ_0 , we can then write the growth rate as $\lambda(t) = \lambda_0 + \eta(t)$. Here, $\eta(t)$ describes a random process modeling the fluctuations of the growth rate due to randomness in the volume fraction of the building blocks. For simplicity, we assume that $\eta(t)$ is Gaussian white noise with

$$\langle \eta(t) \rangle = 0 \quad \text{and} \quad \langle \eta(t)\eta(t') \rangle = \omega \delta(t - t') , \quad (5.8)$$

where $\langle \cdot \rangle$ denotes the ensemble average and ω quantifies the strength of the fluctuations. The differential equation (5.7) therefore becomes a stochastic differential equation with multiplicative noise, which reads

$$\partial_t V(t) = \lambda_0 V(t) + V(t)\eta(t) . \quad (5.9)$$

We postulated that $\eta(t)$ describes external noise due to the diffusion of the A particles. For this situation, the Stratonovich interpretation of the multiplicative noise is appropriate [207]. Using the substitution $V(t) = V_0 e^{z(t)}$, we simplify Eq. (5.9) to

$$\partial_t z(t) = \lambda_0 + \eta(t) , \quad (5.10)$$

which is a stochastic differential equation for $z(t)$ with additive noise $\eta(t)$. Examining this simpler equation will allow us to solve the more complicated Eq. (5.9) and it will also serve as a reference case in the subsequent discussion.

Linear stochastic model with additive noise

The linear model given in Eq. (5.10) can be interpreted as the evolution equation of the position z of an overdamped particle. In this picture, the right hand side consists of a constant velocity λ_0 , which causes a drift of the position, and a random

velocity $\eta(t)$ of average strength ω , which will cause diffusive motion. The evolution of an ensemble of these overdamped particles is described by the associated Fokker-Planck equation, which reads [207]

$$\partial_t P(z, t) = -\lambda_0 \partial_z P(z, t) + \frac{\omega}{2} \partial_z^2 P(z, t) . \quad (5.11)$$

This equation describes how the distribution $P(z, t)$ of z -values changes in time. Here, the drift term causes a steady probability flux proportional to λ_0 , while the random force appears as a diffusive term with a diffusivity proportional to ω . The partial differential equation (5.11) is solved by

$$P(z, t) = \frac{1}{\sqrt{2\pi\omega t}} \exp\left[-\frac{(z - \lambda_0 t)^2}{2\omega t}\right] , \quad (5.12)$$

where we consider the initial condition $z(0) = \delta(0)$, i.e. the quantity z is localized at the origin at time $t = 0$ [207]. We characterize this Gaussian probability distribution by the time evolution of its mean,

$$\langle z \rangle = \int_{-\infty}^{\infty} P(z, t) z dz , \quad (5.13)$$

and its standard deviation,

$$\sigma_z = \left(\int_{-\infty}^{\infty} P(z, t) z^2 dz - \langle z(t) \rangle_z^2 \right)^{\frac{1}{2}} , \quad (5.14)$$

which evaluate to $\langle z \rangle = \lambda_0 t$ and $\sigma_z = \sqrt{\omega t}$. Consequently, both the mean value of z and the mean square displacement σ_z^2 grow linearly in time. The evolution of the mean is exclusively determined by the drift term, while the mean square displacement characterizes the diffusion process.

Autocatalytic stochastic model with multiplicative noise

We now investigate the Langevin equation (5.9) with multiplicative noise, which describes the initial phase of the autocatalytic growth of a droplet. We already showed that the equation can be transformed to the linear model with additive noise that we just discussed. Consequently, we get the solution to the Fokker-Planck equation associated with the autocatalytic model by using the result of the simple system given in Eq. (5.12). After substituting $z = \ln(V/V_0)$, we get the probability density function for the droplet volume V , which reads

$$P(V, t|V_0) = \frac{1}{V\sqrt{2\pi\omega t}} \exp\left[-\frac{(\ln V - \ln V_0 - \lambda_0 t)^2}{2\omega t}\right] , \quad (5.15)$$

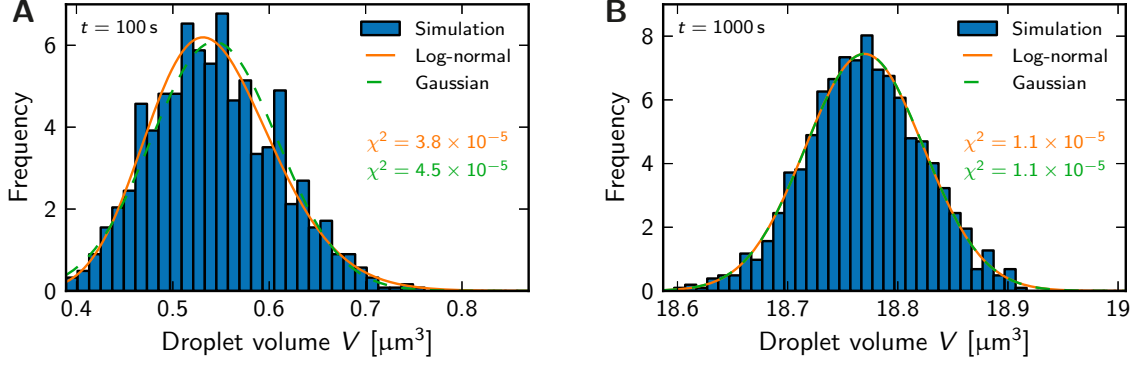


Figure 5.4: Distribution of droplet volumes at time **(A)** $t = 100$ s and **(B)** $t = 1000$ s. Both panels show the measured data (blue histogram) as well as the probability density functions of a log-normal distribution (orange lines) and a Gaussian distribution (green lines) with the same mean and standard deviation as the data. The integrated squared deviations χ^2 between the data and the distributions are indicated. The histogram is obtained by measuring the volume of a single droplet in $n = 1024$ realizations of the stochastic model with parameters taken from Table 5.1.

assuming that the droplet had volume V_0 at time $t = 0$ [207]. This distribution is known as the log-normal distribution, i.e. the logarithm of V is distributed normally [216]. Log-normal distributions often arise when stochastic effects are multiplicative and their logarithm thus follows a Gaussian distribution according to the central limit theorem. Consequently, log-normal distributions appear in many different fields of science, including the size distribution of ultrafine iron particles [217], the distribution of species in ecosystems [218], and the size distribution of galaxies [219]. Generally, distributions of strictly positive quantities where the mean and the standard deviation are comparable are often log-normal [216].

Our result indicates that the volume of autocatalytic droplets also follow a log-normal distribution, which we now test by comparing the probability density function of Eq. (5.15) to a histogram of simulated droplet volumes. We quantify the deviation between these two measures using the squared residual χ^2 , which is defined as

$$\chi^2 = \sum_{j=1}^{\infty} \left([h_j - P(V_j, t)] \Delta V \right)^2, \quad (5.16)$$

where h_j is the frequency of recorded volumes of the simulation in the j -th bin of the histogram, which covers the volume interval $[V_j - \frac{\Delta V}{2}, V_j + \frac{\Delta V}{2}]$. The histogram is normalized, $\sum_j h_j \Delta V = 1$, such that it can be directly compared to the test distribution $P(x, t)$. Consequently, χ^2 quantifies the integrated squared deviations of the measured data from the distribution.

Fig. 5.4 shows the comparison of the simulation data to both a log-normal distribution and a Gaussian distribution. Both distributions were chosen such that they have the same mean and variance as the data. Consequently, they both agree reasonably well with the measured data, especially in the long-time limit shown in panel B. Conversely, for short times the Gaussian distribution deviates stronger than the log-normal distribution. This observation indicates that the volumes of small growing droplets are indeed distributed according to a log-normal distribution, while the two distributions are indistinguishable for large droplets.

We now consider small droplets and assume that their volume is distributed according to a log-normal distribution. The associated mean droplet volume at time t calculated from Eq. (5.13) is then given by

$$\langle V \rangle = V_0 e^{\Lambda t}, \quad (5.17)$$

with the modified growth rate $\Lambda = \lambda_0 + \omega/2$. The standard deviation of the droplet volume as a function of time is defined in Eq. (5.14) and reads

$$\sigma_V = V_0 e^{\Lambda t} \sqrt{e^{\omega t} - 1}. \quad (5.18)$$

The growth equation for the droplet volume with multiplicative noise has the interesting feature that the mean droplet volume depends on the strength of the noise, see Eq. (5.17). It shows an exponential growth, comparable to the deterministic model, albeit with an increased growth rate $\Lambda = \lambda_0 + \omega/2$. This explains why our stochastic simulations show consistently larger droplet volumes compared to the deterministic model, see Fig. 5.2. Such a behavior is not observed in the simple model of Eq. (5.10), where the mean value does not depend on the strength of the noise. The enhancement of the droplet growth rate by the fluctuations is thus an effect of the multiplicative noise caused by the autocatalytic reaction.

The autocatalytic reaction also has an influence on the magnitude of the fluctuations of the droplet volumes. Here, the fluctuations quantified by σ_V increase exponential with time, while they are proportional to the square root of time for a linear model. The rapid growth of the fluctuations observed in Fig. 5.2 can thus only be explained by the autocatalytic reaction causing a positive feedback on the droplet growth.

The simple stochastic model with multiplicative noise given in Eq. (5.9) can thus explain two effects of the initial growth phase: the fluctuations are strongly amplified and the mean droplet volume grows more quickly than expected from the deterministic model. These effects are caused by the autocatalytic growth term, which amplifies fluctuations that increase droplet volume more strongly than it attenuates opposite fluctuations.

5.3 Transient growth regime of multiple droplets

In this section, we investigate the initial amplification of fluctuations for one and two droplets in the same system. The growth curves of single droplets are shown in Fig. 5.5A for different numbers N of particles in the system. The mean volume quantified in panel *B* is independent of N , but the fluctuations quantified by σ_1^V shown in panel *C* decrease with N , as already mentioned in Section 5.1.3.

In the case of two droplets in the same system, the average growth dynamics are again independent of N , see Fig. 5.5D. However, we observe much larger fluctuations of the droplet volume, if we investigate one of the two droplets individually, see panels *E* and *F*. Here, the variations between stationary state droplet volumes of different realizations are increased by about an order of magnitude compared to the case of a single droplet shown in the first row. Conversely, we recover the result of the single droplet if we quantify the total volume V_{tot} of both droplets, see the last row of Fig. 5.5. Taken together, the total volume of both droplets exhibits only small fluctuations while the difference of their volumes is strongly erratic.

The observation that individual droplet volumes vary widely can be explained by the deterministic dynamics in the strong segregation regime, $\psi_+ = 0$, without surface tension, $\gamma = 0$. Using the equations given in Section 4.1, the total droplet volume $V_{\text{tot}} = V_1 + V_2$ evolves according to

$$\partial_t V_{\text{tot}} = [(1 - \psi_-)k_c \bar{\phi} - k_{BA}] V_{\text{tot}} - \frac{(1 - \psi_-)\psi_- k_c}{V_c} V_{\text{tot}}^2, \quad (5.19)$$

which is equivalent to Eq. (2.23) for $m = 1$. Consequently, the total volume behaves as if it would be a single droplet of the simplified scenario B discussed in Section 2.2.2. This already explains why the quantifications of a single droplet are very similar to that of the total droplet volume in the case of multiple droplets, compare the first and the last row of Fig. 5.5.

The stationary state of the total volume of all droplets can be calculated from Eq. (5.19) and is given by Eq. (2.25) for $m = 1$. However, the distribution of this total volume among the individual droplets is not given by this equation, but rather depends on the initial condition. This can be explained qualitatively by noting that the distribution would merely influence the total surface area of the droplets, which is unimportant since we neglect surface tension effects here. Transferred to the stochastic simulations discussed in this chapter, this would mean that the individual volumes are influenced by both the initial conditions as well as the accumulated fluctuations of the growth phase. The fluctuations in individual droplet volumes are thus integrated over the entire growth duration, where they are possibly also enhanced by the autocatalytic mechanism, see Section 5.2. The observed enhanced fluctuations of individual droplet volumes could therefore be an artifact of neglecting surface tension. We thus expect qualitatively different results for more realistic simulations that account for surface tension effects.

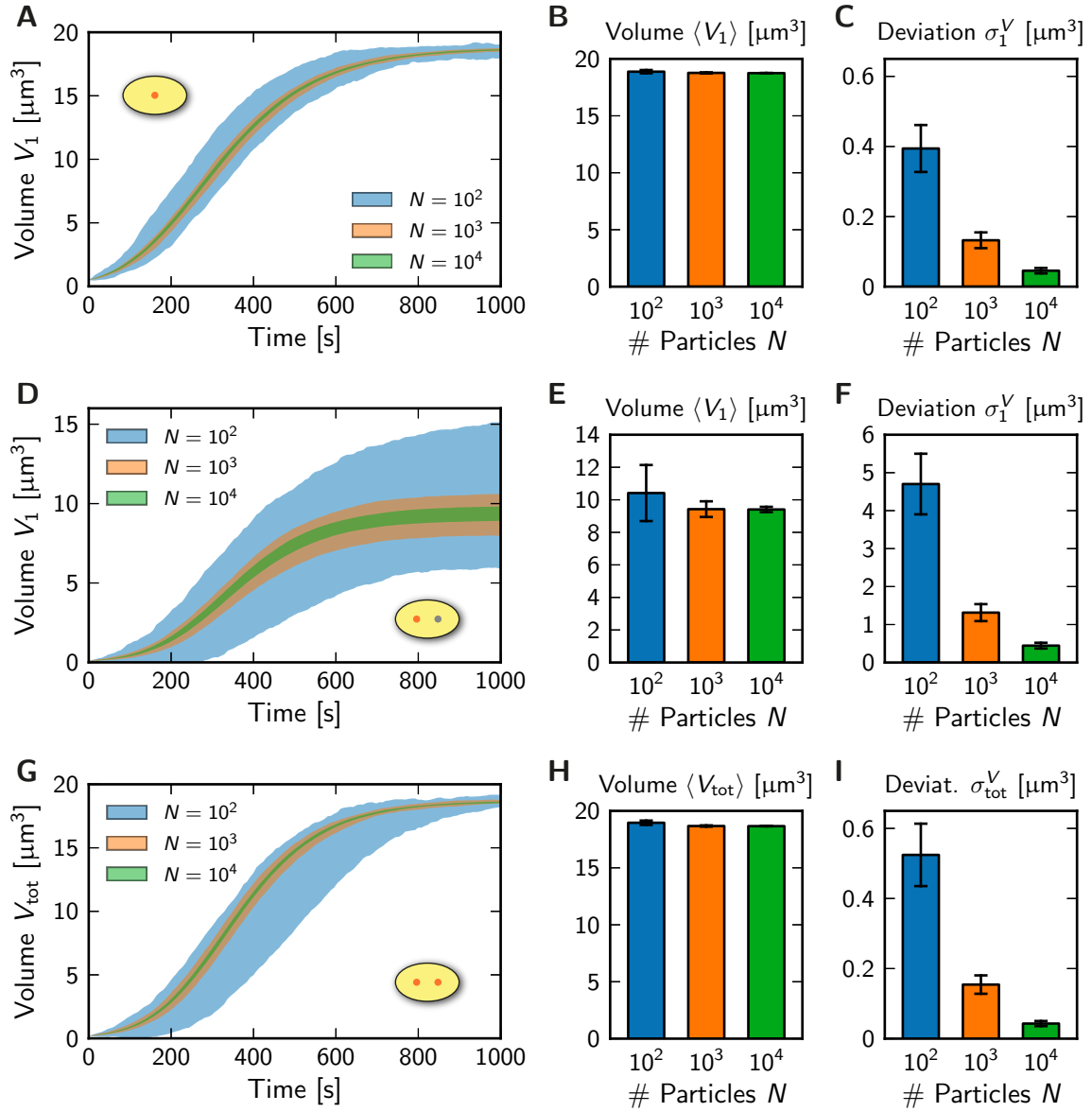


Figure 5.5: Fluctuations of droplet volume in the stochastic model for different particle numbers N . **(A, D, G)** The droplet volume (shaded area is the mean \pm the associated standard deviation) as a function of time is shown. The geometry is illustrated by the yellow insets, where the quantified droplets are shown in orange. **(B, E, H)** The mean droplet volume $\langle V \rangle$ in the stationary state is shown. **(C, F, I)** The associated standard deviation σ_V of droplet volumes is shown. In all panels, ensemble averages from 32 independent runs are compared for the case (A–C) of a single droplet, (D–F) of one of two droplets, and (G–I) of the sum of two droplets. Stationary states are quantified at $t = 2000$ s and error bars indicate 95 % confidence intervals. Model parameters are given in Table 5.1.

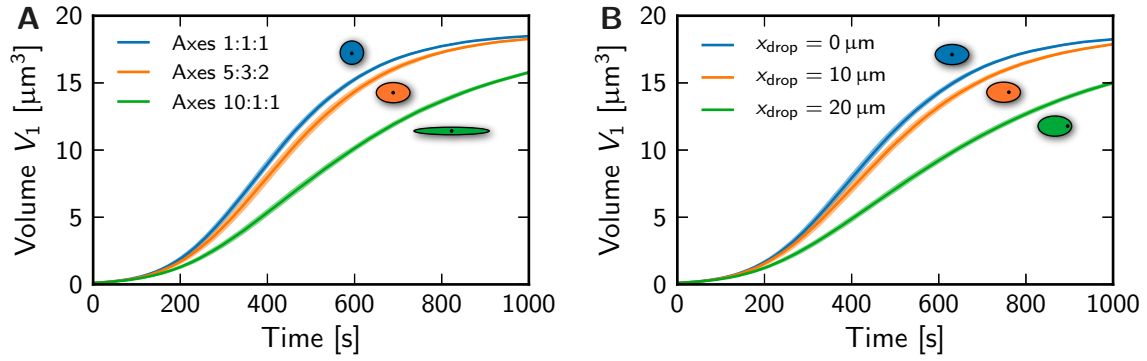


Figure 5.6: Droplet volume of a single droplet as a function of time in different geometries (line: mean; shaded areas: mean \pm standard deviation for an ensemble of 32 trajectories; $N = 10\,000$). **(A)** The system shape is varied. The ratio of the lengths of the three axes of the ellipsoid given in the legend are varied while keeping the volume constant. **(B)** The droplet position x_{drop} is varied along the long axis of a system with axes in a ratio of 5:3:2. Model parameters are given in Table 5.1.

5.4 Influence of the system geometry on the droplet growth

The stochastic simulations additionally allow us to investigate the droplet growth in different geometries of the system. In this section, we first examine the case of a single droplet and then consider multiple droplets, where the relative position will cause differences in their growth behavior.

We first discuss the growth of a single droplet in the center of an ellipsoidal geometry with varying lengths of the principle axes. For instance, the first cell of the *C. elegans* embryo can be approximated by an ellipsoid with principle axes of 50 μm , 30 μm , and 20 μm length [220]. Fig. 5.6A compares simulations with these values to the spherical case with the same volume. Evidently, the growth curves are very similar and the geometry only has a significant influence if the system is very elongated, see the green line. The slower growth in elongated systems is caused by the increased average time it takes for a particle to diffuse to the droplet from a random position in the system. Similarly, the position of the growing droplet in the system is of minor importance, see Fig. 5.6B. The growth only slows down significantly if the droplet is located close to the system boundary.

In summary, the growth of the droplet is rather insensitive to modifications of the system shape or its position therein. Anyhow, a single droplet reaches the same stationary state volume in all cases. This is to be expected since the volume fractions of droplet components in the solvent are approximately homogeneous in the stationary state and the shape of the boundary thus cannot have a strong effect.

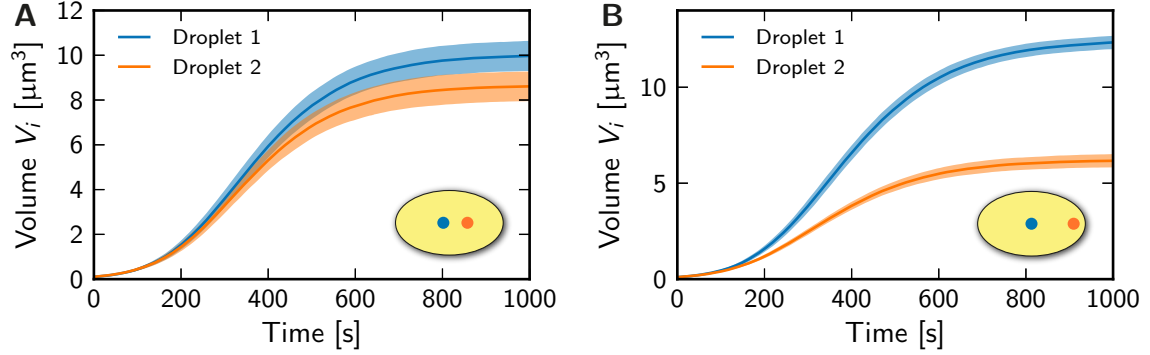


Figure 5.7: Volumes of two droplets as a function of time for different relative positions (line: mean; shaded areas: mean \pm standard deviation for an ensemble of 32 trajectories; $N = 10\,000$). The blue droplet is located at the origin, while the orange one is shifted by x_2 towards the right in a ellipsoidal geometry with axes in a ratio of 5:3:2. **(A)** mild asymmetry, $x_2 = 10 \mu\text{m}$ **(B)** strong asymmetry, $x_2 = 20 \mu\text{m}$. Model parameters are given in Table 5.1.

In the case of two droplets growing in the same system, there is a competition for building blocks between the droplets. The relative position of the droplets determines which part of the system they can access and therefore deplete. Consequently, droplets located closer to the system boundary grow slower, see Fig. 5.7. Additionally, the fluctuations of the volumes of both droplets are reduced, if they grow asymmetrically. These two effects are stronger if the mismatch in position is more pronounced. However, the total volume of both droplets behaves similarly to the case of one droplet.

5.5 Discussion

We introduced a simple stochastic version of our model in this chapter. This simulation reproduces the droplet growth curves of the deterministic model, although the growth rate is slightly higher. We showed that this is likely caused by the interplay of the autocatalytic reaction and the number fluctuations of the soluble building blocks. The non-linear reaction amplifies noise, such that fluctuations increasing the droplet volume dominate over those that decrease it. Interestingly, in the case of multiple droplets, the final volumes of individual droplets can vary significantly. This behavior might be due to the simplification of neglecting surface tension effects in the stochastic simulations. Nevertheless, these simplified simulations show that the geometry of the system has only a minor influence on the growth dynamics. This result thus justifies the spherical geometry that we introduce for convenience in the previous chapters.

Chapter 6

Comparison Between Theory and Experiment

WE derived a general model of centrosome growth in Chapter 2. This model is based on the picture that centrosomes are liquid-like droplets and that their assembly is controlled by chemical reactions. We then analyzed this model in the next three chapters where we focused on the stability of droplets and their nucleation properties. It remains to be shown that the model is able to explain the behavior of centrosomes observed in experiments.

In this chapter, we compare our model with experimental data to establish a set of model parameters that can explain the measurements quantitatively. In the corresponding section, it will turn out that only a single combination of the previously discussed simple scenarios can achieve this: the autocatalytic growth of scenario B accounts for the centrosome growth dynamics, while the catalytic activity at the centrioles, scenario C, is important for the initiation of centrosome formation. Using direct measurements and fits of the model to experimental data, we thus arrive at a parameter set consistent with all experimental measurements that are available to us. We then use these parameters to discuss additional experiments, where the normal centrosome formation has been disrupted. We close this chapter by briefly considering the disintegration phase of centrosomes toward the end of the cell cycle.

6.1 Summary of the experimental observations

The most important quantitative experimental data available to us is the size of the centrosomes measured in *C. elegans* embryos. Decker et al. quantified the centrosome volume by tagging fluorescent probes to centrosome proteins, typically γ -tubulin [24]. Centrosomes then appear as bright spots under the microscope, see Fig. 6.1A and Fig. 6.1B. These spots are then automatically detected and quantified by a computer program [184]. The quantification involves the fitting of a two-dimensional Gaussian function to the observed intensity distribution. Using twice the standard deviation of this Gaussian function gives a first estimate of the centrosome radius. This value is then refined by using the original intensity data from the raw image. Decker et al. define the centrosome radius as the point where the radial intensity distribution

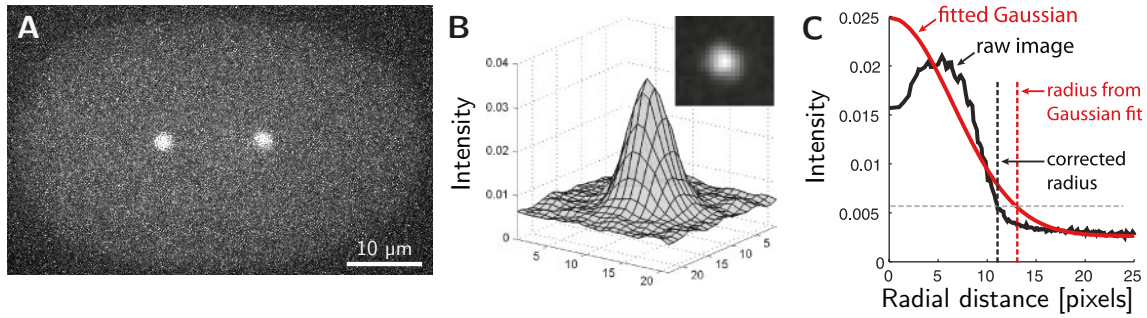


Figure 6.1: Quantification of centrosome size. **(A)** Maximum projection of a z -stack captured with a spinning-disk confocal microscope using γ -tubulin::GFP in *C. elegans* embryos [24]. The image was taken from the centrosome size project [221]. **(B)** Intensity profile of a fluorescently marked centrosome as it appears under the microscopy in a 3D plot and as a grey scale image (inset). **(C)** Analysis of the radial intensity profile (black) to measure the radius of the centrosome involving a Gaussian fit (red). Panel B and C are modified from Ref. [184].

has the value of the fitted Gaussian at the estimated radius, see Fig. 6.1C and Ref. [184]. The volume of the centrosome can then be calculated by assuming that it has a spherical shape. Decker et al. used this method to quantify the centrosome volume using time-lapse microscopy in cells at various developmental stages and under different genetic conditions [24]. We will test our model using this published data and additional unpublished data from our experimental collaborators.[†]

Fig. 6.2 shows the centrosome size versus time for different wild-type cells of the embryo, where the names of the cells correspond to Fig. 1.2C. Generally, centrosome growth starts slowly, followed by a rapid growth phase of about 500 s duration. The centrosomes reach their final size around the time of the nuclear envelope breakdown (NEBD) in the four-cell stage and descendant cells. Such a plateau is not visible in the earlier cell stages, likely because the growth is interrupted by cell division. Typical centrosome growth curves are thus sigmoidal. Decker et al. also quantified the final centrosome size and showed that it depends on the number of centrosomes in the cell and the cell volume. Notably, the combined total volume of all centrosomes is independent of the centrosome number, but is proportional to the cell volume. From this and other observations, the authors conclude that centrosome size is set by the total amount of a limiting component in the cell [24].

The experiments leave many questions unanswered: how is the centrosome assembled and how is its size regulated? What are the important chemical reactions? What is the role of the centrioles? Why does PCM accumulate only around centrioles

[†] M. Decker, S. Jaensch, and A. A. Hyman at the Max Planck Institute of Cell Biology and Genetics, Pfotenhauerstr. 108, 01307 Dresden, Germany [222]

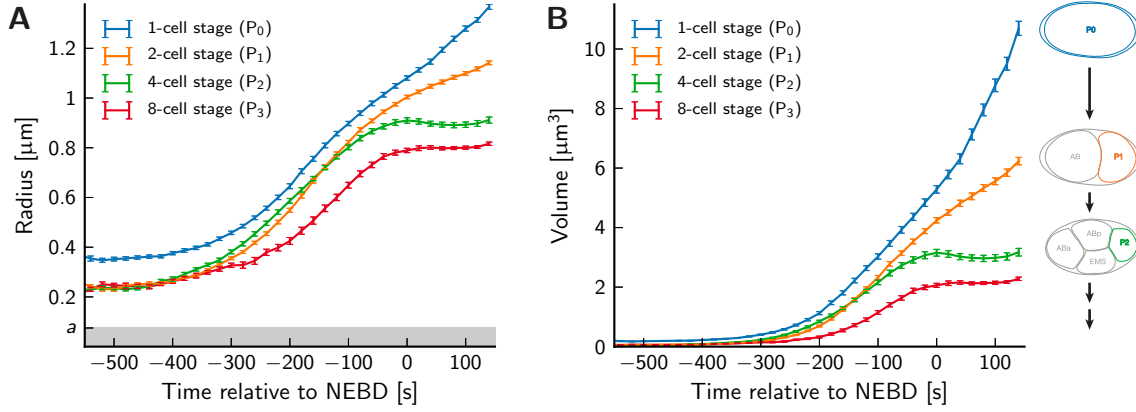


Figure 6.2: Centrosome growth curves measured in *C. elegans* embryos [222]. **(A)** Radius and **(B)** volume as a function of time are shown for several different cells, which are indicated by the schematics on the right. The grey region in (A) marks the centrosomes of radius a as a reference. Error bars are standard error of the mean and times have been measured relative to the nuclear envelope breakdown (NEBD). The schematics on the right were modified from Ref. [24].

and there is no spontaneous accumulation in the cytosol? To clarify some of the above questions, we now compare our model to the experimental data.

6.2 Estimation of key model parameters

Some model parameters are known from experimental studies. We set the radius of the sphere representing the centrosomes, $a = 75$ nm, to half the length of a single centrosome determined by electron microscopy [56]. Decker et al. measured the volume V_c of cells in different early stages of development, see Table 6.1. Diffusion constants were reported for the centrosomal protein PLK-1 [86], which we use to motivate our choice, $D_A = D_B \approx 5 \mu\text{m}^2/\text{s}$. For simplicity, we use the same diffusion constants inside and outside of the droplet, which does not alter the centrosome dynamics qualitatively, see Appendix I. The rate constant of the reaction converting droplet material back to soluble building blocks, $k_{BA} \approx 10^{-3} \text{s}^{-1}$, is chosen consistently with the longest reported turn-over time of centrosomal proteins [16]. Not known are the other chemical reactions rate constants, the parameters describing the phase separation, and the concentrations of the components in the system, see Table 6.2.

Our strategy to determine the remaining parameters was the following. First, we use the known parameters to discuss general features of the growth in the three scenarios that do not depend on precise value of the other parameters. Subsequently, we identify one plausible scenario for which we determine parameter values by fitting the model to the experimental data.

Table 6.1: Measured cell volumes V_c and centrosome volumes V (mean \pm standard deviation) of *C. elegans*. V was quantified 150 s after nuclear envelope breakdown as described in Section 6.1 and V_c was obtained from 3D reconstruction [220].

Cell	Stage	Cell volume V_c	Centrosome volume V	Ratio V_c/V
P ₀	1 cell	22000 μm^3	$(11.5 \pm 2.0) \mu\text{m}^3$	1900
AB	2 cells	12700 μm^3	$(7.6 \pm 1.6) \mu\text{m}^3$	1700
P ₁	2 cells	8600 μm^3	$(6.5 \pm 1.0) \mu\text{m}^3$	1300
AB _a	4 cells	6200 μm^3	$(4.2 \pm 1.1) \mu\text{m}^3$	1500
AB _p	4 cells	6200 μm^3	$(3.9 \pm 1.1) \mu\text{m}^3$	1600
EMS	4 cells	4400 μm^3	$(3.5 \pm 0.6) \mu\text{m}^3$	1300
P ₂	4 cells	4400 μm^3	$(3.2 \pm 1.0) \mu\text{m}^3$	1400
P ₃	8 cells	2200 μm^3	$(2.4 \pm 0.5) \mu\text{m}^3$	920

First order assembly kinetics, scenario A, does not exhibit the observed sigmoidal growth curves, see Fig. 2.3. Note also that in scenario A, nucleation cannot be at the same time strongly favored at the centrioles, while being suppressed in cytosol, see Fig. 3.5A. The growth of scenario B, which assumes autocatalytic assembly, exhibits sigmoidal growth curves, see Fig. 2.4. However, it does not allow for spontaneous nucleation. In scenario C, centrosome assembly happens exclusively at the centrioles. Because of this, growth curves are not sigmoidal. In addition, the typical estimates for the diffusion coefficients do not allow for the observed growth rates. The minimal growth time is $\lambda_D^{-1} = V_c/(4\pi a D_A) \approx 2000$ s, see Eq. (2.31). Here, we used the cell volume, the centriole size, and the diffusion constant that were measured. Thus, scenario C alone cannot account for the observed sigmoidal growth, which lasts about 500 s. Therefore, none of the scenarios on their own can explain the observed growth of centrosomes.

We next test whether a combination of the scenarios is viable. The growth phase of centrosomes must be dominated by the autocatalytic mechanism of scenario B to exhibit sigmoidal growth curves. An additional catalytic activity of the centrioles, as defined in scenario C, can account for the controlled nucleation, which is absent in scenario B on its own. Consequently, the combination of scenario B with a centriole activity results in a growth curve that is consistent with experiments and allows for controlled nucleation at the centrioles. Note that this is the only combination of scenarios that can account for the basic features of centrosome growth.

The scenarios B and C are respectively characterized by the choice of the autocatalytic reaction rate constant k_c and the catalytic activity Q at the centrioles. Here, it is important that the autocatalytic growth dominates for the resulting growth curves to be sigmoidal. We thus determine k_c and Q using the following strategy: Since

the growth dynamics should be dominated by k_c , we first fit a model with $Q = 0$ to the experimental data to determine a plausible value for k_c . We then determine Q from the requirements that it has to be strong enough to initiate droplet growth. At the same time Q must not have a strong influence on the growth curves.

6.3 Fits to experimental data

We now compare the growth curves of scenario B to experimental data to determine the autocatalytic reaction rate constant k_c and the fraction $\bar{\phi}$ of PCM components governing the centrosome growth phase. In Section 2.2.2, we already determined an approximate solution of the growth curve in scenario B by assuming that diffusion is fast. During the subsequent discussion of the general model, however, we found that diffusion plays an important role in scenario C and that it generally affects the stability of small centrosomes. Diffusion of the PCM components might thus also influence the growth curves in scenario B. We will thus use an alternative solution of the model that includes diffusion effects for the quantitative comparison to the experimental data.

We use a numerical algorithm to solve the partial differential equation of the general model defined in Section 2.1. For simplicity, we consider the growth of a single centrosome in a spherical geometry, which does not alter the growth significantly, see Section 5.4. The numerical algorithm explained in detail in Appendix C allows us to simulate the full time evolution of a single droplet. In order to approximate the solution in cases of m droplets in the same system, we divide the system volume in m equal sized, spherical compartments, where the droplets grow independently, thus neglecting all interactions between them.

We first use the numerical solution of the model to assess the influence of the model parameters on the shape of the growth curves. Fig. 6.3 shows that most of the unknown parameters have a weak effect. The final centrosome size is strongly influenced by the cell volume V_c , see Fig. 6.3A. Additionally, the ratio of the fraction $\bar{\phi}$ of the available material and the fraction ψ_- of droplet material in the centrosome effects centrosome size, see Fig. 6.3 panels B, C, and L. All the other parameters only have a weak influence on the final droplet size. However, three additional parameters effect the shape of the growth curve: the fraction $\bar{\phi}$ of available material (Fig. 6.3B), the autocatalytic reaction rate constant k_c (Fig. 6.3D), and the diffusion constant D_A of the building blocks (Fig. 6.3J). These parameters influence the droplet growth dynamics, but have only a minor effect on the stationary state size. Taken together, only four parameters are important for the centrosome growth curves: the cell volume V_c , the diffusion coefficient D_A , the autocatalytic assembly rate constant k_c , and the ratio $\bar{\phi}/\psi_-$ of the average fraction of material to the fraction in the droplet. Note that while $Q > 0$ is needed for nucleation, it is less relevant for the shape of the growth curve.

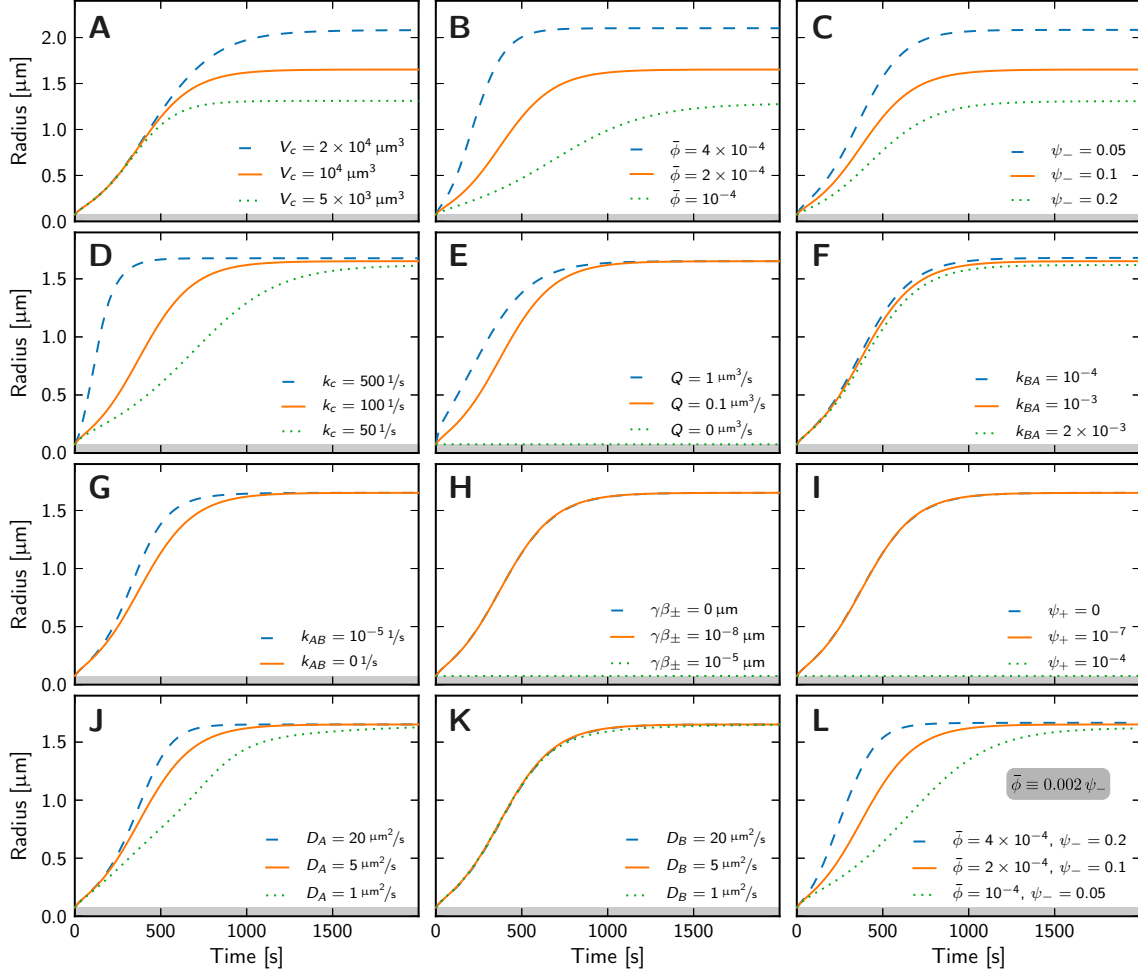


Figure 6.3: Centrosome radius as a function of time in simulations, where model parameters deviate from their standard value. **(A–K)** A single parameter is varied from the standard value (orange line) yielding larger (blue dashed line) or smaller (green dotted line) centrosomes as indicated in the legend. **(L)** The total fraction $\bar{\phi}$ of PCM components and the fraction ψ_- of droplet material in the centrosome are varied with their ratio kept constant. All parameters not given in the legends are taken from the autocatalytic scenario given in Table 6.2.

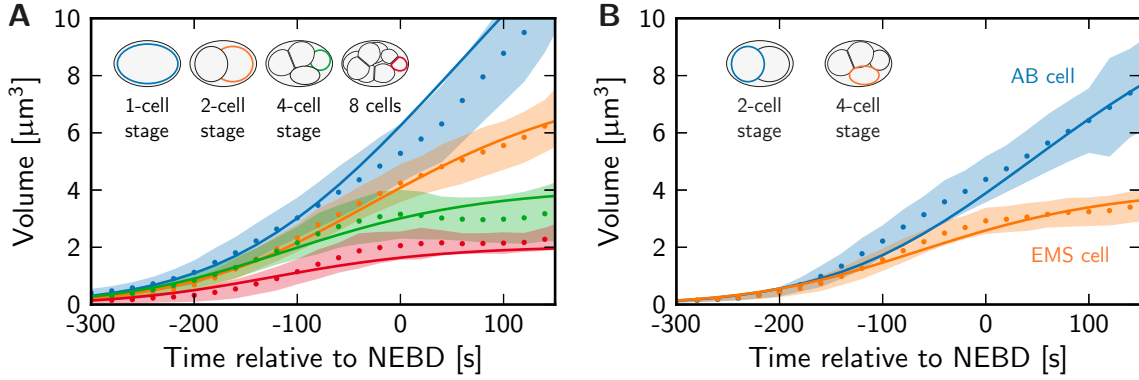


Figure 6.4: Comparison of the centrosome volume as a function of time of the theory (lines) with experimental data (shaded areas, mean \pm standard deviation) of centrosome growth in *C. elegans* for several cell sizes [222]. **(A)** Cells of the P-lineage and **(B)** two other cell types are shown. Time $t = 0$ corresponds to nuclear envelop breakdown (NEBD). The autocatalytic reaction rate $k_c = 100 \text{ s}^{-1}$, the overall fraction of PCM components, $\bar{\phi} = 2 \times 10^{-4}$, and the initial centrosome volumes are determined by a fit of the theoretical curves to the data. All model parameters are summarized in Table 6.2.

We next use the numerical simulations to determine open model parameters by fitting the simulated growth curves to experimental data. Here, we set the parameters with a weak influence on the growth curves to zero and only determine the values of the important parameters. Since the cell volumes V_c , the rate constant k_{BA} , and the diffusion coefficient D_A are known from experimental measurements, the only fit parameters are the autocatalytic rate constant k_c and the ratio $\bar{\phi}/\psi_-$. We determine their value by comparing the simulated growth curves to experimental results from different wild-type cells. To get the best possible estimate of the parameters describing centrosome growth, we include all available data sets, i.e. centrosome growth curves from the eight embryonic *C. elegans* cells P_0 , P_1 , AB, P_2 , EMS, AB_p , AB_a , and P_3 [24]. Each individual data set also possesses an additional fit parameter for the initial volume, since we cannot detect the initiation of centrosome growth. The optimal model parameters are determined by numerically minimizing the squared residual, which is a measure for the distance of the model predictions to the experimental data. The total residual is calculated by adding up the residuals of each individual experimental data set. Using this algorithm, we are able to fit several data sets simultaneously with the same model parameters for each data set.

The fitting procedure allows us to compare the model to the experimental data. Fig. 6.4 shows that they agree quantitatively. The estimated model parameters resulting from the fit are the autocatalytic reaction rate constant, $k_c = 100 \text{ s}^{-1}$, and the ratio of volume fractions, $\bar{\phi}/\psi_- = 0.002$. Assuming a typical fraction of droplet material in the droplet, $\psi_- = 0.1$ [223], we can thus also get the fraction of PCM

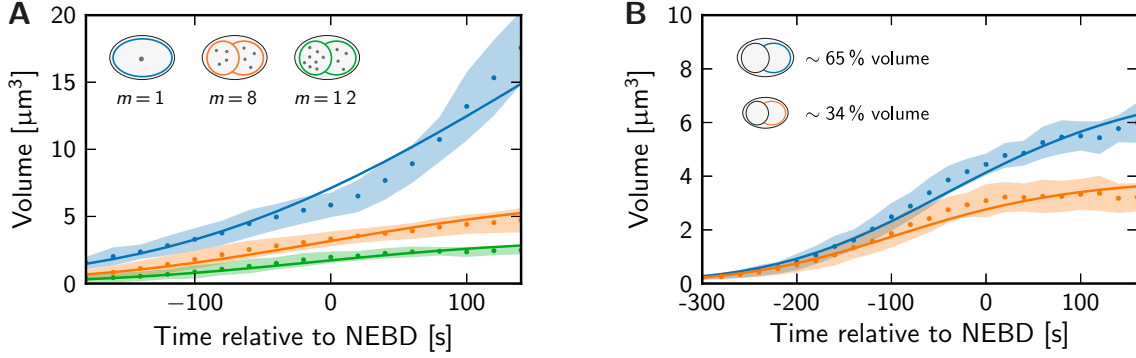


Figure 6.5: Comparison of the centrosome volume as a function of time of the theory (lines) with experimental data (shaded areas, mean \pm standard deviation) of centrosome growth in disturbed *C. elegans* embryos [222]. **(A)** Data from cells with aberrant number m of centrosomes. **(B)** Data from cells with altered cell volume V_c as indicated. Times $t = 0$ corresponds to nuclear envelop breakdown (NEBD) and the initial centrosome volumes are fit parameters in both panels. The model parameters are given in Table 6.2.

components, $\bar{\phi} = 2 \times 10^{-4}$. Using this value together with a typical cell volume, $V_c \approx 10^4 \mu\text{m}^3$ from Table 6.1, and a typical molecular volume $\nu \approx 120 \text{ nm}^3$ of globular proteins [27], we can estimate the number N of PCM components in the cell. The resulting value $N = \bar{\phi}V_c/\nu \approx 2 \times 10^7$ is much bigger than the largest number of particles that we investigated in our stochastic simulations in Chapter 5. We would thus expect to see the stochastic effects investigated there only if the basic building blocks of the PCM have a significantly larger volume than ν and the estimated N would therefore be smaller. This could be the case if pre-assembled building blocks are incorporated at the centrosome.

So far, we only considered the wild-type situation. To also test the model for different number of centrosomes, we next compare the numerical solution to growth curves from disturbed embryos: *zyg-1* mutants show cells with aberrant number of centrosomes [24]. By only adjusting the number m of centrosomes in our simulations, we can reproduce the observed growth curves, see Fig. 6.5A. Similarly, the model agrees with data from cells with altered volume using *ani-2*(RNAi) conditions, see Fig. 6.5B. Here, the cell volume V_c is a fit parameter. Our model can thus quantitatively account for the observed growth curves in wild-type embryos and under mutant conditions.

We determined the most important model parameters to describe centrosome growth in this section. The droplet volume of the approximate model in scenario B is thus fully determined, see Section 2.2.2. Conversely, the parameters of the growth scenarios A and C cannot be determined from experimental observations. To also obtain a parameter set for these scenarios, we set the associated reaction rate constants by demanding that the stationary state volume is comparable to scenario

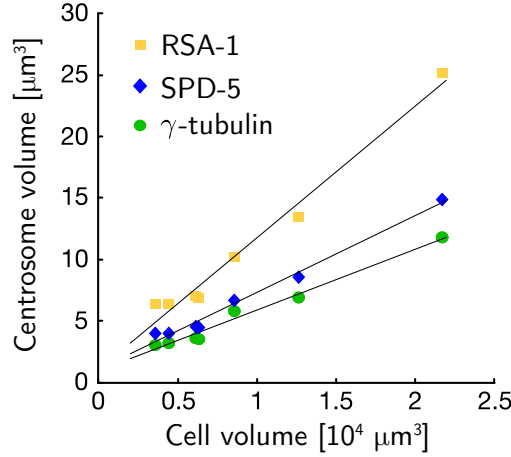


Figure 6.6: Centrosome volume as a function of cell volume. Centrosome volume has been quantified in cells of the *C. elegans* embryo at metaphase. Three different proteins have been marked using GFP and a linear fit has been added to emphasize the correlation. Figure modified from Ref. [24].

B discussed here. The reaction rate constant k_{AB} describing the first-order reaction in scenario A is thus given by combining Eqs. (2.22) and (2.25). Solving for the reaction rate constant yields $k_{AB} = (1 - \psi_-)\bar{\phi}k_c - k_{BA} \approx 0.016 \text{ s}^{-1}$. For scenario C, a similar consideration leads to the estimate $Q \approx k_{BA}V_c \approx 10 \mu\text{m}^3/\text{s}$. The parameters derived in this section are summarized in Table 6.2. They are the standard set of parameters used in most plots of this thesis.

6.4 Dependence of centrosome size on cell volume and centrosome count

We identified the cell volume as a major factor determining centrosome size in the previous section. In fact, centrosome volume shows a strong correlation with cell volume in experiments, see Fig. 6.6. Interestingly, the reported centrosome size depends on the chosen marker protein, but the correlation with the cell volume is always present irrespective of that choice. Consequently, all reported centrosome volumes are only correct to a constant factor, which depends on the chosen marker protein and the measurement procedure.

Assuming that the final measured centrosome size represents the stationary state value, we can relate our model to the experimental observation. The stationary state centrosome volume of the autocatalytic scenario,

$$V = \frac{V_c}{m\psi_-} \left(\bar{\phi} - \frac{k_{BA}}{(1 - \psi_-)k_c} \right), \quad (6.1)$$

Table 6.2: Standard values of the parameters used in this thesis. The top part lists general parameters, while the three sections at the bottom give parameters for the simple growth scenarios. The physiological relevant parameters for centrosomes in *C. elegans* correspond to the autocatalytic growth scenario.

Quantity	Symbol	Value	Source of the value
General parameters:			
Cell volume	V_c	$10^4 \mu\text{m}^3$	Typical value, see Table 6.1
Number of centrosomes	m	2	Wild-type count [24]
Size of centrioles	a	75 nm	Half of centriole length [56]
Rate constant of $B \rightarrow A$	k_{BA}	$10^{-3} 1/\text{s}$	Slowest PCM turnover rate [16]
Concentration in droplet	ψ_-	0.1	Typical value [223]
Diffusion constants	D_A, D_B	$5 \frac{\mu\text{m}^2}{\text{s}}$	Typical value for PLK-1 [86]
Concentration in cytosol	ψ_+	0	Minor influence, neglected
Surface tension	γ	$1 \frac{\text{pN}}{\mu\text{m}}$	Typical value [101]
Surface tension parameter	β_-	$0 \frac{\mu\text{m}^2}{\text{pN}}$	Minor influence, neglected
Fraction of PCM components	$\bar{\phi}$	2×10^{-4}	Fit result, see Section 6.3
Initial centrosome volume	V_0	various	Fit result for each data set
Scenario A: First-order kinetics:			
Rate constant of $A \rightarrow B$	k_{AB}	$0.016 1/\text{s}$	Drop size similar to scenario B
Autocatalytic rate constant	k_c	$0 1/\text{s}$	Neglected in scenario A
Centriolar activity	Q	$0 \frac{\mu\text{m}^3}{\text{s}}$	Minor influence, neglected
Surface tension parameter	β_+	$10^{-6} \frac{\mu\text{m}^2}{\text{pN}}$	Similar effect as in scenario B
Scenario B: Autocatalytic growth (<i>C. elegans</i> centrosomes):			
Rate constant of $A \rightarrow B$	k_{AB}	$0 1/\text{s}$	Neglected in scenario B
Autocatalytic rate constant	k_c	$100 1/\text{s}$	Fit result, see Section 6.3
Centriolar activity	Q	$0.1 \frac{\mu\text{m}^3}{\text{s}}$	Estimated, see Section 6.5
Surface tension parameter	β_+	$10^{-8} \frac{\mu\text{m}^2}{\text{pN}}$	Estimated, see Section 6.5
Scenario C: Incorporation at the centrioles:			
Rate constant of $A \rightarrow B$	k_{AB}	$0 1/\text{s}$	Neglected in scenario C
Autocatalytic rate constant	k_c	$0 1/\text{s}$	Neglected in scenario C
Centriolar activity	Q	$10 \frac{\mu\text{m}^3}{\text{s}}$	Drop size similar to scenario B
Surface tension parameter	β_+	$10^{-7} \frac{\mu\text{m}^2}{\text{pN}}$	Similar effect as in scenario B

has already been derived in Eq. (2.25). It is proportional to the cell size V_c in accordance with experiments, see Fig. 6.6. This formula also predicts that the volume is inversely proportional to the number m of centrosomes. There are always two centrosomes growing in embryonic cells of *C. elegans* under wild-type conditions. Using several mutants, Decker et al. were able to have only a single centrosome in the one-cell stage or up to twelve centrosomes in the two-cell stage, where only four centrosomes are found in wild-type embryos [24]. Irrespective of the perturbation, the total volume of all measured centrosomes always adds up to the same value, indicating that the volume of a single centrosome indeed scales inversely with the number of centrosomes. These data show that the total amount of centrosome material sets centrosome size [24].

Our model can quantitatively account for the full centrosome dynamics in wild-type embryonic cells and under disturbed conditions with aberrant number of centrosomes or cell sizes. Due to the underlying phase separation process, the total droplet volume is essentially given by the total amount of material, see Section 1.5. This explains the dependence of the centrosome volume on the cell size and the number of centrosomes.

6.5 Nucleation and stability of centrosomes

The comparison of the theory to the observed growth curves does not allow us to determine the values of the catalytic activity Q of the centrioles and the surface tension parameter $\gamma\beta_+$. These parameters, however, play an important role in centrosome nucleation and stability.

An upper bound on the value of Q exists because the combination of scenarios B and C shows a sigmoidal growth curve only if the autocatalytic assembly dominates over the centriole activity. The integrated reaction fluxes associated with the reaction at the centrioles, the first-order reaction, and the autocatalytic reaction read $Q\phi^A$, $k_c V \psi_- \phi^A$, and $k_{AB} V_c \phi^A$, respectively. Here, we consider a homogeneous distribution of the soluble building blocks for simplicity. In order to show sigmoidal growth, the autocatalytic term must be dominant over the other two reactions. This leads to conditions, which read

$$Q \ll k_c V \psi_- \approx 3 \mu\text{m}^3/\text{s} \quad (6.2a)$$

$$k_{AB} \ll k_c \frac{V \psi_-}{V_c} \approx 3 \times 10^{-3} \text{ s}^{-1} . \quad (6.2b)$$

Here, the numerical estimates are obtained for the smallest centrosome volume for which sigmoidal growth can be observed, $V \approx 0.3 \mu\text{m}^3$, see Fig. 6.2. Although a small first-order reaction rate constant k_{AB} is allowed by the data, see Eq. (6.2b), we still set this value to zero for simplicity, $k_{AB} = 0$. Conversely, we cannot assume that Q vanishes, since it is important to ensure that droplets nucleate and that more than one centrosome is stable. We thus set $Q = 0.1 \mu\text{m}^3/\text{s}$ to fulfill the condition given

in Eq. (6.2a). Using the estimated molecular volume $\nu \approx 120 \text{ nm}^3$ [27], and the maximal fraction of building blocks $\phi^A \approx \bar{\phi} = 2 \times 10^{-4}$, we can evaluate the rate at which PCM components are incorporated at the centrioles, $Q\phi^A/\nu \approx 170 \text{ s}^{-1}$. This number is not extraordinarily large and the chosen value of the catalytic activity Q seems thus plausible.

The chosen value for the catalytic activity Q must be large enough to ensure droplet nucleation and to stabilize multiple centrosomes. The two associated threshold values $Q_{\text{crit}}^{\text{B}}$ and $Q_{\text{stab}}^{\text{B}}$ depend on $\gamma\beta_+$, see Eqs. (3.9) and (4.17). This provides two upper bounds for $\gamma\beta_+$. From the requirement of the stability of two centrosomes it follows that $\gamma\beta_+ < k_{BA}Q/(4\pi k_c D_B) \approx 1.6 \times 10^{-14} \text{ m}$. Note that $\gamma\beta_+$ must be positive in order to suppress spontaneous nucleation in the cytosol. This motivates our choice, $\gamma\beta_+ = 10^{-14} \text{ m}$. Choosing a typical surface tension $\gamma = 1 \text{ pN}/\mu\text{m}$ for soft interfaces [101], we thus also get $\beta_+ = 10^{-8} \mu\text{m}^2/\text{pN}$. At first sight, these numbers seem to be unphysical small since $\gamma\beta_+$ is on the order of the diameter of a proton. However, $\gamma\beta_+$ is not a physical length, but determines corrections to volume fractions, see Eq. (1.8). According to this equation, $\gamma\beta_+$ divided by a typical droplet radius, e.g. $R \approx 1 \mu\text{m}$, should be comparable to typical volume fractions. In fact, we already estimated β_+ from physical arguments in Section 1.5.2, which led to $\beta_+ \approx 2\nu\psi_+/(k_B T\psi_-)$, see Eq. (1.9). Using a typical molecular volume $\nu \approx 120 \text{ nm}^3$ of globular proteins [27], $k_B T \approx 4 \text{ pN nm}$, and $\psi_- = 0.1$, we thus arrive at $\beta_+ \approx 6 \times 10^{-4} \mu\text{m}^2/\text{pN} \cdot \psi_+$, which explains the typical small value of $\gamma\beta_+$. For this reason, the surface tension parameter $\gamma\beta_-$ for the volume fraction inside the droplet has only a minor effect, since ψ_- is large compared to the effect of surface tension, see Eq. (1.8). We thus set $\beta_- = 0$ for simplicity. This concludes the choice of parameters for the scenario B, which describes centrosome growth in *C. elegans*.

The surface tension parameter of scenario A can be estimate by comparing its critical droplet size, see Eq. (3.5), with that of scenario B, see Eq. (3.6). We estimate the order of magnitudes of the involved quantities and arrive at $\beta_+ = 10^{-6} \mu\text{m}^2/\text{pN}$ for scenario A, which produces comparable critical droplet radii, see Fig. 3.3. Surface tension has a weaker influence in scenario C and we thus chose $\beta_+ = 10^{-7} \mu\text{m}^2/\text{pN}$ there.

In summary, we choose values for the catalytic activity Q and the surface tension parameter $\gamma\beta_+$ of scenario B that are consistent with the requirements to (i) suppress spontaneous centrosome formation in the cytosol, (ii) ensure nucleation of centrosomes at the centrioles, (iii) stabilize multiple centrosomes, and (iv) account for the observed sigmoidal growth. The value of $\gamma\beta_+$ in the other two scenarios is then determined by comparing the critical radius to scenario B. We thus arrive at a standard set of parameters for all three scenarios, which are summarized in Table 6.2. These parameters have also been used in various figures throughout this thesis.

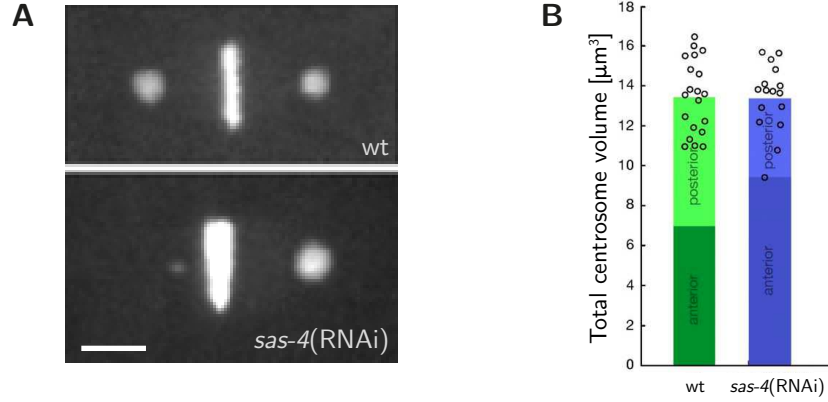


Figure 6.7: Centrosomes with unequal sizes. **(A)** Representative image of centrosomes and DNA in wild-type (wt, top panel), and disturbed (*sas-4*(RNAi), lower panel) cells. The scale bar represents 5 μm . Panel modified from Ref. [30]. **(B)** Total centrosome volume in wild-type (wt, green), and disturbed (*sas-4*(RNAi), blue) cells. Individual data points are shown as circles and the mean individual volume of the centrosomes located in the anterior and posterior part of the cell are shown as different shades inside the bars. Panel modified from Ref. [24].

6.6 Multiple centrosomes with unequal sizes

Centrosomes can have unequal sizes if their centrioles are perturbed, see Fig. 6.7A. In these experiments, centrioles within the same cell were compromised to different extents thus leading to the observed unequal sizes of the respective centrosomes [68]. Interestingly, the total volume of the two centrosomes in a cell was equal in the perturbed and the unperturbed case, see Fig. 6.7B. This can be explained by the droplet picture of centrosomes, where the total size is set by the amount of droplet material. If the two centrosomes have an unequal size, the large one must thus be larger than in the unperturbed case, where they are of equal size.

We now investigate whether our theory can account for the observed unequal sizes. In the model, centrioles control the PCM formation around them by virtue of their catalytic activity Q . We thus model unequal centrioles by assuming different values of Q for the two pairs of centrioles in the cell. For simplicity, we consider the strong segregation regime, $\psi_+ = 0$, ignore surface tension effects, $\gamma = 0$, and assume that soluble building blocks diffuse fast. The growth rates $\partial_t V_1$ and $\partial_t V_2$ of the two centrosomes then follow from Eqs. (2.18) and (2.19). They read

$$\partial_t V_i \approx \frac{k_c \psi_- V_i + Q_i}{\psi_-} (1 - \psi_-) \phi_0^A - k_{BA} V_i, \quad (6.3)$$

where $i = 1, 2$ and generally $Q_1 \neq Q_2$. These are two ordinary differential equations, which are coupled via the volume fraction ϕ_0^A of soluble building blocks. Its value is given by the conservation of material in the cell and reads $\phi_0^A \approx \bar{\phi} - (V_1 + V_2)\psi_-/V_c$. We analyze Eq. (6.3) by first considering the total centrosome volume $V_{\text{tot}} = V_1 + V_2$. Solving for the stationary state, we get

$$V_{\text{tot}}^* \approx \frac{V_c}{\psi_-} \left(\bar{\phi} - \frac{k_{BA}}{(1 - \psi_-)k_c} \right) + \frac{(Q_1 + Q_2)k_{BA}}{[(1 - \psi_-)k_c\bar{\phi} - k_{BA}]k_c\psi_-}. \quad (6.4)$$

This expression is identical to the stationary state volume of a single droplet with catalytic activity $Q_1 + Q_2$, see Eq. (G.7a) in the Appendix G. Using the parameters describing centrosomes under wild-type conditions, see Table 6.2, the first term is four orders of magnitude larger than the second one and the influence of the catalytic activities on the total volume is thus negligible. This is in line with the observation that the catalytic activities hardly affect centrosome volume for a single centrosome, see Fig. 6.3E. The total volume of the two centrosomes is thus set by the amount of droplet material, explaining the experimental observation shown in Fig. 6.7B.

The individual volumes V_i^* of the centrosomes in stationary state follow from Eq. (6.3) by setting the time derivative to zero and solving for V_i , which yields

$$V_i^* = Q_i \frac{1 - \psi_-}{\psi_-} \frac{\phi_0^A}{k_{BA} - (1 - \psi_-)k_c\phi_0^A}. \quad (6.5)$$

Note that the volume of a centrosome is proportional to the activity of its centrioles, $V_i^* \propto Q_i$. Here, the factor of proportionality only depends on global quantities and is thus the same for both centrosomes. Consequently, the individual volumes of the centrosomes read $V_i^* = V_{\text{tot}}^* Q_i / (Q_1 + Q_2)$.

We next analyze the full dynamics of the individual centrosome volumes. The temporal evolution of the ratio of the two volumes can be written as

$$\frac{d}{dt} \left(\frac{V_1}{V_2} \right) = \frac{V_2 Q_1 - V_1 Q_2}{V_2^2} \cdot \frac{(1 - \psi_-)\phi_0^A}{\psi_-}, \quad (6.6)$$

which is derived from Eq. (6.3). The right hand side of this equation vanishes if the ratio of the volumes is equal to the ratio of the catalytic activities, $V_1/V_2 = Q_1/Q_2$. If the system is prepared with bare centrioles, the droplet volumes vanish initially, $V_i(0) = 0$. In the early growth phase, droplet material is then predominately produced by the centrioles and the growth rate is thus directly proportional to their catalytic activity, $\partial_t V_i \approx Q_i \phi_0^A / \psi_-$. For small centrosomes, we thus get $V_i \propto Q_i$ and the right hand side of Eq. (6.6) vanishes. This implies that the ratio of the volumes stays constant all the time. Hence, $V_1/V_2 = Q_1/Q_2$ holds for the entire growth process and the ratio of the volumes of the two centrosomes is always dictated by the activity of their centrioles.

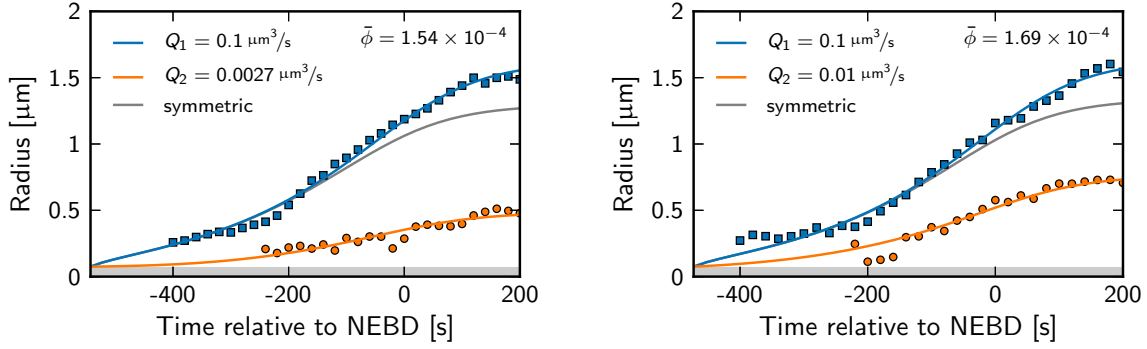


Figure 6.8: Radii of two centrosomes with unequal centrioles as a function of time for two representative cases. The solid lines show fits of the theory to the experimental data (squares and circles) obtained in the 2-cell stage (AB-cell) of *C. elegans* [222]. Fit parameters are the catalytic activity Q_2 of one centriole pair, the overall fraction $\bar{\phi}$ of PCM components, and the time t_0 of growth initiation. The remaining model parameters are taken from Table 6.2. The symmetric model with $Q_1 = Q_2 = 0.1 \mu\text{m}^3/\text{s}$ is shown as a comparison (grey line).

Experimentally, Kirkham et al. found that the ratio of the sizes of the large to the small centrosome correlates strongly with the respective ratio of the fluorescent intensities of the protein SAS-4, which typically localizes to the centrioles [68]. If we assume that the activity at the centrioles is determined by the amount of SAS-4, we can thus explain the experimental observation. To investigate this point further, we finally solve Eq. (6.3) numerically in order to compare the model of unequal centrosomes with experimental data. Here, we use the parameters of the autocatalytic scenario given in Table 6.2, which we found to account for the observed centrosome growth in unperturbed cells. Note that there are three parameters that might have changed due to the perturbations in the experiment: the catalytic activity Q_2 at one of the centriole pairs, the fraction $\bar{\phi}$ of PCM components, and the time point where both centrosomes start to grow. We determine these parameters by fitting the centrosome growth curves of the model to the experimental data. Here, we keep the catalytic activity of one of the centrioles fixed to the standard value, $Q_1 = 0.1 \mu\text{m}^3/\text{s}$. Fig. 6.8 shows that the model considered in this section can account for the growth curves of centrosomes with compromised centrioles. The fits suggest that the catalytic activity of the compromised centriole is reduced by about an order of magnitude.

The analysis in this section underlines the importance of the catalytic activity at the centrioles for the formation of centrosomes. In our model, centrioles directly determine how the PCM is distributed between the centrosomes. It is important to note that we neglected surface tension effects in the analysis presented here. This analysis might thus be oversimplified since Ostwald ripening effects are absent. On

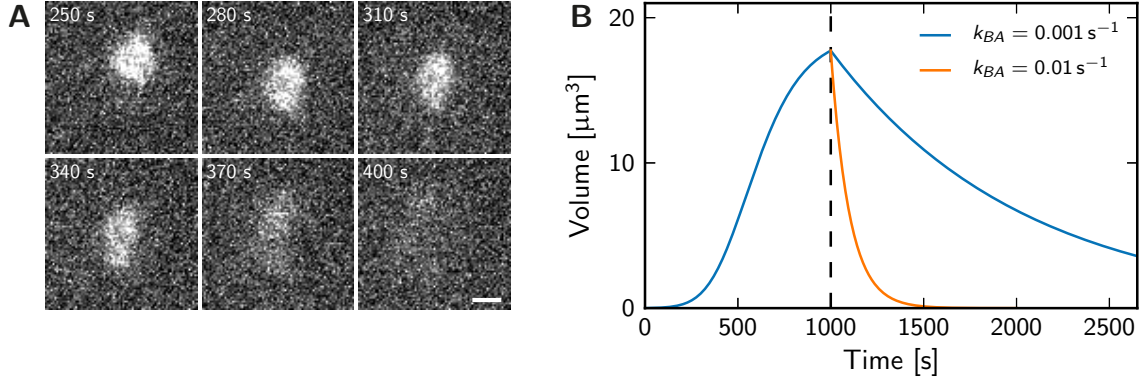


Figure 6.9: Disintegration of a centrosome. **(A)** Sequence of images of a disintegrating centrosome located in the posterior region of a *C. elegans* embryo in the one-cell stage. A maximum projections of a z -stack, which was captured with a spinning-disk confocal microscope using γ -tubulin::GFP embryos, is shown [24]. The time indicated in the panels is measured relative to the nuclear envelope breakdown and the scale bar indicates 2 μm . Raw image data were taken from the centrosome size project [221]. **(B)** Centrosome volume as a function of time. A growth phase lasting 1000 s is followed by a dissolution phase modeled by setting $Q = 0$ and $k_c = 0$ at the point indicated by the black dashed line. Here, simulations for two different reaction rate constants k_{BA} turning the droplet material back to the soluble building blocks are shown. The other parameters have been taken from the scenario B given in Table 6.2.

the other hand, the time scale of redistribution of PCM between centrosomes due to Ostwald ripening is approximately given by $k_c \bar{V} \psi_- / k_{BA} \approx 10^3 \text{ min}$, see Eq. (4.15). Ostwald ripening is thus slow and might be irrelevant in the case of *C. elegans* embryos, where centrosomes are typically observed over shorter durations [24].

6.7 Disintegration phase of centrosomes

Centrosomes disintegrate by dissolving their PCM at the end of the cell cycle. After cell division, each daughter cell inherits one pair of centrioles without much PCM, see Fig. 1.4. This disintegration phase can also be observed under the microscope, see Fig. 6.9A. Unfortunately, this process is far less stereotypical than the growth phase. While disintegrating, centrosomes often deform and fragment, which is partly caused by forces exerted on the centrosome by microtubules that are responsible for the segregation of the DNA [24]. These forces are visible in the periodic movement of the mitotic spindle and therefore also the centrosomes [224, 225]. They also deform the centrosome from a spherical shape, see Fig. 6.9A. A thorough quantification of the disintegration phase is thus difficult.

The qualitative picture shown in Fig. 6.9A suggests that centrosomes do not shrink significantly in their disintegration phase. They rather seem to dissolve by gradually reducing the volume fraction of droplet material in the entire volume. Our theory does not support such a process, since it would require that the coexisting volume fractions given in Eq. (2.7) change over time. Such a change could be caused by gradually varying the physical properties of the droplet material, which we do not consider. Consequently, we do not aim at describing the disintegration phase in detail, but we will still consider a possible disintegration scenario.

In our model, centrosomes form because the phase separating form B of the PCM components segregate from the cytosol. Conversely, droplets disintegrate if this droplet material is turned back to its soluble form. To achieve that, the equilibrium of the chemical reaction $A \rightleftharpoons B$ must be strongly biased towards the soluble form A . To get an idea of the possible disintegration time scales, we thus consider a scenario where only the reaction $B \rightarrow A$ remains. In this case, the rate constant k_{BA} of this reaction determines the time scale of the dissolution. If we use the value $k_{BA} = 0.001 \text{ s}^{-1}$ suggested by the slowest turn-over of centrosome components [16], dissolution would take about 20 min, which is much longer than the observed time scale of a few minutes [24]. In order to account for this quick disintegration, we would thus have to increase k_{BA} by about an order of magnitude, see Fig. 6.9B. Such a model would lead to droplets that disintegrate fast enough, although they do this by decreasing their volume instead of gradually reducing the volume fraction of droplet material.

Consequently, in order to have droplets dissolving fast enough, the reaction rate constants of our model have to be changed completely: the reactions producing droplet material from soluble building blocks have to cease, while the opposing reaction has to become stronger. Such a change of the rate constants is conceivable assuming that regulating enzymes play an important role. On the other hand, our model cannot account for the gradual disintegration observed in experiments and thus likely does not capture the disintegration phase correctly.

Chapter 7

Summary and Outlook

IN this thesis, we developed and discussed a model of active droplets. Most importantly, this model can explain the formation of centrosomes and quantitatively accounts for all experimental data available to us. This is surprising, since the model is based on only a few main ideas and does not contain detailed biochemical information. The key feature of the model is the interplay of phase separation with chemical reactions, which allows for controlled nucleation and leads to non-equilibrium effects like stable states with multiple droplets.

Centrosomes are autocatalytic droplets of PCM organized by centrioles

It is long been known that centrosomes have an amorphous structure formed by assembly and disassembly of PCM components. This growth is nucleated and organized by centrioles. However, the principles governing centrosome dynamics and mechanisms of centrosome assembly remain unclear. What type of material is the centrosome made of? How do the subunits from the cytosol become incorporated in the PCM?

Any model for centrosome growth in *C. elegans* must explain why PCM only grows near centrioles but does not form spontaneously in the cytosol, why two centrosomes have the same size, and why centrosomes in smaller cells are smaller. Here, we show that a model based on the idea of centrosomes forming around centrioles by autocatalytic growth of a PCM droplet phase in the cytosol can quantitatively account for key features of centrosome growth in *C. elegans*. The model has three key ingredients: (i) the PCM components exist in a soluble, cytosolic and a condensed, PCM phase. The PCM phase corresponds to the droplet phase in the model. (ii) The interconversion between these two phases is driven by a centrosome-localized autocatalytic chemical reaction, which can also be catalyzed by the centrioles. (iii) The dense phase segregates from the cytosol by phase separation.

One of the problems in considering the centrosome as a droplet phase is that two centrosomes do coexist. This is interesting because Ostwald ripening would lead in passive systems to the growth of a larger droplet at the expense of smaller droplets. Even if two droplets have the same size initially, this state would be unstable. Our model accounts for the absence of this instability in the case of centrosomes, because

of the effect of centriole activity that suppresses Ostwald ripening if surface tension is low enough.

Another problem with considering the centrosome as a droplet phase is the fact that PCM grows only at centrioles and accidental nucleation in the cytosol is absent. If centrosome formation were only dependent on nucleation and growth, spontaneous nucleation might occasionally occur in the cytosol. This spontaneous nucleation would be rare because surface tension suppresses the growth of small droplets. However, in our model nucleation is suppressed even more strongly because of the autocatalytic nature of growth. Therefore, spontaneous nucleation is strongly suppressed even for small surface tension where Ostwald ripening does not occur. Because of the suppression of nucleation in the cytosol, the centriole activity is required to initiate droplet growth. The centriole activity thus plays a double role: it reliably controls the droplet nucleation and it suppresses Ostwald ripening. Thereby, our model provides a robust mechanism by which centrioles control the location and timing of centrosome formation, while the centrosome size is determined by the amount of PCM components in the cell and thus by the cell volume. Interestingly, the catalytic activity of the centrioles can also explain why they are centered in the centrosome.

The centrosome joins a growing class of biological compartments that have liquid-like properties driven by the colloidal nature of biological macromolecules [102, 105, 191]. The phase separation process that controls the formation of these compartments also leads to a clear interface between the centrosome and cytosol. Such phase separated compartments in the cytosol therefore provide specific chemical environments and permit the cell to separate different chemical reactions in space without using membranes. One advantage of such an organization is that the compartments can be regulated in synchrony with the cell cycle and might thus provide a cue for a large number of dependent reactions. For instance, the centrosome is largest during mitosis and it might function as a signaling hub during this period [226]. In this way, the centrosomes could organize cell division not only mechanically by controlling the microtubules, but also chemically by providing a suitable reaction container. Such phase separated compartments found in biology provide a paradigm for a new class of non-equilibrium emulsions that couple phase separation with chemical reactions.

Active droplets can suppress Ostwald ripening

There is a growing interest in physics and chemistry to study chemical reactions that couple to phase separation. Interesting phenomena including stable emulsions and pattern formation have been reported for such systems [159, 174, 227]. The example from biology discussed here adds new elements to such systems, namely the autocatalytic phase separation and chemically induced nucleation. To capture different aspects of active droplets, we consider three different scenarios, where either the usually discussed first-order reaction, an autocatalytic reaction, or a catalytic activity at a stable core structure is dominant.

Table 7.1: Summary of the main results of the physics of active droplets discussed in this thesis. Each table row corresponds to a different limit of the parameters of the model for the droplet dynamics: **(Eq)** Equilibrium phase separation is contrasted with three non-equilibrium scenarios: **(A)** First-order kinetics, **(B)** Autocatalytic growth, and **(C)** Incorporation at the active cores. The references above the approximate signs indicate the equations where the respective results have been derived in this thesis. Here, we consider the simplified case of strong phase separation, $\psi_+ = 0$, and define the abbreviations $\kappa \equiv k_{AB}/(k_{AB} + k_{BA})$, $\tilde{k}_{BA} = k_{BA}/(1 - \psi_-)$, $\tilde{D}_B \equiv 4\pi D_B/(1 - \psi_-)$, and $\Gamma \equiv \gamma\beta_+$ for conciseness.

	Droplet volume in stationary state	Minimal fraction $\bar{\phi}$ to grow droplets	Critical size to grow a droplet	Perturbation growth rate of m equal-sized droplets
Eq:	$V^{\text{eq}} \stackrel{(1.11)}{\approx} \frac{\bar{\phi} V_c}{\psi_-}$	$\bar{\phi}_{\min}^{\text{eq}} \stackrel{(1.13)}{\approx} \frac{4}{3} \left[\frac{4\pi\Gamma^3\psi_-}{V_c} \right]^{\frac{1}{4}}$	$R_{\text{crit}}^{\text{eq}} \stackrel{(1.12)}{\approx} \frac{\Gamma}{\bar{\phi}}$	$\lambda_{\text{m}}^{\text{eq}} \stackrel{(4.21)}{\approx} \frac{4\pi m D_B \Gamma}{3\psi_- V^{\text{eq}}}$
A:	$V^{\text{A}} \stackrel{(2.22)}{\approx} \frac{\kappa\bar{\phi} V_c}{m\psi_-}$	$\bar{\phi}_{\min}^{\text{A}} \stackrel{(3.11)}{\approx} \frac{4}{3} \left[\frac{4\pi\Gamma^3\psi_-}{\kappa^3 V_c} \right]^{\frac{1}{4}}$	$R_{\text{crit}}^{\text{A}} \stackrel{(3.5)}{\approx} \frac{\Gamma}{\kappa\bar{\phi}}$	$\lambda_{\text{m}}^{\text{A}} \stackrel{(4.13)}{\approx} \frac{4\pi D_B \Gamma}{3\psi_- V^{\text{A}}} - \frac{2k_{BA}}{3}$
B:	$V^{\text{B}} \stackrel{(2.25)}{\approx} \frac{V_c}{m\psi_-} \left[\bar{\phi} - \frac{\tilde{k}_{BA}}{k_c} \right]$	$\bar{\phi}_{\min}^{\text{B}} \stackrel{(2.26)}{\approx} \frac{\tilde{k}_{BA}}{k_c}$	$V_{\text{crit}}^{\text{B}} \stackrel{(3.6)}{\approx} \frac{\tilde{D}_B \Gamma - Q\bar{\phi}}{(k_c\bar{\phi} - \tilde{k}_{BA})\psi_-}$	$\lambda_{\text{m}}^{\text{B}} \stackrel{(4.16)}{\approx} \frac{4\pi D_B \Gamma}{3\psi_- V^{\text{B}}} - \frac{k_{BA} Q}{k_c\psi_- V^{\text{B}}}$
C:	$V^{\text{C}} \stackrel{(2.29)}{\approx} \frac{\bar{\phi} Q V_c}{(V_c \tilde{k}_{BA} + mQ)\psi_-}$	$\bar{\phi}_{\min}^{\text{C}} \stackrel{(4.18)}{\approx} \frac{\tilde{D}_B \Gamma}{Q}$	—	$\lambda_{\text{m}}^{\text{C}} \stackrel{(4.20)}{\approx} \frac{4\pi D_B \Gamma}{3\psi_- V^{\text{C}}} - k_{BA}$

Table 7.1 summarizes the results for these three scenarios and contrasts it with the equilibrium situation. Our scenario A is very close to the systems already discussed in the literature, since it contains only first-order reactions. Interestingly, the expression for the droplet size and also the critical radius predicted by this scenario are very similar to the ones found for equilibrium systems, albeit with a correction factor due to the chemical reactions. The major difference to the equilibrium picture is that multiple droplets can be stable and Ostwald ripening is thus suppressed, see Fig. 4.4. In the analysis of our model we generally find that multiple droplets can be stable if either the first-order reaction or the catalytic activity at the core is strong enough. These stabilizing features are counteracted by surface tension effects and the autocatalytic reaction, which both destabilize multiple droplets. In summary, we thus find that droplet coarsening can be prevented due to non-equilibrium conditions created by chemical reactions.

Furthermore, we found that the autocatalytic reaction has the interesting effect of strongly suppressing spontaneous droplet nucleation. However, a core structure that has a small catalytic activity can overcome this suppression and efficiently nucleate these active droplets. Such an active core can therefore be used to control the droplet formation, see Fig. 3.12. Interestingly, this catalytic activity also centers the core within the droplet. This system could therefore also be exploited to engineer droplets with a stable core at their center. Here, the suppression of homogeneous nucleation would simultaneously prevent the formation of droplets without this core.

Systems that combine phase separation and chemical reactions can thus produce nanometer sized patterns [227]. More generally, “[...] open physiochemical systems far from equilibrium and involving nonlinear feedback processes are endowed by the capacity to undergo self-organization processes” [228]. It is thus not surprising that self-organization has been observed in various other system, e.g. in reaction-diffusion system without phase separation. Here, the coupling of autocatalysis and lateral inhibition can produced patterns [229]. In fact, this process is thought of producing many patterns found in biological organisms [230]. These patterns typically have a fuzzy boundary and may therefore be inefficient in forming well-defined structures on small scales. Conversely, such structures can be formed by the combination of a reaction-diffusion system with phase separation, as we showed in this thesis. It might thus be interesting to investigate whether phase separation also plays a role in other reaction-diffusion systems.

Other biological problems where our model might be applicable

Despite being interesting for applications in physical chemistry and chemical engineering, our model might also be useful to examine other biological problems. There are many membrane-less organelles in cells that could potentially be organized similar to centrosomes [101]. Some of these organelles, e.g. the Cajal bodies and the nuclear bodies, lack stable cores like the centrioles in the case of centrosomes. For these structures, a description based on the scenario A of our model might be more

suitable. It would still allow multiple stable structures of controlled size, but the nucleation would be more erratic.

The model might also apply on larger scales, for instance on the tissue level where cells might phase separate from one another [231]. In a coarse grained description, cell division and cell death could be described by chemical reactions similar to the ones considered in our model. Here it might be necessary to account for viscoelastic effects, which tissues usually show [232, 233]. Our scenario B with autocatalytic growth might then be adequate for describing tumor growth in cancer. This is because the cells in a tumor typically divide rapidly and the growth of a tumor is thus self-reinforcing [234–236]. Here, the soluble building blocks of our model could mimic nutrition factors diffusion through the tissue and the droplet material could be identified with the cancerous cells, which phase separate from the healthy tissue due to adhesive interactions between the cancer cells. The resulting interface between the cancer and the healthy tissue is usually soft and the stability of the shape is a common question in the field [237]. It is likely that our model has to be extended in order to describe tissues satisfactorily, but the results obtained here could serve as a starting point.

Possible extensions of our model

The model developed in this thesis makes many simplifying assumptions. For instance, viscoelastic effects could play a role on intermediate time scales or when other materials such as tissues are described. The associated theory of viscoelastic phase separation, among other things, predicts a «moving droplet phase» where droplet coalescence is suppressed [238, 239]. Such effects could change the phase separation physics and taking them into account might be necessary. This would likely also influence the Ostwald ripening of multiple droplets, which we only considered using a mean-field model in Chapter 4. If the direct interaction of the concentration fields of droplets would be taken into account, we could examine whether droplet growth and coalescence is facilitated or attenuated. Phenomena like these have been studied for passive systems undergoing Ostwald ripening, where they are important if droplets are close together [240–242]. Depending on their size, these droplets can either exhibit an attractive or a repulsive interaction, which leads to directed movement [243]. It would be interesting to examine this problem in the case of active droplets to investigate whether the turnover induced by the chemical reactions has a significant impact. Here, numerical simulations similar to the ones presented in Chapter 5 including surface tension effects could be helpful. We currently work on an extension of our stochastic model together with the master student Coleman Broaddus, where we incorporate the local equilibration at the droplet surface to study the interaction of active droplets numerically.

Appendix

A Coexistence conditions in a ternary fluid

A ternary fluid can be characterized by the volume fractions ϕ^A and ϕ^B of two components, while the volume fraction of the third component is given by $\phi^C = 1 - \phi^A - \phi^B$. We consider a fluid undergoing phase separation, which is described by a simplified Flory-Huggins free energy density [131, 132] reading

$$f_{\text{FH}}(\phi^A, \phi^B) = \frac{k_{\text{B}}T}{\nu} \cdot \left(\phi^A \ln \phi^A + \phi^B \ln \phi^B + \phi^C \ln \phi^C \right) + \chi \phi^B \cdot (\phi^A + \phi^C), \quad (\text{A.1})$$

where ν is a molecular volume, which is assumed to be equal for all components. Here, the first term describes the entropy of mixing proportional to the temperature T and the last term accounts for enthalpic effects. Phase separation of form B from A and C occurs if the interaction parameter χ is large enough. The free energy F of a system with two compartments of respective volume V_- and V_+ reads

$$F(\phi_-^A, \phi_+^A, \phi_-^B, \phi_+^B, V_-, V_+) = V_- f(\phi_-^A, \phi_-^B) + V_+ f(\phi_+^A, \phi_+^B) + \gamma A, \quad (\text{A.2})$$

where the “ $-$ ” and “ $+$ ” used as indices distinguish the values in the two compartments, A is the area of the interface between the compartments, and γ is an associated surface energy. Additionally, there are conservation laws for the volume and the amount of material, $dV_- = -dV_+$, $d(\phi_-^A V_-) = -d(\phi_+^A V_+)$, and $d(\phi_-^B V_-) = -d(\phi_+^B V_+)$. The energy F must be minimal in equilibrium, yielding the coexistence conditions

$$0 = \tilde{\mu}_-^A - \tilde{\mu}_+^A \quad (\text{A.3a})$$

$$0 = \tilde{\mu}_-^B - \tilde{\mu}_+^B \quad (\text{A.3b})$$

$$0 = (\phi_+^A - \phi_-^A) \tilde{\mu}_-^A + (\phi_+^B - \phi_-^B) \tilde{\mu}_-^B + f(\phi_-^A, \phi_-^B) - f(\phi_+^A, \phi_+^B) + 2\gamma H, \quad (\text{A.3c})$$

where $\tilde{\mu}_\pm^x = \partial f(\phi_\pm^A, \phi_\pm^B) / \partial \phi_\pm^x$ is proportional to the chemical potential of component $x = A, B$ and $H = \frac{1}{2} \partial A / \partial V$ denotes the mean curvature of the interface, which we assume to be constant. It is given by $H = 1/R$ for a spherical compartment of radius R . For the free energy f_{FH} given in Eq. (A.1), condition (A.3a) yields

$$\frac{\phi_-^A}{\phi_+^A} = \frac{1 - \phi_-^B}{1 - \phi_+^B}. \quad (\text{A.4})$$

If the component A only occupies a small fraction, $\phi^A \ll \phi^C$, the system reduces to a binary fluid described by a free energy density $f(\phi^B) = \lim_{\phi^A \rightarrow 0} f_{\text{FH}}(\phi^A, \phi^B)$ and coexistence conditions given by Eqs. (1.6). For a flat interface, we define their solutions as ψ_- and ψ_+ , since they only depend on material parameters. We can then expand the free energy density $f(\phi^B)$ around ψ_- and ψ_+ and use the abbreviations $\Delta\phi_{\pm} = \phi_{\pm}^B - \psi_{\pm}$ to turn the coexistence conditions into

$$0 \approx f''(\psi_-)\Delta\phi_- - f''(\psi_+)\Delta\phi_+ \quad (\text{A.5a})$$

$$0 \approx (\phi_+ - \phi_-) f''(\psi_-)\Delta\phi_- + \frac{f''(\psi_-)}{2}\Delta\phi_-^2 - \frac{f''(\psi_+)}{2}\Delta\phi_+^2 + 2\gamma H. \quad (\text{A.5b})$$

Solving the first equation for $\Delta\phi_+$ and substituting the result into the second one leads to a single equation for $\Delta\phi_-$, which reads

$$0 \approx \frac{[f''(\psi_-) - f''(\psi_+)]f''(\psi_-)}{2f''(\psi_+)}\Delta\phi_-^2 - (\psi_- - \psi_+)f''(\psi_-)\Delta\phi_- + 2\gamma H. \quad (\text{A.6})$$

For small $\Delta\phi_-$ or the symmetric case $f''(\psi_-) = f''(\psi_+)$, the right hand side is dominated by the last two terms and we thus get the approximate solution

$$\Delta\phi_- \approx \frac{2\gamma H}{(\psi_- - \psi_+)f''(\psi_-)}. \quad (\text{A.7})$$

The same result can also be obtained by solving the quadratic equation and expanding the result to linear order in γH . Introducing the abbreviations

$$\beta_- = \frac{2}{(\psi_- - \psi_+)f''(\psi_-)} \quad \text{and} \quad \beta_+ = \frac{2}{(\psi_- - \psi_+)f''(\psi_+)}, \quad (\text{A.8})$$

the result reduces to Eq. (1.8). The sensitivity parameters β_- and β_+ measure the influence of surface tension on the volume fractions in local equilibrium. In the case of the ternary fluid introduced in Eq. (A.1), we thus obtain the solutions

$$\phi_-^B \approx \psi_- + \beta_- \gamma H \quad \text{and} \quad \phi_+^B \approx \psi_+ + \beta_+ \gamma H. \quad (\text{A.9})$$

The coefficients β_- and β_+ for the free energy density f_{FH} given in Eq. (A.1) read

$$\beta_{\pm} \approx \frac{2}{\psi_- - \psi_+} \left(\frac{k_B T}{\nu} \left[\frac{1}{\psi_{\pm}} + \frac{1}{1 - \psi_{\pm}} \right] - 2\chi \right)^{-1}, \quad (\text{A.10})$$

where we again considered the case of a dilute fraction of A , $\phi^A \ll 1$. For small ψ_+ , we get $\beta_+ \approx 2\nu\psi_+/(k_B T\psi_-)$, which we also obtained from physical arguments, see Section 1.5.2.

B Instability of multiple equilibrium droplets

We consider m spherical droplets of radii R_i with volumes $V_i = 4\pi R_i^3/3$ and surface areas $A_i = 4\pi R_i^2$ for $i = 1, \dots, m$. The free energy F is given in Eq. (1.14) and reads

$$F(\phi, \mathbf{V}) = V_c f(\phi_0) + \sum_{i=1}^m [f(\phi_i) - f(\phi_0)] V_i + \gamma \sum_{i=1}^m A_i, \quad (\text{B.1})$$

where the ϕ_i are the volume fractions inside droplets, $f(\phi)$ is the free energy density describing the fluid, γ denotes the surface tension, $\phi_0 = (\bar{\phi} V_c - \sum_i V_i \phi_i)/V_0$, and $V_0 = V_c - \sum_i V_i$.

Equilibrium configurations are necessarily stationary points of F . Here, the partial derivatives with respect to all state variables vanish. A stationary point is only stable, if the Hessian matrix \mathcal{H} evaluated at the point is positive definite. \mathcal{H} is defined as

$$\mathcal{H} = \begin{pmatrix} \frac{\partial^2 F}{\partial \phi^2} & \frac{\partial^2 F}{\partial \phi \partial \mathbf{V}} \\ \frac{\partial^2 F}{\partial \phi \partial \mathbf{V}} & \frac{\partial^2 F}{\partial \mathbf{V}^2} \end{pmatrix}. \quad (\text{B.2})$$

The matrix elements of \mathcal{H} follow from the derivatives of $F(\phi, \mathbf{V})$ and read

$$\left(\frac{\partial^2 F}{\partial \phi^2} \right)_{ij} = \frac{\partial^2 F}{\partial \phi_i \partial \phi_j} = \frac{V_i V_j}{V_0} f''(\phi_0) + V_i f''(\phi_i) \delta_{ij} \quad (\text{B.3a})$$

$$\left(\frac{\partial^2 F}{\partial \mathbf{V}^2} \right)_{ij} = \frac{\partial^2 F}{\partial V_i \partial V_j} = \frac{f''(\phi_0)}{V_0} (\phi_0 - \phi_i)(\phi_0 - \phi_j) - \frac{\gamma \delta_{ij}}{2\pi R_i^4} \quad (\text{B.3b})$$

$$\left(\frac{\partial^2 F}{\partial \phi \partial \mathbf{V}} \right)_{ij} = \frac{\partial^2 F}{\partial \phi_i \partial V_j} = \frac{V_i}{V_0} (\phi_j - \phi_0) f''(\phi_0), \quad (\text{B.3c})$$

where $i, j = 1, 2, \dots, m$. We construct a vector \mathbf{x} according to

$$\mathbf{x} = \left(\sqrt{2} V_1^{-1}, -\sqrt{2} V_2^{-1}, \underbrace{0, \dots, 0}_{m-2 \text{ times}}, (\phi_1 - \phi_0)^{-1}, (\phi_2 - \phi_0)^{-1}, \underbrace{0, \dots, 0}_{m-2 \text{ times}} \right)^\top, \quad (\text{B.4})$$

which is only defined for multiple droplets, $m \geq 2$. From this, we calculate

$$\mathbf{x}^\top \mathcal{H} \mathbf{x} = -\frac{\gamma}{2\pi} \left(\frac{1}{(\phi_0 - \phi_1)^2 R_1^4} + \frac{1}{(\phi_0 - \phi_2)^2 R_2^4} \right). \quad (\text{B.5})$$

The expression $\mathbf{x}^\top \mathcal{H} \mathbf{x} / \mathbf{x}^2$ gives an upper bound to the largest eigenvalue of the symmetric, real matrix \mathcal{H} . Since $\mathbf{x}^\top \mathcal{H} \mathbf{x}$ is negative, \mathcal{H} has at least one negative eigenvalue, \mathcal{H} is not positive definite, and all stationary points are unstable. Consequently, multiple droplets are always unstable in equilibrium systems if $\gamma > 0$.

C Numerical solution of the droplet growth

We consider the simplified case of a single droplet growing in a spherical geometry.. The system is thus described by the droplet radius $R(t)$ and the two volume fraction profiles $\phi^A(r, t)$ and $\phi^B(r, t)$. We discretize the radial coordinate r using an adaptive grid [200, 244], with N supporting points $\mathbf{r}^{(j)}$ defined at

$$\mathbf{r}^{(j)}(R) = \begin{cases} a + (j + \frac{1}{2}) \Delta x_-(R) & j \in \{0, 1, \dots, M-2\} \\ R & j \in \{M, M-1\} \\ R + (j - M - \frac{1}{2}) \Delta x_+(R) & j \in \{M+1, M+2, \dots, N-1\} \end{cases}, \quad (\text{C.1})$$

where $\Delta x_-(R) = (R - a)/(M - 1)$ and $\Delta x_+(R) = (R_c - R)/(N - M - 1)$. Here, R_c is the system radius and a denotes the radius of the core at the center. Furthermore, M and $N - M$ are the number of supporting points inside and outside of the droplet, respectively. The adaptive grid introduced here simplifies the evaluation of the interface conditions, since the interface at $r = R(t)$ will always lie on a supporting point. We thus define the discretized volume fractions $\mathbf{f}_x^{(j)}(t) = \phi^x(\mathbf{r}^{(j)}, t)$ for $x = A, B$. The associated time derivatives then read

$$\partial_t \mathbf{f}_x^{(j)}(t) = \left[\frac{\partial \phi^x(r, t)}{\partial t} + \frac{\partial \phi^x(r, t)}{\partial r} \partial_t \mathbf{r}^{(j)} \right]_{r=\mathbf{r}^{(j)}}, \quad (\text{C.2})$$

where the speed $\partial_t \mathbf{r}^{(j)}$ of the j -th grid line enters [200]. It can be calculated from the speed $\partial_t R$ of the interface and evaluates to

$$\partial_t \mathbf{r}^{(j)} = \begin{cases} \frac{\mathbf{r}^{(j)} - a}{R - a} \partial_t R & j < M \\ \frac{R_c - \mathbf{r}^{(j)}}{R_c - R} \partial_t R & M \leq j, \end{cases} \quad (\text{C.3})$$

where a is the radius of the inner core. The discretization in time is given by the time step Δt , leading to the definitions $\mathbf{R}^{(l)} = R(l\Delta t)$, $\mathbf{f}_x^{(j,l)} = \phi^x(\mathbf{r}^{(j,l)}, l\Delta t)$, and $\mathbf{r}^{(j,l)} = \mathbf{r}^{(j)}(\mathbf{R}^{(l)})$ for the discretization of the radius, the volume fractions $x = A, B$, and the grid lines, respectively. Using the Forward-Time Central-Space method [245], we discretize the partial differential equation (2.1), which yields

$$\frac{\mathbf{f}_x^{(j,l+1)} - \mathbf{f}_x^{(j,l)}}{\Delta t} = \eta_x \mathbf{s}^{(j,l)} + D_x \frac{\mathbf{f}_x^{(j-1,l)} - 2\mathbf{f}_x^{(j,l)} + \mathbf{f}_x^{(j+1,l)}}{\Delta x_\pm^2} + \mathbf{z}_x^{(j,l)} \frac{\mathbf{f}_x^{(j+1,l)} - \mathbf{f}_x^{(j-1,l)}}{2\Delta x_\pm}, \quad (\text{C.4})$$

where the D_x are the diffusivities and $\eta_x = -1, +1$ for $x = A, B$, respectively. Here, the reaction rate $\mathbf{s}^{(j,l)} = k_{AB}\mathbf{f}_A^{(j,l)} - k_{BA}\mathbf{f}_B^{(j,l)} + k_c\mathbf{f}_B^{(j,l)}\mathbf{f}_A^{(j,l)}$ follows from Eq. (2.2) and we introduced

$$\mathbf{z}_x^{(j,l)} = \frac{2D_x}{\mathbf{r}^{(j,l)}} + \partial_t \mathbf{r}^{(j)} \quad (\text{C.5})$$

for $x = A, B$, where the first term on the right hand side stems from the Laplace operator in spherical coordinates and the second term accounts for the moving grid, see Eq. (C.2). The solution of the discretized diffusion equation is numerically stable if $\Delta t < \Delta t_{\max}$, where $\Delta t_{\max} = 0.5 (\Delta x)^2 / D_{\max}$ and D_{\max} denotes the largest diffusion constant in the system [246]. We use an adaptive time step Δt chosen such that it is smaller than $\Delta t_{\max}/2$ to obey this stability condition.

Eq. (C.4) can be solved for the values $\mathbf{f}_x^{(j,l+1)}$ at the next time step if $\mathbf{f}_x^{(-1,l)}$ and $\mathbf{f}_x^{(N,l)}$ at the boundary are known. We derive expressions for these virtual supporting points using the boundary conditions of the continuous equations. We get $\mathbf{f}_x^{(N,l)} = \mathbf{f}_x^{(N-1,l)}$ for the no-flux condition at $r = R_c$. The catalytic activity at the core imposes

$$\mathbf{f}_A^{(-1,l)} = \mathbf{f}_A^{(0,l)} \frac{2D_A - q\Delta x_-}{2D_A + q\Delta x_-} \quad \text{and} \quad \mathbf{f}_B^{(-1,l)} = \frac{q\Delta x_-}{2D_B} \left(\mathbf{f}_A^{(0,l)} + \mathbf{f}_A^{(-1,l)} \right) + \mathbf{f}_B^{(0,l)}, \quad (\text{C.6})$$

where $q = Q/(4\pi a^2)$. The values at the supporting points $\mathbf{r}^{(M-1)}$ and $\mathbf{r}^{(M)}$ at the interface can be directly computed from the interface conditions given in Eqs. (2.7), (2.8), and (2.11). The rate of droplet growth follows directly from Eq. (2.10).

The discretization given in Eq. (C.1) breaks down for small radii, $R \rightarrow a$, since then $\Delta x_- \rightarrow 0$, which would also require $\Delta t \rightarrow 0$ for a stable simulation. For small droplets we thus use an alternative scheme assuming that the volume fraction profiles inside the droplet are in stationary state. We can solve for these profiles analytically, see Section 3.1, and use the results instead of the discretized version presented here. Taken together, we are able to solve for the time evolution of the droplet growth for all droplet sizes.

D Diffusion-limited growth of a single droplet

For simplicity, we consider a single droplet in a spherical geometry of radius R_c resulting in spherical symmetric volume fractions $\phi^A(r, t)$ and $\phi^B(r, t)$, where r is the distance from the center. We furthermore consider $k_{AB} = k_{BA} = 0$, $k_c = 0$, $\gamma = 0$, $\psi_+ = 0$, and large Q for simplicity. The dynamics of the soluble building blocks are then given by $\partial_t \phi^A = D_A \nabla^2 \phi^A$ with reflective boundary conditions at $r = R_c$ and an absorbing boundary condition $\phi^A(a) = 0$ due to the large enzymatic activity Q at the core. The full solution then reads [245]

$$\phi^A(r, t) = \sum_k b_k \frac{\sin[(r - a)\alpha_k]}{r} e^{-D_A \alpha_k^2 t}, \quad (\text{D.1})$$

where the length scales α_k^{-1} are solutions to

$$\alpha_k R_c = \tan[(R_c - a)\alpha_k], \quad (\text{D.2})$$

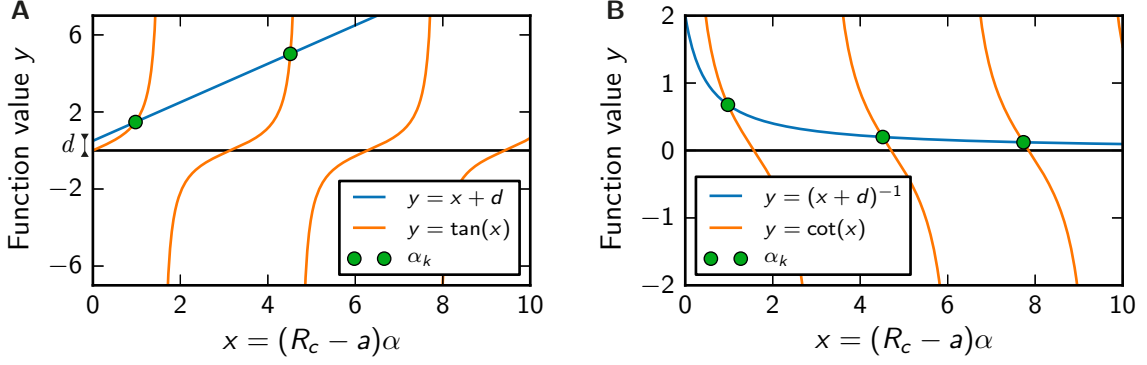


Figure D.1: Graphical solution of Eq. (D.2) defining the admissible length scales of diffusion-limited growth. The solutions (green dots) are given by the intersection of the left hand side (blue line) and the right hand side (orange line). Here, $d = \alpha a$. **(A)** Original equation (D.2). **(B)** Reciprocal equation.

see Fig. D.1. Approximating $\tan(x) \approx x + x^3/3$, the smallest, positive solution reads

$$\alpha_1 \approx \sqrt{\frac{3a}{(R_c - a)^3}}. \quad (\text{D.3})$$

The inverse of Eq. (D.2), $1 = \alpha_k R_c \cot[(R_c - a)\alpha_k]$, is used to approximate the solutions for $k \geq 2$, $\alpha_k \approx (2k-1)\pi/[2(R_c - a)]$. The amplitudes b_k of the fundamental solutions are set by the initial condition, $\phi(r, 0) = \bar{\phi}$, and given by

$$b_k = \frac{(2 + 2R_c^2\alpha_k^2)\bar{\phi}a}{(R_c - a)R_c^2\alpha_k^3 - a\alpha_k}, \quad (\text{D.4a})$$

where we used the orthogonality of the fundamental functions. The droplet volume,

$$V(t) = \frac{\bar{\phi}}{\psi_-} \left[V_c - \sum_{k=1}^{\infty} \frac{(2 + 2R_c^2\alpha_k^2)4\pi a^2}{(R_c - a)R_c^2\alpha_k^4 - a\alpha_k^2} e^{-D_A\alpha_k^2 t} \right], \quad (\text{D.5})$$

is given by the amount of material that left the system divided by the volume fraction ψ_- in the droplet. The slowest associated timescale is

$$\tau_1 = \frac{1}{D_A\alpha_1^2} \approx \frac{(R_c - a)^3}{3D_A a}, \quad (\text{D.6})$$

see Eq. (D.3). τ_1 is the important time scale which determines the relaxation behavior of the system.

E Approximate efflux of droplet material

We calculate the compositional flux J_+^B of droplet material away from the droplet surface by evaluating the gradient of the volume fraction ϕ^B . For simplicity, we consider a droplet of radius R in a spherical geometry such that all volume fractions are spherically symmetric and we have $J_+^B = -4\pi D_B r^2 \partial_r \phi^B(r, t)|_{r=R}$. In general, the functional form of $\phi^B(r, t)$ is governed by the reaction-diffusion equation (2.1b) augmented with boundary conditions on the droplet surfaces, Eq. (2.7b), and a no-flux condition at the system boundary, Eq. (2.3). For simplicity, we assume that ϕ^B is in the stationary state and thus obeys

$$0 = \frac{D_B}{r^2} \frac{\partial}{\partial r} r^2 \partial_r \phi^B(r) + j_{AB} - k_{BA} \phi^B(r), \quad (\text{E.1})$$

where D_B is the diffusivity of the component and k_{BA} is the rate constant of the first-order reaction $B \rightarrow A$. Here, j_{AB} accounts for the creation of components of form B , which we assume to be homogeneous and constant for simplicity. The differential equation (E.1) is solved by basis functions of the form $e^{\pm r\alpha}/r$ with $\alpha = \sqrt{k_{BA}/D_B}$. Interestingly, the volume fraction falls off faster than exponential and any direct interactions between the concentration fields of droplets will therefore be short-ranged. This functional form is very similar to a Yukawa potential, which has historically been used to describe the exchange interaction of massive particles encountered in particle physics [247].

The full solution $\phi^B(r)$ to Eq. (E.1) additionally has to fulfill the two boundary conditions $\phi^B(R) = \phi_+^B(R)$ and $\partial_r \phi^B(r)|_{r=R_c} = 0$, which fix the integration constants. For simplicity, we consider the case of a large system, $R_c \gg \alpha^{-1}$, which results in

$$\phi^B(r) \approx \phi_0^B + (\phi_+^B - \phi_0^B) \frac{e^{\alpha(R-r)} R}{r}. \quad (\text{E.2})$$

Here, $\phi_0^B = j_{AB}/k_{BA}$ is the fraction of form B at the boundary, i.e. far away from the droplet. The flux $J_+^B(R)$ at the droplet surface then reads

$$J_+^B(R) \approx 4\pi D_B R \cdot (1 + \alpha R) (\phi_+^B(R) - \phi_0^B) \quad (\text{E.3})$$

and is driven by the difference of the fractions ϕ_+^B at the droplet surface and the fraction ϕ_0^B far away. For the parameters considered in this thesis, see Table 6.2, the correction due to the chemical reactions are negligible, $\alpha R \ll 1$. Hence,

$$J_+^B(R) \approx 4\pi D_B R \cdot (\phi_+^B(R) - \phi_0^B). \quad (\text{E.4})$$

This form has also been used in the seminal paper by Lifshitz and Slyozov [138].

F Determining stationary states of single droplets

For simplicity, we solve for the stationary state of a single droplet in a spherical geometry, where the volume fractions $\bar{\phi}^A(r)$ and $\bar{\phi}^B(r)$ are only functions of the radial coordinate r . They must be solutions to the dynamical equations (2.12) with vanishing time derivatives, where we linearize the non-linearity in the reaction rate according to Eq. (3.1) in Section 3.1. $\bar{\phi}^A(r)$ and $\bar{\phi}^B(r)$ must thus fulfill

$$0 = \frac{D_A}{r^2} \partial_r [r^2 \partial_r \bar{\phi}_\pm^A(r)] - k_{AB} \bar{\phi}_\pm^A(r) + k_{BA} \bar{\phi}_\pm^B(r) - k_c \psi_\pm \bar{\phi}_\pm^A(r) \quad \text{and} \quad (\text{F.1a})$$

$$0 = \frac{D_B}{r^2} \partial_r [r^2 \partial_r \bar{\phi}_\pm^B(r)] + k_{AB} \bar{\phi}_\pm^A(r) - k_{BA} \bar{\phi}_\pm^B(r) + k_c \psi_\pm \bar{\phi}_\pm^A(r), \quad (\text{F.1b})$$

where the suffixes “−” and “+” distinguish the volume fractions inside and outside of the droplet. Here, D_A and D_B are diffusivities, k_{AB} and k_{BA} are first-order reaction rate constants, k_c is the rate constant of the autocatalytic reaction, and ψ_- and ψ_+ denote the volume fractions at a flat interface. These equations are supplemented by eight boundary conditions,

$$0 = \bar{\phi}_+^{A'}(R_c) = \bar{\phi}_+^{A'}(R_c), \quad \frac{Q \bar{\phi}_-^A(a)}{4\pi a^2} = D_A \bar{\phi}_-^{A'}(a) = -D_B \bar{\phi}_-^{B'}(a), \quad (\text{F.2a})$$

$$\bar{\phi}_-^{A'}(\bar{R}) = \bar{\phi}_+^{A'}(\bar{R}), \quad \bar{\phi}_-^{B'}(\bar{R}) = \bar{\phi}_+^{B'}(\bar{R}), \quad (\text{F.2b})$$

$$\bar{\phi}_\pm^B(\bar{R}) = \psi_\pm + \frac{\gamma \beta_\pm}{\bar{R}}, \text{ and } \quad \bar{\phi}_+^A(\bar{R}) = \frac{1 - \bar{\phi}_+^B(\bar{R})}{1 - \bar{\phi}_-^B(\bar{R})} \bar{\phi}_-^A(\bar{R}), \quad (\text{F.2c})$$

see Eqs. (2.13)–(2.16). Here, R_c is the system radius, Q parameterizes the catalytic activity of the core with radius a , γ is the surface tension, β_\pm denote its effect onto the volume fractions, and \bar{R} is the unknown droplet radius. Solving the sum of the Eqs. (F.1), we find a relation between the two volume fraction profiles,

$$\bar{\phi}_\pm^B(r) = \Delta\phi_\pm - \frac{D_A}{D_B} \bar{\phi}_\pm^A(r), \quad (\text{F.3})$$

where $\Delta\phi_-$ and $\Delta\phi_+$ are two unknown constants. Eq. (F.1a) is then solved by

$$\bar{\phi}_\pm^A(r) = \frac{k_{BA}}{k_\pm} \Delta\phi_\pm + \frac{C_1^\pm}{r} e^{-r\alpha_\pm} + \frac{C_2^\pm}{r} e^{r\alpha_\pm} \quad (\text{F.4})$$

with $k_\pm = k_{AB} + k_c \psi_\pm + k_{BA} D_A / D_B$ and $\alpha_\pm = \sqrt{k_\pm / D_A}$. Together with Eq. (F.3), we can thus substitute $\bar{\phi}^A(r)$ and $\bar{\phi}^B(r)$ in the boundary conditions to get a set of linear equations for the six coefficients $\Delta\phi_\pm$, C_1^\pm , and C_2^\pm . These equations can be solved analytically, although the resulting expressions are lengthy and therefore omitted here. The stationary droplet radius \bar{R} is determined by the total amount Φ^A

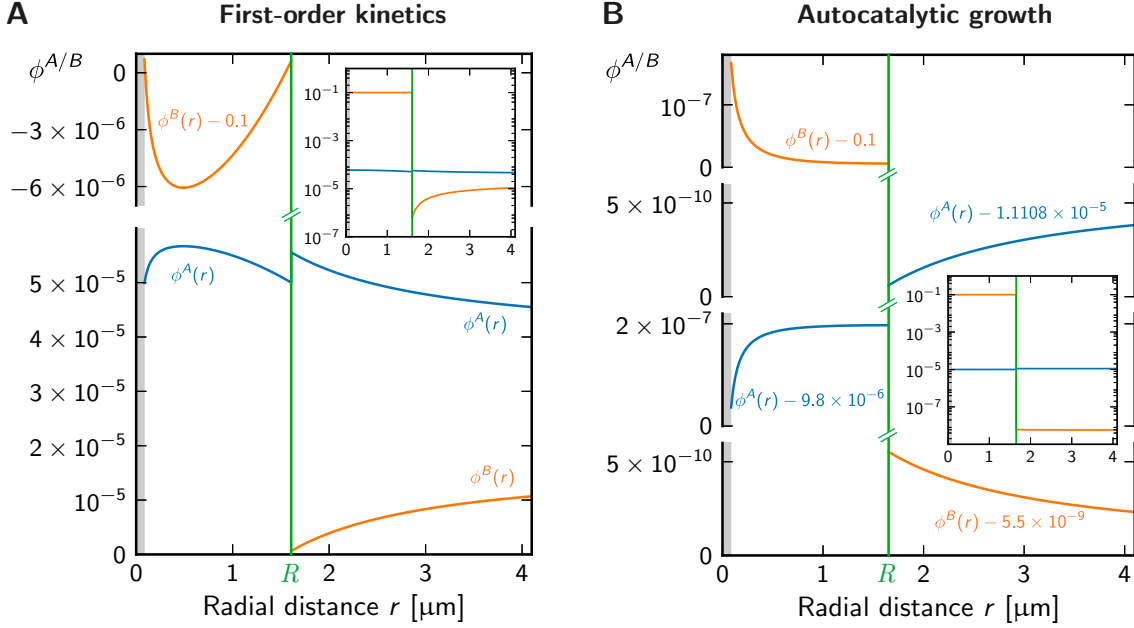


Figure F.1: Stationary volume fractions as a function of the radial coordinate r . The volume fraction of the soluble building blocks (blue) and the droplet material (orange) are shifted by an amount indicated by the label next to the curves and have been put on a broken y-axis to account for the different orders of magnitudes. The insets show the same data in a semi-logarithmic plot. The droplet extends from the core (grey area) to the interface at $r = R$ (green line). **(A)** First-order kinetics with catalytic activity $Q = 1 \mu\text{m}^3/\text{s}$ at the core and the remaining parameters given in Fig. 2.3. **(B)** Autocatalytic growth with $Q = 0.1 \mu\text{m}^3/\text{s}$ and remaining parameters given in Fig. 2.4.

and Φ^B of droplet components in the system given by the integrals of the volume fractions, which depend on \bar{R} . The conservation equation (2.4) thus becomes

$$\bar{\phi}V_c = \Phi^A(\bar{R}) + \Phi^B(\bar{R}). \quad (\text{F.5})$$

We plot the right hand side of this expression against the amount $\bar{\phi}V_c$ of droplet components, e.g. in Figs. 3.3–3.5. This can be interpreted as the necessary amount needed to support a given stationary state radius \bar{R} .

Additionally, we show the function $\phi^A(r)$ and $\phi^B(r)$ for two representative choices of model parameters in Fig. F.1. The volume fractions of the different forms differ in their order of magnitude, which makes the plot difficult to read. This is mainly caused by the phase separation process, which concentrates droplet material of form B inside the droplet leading to much higher volume fractions there.

Next, we analyze small perturbations of the stationary state by a linear stability analysis. We expand the volume fractions ϕ^A and ϕ^B to linear order around their stationary state value, which yields

$$\phi_{\pm}^x(r, t) = \bar{\phi}_{\pm}^x(r) + \varepsilon F_{\pm}^x(\lambda, r) e^{\lambda t}, \quad (\text{F.6})$$

for $x = A, B$. Here, ε is the amplitude of the perturbation, which evolves with a growth rate λ in time [201]. The functions $F_{\pm}^x(\lambda, r)$ encode the spatial perturbations of the volume fractions and can be derived from the differential equations, which result from plugging Eq. (F.6) into the Eqs. (2.12). We can solve these equations using the linearization introduced in Eq. (3.1) and assuming that the diffusion constant is the same for both forms, $D_A = D_B = D$. The complete solution then reads

$$F_{\pm}^A(\lambda, r) = \frac{k_{BA}\hat{C}_1^{\pm}}{r} e^{-\alpha_{\lambda} r} + \frac{k_{BA}\hat{C}_2^{\pm}}{r} e^{\alpha_{\lambda} r} + \frac{\hat{C}_3^{\pm}}{r} e^{-\alpha_{\lambda}^{\pm} r} + \frac{\hat{C}_4^{\pm}}{r} e^{\alpha_{\lambda}^{\pm} r} \quad (\text{F.7a})$$

$$F_{\pm}^B(\lambda, r) = \frac{\tilde{k}_{\pm}\hat{C}_1^{\pm}}{r} e^{-\alpha_{\lambda} r} + \frac{\tilde{k}_{\pm}\hat{C}_2^{\pm}}{r} e^{\alpha_{\lambda} r} - \frac{\hat{C}_3^{\pm}}{r} e^{-\alpha_{\lambda}^{\pm} r} - \frac{\hat{C}_4^{\pm}}{r} e^{\alpha_{\lambda}^{\pm} r}, \quad (\text{F.7b})$$

where we introduced $\tilde{k}_{\pm} = k_{AB} + k_c \psi_{\pm}$ as well as the inverse length scales $\alpha_{\lambda} = \sqrt{\lambda/D}$ and $\alpha_{\lambda}^{\pm} = \sqrt{(k_{\pm} + k_{BA} + \lambda)/D}$. The eight coefficients \hat{C}_1^{\pm} , \hat{C}_2^{\pm} , \hat{C}_3^{\pm} , and \hat{C}_4^{\pm} can be determined from a linear set of equations that is obtained by inserting Eqs. (F.7) into the boundary and interface conditions given by Eqs. (2.13)–(2.16). The perturbation growth rate λ can be determined by a linearized version of the droplet growth rate given by Eq. (2.14). This leads to an expression for λ , which reads

$$\lambda = \frac{D}{\psi_- - \psi_+} \cdot \left[\partial_r^2 \bar{\phi}_+^B(r) - \partial_r^2 \bar{\phi}_-^B(r) + \partial_r F_+^B(\lambda, r) - \partial_r F_-^B(\lambda, r) \right]_{r=\bar{R}}, \quad (\text{F.8})$$

where we approximated $\phi_{\pm}^B(R)$ by ψ_{\pm} in the denominator of Eq. (2.10) for simplicity. Both the stationary state profiles $\bar{\phi}^x(r)$ and the spatial perturbation functions $F^x(\lambda, r)$ for $x = A, B$ have been determined above. Eq. (F.8) is thus a single, non-linear equation for the perturbation growth rate λ . The solution with the largest real part then determines the evolution of the stationary state, which is stable if this value is negative.

G Droplet size including surface tension effects

Surface tension effects typically influence the stable stationary droplet volumes only slightly, see Section 3.2. Here, we show this by explicitly taking the surface tension γ into account to derive expressions for the droplet volume that are more accurate than the ones given for the simple scenarios discussed in Section 2.2.

Scenario A: First-order kinetics

If first-order kinetics dominate, $k_{AB} > 0$, $k_c = 0$, $Q = 0$, droplet material is mainly produced in the solvent and converted back to soluble building blocks inside the droplet. This latter conversion is quantified by the reaction flux $J_-^S \approx -k_{BA}\psi_-V$, where we neglect the reaction $A \rightarrow B$ inside the droplet for simplicity. J_-^S must be balanced by the compositional flux J_+^B at the droplet surface given by Eq. (E.4). Using $J_-^S = J_+^B$, we arrive at a cubic equation for the droplet radius R ,

$$\frac{k_{BA}\psi_-}{3D_B}R^3 - (\phi_0^B - \psi_+)R + \gamma\beta_+ = 0, \quad (\text{G.1})$$

that must be fulfilled in stationary state. Here, D_B is the diffusivity of building blocks and $\gamma\beta_+$ quantify the surface tension effects. This equation only has real solutions if its discriminant is positive. We use this condition to derive the minimal fraction $\phi_{0,\min}^B$ of droplet material in the solvent necessary to have any droplets, which reads

$$\phi_{0,\min}^B = \left(\frac{9(\gamma\beta_+)^2 k_{BA}\psi_-}{4D_B} \right)^{\frac{1}{3}} + \psi_+. \quad (\text{G.2})$$

The volume fraction ϕ_0^B of droplet material outside of droplets can be estimated from the balance of reaction fluxes in the complete system, $mJ_-^S + J_+^S = 0$, where the flux in the solvent reads $J_+^S = (k_{AB}\phi_0^A - k_{BA}\phi_0^B)V_c$. Additionally using the conservation of material, $\bar{\phi}V_c = (\phi_0^A + \phi_0^B)V_c + m\psi_-V/V_c$, we thus get

$$\phi_0^A = \frac{k_{BA}}{k_{AB} + k_{BA}}\bar{\phi} \quad \text{and} \quad \phi_0^B = \frac{k_{AB}}{k_{AB} + k_{BA}}\bar{\phi} - \frac{m\psi_-V}{V_c}. \quad (\text{G.3})$$

Putting $\phi_0^B = \phi_{0,\min}^B$, we can thus solve for V , yielding the result

$$V^A = \frac{V_c}{m\psi_-} \left[\frac{k_{AB}}{k_{AB} + k_{BA}}\bar{\phi} - \left(\frac{9(\gamma\beta_+)^2 k_{BA}\psi_-}{4D_B} \right)^{1/3} - \psi_+ \right]. \quad (\text{G.4})$$

This expression gives an approximation to the droplet volume in scenario A assuming that the fraction of building blocks in the solvent assumes the minimal value $\phi_{0,\min}^B$. At this value, droplets cannot grow further and the stationary state is thus reached.

Scenario B: Autocatalytic growth

In scenario B, the production of droplet material is predominately driven by the autocatalytic reaction with a rate constant k_c . For simplicity, we consider $k_{AB} = 0$ and $\psi_+ = 0$, but allow for a catalytic activity Q at the core. The droplet material is then predominately produced inside the droplet by the associated reaction flux $J_-^S \approx (1 - \psi_-)(Q + k_c\psi_-V)\phi_0^A - k_{BA}V\psi_-$. The efflux of material is quantified by $J_+^B \approx 4\pi D_B\gamma\beta_+$ and the conversion back to the soluble building blocks is captured by the reaction flux $J_+^S \approx -k_{BA}V_c\phi_0^B$ in the solvent. The stationary state droplet volume V can then be determined from the balance of the reaction fluxes in the system, $J_+^S + mJ_-^S = 0$, the balance of fluxes in a droplet, $J_-^S = J_+^B$, and the conservation of material in the complete system, $\bar{\phi}V_c \approx (\phi_0^A + \phi_0^B)V_c + m\psi_-V$. Putting everything together, we arrive at an equation for the droplet volume V^B in scenario B, which reads

$$(mQ + k_{BA}V_c)J_+^B + k_{BA}Q\bar{\phi}V_c = mk_{BA}k_c\psi_-^2(V^B)^2 + [(k_{BA} - k_c\bar{\phi})V_c + mQ]k_{BA} - mk_cJ_+^B \psi_-V^B. \quad (\text{G.5})$$

This quadratic equation is solved by

$$V^B = \pm \sqrt{\frac{k_{BA}QV_c\bar{\phi} + (mQ + \frac{k_{BA}}{1-\psi_-}V_c)J_+^B}{k_{BA}k_cm^2\psi_-^2} + \left[\frac{mQ + (k_c\bar{\phi} - \frac{k_{BA}}{1-\psi_-})V_c}{2k_cm\psi_-} - \frac{J_+^B}{2k_{BA}\psi_-} \right]^2} + \frac{J_+^B}{2k_{BA}\psi_-} + \frac{mQ + (k_c\bar{\phi} - \frac{k_{BA}}{1-\psi_-})V_c}{2k_cm\psi_-}. \quad (\text{G.6})$$

These solutions must be real, at least in the parameter region, where droplets can exist. We can furthermore develop the two solutions to first order in Q and γ , which yields

$$V_{\text{large}}^B \approx \frac{V_c}{m\psi_-} \left[\bar{\phi} - \frac{k_{BA}}{(1-\psi_-)k_c} \right] + \frac{k_{BA}^2Q - 4\pi(1-\psi_-)^2D_B\gamma\beta_+k_c^2\bar{\phi}}{[(1-\psi_-)k_c\bar{\phi} - k_{BA}]k_ck_{BA}\psi_-} \quad (\text{G.7a})$$

$$V_{\text{small}}^B \approx \frac{4\pi D_B\gamma\beta_+ - Q\bar{\phi}}{k_c\bar{\phi}\psi_- - k_{BA}\psi_-}. \quad (\text{G.7b})$$

Here, V_{large}^B corresponds to the larger droplet, where both Q and γ only have a minor effect on the volume, see Section 3.2. Specifically, we recover Eq. (2.25) from V_{large}^B in the limit $Q \rightarrow 0$ and $\gamma \rightarrow 0$. Conversely, V_{small}^B represents a small stationary state caused by surface tension effects, which can be interpreted as a critical size, see Section 3.2. This critical size can be overcome by the catalytic activity Q , since V_{small}^B has no positive solutions for large enough Q . Note that Eq. (G.7b) is identical to the expression for the critical size given in Eq. (3.6).

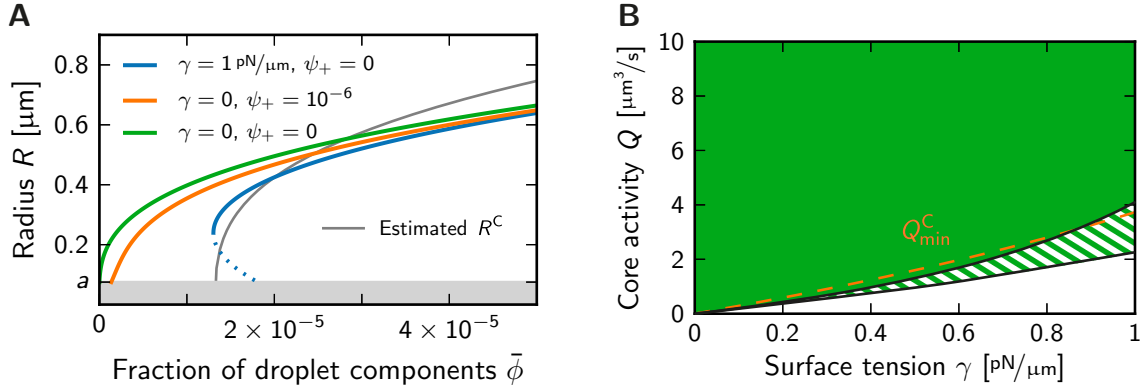


Figure G.1: Stationary states of a single droplet organized by the catalytic activity at the centriole (scenario C) **(A)** Droplet radius as a function of the fraction $\bar{\phi}$ for $Q = 10 \mu\text{m}^3/\text{s}$ and different values of the surface tension γ and the basal volume fraction ψ_+ outside of droplets. The grey line indicates the estimate of Eq. (G.8). **(B)** Stability diagram with either no droplets (white regions), one stable droplet (green filled region), or a combination (hatched regions). Here, the total amount of material was kept fixed at $\bar{\phi}V_c = 0.25$. The orange dashed line shows the threshold given in Eq. (G.9b). The model parameters in both panels are given in Fig. 2.5.

Scenario C: Incorporation at the centrioles

The solution in scenario C, $k_{AB} = 0$, $k_c = 0$, $Q > 0$, is already contained in Eq. (G.6) for a vanishing rate constant k_c of the autocatalytic reaction. The associated droplet volume V^C then reads

$$V^C = \frac{1}{\psi_-} \left[\frac{(1 - \psi_-)\bar{\phi}QV_c}{V_c k_{BA} + (1 - \psi_-)mQ} - \frac{4\pi D_B \gamma \beta_+}{k_{BA}} \right]. \quad (\text{G.8})$$

This expression reduces to Eq. (2.29) if surface tension effects are neglected, $\gamma = 0$. Note that the expression derived here predicts significantly larger droplets than the detailed numerical calculations, see Fig. G.1A. This is caused by the simplified treatment of the diffusion of building blocks, which overestimates its fraction at the core. Nonetheless, the minimal values of $\bar{\phi}$ and Q necessary to form droplets can be obtained from the condition $V^C > 0$ and read

$$\bar{\phi}_{\min}^C = \frac{4\pi D_B \gamma \beta_+}{1 - \psi_-} \left[\frac{(1 - \psi_-)m}{k_{BA} V_c} + \frac{1}{Q} \right] \quad (\text{G.9a})$$

$$Q_{\min}^C = \frac{4\pi k_{BA} V_c D_B \gamma \beta_+}{(1 - \psi_-)(k_{BA} V_c \bar{\phi} - 4\pi m D_B \gamma \beta_+)}. \quad (\text{G.9b})$$

These thresholds agree well with the numerical results, see Fig. G.1.

H Distortions of the spherical droplet shape

Distortions of a spherical shape can generally be described by spherical harmonic functions. Here, we first introduced the mathematical tools and then apply them in a linear stability analysis of a stationary spherical droplet.

H.1 Harmonic distortions of a sphere

We use spherical coordinates $\mathbf{r} = (r, \theta, \varphi)$ defined by their conversion,

$$\begin{pmatrix} x \\ y \\ z \end{pmatrix} = \begin{pmatrix} r \cos \varphi \sin \theta \\ r \sin \varphi \sin \theta \\ r \cos \theta \end{pmatrix} \quad 0 \leq \theta \leq \pi, \quad 0 \leq \varphi < 2\pi, \quad (\text{H.1})$$

to Cartesian coordinates (x, y, z) . We give the spherical harmonic functions,

$$Y_l^m(\theta, \varphi) = \sqrt{\frac{2l+1}{4\pi} \cdot \frac{(l-m)!}{(l+m)!}} \cdot e^{im\varphi} \cdot P_l^m(\cos \theta), \quad (\text{H.2})$$

with the degree $l \in \mathbb{N}$ and the order $m \in \mathbb{Z}$, $-l \leq m \leq l$, where $P_l^m(x)$ are the associated Legendre polynomials [248]. The $Y_l^m(\theta, \varphi)$ are complex functions, which can be used to define the real spherical harmonics $Y_{l,m}$ reading

$$Y_{l,m} = \begin{cases} \frac{1}{\sqrt{2}} (Y_l^m + (-1)^m Y_l^{-m}) & \text{if } m > 0 \\ Y_l^m & \text{if } m = 0 \\ \frac{1}{i\sqrt{2}} (Y_l^{-m} - (-1)^m Y_l^m) & \text{if } m < 0. \end{cases} \quad (\text{H.3})$$

To simplify the notation, we introduce a single index, $k = l \cdot (l+1) + m \in \mathbb{N}$, from which the original indices follow using the relations $l_k = \lfloor \sqrt{k} \rfloor$ and $m_k = k - l_k \cdot (l_k + 1)$, where $\lfloor x \rfloor$ is the largest integer not greater than x . Defining $Y_k(\theta, \varphi) = Y_{l_k, m_k}(\theta, \varphi)$, we introduce the functional

$$\mathcal{I}_K[f(\theta, \varphi)] = \int_{-\pi}^{\pi} d\varphi \int_0^{\pi} d\theta \sin \theta Y_K(\theta, \varphi) f(\theta, \varphi) \quad (\text{H.4})$$

to summarize the normalization, $\mathcal{I}_K[1] = 2\sqrt{\pi}\delta_{K0}$, and the orthogonality relation, $\mathcal{I}_K[Y_k(\theta, \varphi)] = \delta_{Kk}$ [248].

We consider the perturbations of a spherical droplet of radius \bar{R} located at the origin of the coordinate system. The perturbed surface \mathcal{A} is then defined by the distance $R(\theta, \varphi)$ of each surface point to the origin, which reads

$$R(\theta, \varphi) = \bar{R} + \sum_{K=0}^{\infty} \varepsilon_K Y_K(\theta, \varphi), \quad (\text{H.5})$$

where $|\varepsilon_K| \ll \bar{R}$. The droplet volume V enclosed by the surface \mathcal{A} reads

$$V = \int_{-\pi}^{\pi} d\varphi \int_0^{\pi} \sin(\theta) d\theta \int_a^{R(\theta)} r^2 dr = \bar{V} + \varepsilon_0 \hat{V} + \mathcal{O}(\varepsilon^2) , \quad (\text{H.6})$$

where $\bar{V} = (\bar{R}^3 - a^3)4\pi/3$ and $\hat{V} = 2\sqrt{\pi}\bar{R}^2$. Up to linear order of the perturbation, the volume is thus only influenced by the first mode $k = 0$. The normal vector \mathbf{n} of the surface \mathcal{A} in spherical coordinates reads

$$\mathbf{n}(\theta, \varphi) \approx \left(1, -\sum_{k=0}^{\infty} \frac{\varepsilon_k \partial_{\theta} Y_k}{\bar{R}}, -\sum_{k=0}^{\infty} \frac{\varepsilon_k \partial_{\varphi} Y_k}{\bar{R} \sin \theta} \right)^{\top} . \quad (\text{H.7})$$

The mean curvature $H(\theta, \varphi)$ is given by the divergence of \mathbf{n} , which yields

$$2H(\theta, \varphi) = \nabla \mathbf{n} \approx \frac{2}{\bar{R}} - \sum_{k=0}^{\infty} \frac{\varepsilon_k}{\bar{R}^2} \left\{ 2Y_k + \partial_{\theta}^2 Y_k + \cot \theta \cdot \partial_{\theta} Y_k + \frac{\partial_{\varphi}^2 Y_k}{\sin^2 \theta} \right\} . \quad (\text{H.8})$$

The last term becomes $\partial_{\varphi}^2 Y_k = -m_k^2 Y_k$, following from the definition of the spherical harmonics. The remaining derivatives read

$$\partial_{\theta}^2 Y_l^m + \cot \theta \cdot \partial_{\theta} Y_l^m \propto [\sin^2 \theta \cdot \partial_u^2 P_l^m(u) - 2 \cos \theta \cdot \partial_u P_l^m(u)]_{u=\cos \theta} , \quad (\text{H.9})$$

where the constant of proportionality can be read of Eq. (H.2). Substituting $u = \cos \theta$, the right hand side of Eq. (H.9) simplifies to

$$\begin{aligned} \partial_u [(1 - u^2) \partial_u P_l^m(u)] &= \partial_u [(l + m) P_{l+1}^m(u) - l u P_l^m(u)] \\ &= \frac{(l + m)(l + 1) u P_{l+1}^m(u) - (l + m)(l + m + 1) P_{l+2}^m(u)}{u^2 - 1} \\ &\quad + \frac{l u (l + m) P_{l+1}^m(u) - (l u)^2 P_l^m(u)}{u^2 - 1} \\ &= \frac{l^2 + l - m^2 - (1 + l) l u^2}{u^2 - 1} \cdot P_l^m(u) , \end{aligned} \quad (\text{H.10})$$

where the derivatives and the recurrence theorem for the associated Legendre polynomials $P_l^m(u)$ have been taken from Ref. [248]. In summary, Eq. (H.8) yields

$$H(\theta, \varphi) = \frac{1}{\bar{R}} + \sum_{k=0}^{\infty} \frac{\varepsilon_k h_k Y_k(\theta, \varphi)}{\bar{R}^2} , \quad (\text{H.11})$$

where we defined the strength $h_k = (l_k^2 + l_k - 2)/2$ of the curvature effect. Interestingly, the deviation of the curvature only depends on the degree l_k of the perturbation and is proportional to the radial deviation $\varepsilon_k Y_k(\theta, \varphi)$ at any surface point.

H.2 Physical description of the perturbed droplet

For simplicity, we consider the case where the volume fractions are in stationary state such that the droplet shape described by Eq. (H.5) is the only dynamic variable. Its dynamics are deduced from Eq. (2.10) and read

$$\partial_t R \cdot \mathbf{e}_r \approx D_B \cdot \frac{\partial_r \phi_+^B(\mathbf{r}) - \partial_r \phi_-^B(\mathbf{r})}{\psi_- - \psi_+} \cdot \mathbf{e}_r \quad \forall \mathbf{r} \in \mathcal{A}, \quad (\text{H.12})$$

where surface points only move radially to first order in the perturbation. Here, \mathbf{e}_r is the radial unit vector, D_B is the diffusivity of droplet components, $\psi_- - \psi_+$ approximates the volume fraction difference between the inside and the outside of the droplet, and $\phi_\pm^B(\mathbf{r})$ is the associated volume fraction profile of the droplet material, which now also depends on the angular coordinates θ and φ . We neglect the influence of surface tension in the denominator of Eq. (2.10), since ψ_- dominates this expression. Note that this approximation is exact if $\beta_- = \beta_+$. Furthermore, we consider that soluble building blocks of form A diffusive quickly, since their distribution does not enter Eq. (H.12) directly. This leads to homogeneous fractions ϕ_-^A and ϕ_+^A respectively inside and outside the droplet, which approximately obey $\phi_+^A \approx \phi_-^A / (1 - \psi_-)$, see Eq. (2.8). The stationary state of ϕ^B is given by Eq. (2.1b) with vanishing time derivatives together with the linearization of Eq. (3.1) yielding

$$0 = D_B \nabla^2 \phi_-^B - k_{BA} \phi_-^B + \nu_- \phi_-^A \quad \forall \mathbf{r} \in \mathcal{V} \quad (\text{H.13a})$$

$$0 = D_B \nabla^2 \phi_+^B - k_{BA} \phi_+^B + \nu_+ \phi_-^A \quad \forall \mathbf{r} \notin \mathcal{V}, \quad (\text{H.13b})$$

where \mathcal{V} denotes the droplet region and we defined $\nu_- = (k_c \psi_- + k_{AB}) / k_{BA}$ and $\nu_+ = k_{AB} / [(1 - \psi_-) k_{BA}]$. The boundary conditions for these equations follow from Eqs. (2.3)–(2.7) and read

$$D_B \partial_r \phi_-^B(\mathbf{r}) = -q \phi_-^A \quad \text{for } |\mathbf{r}| = a \quad (\text{H.14a})$$

$$\phi_-^B(\mathbf{r}) = \psi_- + \gamma \beta_- H(\mathbf{r}) \quad \text{for } \mathbf{r} \in \mathcal{A} \quad (\text{H.14b})$$

$$\phi_+^B(\mathbf{r}) = \psi_+ + \gamma \beta_+ H(\mathbf{r}) \quad \text{for } \mathbf{r} \in \mathcal{A} \quad (\text{H.14c})$$

$$\partial_r \phi_+^B(\mathbf{r}) = 0 \quad \text{for } |\mathbf{r}| = R_c, \quad (\text{H.14d})$$

where $q = Q / (4\pi a^2)$ and R_c is the system radius. The boundary conditions at the droplet surface depend on the mean curvature, similarly to Eqs. (A.9).

H.3 Volume fraction profiles in the perturbed droplet

The partial differential equations (H.13) are Helmholtz equations solved by

$$\phi_\pm^B(\mathbf{r}) = \nu_\pm \phi_-^A + \sum_{k=0}^{\infty} \tilde{f}_k(r) \cdot Y_k(\theta, \varphi), \quad (\text{H.15})$$

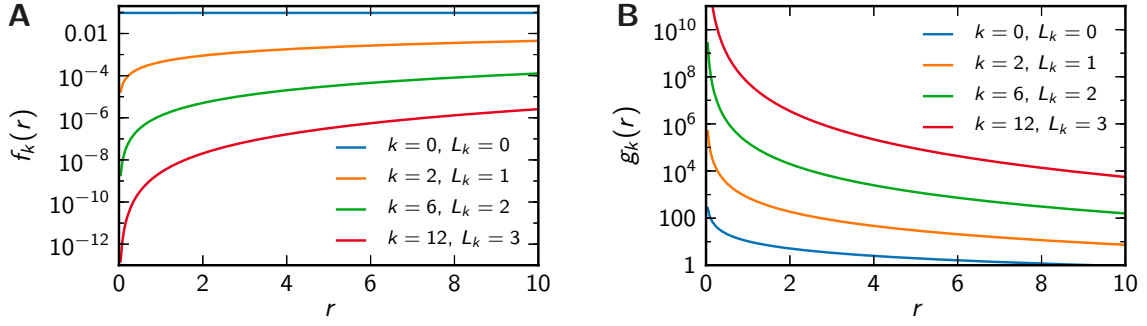


Figure H.1: Fundamental spatial solutions of the differential equation (H.13) for the inverse length scale $\lambda = \sqrt{k_{BA}/D_B} \approx 0.014 \mu\text{m}^{-1}$ used in the model.

leading to an ordinary differential equation for the fundamental spatial modes \tilde{f}_k ,

$$0 = \frac{D_B}{r^2} \frac{\partial}{\partial r} \left(r^2 \frac{\partial \tilde{f}_k(r)}{\partial r} \right) - \left(\frac{D_B l_k(l_k + 1)}{r^2} + k_{BA} \right) \tilde{f}_k(r). \quad (\text{H.16})$$

This second order equation is solved by $\tilde{f}_k(r) = A_k f_k(r) + B_k g_k(r)$, where

$$f_k(r) = \frac{1}{\sqrt{r}} I_{\frac{1}{2}+l_k} \left(r \sqrt{\frac{k_{BA}}{D_B}} \right) \quad \text{and} \quad g_k(r) = \frac{1}{\sqrt{r}} K_{\frac{1}{2}+l_k} \left(r \sqrt{\frac{k_{BA}}{D_B}} \right) \quad (\text{H.17})$$

are the fundamental solutions, see Fig. H.1, while A_k and B_k are coefficients that we determine later. Here, $I_n(x)$ and $K_n(x)$ are the modified Bessel functions [248]. The volume fraction of the droplet material,

$$\phi_{\pm}^B(\mathbf{r}) = \nu_{\pm} \phi_{\pm}^A + \sum_{k=0}^{\infty} (A_k^{\pm} f_k(r) + B_k^{\pm} g_k(r)) \cdot Y_k(\theta, \varphi), \quad (\text{H.18})$$

is thus a linear combination of the fundamental spatial solutions. The series coefficients A_k^{\pm} and B_k^{\pm} must be linear functions of the magnitudes of the perturbation,

$$A_k^{\pm} = \bar{A}_k^{\pm} + \sum_{K=0}^{\infty} \varepsilon_K \hat{A}_{kK}^{\pm} \quad \text{and} \quad B_k^{\pm} = \bar{B}_k^{\pm} + \sum_{K=0}^{\infty} \varepsilon_K \hat{B}_{kK}^{\pm}. \quad (\text{H.19})$$

Similarly, the volume fraction profiles of form A and B can be decomposed as

$$\phi_{\pm}^A = \bar{\phi}_{\pm}^A + \sum_{K=0}^{\infty} \varepsilon_K \hat{\phi}_{\pm,K}^A \quad \text{and} \quad \phi_{\pm}^B(\mathbf{r}) = \bar{\phi}_{\pm}^B(r) + \sum_{K=0}^{\infty} \varepsilon_K \hat{\phi}_{\pm,K}^B(\mathbf{r}). \quad (\text{H.20})$$

In general, bars denote stationary state quantities and hats indicate derivations therefrom, which depend on the perturbation mode K . The series coefficients,

\bar{A}_k^\pm , \hat{A}_{kK}^\pm , \bar{B}_k^\pm , and \hat{B}_{kK}^\pm , are determined by plugging Eq. (H.18) into the boundary conditions, Eqs. (H.14), and the conservation of material. The latter follows from Eq. (2.4) and reads

$$V_c \bar{\phi} = (V_c - V) \phi_+^A + V \phi_-^A + \int_{V_c} \phi^B(\mathbf{r}) d^3r. \quad (\text{H.21})$$

Additionally, the total integrated reaction flux must vanish in the stationary state,

$$0 = k_{BA} \int_{\text{cell}} \bar{\phi}^B(\mathbf{r}) d^3r - (\psi_- k_c + k_{AB}) \bar{V} \bar{\phi}_-^A - k_{AB} \cdot (V_c - \bar{V}) \bar{\phi}_+^A - Q \bar{\phi}_-^A. \quad (\text{H.22})$$

We now expand these conditions to linear order in the perturbations.

Boundary conditions: The boundary conditions at the core, Eq. (H.14a), yield

$$f'_k(a) \bar{A}_k^- + g'_k(a) \bar{B}_k^- = -\frac{2\sqrt{\pi}q}{D_B} \cdot \delta_{k0} \bar{\phi}_-^A \quad (\text{H.23a})$$

$$f'_k(a) \hat{A}_{kK}^- + g'_k(a) \hat{B}_{kK}^- = -\frac{2\sqrt{\pi}q}{D_B} \cdot \delta_{k0} \hat{\phi}_{-,K}^A, \quad (\text{H.23b})$$

where $k, K \in \mathbb{N}$. Equivalently, we get

$$f'_k(R_c) \bar{A}_k^+ + g'_k(R_c) \bar{B}_k^+ = 0 \quad (\text{H.24a})$$

$$f'_k(R_c) \hat{A}_{kK}^+ + g'_k(R_c) \hat{B}_{kK}^+ = 0 \quad (\text{H.24b})$$

for the outer system boundary, Eq. (H.14d).

Coexistence conditions at the droplet surface: Eq. (H.14b) leads to

$$\begin{aligned} & \sum_{k=0}^{\infty} \left(\left[A_k^- f_k(\bar{R}) + B_k^- g_k(\bar{R}) \right] \cdot \delta_{k'k} + \left[\bar{A}_k^- f'_k(\bar{R}) + \bar{B}_k^- g'_k(\bar{R}) \right] \cdot \sum_{K=0}^{\infty} \varepsilon_K C_{k'Kk} \right) \\ &= 2\sqrt{\pi} \delta_{k'0} \cdot \left(\psi_- + \frac{\gamma \beta_-}{\bar{R}} - \nu_- \cdot \left(\bar{\phi}_-^A + \sum_{K=0}^{\infty} \varepsilon_K \hat{\phi}_{-,K}^A \right) \right) + \frac{\gamma \beta_-}{\bar{R}^2} \varepsilon_{k'} h_{k'}. \end{aligned} \quad (\text{H.25})$$

which is one equation for each $k' \in \mathbb{N}$. Here, the $C_{k'Kk} = \mathcal{I}_{k'}[Y_K(\theta, \varphi) Y_k(\theta, \varphi)]$ are Clebsch-Gordan coefficients [247]. In particular, $C_{kK0} = \delta_{kK}/(2\sqrt{\pi})$. Furthermore, \bar{A}_k and \bar{B}_k vanish for $k \geq 1$ due to the spherical symmetry, reducing Eq. (H.25) to

$$\begin{aligned} & \hat{A}_{k'K}^- f_{k'}(\bar{R}) + \hat{B}_{k'K}^- g_{k'}(\bar{R}) + \left[\bar{A}_0^- f'_0(\bar{R}) + \bar{B}_0^- g'_0(\bar{R}) \right] \cdot \frac{\delta_{k'K}}{2\sqrt{\pi}} \\ &= \frac{\gamma \beta_-}{\bar{R}^2} h_{k'} \delta_{k'K} - 2\sqrt{\pi} \nu_- \hat{\phi}_{-,K}^A \cdot \delta_{k'0}. \end{aligned} \quad (\text{H.26})$$

The analogous equation (H.14c) right outside of the droplet surface follows analogously. Taken together with Eqs. (H.23), we find that the perturbations \hat{A}_{kK}^- and \hat{B}_{kK}^- are diagonal matrices. We thus use a simplified notation, $\hat{A}_{kK}^\pm = \hat{A}_k^\pm \delta_{kK}$ and $\hat{B}_{kK}^\pm = \hat{B}_k^\pm \delta_{kK}$. In summary, Eqs. (H.23), (H.24), and (H.26) completely define the series coefficients for the profile of the droplet material if the values $\bar{\phi}_-^A$, $\hat{\phi}_{-,K}^A$, and \bar{R} are known.

Global conditions on the volume fractions: The material conservation, Eq. (H.21), and the total reaction flux at the stationary state, Eq. (H.22), contain the integral

$$\int_{V_c} \phi^B d^3r = \int_0^{2\pi} d\varphi \int_0^\pi d\theta \sin \theta \left\{ \int_a^{R(\theta,\varphi)} \phi_-^B r^2 dr + \int_{R(\theta,\varphi)}^{R_c} \phi_+^B r^2 dr \right\}. \quad (\text{H.27})$$

Expanding the first term in the bracket to linear order in ε , we get

$$\int_a^{R(\theta,\varphi)} \phi_-^B(r, \theta, \varphi) r^2 dr \approx \int_a^{\bar{R}} \phi_-^B(r, \theta, \varphi) r^2 dr + \int_{\bar{R}}^{R(\theta,\varphi)} \bar{\phi}_-^B(r) r^2 dr. \quad (\text{H.28})$$

Using a Taylor expansion, the integral over the shape deviations becomes

$$\int_0^{2\pi} d\varphi \int_0^\pi d\theta \sin \theta \int_{\bar{R}}^{R(\theta,\varphi)} \bar{\phi}_-^B(r) r^2 dr \approx \varepsilon_0 \bar{R}^2 \bar{\phi}_-^B(\bar{R}). \quad (\text{H.29})$$

We abbreviate the integrals over the basis functions,

$$F_0^- = 2\sqrt{\pi} \int_a^{\bar{R}} f_0(r) r^2 dr, \quad F_0^+ = 2\sqrt{\pi} \int_{\bar{R}}^{R_c} f_0(r) r^2 dr, \quad (\text{H.30a})$$

$$G_0^- = 2\sqrt{\pi} \int_a^{\bar{R}} g_0(r) r^2 dr, \quad \text{and} \quad G_0^+ = 2\sqrt{\pi} \int_{\bar{R}}^{R_c} g_0(r) r^2 dr, \quad (\text{H.30b})$$

to write the first term of Eq. (H.27) as

$$\begin{aligned} & \int_0^{2\pi} d\varphi \int_0^\pi d\theta \sin \theta \int_a^{R(\theta,\varphi)} dr r^2 \phi_-^B(r, \theta, \varphi) \\ & \approx \nu_- \phi_-^A \bar{V} + A_0^- F_0^- + B_0^- G_0^- + [2\sqrt{\pi} \nu_- \bar{\phi}_-^A + \bar{A}_0^- f_0(\bar{R}) + \bar{B}_0^- g_0(\bar{R})] \varepsilon_0 \bar{R}^2. \end{aligned} \quad (\text{H.31})$$

The second term of Eq. (H.27) follows analogously, and Eq. (H.21) becomes

$$\begin{aligned} V_c \bar{\phi} = & \left[\left(\frac{1 - \psi_+}{1 - \psi_-} + \nu_+ \right) V_c + \left(\nu_- + \frac{\psi_+ - \psi_-}{1 - \psi_-} - \nu_+ \right) \bar{V} + \left(\frac{\psi_+ - \psi_-}{1 - \psi_-} \right) \varepsilon_0 \hat{V} \right] \phi_-^A \\ & + \bar{R}^2 \varepsilon_0 \cdot \left[2\sqrt{\pi} (\nu_- - \nu_+) \bar{\phi}_-^A + (\bar{A}_0^- - \bar{A}_0^+) f_0(\bar{R}) + (\bar{B}_0^- - \bar{B}_0^+) g_0(\bar{R}) \right] \\ & + A_0^- F_0^- + B_0^- G_0^- + A_0^+ F_0^+ + B_0^+ G_0^+, \end{aligned} \quad (\text{H.32})$$

Because the perturbations ε_k can be arbitrary, the above equations must hold for all values of ε . This allows us to separate the terms without any ε_k ,

$$V_c \bar{\phi} = (\Xi_c V_c + \Xi \bar{V}) \cdot \bar{\phi}_-^A + \bar{A}_0^- F_0^- + \bar{B}_0^- G_0^- + \bar{A}_0^+ F_0^+ + \bar{B}_0^+ G_0^+ , \quad (\text{H.33})$$

from the terms containing ε_0 ,

$$\begin{aligned} 0 = & \Xi_c V_c \hat{\phi}_{-,0}^A + \Xi \bar{V} \hat{\phi}_{-,0}^A + \hat{A}_{0,0}^- F_0^- + \hat{B}_{0,0}^- G_0^- + \hat{A}_{0,0}^+ F_0^+ + \hat{B}_{0,0}^+ G_0^+ \\ & + \Xi \bar{\phi}_-^A \hat{V} + \bar{R}^2 \cdot \left[(\bar{A}_0^- - \bar{A}_0^+) f_0(\bar{R}) + (\bar{B}_0^- - \bar{B}_0^+) g_0(\bar{R}) \right] , \end{aligned} \quad (\text{H.34})$$

and the ones containing ε_k with $k \geq 1$,

$$0 = (\Xi_c V_c + \Xi \bar{V}) \cdot \hat{\phi}_{-,k}^A , \quad (\text{H.35})$$

where $\Xi_c = \nu_+ + (1 - \psi_+)/ (1 - \psi_-)$ and $\Xi = 1 + \nu_- - \nu_+ - (1 - \psi_+)/ (1 - \psi_-)$. Using Eq. (H.35), we find that $\hat{\phi}_{-,k}^A$ vanishes for $k \geq 1$, which is consistent with the idea that these perturbations do not influence the droplet volume, see Eq. (H.6). Furthermore, the condition that the integrated reaction flux vanish in the stationary state, see Eq. (H.22), yields

$$\frac{Q}{k_{BA}} \cdot \bar{\phi}_-^A = \bar{A}_0^- F_0^- + \bar{B}_0^- G_0^- + \bar{A}_0^+ F_0^+ + \bar{B}_0^+ G_0^+ . \quad (\text{H.36})$$

The droplet radius \bar{R} and the fractions $\bar{\phi}_-^A$ and $\hat{\phi}_{-,k}^A$ of the building blocks are then obtained by solving Eqs. (H.33)–(H.36).

Resulting stationary state conditions: The stationary state values are obtained from the above equations by setting $\varepsilon = \mathbf{0}$. This leads to a system of linear equations for the five unknowns \bar{A}_0^\pm , \bar{B}_0^\pm , and $\bar{\phi}_-^A$, which reads

$$\bar{A}_0^- f_0'(a) + \bar{B}_0^- g_0'(a) + \bar{\phi}_-^A \cdot \frac{2\sqrt{\pi}q}{D_B} = 0 \quad (\text{H.37a})$$

$$\bar{A}_0^- f_0(\bar{R}) + \bar{B}_0^- g_0(\bar{R}) + 2\sqrt{\pi}\nu_- \bar{\phi}_-^A = 2\sqrt{\pi} \left(\psi_- + \frac{\gamma\beta_-}{\bar{R}} \right) \quad (\text{H.37b})$$

$$\bar{A}_0^+ f_0'(R_c) + \bar{B}_0^+ g_0'(R_c) = 0 \quad (\text{H.37c})$$

$$\bar{A}_0^+ f_0(\bar{R}) + \bar{B}_0^+ g_0(\bar{R}) + 2\sqrt{\pi}\nu_+ \bar{\phi}_-^A = 2\sqrt{\pi} \left(\psi_+ + \frac{\gamma\beta_+}{\bar{R}} \right) \quad (\text{H.37d})$$

$$\bar{A}_0^- F_0^- + \bar{B}_0^- G_0^- + \bar{A}_0^+ F_0^+ + \bar{B}_0^+ G_0^+ - \frac{Q}{k_{BA}} \bar{\phi}_-^A = 0 . \quad (\text{H.37e})$$

The solution can be obtained analytically, but they are complicated and therefore omitted here.

Conditions for the perturbations of the volume fraction profiles: The series coefficients of the perturbations, \hat{A}_k^\pm , \hat{B}_k^\pm , and $\hat{\phi}_{-,0}^A$, are obtained by matching terms with the same power in ε_k . The resulting system of linear equations reads

$$\hat{A}_k^- f'_k(a) + \hat{B}_k^- g'_k(a) + \hat{\phi}_{-,0}^A \cdot \frac{2\sqrt{\pi}q}{D_B} \cdot \delta_{k0} = 0 \quad (\text{H.38a})$$

$$\hat{A}_k^- f_k(\bar{R}) + \hat{B}_k^- g_k(\bar{R}) + 2\sqrt{\pi}\nu_- \hat{\phi}_{-,0}^A \cdot \delta_{k0} = \frac{\gamma\beta_-}{\bar{R}^2} h_k - \frac{\bar{A}_0^- f'_0(\bar{R}) + \bar{B}_0^- g'_0(\bar{R})}{2\sqrt{\pi}} \quad (\text{H.38b})$$

$$\hat{A}_k^+ f_k(\bar{R}) + \hat{B}_k^+ g_k(\bar{R}) + 2\sqrt{\pi}\nu_+ \hat{\phi}_{-,0}^A \cdot \delta_{k0} = \frac{\gamma\beta_+}{\bar{R}^2} h_k - \frac{\bar{A}_0^+ f'_0(\bar{R}) + \bar{B}_0^+ g'_0(\bar{R})}{2\sqrt{\pi}} \quad (\text{H.38c})$$

$$\hat{A}_k^+ f'_k(R_c) + \hat{B}_k^+ g'_k(R_c) = 0, \quad (\text{H.38d})$$

$$\begin{aligned} \hat{A}_0^- F_0^- + \hat{B}_0^- G_0^- + \hat{A}_0^+ F_0^+ + \hat{B}_0^+ G_0^+ + (\Xi_c V_c + \Xi \bar{V}) \hat{\phi}_{-,0}^A \\ = \bar{R}^2 \cdot \left[(\bar{A}_0^+ - \bar{A}_0^-) f_0(\bar{R}) + (\bar{B}_0^+ - \bar{B}_0^-) g_0(\bar{R}) \right] - \Xi \bar{V} \hat{\phi}_-^A, \end{aligned} \quad (\text{H.38e})$$

where we used the fact that the droplet volume is only affected by the isotropic perturbation mode, see Eq. (H.6). The Eqs. (H.38) hold for each $k \in \mathbb{N}$, giving rise to solutions for the unknowns \hat{A}_k^\pm , \hat{B}_k^\pm , and $\hat{\phi}_{-,0}^A$. Note that these equations contain the stationary state series coefficients, which therefore have to be calculated first.

H.4 Perturbation growth rates

The dynamical equation (H.12) together with the definition of the droplet surface, Eq. (H.5), lead to the evolution equation for the perturbations,

$$\partial_t \varepsilon_k = \frac{D_B}{\psi_- - \psi_+} \cdot \mathcal{I}_k \left[\partial_r \phi_+^B(R(\theta, \varphi), \theta, \varphi) - \partial_r \phi_-^B(R(\theta, \varphi), \theta, \varphi) \right]. \quad (\text{H.39})$$

The right hand side of this equation is linear in ε . It turns out that the different modes do not interact, i.e. the right hand side of Eq. (H.39) only depends on ε_k . Consequently, the perturbations evolve exponentially, $\varepsilon_k(t) = \varepsilon_k(0) \cdot e^{\lambda_k t}$, defining the perturbation growth rates λ_k . Inserting the volume fraction profile given in Eq. (H.18) into Eq. (H.39), we arrive at an implicit condition for the λ_k , which reads

$$\begin{aligned} \lambda_k = \frac{D_B}{\psi_- - \psi_+} \cdot \left(\left(\hat{A}_k^+ - \hat{A}_k^- \right) f'_k(\bar{R}) + \left(\hat{B}_k^+ - \hat{B}_k^- \right) g'_k(\bar{R}) \right. \\ \left. + \frac{1}{2\sqrt{\pi}} \cdot \left[(\bar{A}_0^+ - \bar{A}_0^-) f''_0(\bar{R}) + (\bar{B}_0^+ - \bar{B}_0^-) g''_0(\bar{R}) \right] \right). \end{aligned} \quad (\text{H.40})$$

Note that growth rates λ_k only depend on the degree of the perturbation $l = \lfloor \sqrt{k} \rfloor$. This is because both the curvature of the droplet surface, see Eq. (H.11), and the fundamental solutions of the volume fractions, see Eq. (H.17), are independent of

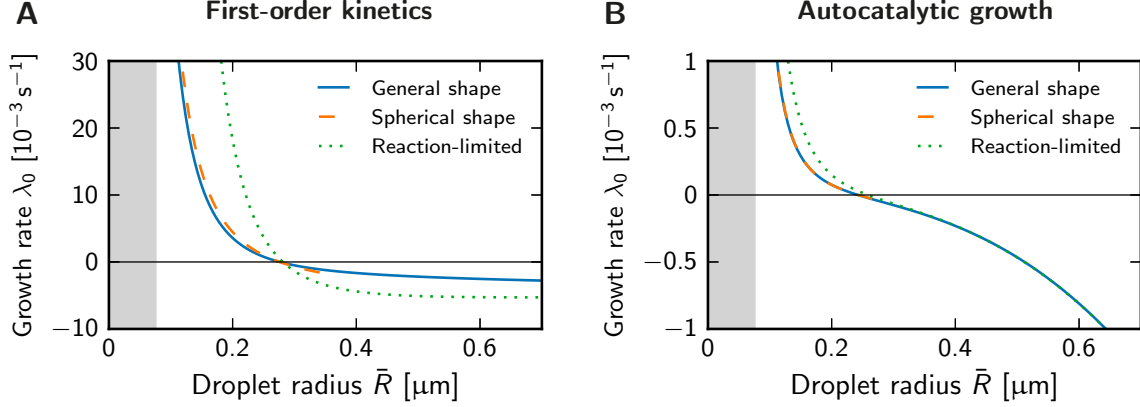


Figure H.2: Growth rate λ_0 of perturbations preserving spherical symmetry as a function of the droplet radius \bar{R} calculated in three different approximations: for general distortions described by spherical harmonics (blue solid line, this appendix), for a spherical droplet with the full dynamics of the volume fractions (orange dashed line, see Section 3.2), and for the reaction-limited case (green dotted line, see Section 2.2). **(A)** First-order kinetics with parameters given in Fig. 2.3. **(B)** Autocatalytic growth with parameters given in Fig. 2.4. The stationary state radius \bar{R} is varied by adjusting $\bar{\phi}$. Grey areas mark the region of the passive core with $Q = 0$.

the order m_k . The growth rates given in Eq. (H.40) allow us to define the speed of each interface point, $v = \partial_t R$, which reads

$$v(\theta, \varphi) = \sum_{k=0}^{\infty} \lambda_k \varepsilon_k Y_k(\theta, \varphi) . \quad (\text{H.41})$$

We verify the calculations of this section by relating the growth rates of isotropic perturbations, $k = 0$, to the spherical symmetric perturbation analysis of Section 3.2. Fig. H.2 shows the associated perturbation growth rates as a function of the droplet radius. The curves generally agree very well, compare the blue solid and the orange dashed line. We attribute the small deviations to the fact that we consider the limit of fast diffusion of the building blocks in this section. Additionally, we show the perturbation growth rates of a reaction-limited model, where we also consider fast diffusion of the droplet material, see green dotted line in Fig. H.2. Here, the deviations are larger, but the transition point, where the system switches from an unstable to a stable configuration, is well captured by all three cases. The verification presented here obviously only confirms the correctness for the isotropic case, $k = 0$, but since this requires the most sophisticated calculation and the other cases use the same formulas, we trust the result for all k .

I Multiple droplets with gradients inside droplets

The model of multiple droplets presented in Section 4.1 considers the simplified case of homogeneous distributions of building blocks within droplets. Here, we test whether this approximation is also applicable in the autocatalytic scenario, where soluble building blocks entering the droplet have a high propensity to get converted to droplet material. This generally leads to a dilution of building blocks away from the droplet surface and may thus impair the effect of the catalytic core.

In this section, we extend the approximate model introduced in Section 4.1 to also take into account the spatial distribution of components inside droplets. For simplicity, we consider a spherical geometry for each droplet and assume that the distributions $\phi^A(r)$ and $\phi^B(r)$ are in stationary state. They are thus determined by the Eqs. (2.1) with vanishing time derivatives. Adding these two equations, we retrieve $0 = \partial_r j$ with the local flux $j = -D_A \partial_r \phi^A - D_B \partial_r \phi^B$, where j vanishes both at the cores and at the system boundary. j is therefore zero everywhere and we use this property to relate the two profiles, $D_A \phi^A(r) + D_B \phi^B(r) = D_A \phi_-^A(R) + D_B \psi_-$, where we integrated j once and derived the right hand side using the fractions at the inner droplet surface, which read $\phi_-^A(R) \approx (1 - \psi_-) \phi_0^A$ and $\phi_-^B \approx \psi_-$, respectively. Using this relation between the volume fractions, we get a single reaction-diffusion equation for the fraction of the soluble building blocks, which reads

$$0 = \frac{D_A}{r^2} \frac{\partial}{\partial r} (r^2 \partial_r \phi^A(r)) - k_- \phi^A(r) + \left(\psi_- + \frac{D_A}{D_B} \phi_-^A(R) \right) k_{BA}, \quad (\text{I.1})$$

where $k_- = k_c \psi_- + k_{AB} + k_{BA} D_A / D_B$ and we used the linearization presented in Eq. (3.1). The associated boundary conditions read $D_A \partial_r \phi^A(r)|_{r=a} = q \phi^A(a)$ and $\phi^A(R) = \phi_-^A(R)$, where $q = Q/(4\pi a^2)$. The solution to this ordinary differential equation evaluated at the surface of the core reads

$$\begin{aligned} \phi^A(a) = & \frac{2D_A e^{(a+R)\alpha_-^A}}{D_B k_- \cdot \left(e^{2R\alpha_-^A} [D_A + aq + aD_A \alpha_-^A] - e^{2a\alpha_-^A} [D_A + aq - aD_A \alpha_-^A] \right)} \\ & \cdot \left[k_{BA} \cdot (D_A \phi_-^A(R) + D_B \psi_-) (a\alpha_-^A \cosh[(a-R)\alpha_-^A] - \sinh[(a-R)\alpha_-^A]) \right. \\ & \left. + R\alpha_-^A \cdot ((D_B k_- - D_A k_{BA}) \phi_-^A(R) - D_B k_{BA} \psi_-) \right], \quad (\text{I.2}) \end{aligned}$$

where $\alpha_-^A = \sqrt{k_- / D_A}$. Fig. I.1A shows $\phi^A(a)$ as a function of the droplet radius R . Apparently, the fraction of building blocks at the core is reduced due to the gradients inside the droplet. However, this reduction is small for the standard parameters given in Table 6.2, although it depends strongly on the diffusion constant D_A of the building blocks, which directly enters the decay constant α_-^A of the exponential functions in Eq. (I.2). We therefore also show $\phi^A(a)$ for a reduced diffusivity, $D_A = 1 \mu\text{m}^3/\text{s}$, using dashed lines in Fig. I.1A. Clearly, the reduction of the volume fraction of building

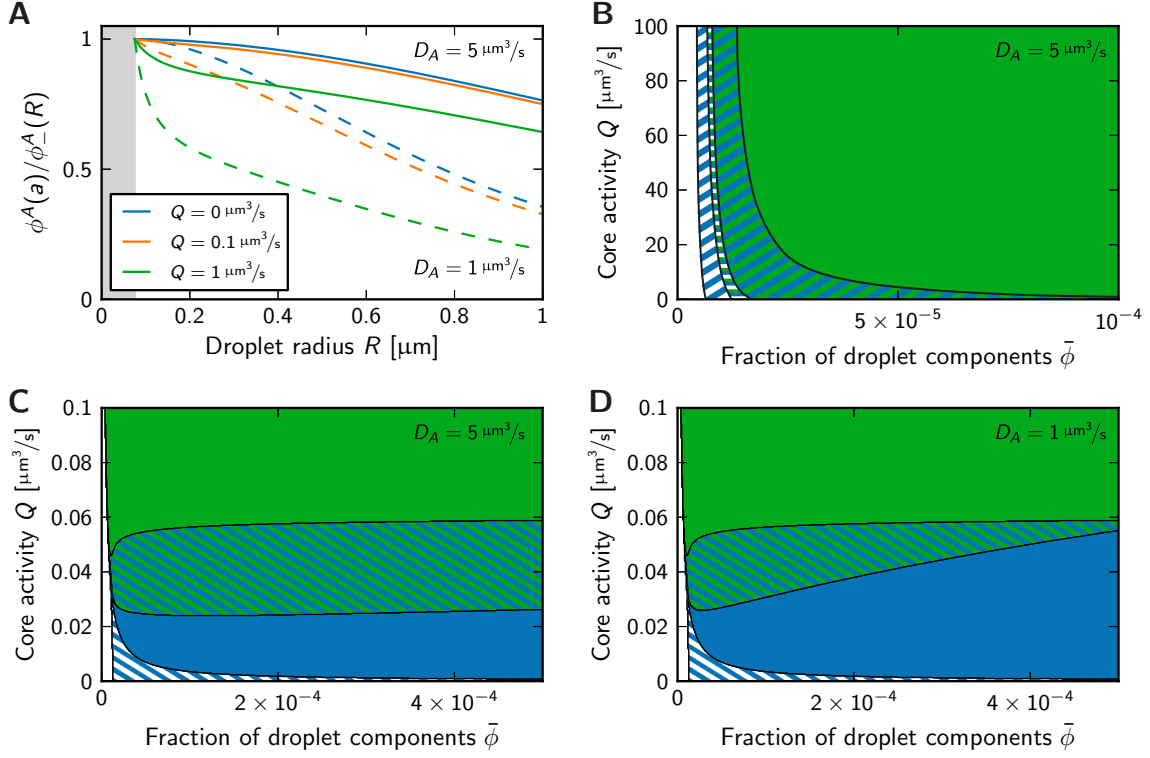


Figure I.1: Approximate model with gradients inside the droplets. **(A)** Fraction $\phi^A(a)$ of building blocks at the core normalized to the value ϕ_-^A close to the surface as a function of the droplet radius R for diffusivities $D_A = 5 \mu\text{m}^3/\text{s}$ (solid lines) and $D_A = 1 \mu\text{m}^3/\text{s}$ (dashed lines). **(B–D)** Stability diagrams showing regions with no droplets (white region), one stable droplet (blue region), and two stable droplets (green region). Regions with multistability are drawn in a hatched style with colors corresponding to the possible stable states. The model parameters of (B) first-order kinetics and (A, C, D) autocatalytic growth are given in Fig. 2.3 and Fig. 2.4, respectively.

blocks at the core is now stronger than in the case for the standard diffusivity. Since the diffusivity inside centrosomes has not been measured and it is quite reasonable to assume that it is lower there [86], we use the arbitrarily reduced diffusivity $D_A = 1 \mu\text{m}^3/\text{s}$ to discuss the effect of gradients on the droplet stability.

We repeat the stability analysis presented in Section 4.4 using the reduced concentration profiles of the soluble building blocks obtained in this section. Fig. I.1 shows the results for both scenarios A and B and for different diffusivities D_A . Apparently, multiple droplets can still be stable in all cases, but the stability thresholds are shifted with respect to the simplified model discussed in the main text, e.g. compare Fig. I.1D to Fig. 4.8F. All in all, accounting for the diffusion profile within the droplets changes the results quantitatively, but multiple droplets can still be stable and the qualitative conclusions drawn in Section 4.4 thus still hold.

J Numerical stability analysis of multiple droplets

The dynamics of multiple droplets are captured by a system of ordinary differential equations, see Section 4.1. In a stationary state of such a system all proper droplets must have the same volume, since otherwise there would be a flux of material between the droplets, see Section 4.3. We can thus generally classify stationary states configurations by the number m_1 of proper droplets with volume V and consequently $m_0 = m - m_1$ bare cores without surrounding droplet material. For example, in the case of two cores in a common system, there are three possible stationary configurations: $\mathbf{V}^{(0)} = \{0, 0\}$, $\mathbf{V}^{(1)} = \{V, 0\}$, and $\mathbf{V}^{(2)} = \{V, V\}$. We then

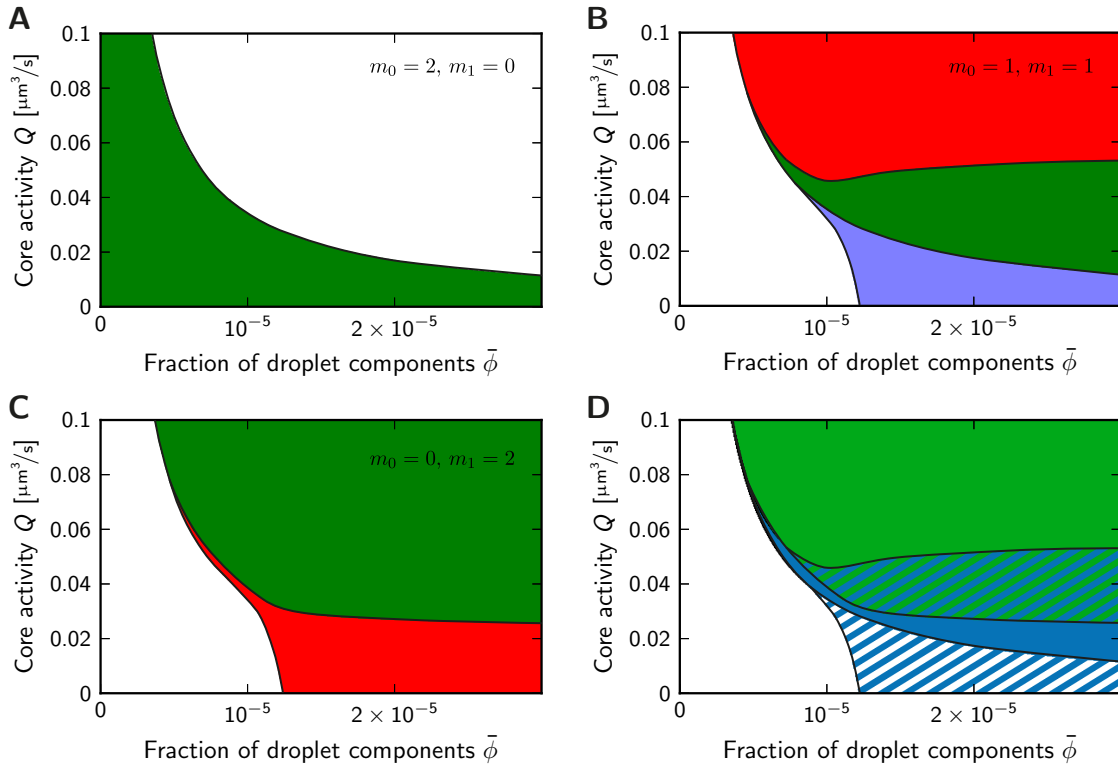


Figure J.1: Stability diagrams of at most two droplets forming in the autocatalytic scenario. The catalytic activity Q of the cores and the fraction $\bar{\phi}$ of droplet material are varied. **(A–C)** Stability of $m_1 = 0, 1, 2$ proper droplets, which are either stable (green), unstable (red), or have both stable and unstable solutions (blue). No stationary states exist in the white regions. **(D)** Combined result of panels A–C (identical to Fig. 4.8B). Here, two bare cores (white region), a single droplet (blue region), or two droplets (green region) can be stable. Regions with multistability are drawn in a hatched style with colors corresponding to the possible states. In all panels, the model parameters are taken from Fig. 2.4.

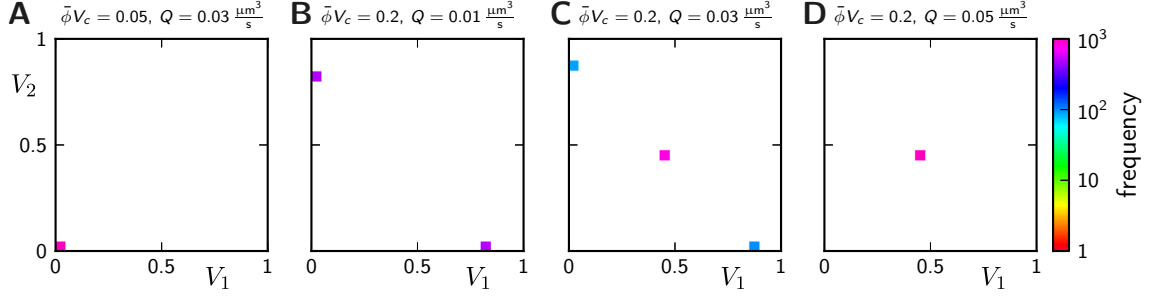


Figure J.2: Histograms of stationary droplet volumes obtained from numerical simulations of two droplets. For each panel, 10^3 simulations with random initial conditions were performed and the final volumes V_1 and V_2 of the two droplets were recorded. All panels share the same ordinate and the model parameters of the autocatalytic growth given in Fig. 2.4 are used. The total amount of material $\bar{\phi}V_c$ and the catalytic activity Q were modified as indicated to highlight common scenarios: **(A)** no droplets; **(B)** a single droplet and a bare core; **(C)** a multistable state with either a single or two droplets; **(D)** a pair of droplets.

determine their stability by numerically calculating the eigenvalues of the associated Jacobian given by Eq. (4.7). This procedure is performed for all possible droplet configurations, see panels A–C of Fig. J.1. We thus identify regions of parameter values where different number of droplets can be stable. By using different colors for these states, the results can be summarized in a single stability diagram, see Fig. J.1D.

We also present an alternative way of determining stability diagrams, which relies on the numerical solution of the evolution equation (4.1). Here, we randomly choose the initial droplet volumes $V_i(t=0)$ from the interval $[0, V_{\max}]$ with $V_{\max} = \bar{\phi}V_c/(m\psi_-)$. For each parameter point investigated, we simulate 10^3 trajectories with different initial conditions for a duration of 10^7 s. We record the final droplet volumes corresponding to stationary states and summarize these data in histograms like the ones shown in Fig. J.2. The clusters in these histograms are then classified according to the number of proper droplets they contain. This procedure allows us to determine the possible stationary state configurations for each parameter point, which we then plot in a stability diagram, see Fig. 4.10.

K Numerical implementation of the stochastic model

We developed a stochastic version of our active droplet model in Chapter 5. For simplicity, we neglect the creation of droplet material in the solvent, $k_{AB} = 0$, ignore surface tension effects, $\gamma = 0$, and consider strong phase separation, $\psi_+ = 0$, which abolishes droplet material in the solvent. Consequently, the state variables of the system are the number N_i^B of B particles inside droplet i and the positions \mathbf{x}_j of A particles, where $j = 1, \dots, N_A$. Here, we give detailed information on the numerical implementation, which is summarized in the illustration Algorithm A.

Diffusion of A particles: We simulate the diffusion of A particles using Brownian dynamics [249, 250], where we discretize time with a constant time step Δt , which is a parameter of the algorithm. At each time step, the position $\mathbf{x}_j = (x_j, y_j, z_j)^\top$ of the j -th particle is changed by a random amount,

$$\mathbf{x}_j(t + \Delta t) = \mathbf{x}_j(t) + \Delta \mathbf{x}_j(\Delta t) , \quad (\text{K.1})$$

where $\Delta \mathbf{x}_j$ is a vector of three random variable chosen from the step size distribution,

$$P(\Delta x; \Delta t) = \frac{1}{\sqrt{4\pi D_A \Delta t}} e^{-\frac{\Delta x^2}{4D_A \Delta t}} , \quad (\text{K.2})$$

which depends on Δt and the diffusivity D_A [215]. The standard deviation of this distribution sets the typical step size $\sigma_P = \sqrt{2D_A \Delta t}$. Due to the no-flux condition at the system boundary, this stepping scheme must be modified there. We approximate the boundary by a plane, since its radius of curvature is much larger than σ_P . The associated probability distribution of step sizes can be determined analytically [251]. In the one-dimensional case with a boundary at $x = x_0$, it reads

$$P_{\text{wall}}(\Delta x|x_0; \Delta t) = P(\Delta x; \Delta t) + P(2x_0 - \Delta x; \Delta t) , \quad (\text{K.3})$$

where $\Delta x \leq x_0$ [251]. This solution can be interpreted as placing a mirror particle on the opposite side of the boundary, which can be generalized to higher dimension. However, we avoid the required geometrical calculations by using an alternative stepping scheme, where we reject a step if a particle would move out of the system, see lines 3–10 in Algorithm A. This is equivalent to replacing the second term on the right hand side of Eq. (K.3) by a Dirac delta function with an appropriate weight,

$$\tilde{P}_{\text{wall}}(\Delta x|x_0; \Delta t) = P(\Delta x; \Delta t) + \delta(\Delta x) \int_{x_0}^{\infty} P(x'; \Delta t) dx' , \quad (\text{K.4})$$

where again $\Delta x \leq x_0$. This expression obeys detailed balance in equilibrium, but it reduces the diffusion constant in a layer of thickness σ_P near the boundary, which is unimportant for our results, since the droplets are far away from the boundary.

```

Data: model parameters and initial droplet configuration
Result: droplet volumes  $V_i$  over time  $t$ 

1 initialization of particle positions and types;
2 while  $t < t_{\text{end}}$  do
3   foreach particle  $A$  do
4     try a step of the random walk with time step  $\Delta t$ ;
5     if new position is inside the system then
6       place particle at new position;
7     else
8       keep particle at old position;
9     end
10  end
11  foreach droplet  $i$  do
12    foreach particle  $A$  inside droplet  $i$  do
13      if  $\text{UniformRandom}(0, 1) < k\Delta t$  then      //  $A \rightarrow B$  in droplet
14        increase  $N_i^B$  by one;
15        turn particle into type  $B$ ;
16      end
17      if particle inside core of droplet  $i$  and
18         $\text{UniformRandom}(0, 1) < k_Q\Delta t$  then    //  $A \rightarrow B$  at core
19        increase  $N_i^B$  by one;
20        turn particle into type  $B$ ;
21      end
22    end
23    foreach particle  $B$  inside droplet  $i$  do
24      if  $\text{UniformRandom}(0, 1) < k_{BA}\Delta t$  then //  $B \rightarrow A$  in droplet
25        decrease  $N_i^B$  by one;
26        turn particle into type  $A$ ;
27        choose position of particle randomly within droplet  $i$ ;
28      end
29    end
30    calculate droplet volume  $V_i$  based on  $N_i^B$ ;
31  end
32   $t = t + \Delta t$ ;
33 end

```

Algorithm A: Summarized logic of the stochastic simulations. In this pseudocode, $\text{UniformRandom}(0, 1)$ denotes a function that returns a pseudo random number chosen from the uniform distribution over the interval $[0, 1)$.

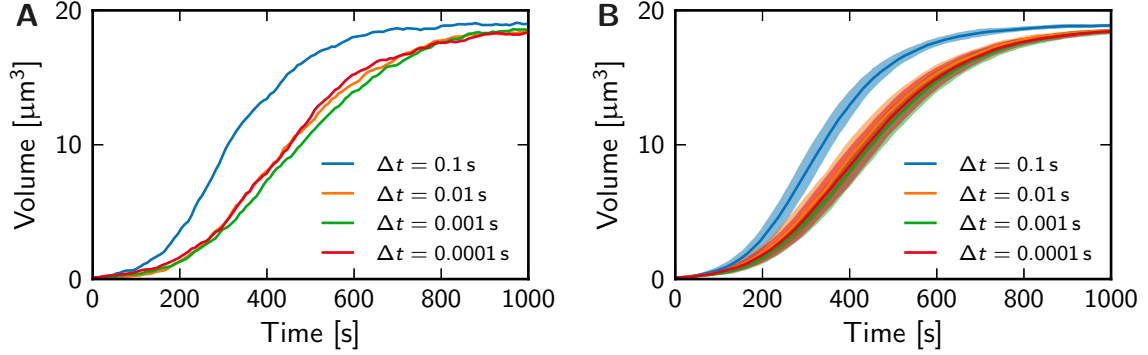


Figure K.1: Droplet volume as a function of time for different time steps Δt in the stochastic model with $N = 1\,000$ particles. **(A)** Single realizations. **(B)** Ensemble average of 32 independent runs (line: mean volume; shaded areas: mean \pm standard deviation).

Chemical reactions: The autocatalytic reaction catalyzes the production of droplet material B from soluble building blocks A inside the droplet. The probability to turn a single A particle into the B form during a time step Δt is approximated by $k\Delta t$, where $k = \psi_- k_c$ is the associated rate constant. This transition is implemented by comparing $k\Delta t$ to a random number chosen uniformly from the interval $[0, 1)$, see lines 13–16 of Algorithm A, and thus only works reliably if $\Delta t \ll k^{-1}$. The catalytic activity of the cores is implemented similarly, where we allow particles to diffuse into the core of volume $V_a = 4\pi a^3/3$ where they become B particles with probability $k_Q\Delta t$, see lines 17–20 in Algorithm A. Here, $k_Q = Q/V_a$ is the associated rate constant, where Q parameterizes the core activity.

Likewise, each B particle can become an A particle with rate k_{BA} , see lines 23–27 in Algorithm A. After the reaction occurred, we also assign a random position within the droplet, since we do not keep track of the position of B particles.

Choosing the optimal time step: The run time required to simulate Algorithm A scales linearly both with the number N of particles and with the inverse time step Δt^{-1} if we simulate the system for a fixed duration t_{end} . Here, a single computation step is given by the lines 2–31 in Algorithm A. To minimize the run time, it is therefore advisable to choose large time steps. However, the diffusing particles only sample space fine enough if $\Delta t \lesssim a^2/D_A$, where the radius a of the core marks the smallest length scale in the system. Additionally, the chemical reactions are only simulated correctly if $\Delta t \ll k_Q^{-1}$, where k_Q is assumed to be the largest reaction rate constant. Taken together, we thus get $\Delta t \lesssim 1$ ms using the parameters of the autocatalytic scenario from Table 6.2. Using $\Delta t = 1$ ms gives reasonable growth curves, see Fig. K.1, and we thus use it for all simulations shown in this thesis.

Nomenclature

This is a list of important symbols and abbreviations used in this thesis:

A	Surface area of a droplet; $A = 4\pi R^2$ for a spherical shape
a	Size of the core (the centrioles) located at the center of the droplet, page 31
D	Diffusion constant, page 29
F	Helmholtz free energy, page 14
f	Helmholtz free energy density
J	Integrated material flux, page 31
k_{AB}	Rate constant for the chemical reaction $A \rightarrow B$, page 29
k_B	Boltzmann constant, $k_B \approx 1.38 \times 10^{-23}$ J/K, page 12
k_{BA}	Rate constant for the chemical reaction $B \rightarrow A$, page 29
k_c	Rate constant for the chemical reaction $A + B \rightarrow 2B$, page 29
m	Number of droplets in the system, page 35
N	Total number of molecules
n	Number density, page 12
NEBD	<u>N</u> uclear <u>e</u> nvelope <u>b</u> reak <u>d</u> own; time cue used to align data, page 104
\mathbf{n}	Surface normal vector, page 30
p	Pressure, page 17
$P(x; y)$	Probability distribution of x given y
PCM	<u>P</u> ericentriolar <u>m</u> aterial; surrounds centrioles to define centrosomes, page 7
Q	Strength of the catalytic activity at the core (the centrioles), page 31
(r, θ, φ)	Spherical coordinate system, see Eq. (H.1), page 140
R	Droplet radius

RNAi	RNA interference; reduces the amount of a specific protein in a cell, page 4
S	Entropy, page 19
T	Temperature
t	Time
V	Droplet volume; $V = 4\pi R^3/3$ for a spherical shape
V_c	System (cell) volume
(x, y, z)	Cartesian coordinate system, page 140
$Y_{L,M}$	Real spherical harmonic function with degree L and order M , page 58
α	Inverse length scale, e.g. for solving diffusion equations, page 41
β_-, β_+	Sensitivity parameters determining the influence of surface tension onto the coexisting volume fractions at the interface, page 18
χ^2	Squared residual quantifying the difference between the model and experimental data, page 109
$\delta(x)$	Delta-distribution, which is only non-zero if $x = 0$, page 24
Δt	Time step in numerical simulations, page 92
ϕ	Volume fraction given by $\phi = \nu n$, page 12
$\bar{\phi}$	Average fraction of droplet components in the system, page 15
γ	Surface tension, page 14
λ	Growth rate (of a droplet or of a perturbation)
$\tilde{\mu}$	Derivative of the free energy density f with respect to the volume fraction ϕ . Here, $\mu = \nu\tilde{\mu}$ is the chemical potential, page 15
ν	Molecular volume, page 12
Π	Laplace pressure, $\Pi = 2\gamma/R$ for a spherical droplet of radius R , page 17
τ	Droplet growth time scale, page 41
ψ_-, ψ_+	Coexisting volume fractions at a flat interface between two phases, page 18

List of Figures

1.1	Internal organization of a cell	2
1.2	Anatomy of the model organism <i>Caenorhabditis elegans</i>	3
1.3	Role of centrosomes in cells	4
1.4	Schematic lifecycle of centrosomes	5
1.5	Electron micrographs of centrioles	6
1.6	Structure of a centrosome	8
1.7	Examples of organelles without a membrane	10
1.8	Free energy density of a binary fluid	12
1.9	Phase diagram of a binary mixture	13
1.10	Droplet formation by phase separation	14
1.11	Free energy of the system with a single droplet	16
1.12	Maxwell construction to solve the coexistence conditions	18
1.13	Pattern formation by phase separation and chemical reactions	22
2.1	Schematic representation of the centrosome model	28
2.2	Schematic representation of the conditions at the interface	32
2.3	Typical droplet growth driven by first-order kinetics, scenario A	37
2.4	Typical droplet growth driven by autocatalytic kinetics, scenario B	38
2.5	Typical droplet growth driven by a catalytic core, scenario C	40
3.1	Schematic volume fraction profiles in stationary state	47
3.2	Reaction fluxes in stationary state as a function of droplet size	48
3.3	Stationary states of a single droplet with a passive core	49
3.4	Stationary states of a single droplet built by an active core	51
3.5	Stationary states of a single droplet with an active core	53
3.6	Stability diagrams of stationary states of single droplets	54
3.7	Bistable stationary states of a single droplet with an active core	56
3.8	Perturbation modes of the spherical droplet shape	58
3.9	Stability of perturbations of the core position	60
3.10	Stability of perturbations of the droplet shape	61
3.11	Stability diagrams of a single droplet	63
3.12	Summarized behavior of isolated active droplets	65
4.1	Schematic drawing of a system with multiple droplets	68
4.2	Comparison of full and approximate model for a single droplet	69
4.3	Schematic explanation of Ostwald ripening	72

4.4	Possible growth dynamics of two droplets	73
4.5	Stationary states and stability of two droplets	74
4.6	Transient dynamics of two droplets	76
4.7	Stationary states and stability of two droplets built by active cores . .	78
4.8	Stability diagrams of two droplets in scenarios A and B	81
4.9	Stability diagrams of two droplets in scenario C	82
4.10	Numerical stability diagrams of two droplets	83
4.11	Stability diagrams with up to four droplets	85
5.1	Schematic representation of the stochastic model	90
5.2	Comparison of the stochastic and the deterministic growth model . .	92
5.3	Ensemble and time average of the stochastic droplet volume	93
5.4	Distribution of droplet volumes at different times	97
5.5	Influence of particle number on fluctuations in the stochastic model .	100
5.6	Growth of a single droplet in different geometries	101
5.7	Influence of the relative position of two droplets	102
6.1	Quantification of centrosome size	104
6.2	Centrosome growth curves in <i>C. elegans</i> embryos	105
6.3	Parameter study of the autocatalytic model	108
6.4	Fit of the centrosome model to wild-type experimental data	109
6.5	Fit of the centrosome model to experimental data of mutants	110
6.6	Centrosome size versus cell size	111
6.7	Centrosomes with unequal sizes	115
6.8	Growth curves of centrosomes with unequal volume	117
6.9	Disintegration of a centrosome	118
D.1	Admissible length scales in diffusion-limited growth	132
F.1	Volume fraction profiles in stationary state	135
G.1	Stationary states of a single droplet in scenario C	139
H.1	Fundamental solutions of the Helmholtz equation	143
H.2	Verification of the shape fluctuation analysis	148
I.1	Approximate model with gradients inside the droplets	150
J.1	Detailed stability diagrams of two droplets for autocatalytic growth .	151
J.2	Histograms of numerical simulations of multiple droplets	152
K.1	Simulations of the stochastic model with different time steps	155

Bibliography

- [1] B. Alberts, A. Johnson, J. Lewis, M. Raff, K. Roberts, and P. Walter. *Molecular Biology of the Cell*. Garland, 4th edition, (2002).
- [2] W. Flemming. *Zellsubstanz, Kern und Zelltheilung*. Verlag von FCW Vogel, Leipzig, (1882).
- [3] E. Schrödinger. *Was ist Leben?* Piper, (1989).
- [4] J. Travis. How does the cell position its proteins? *Science* **334**, 1048–1049 (2011).
- [5] N. Campbell, J. Reece, M. Taylor, and E. Simon. *Biology: Concepts and Connections*. Pearson Education, Inc., Upper Saddle River, NJ, 5th edition, (2006).
- [6] S. I. Sandler. Thermodynamics and bioenergetics. *Biophys. Chem.* **97**, 87–111 (2002).
- [7] E. B. Wilson. *The Cell in Development and Heredity*. Macmillan, New York, 3rd edition, (1925).
- [8] Organelle. *Encyclopædia Britannica Online*, (2013). URL: <http://www.britannica.com/EBchecked/topic/431912/organelle>. Accessed: February 20, 2013.
- [9] Organelle. *Wikipedia, The Free Encyclopedia*, (2013). URL: <http://en.wikipedia.org/w/index.php?title=Organelle&oldid=539176339>. Accessed: February 20, 2013.
- [10] Y. Hara and A. Kimura. Cell-size-dependent control of organelle sizes during development. In *Cell Cycle in Development*, volume 53 of *Results and Problems in Cell Differentiation*, 93–108. Springer Berlin Heidelberg (2011).
- [11] Y. M. Chan and W. F. Marshall. Scaling properties of cell and organelle size. *Organogenesis* **6**, 88–96 (2010).
- [12] F. Neumann and P. Nurse. Nuclear size control in fission yeast. *J. Cell Biol.* **179**, 593–600 (2007).
- [13] Y. M. Chan and W. F. Marshall. How cells know the size of their organelles. *Science* **337**, 1186–1189 (2012).
- [14] S. M. Rafelski and W. F. Marshall. Building the cell: design principles of cellular architecture. *Nat. Rev. Mol. Cell Bio.* **9**, 593–602 (2008).

- [15] W. F. Marshall. Cellular length control systems. *Annu. Rev. Cell Dev. Biol.* **20**, 677–693 (2004).
- [16] R. Mahen and A. R. Venkitaraman. Pattern formation in centrosome assembly. *Curr. Opin. Cell Biol.* **24**, 14–23 (2012).
- [17] Z. F. Altun and D. H. Hall. Handbook of *C. elegans* Anatomy. In *WormAtlas*. The *C. elegans* Research Community (2005). URL: <http://www.wormatlas.org/ver1/handbook/contents.htm>. Accessed: February 21, 2013.
- [18] P. Gönczy and L. S. Rose. Asymmetric cell division and axis formation in the embryo. In *Wormbook*. The *C. elegans* Research Community (2005). URL: http://www.wormbook.org/chapters/www_asymcelldiv/asymcelldiv.html. Accessed: February 21, 2013.
- [19] S. Brenner. The genetics of *Caenorhabditis elegans*. *Genetics* **77**, 71–94 (1974).
- [20] J. Sulston, E. Schierenberg, J. White, and J. N. Thomson. The embryonic cell lineage of the nematode *Caenorhabditis elegans*. *Dev. Biol.* **100**, 64–119 (1983).
- [21] C. Sequencing Consortium. Genome sequence of the nematode *C. elegans*: a platform for investigating biology. *Science* **282**, 2012–2018 (1998).
- [22] A. Fire, S. Xu, M. Montgomery, S. Kostas, S. Driver, and C. Mello. Potent and specific genetic interference by double-stranded RNA in *Caenorhabditis elegans*. *Nature* **391**, 806–811 (1998).
- [23] A. Z. Fire and C. C. Mello. The Nobel Prize in Physiology or Medicine, (2006). URL: http://www.nobelprize.org/nobel_prizes/medicine/laureates/2006/.
- [24] M. Decker, S. Jaensch, A. Pozniakovsky, A. Zinke, K. F. O’Connell, W. Zachariae, E. Myers, and A. A. Hyman. Limiting Amounts of Centrosome Material Set Centrosome Size in *C. elegans* Embryos. *Curr. Biol.* **21**, 1259–1267 (2011).
- [25] M. Uhlén, E. Björling, C. Agaton, C. A. Szigarto, B. Amini, E. Andersen, A. Andersson, P. Angelidou, A. Asplund, C. Asplund, L. Berglund, K. Bergström, H. Brumer, D. Cerjan, M. Ekström, A. Elobeid, C. Eriksson, L. Fagerberg, R. Falk, J. Fall, M. Forsberg, M. G. Björklund, K. Gumbel, A. Halimi, I. Hallin, C. Hamsten, M. Hansson, M. Hedhammar, G. Hercules, C. Kampf, K. Larsson, M. Lindskog, W. Lodewyckx, J. Lund, J. Lundeberg, K. Magnusson, E. Malm, P. Nilsson, J. Odling, P. Oksvold, I. Olsson, E. Oster, J. Ottosson, L. Paavilainen, A. Persson, R. Rimini, J. Rockberg, M. Runeson, A. Sivertsson, A. Sköllerö, J. Steen, M. Stenvall, F. Sterky, S. Strömberg, M. Sundberg, H. Tegel, S. Tourle, E. Wahlund, A. Waldén, J. Wan, H. Wernérus, J. Westberg, K. Wester, U. Wrethagen, L. L. Xu, S. Hober, and F. Pontén. A human protein atlas for normal and cancer tissues based on antibody proteomics. *Mol. Cell. Proteomics* **4**, 1920–1932 (2005).

- [26] A. Krämer, B. Maier, and J. Bartek. Centrosome clustering and chromosomal (in)stability: a matter of life and death. *Mol. Oncol.* **5**, 324–335 (2011).
- [27] J. Howard. *Mechanics of Motor Proteins and the Cytoskeleton*. Palgrave Macmillan, (2001).
- [28] M. Bornens. The centrosome in cells and organisms. *Science* **335**, 422–426 (2012).
- [29] W. C. Zimmerman, C. A. Sparks, and S. J. Doxsey. Amorphous no longer: the centrosome comes into focus. *Curr. Opin. Cell Biol.* **11**, 122–128 (1999).
- [30] G. Greenan, C. P. Brangwynne, S. Jaensch, J. Gharakhani, F. Jülicher, and A. A. Hyman. Centrosome size sets mitotic spindle length in *Caenorhabditis elegans* embryos. *Curr. Biol.* **20**, 353–358 (2010).
- [31] A. A. Hyman and J. G. White. Determination of cell division axes in the early embryogenesis of *Caenorhabditis elegans*. *J. Cell Biol.* **105**, 2123–2135 (1987).
- [32] R. Basto, J. Lau, T. Vinogradova, A. Gardiol, C. G. Woods, A. Khodjakov, and J. W. Raff. Flies without centrioles. *Cell* **125**, 1375–1386 (2006).
- [33] A. Debec, W. Sullivan, and M. Bettencourt-Dias. Centrioles: active players or passengers during mitosis? *Cell. Mol. Life Sci.* **67**, 2173–2194 (2010).
- [34] J. L. Salisbury, C. M. Whitehead, W. L. Lingle, and S. L. Barrett. Centrosomes and cancer. *Biol. Cell* **91**, 451–460 (1999).
- [35] J. Marx. Do Centrosome Abnormalities Lead to Cancer? *Science* **292**, 426–429 (2001).
- [36] W. Saunders. Centrosomal amplification and spindle multipolarity in cancer cells. *Semin. Cancer. Biol.* **15**, 25–32 (2005).
- [37] D. Zyss and F. Gergely. Centrosome function in cancer: guilty or innocent? *Trends Cell Biol.* **19**, 334–346 (2009).
- [38] J. Y. Chan. A clinical overview of centrosome amplification in human cancers. *Int. J. Biol. Sci.* **7**, 1122–1144 (2011).
- [39] A. B. D’Assoro, W. L. Lingle, and J. L. Salisbury. Centrosome amplification and the development of cancer. *Oncogene* **21**, 6146–6153 (2002).
- [40] K. Fukasawa. Centrosome amplification, chromosome instability and cancer development. *Cancer Lett.* **230**, 6–19 (2005).
- [41] N. J. Ganem, S. A. Godinho, and D. Pellman. A mechanism linking extra centrosomes to chromosomal instability. *Nature* **460**, 278–282 (2009).
- [42] A. Duensing and S. Duensing. Centrosomes, polyploidy and cancer. *Adv. Exp. Med. Biol.* **676**, 93–103 (2010).

- [43] S. J. Anderhub, A. Krämer, and B. Maier. Centrosome amplification in tumorigenesis. *Cancer Lett.* **322**, 8–17 (2012).
- [44] B. D. Vitre and D. W. Cleveland. Centrosomes, chromosome instability (CIN) and aneuploidy. *Curr. Opin. Cell Biol.* **24**, 809–815 (2012).
- [45] H. Schatten and Q. Sun. The Significant Role of Centrosomes in Stem Cell Division and Differentiation. *Microsc. Microanal.* **17**, 506–512 (2011).
- [46] S. J. Doxsey, W. C. Zimmerman, and K. Mikule. Centrosome control of the cell cycle. *Trends Cell Biol.* **15**, 303–311 (2005).
- [47] G. Sluder. Two-way traffic: centrosomes and the cell cycle. *Nat. Rev. Mol. Cell Bio.* **6**, 743–748 (2005).
- [48] H. Hehnlly, C. Chen, C. M. Powers, H. Liu, and S. J. Doxsey. The Centrosome Regulates the Rab11- Dependent Recycling Endosome Pathway at Appendages of the Mother Centriole. *Curr. Biol.* **22**, 1944–1950 (2012).
- [49] E. A. Nigg and J. W. Raff. Centrioles, centrosomes, and cilia in health and disease. *Cell* **139**, 663–678 (2009).
- [50] M. Bettencourt-Dias. Q&A: Who needs a centrosome? *BMC Biol.* **11**, 28 (2013).
- [51] G. M. G. B. M. M Mazzorana. The Centrosome: A Target for Cancer Therapy. *Curr. Cancer Drug Targets* **11**, 600–612 (2011).
- [52] P. Gönczy. Towards a molecular architecture of centriole assembly. *Nat. Rev. Mol. Cell Bio.* **13**, 425–435 (2012).
- [53] J. Azimzadeh and W. F. Marshall. Building the centriole. *Curr. Biol.* **20**, R816–R825 (2010).
- [54] E. A. Nigg and T. Stearns. The centrosome cycle: Centriole biogenesis, duplication and inherent asymmetries. *Nat. Cell Biol.* **13**, 1154–1160 (2011).
- [55] D. Kitagawa, I. Vakonakis, N. Olieric, M. Hilbert, D. Keller, V. Olieric, M. Bortfeld, M. C. Erat, I. Flückiger, P. Gönczy, and M. O. Steinmetz. Structural Basis of the 9-Fold Symmetry of Centrioles. *Cell* **144**, 364–375 (2011).
- [56] L. Pelletier, E. T. O’Toole, A. Schwager, A. A. Hyman, and T. Müller-Reichert. Centriole assembly in *Caenorhabditis elegans*. *Nature* **444**, 619–623 (2006).
- [57] T. Avidor-Reiss and J. Gopalakrishnan. Building a centriole. *Curr. Opin. Cell Biol.* **25**, 72–77 (2012).
- [58] L. Pelletier and Y. M. Yamashita. Centrosome asymmetry and inheritance during animal development. *Curr. Opin. Cell Biol.* **24**, 541–546 (2012).

- [59] W. Wang, R. K. Soni, K. Uryu, and M. Bryan Tsou. The conversion of centrioles to centrosomes: essential coupling of duplication with segregation. *J. Cell Biol.* **193**, 727–739 (2011).
- [60] P. Strnad and P. Gönczy. Mechanisms of procentriole formation. *Trends Cell Biol.* **18**, 389–396 (2008).
- [61] W. F. Marshall, Y. Vucica, and J. L. Rosenbaum. Kinetics and regulation of de novo centriole assembly. Implications for the mechanism of centriole duplication. *Curr. Biol.* **11**, 308–317 (2001).
- [62] A. Rodrigues-Martins, M. Riparbelli, G. Callaini, D. M. Glover, and M. Bettencourt-Dias. Revisiting the role of the mother centriole in centriole biogenesis. *Science* **316**, 1046–1050 (2007).
- [63] W. F. Marshall. Centriole evolution. *Curr. Opin. Cell Biol.* **21**, 14–19 (2009).
- [64] Z. Carvalho-Santos, J. Azimzadeh, J. B. Pereira-Leal, and M. Bettencourt-Dias. Evolution: Tracing the origins of centrioles, cilia, and flagella. *J. Cell Biol.* **194**, 165–175 (2011).
- [65] J. Azimzadeh and M. Bornens. Structure and duplication of the centrosome. *J. Cell Sci.* **120**, 2139–2142 (2007).
- [66] E. P. Lucas and J. W. Raff. Maintaining the proper connection between the centrioles and the pericentriolar matrix requires *Drosophila* centrosomin. *J. Cell Biol.* **178**, 725–732 (2007).
- [67] P. T. Conduit, K. Brunk, J. Dobbelaere, C. I. Dix, E. P. Lucas, and J. W. Raff. Centrioles regulate centrosome size by controlling the rate of Cnn incorporation into the PCM. *Curr. Biol.* **20**, 2178–2186 (2010).
- [68] M. Kirkham, T. Müller-Reichert, K. Oegema, S. W. Grill, and A. A. Hyman. SAS-4 is a *C. elegans* centriolar protein that controls centrosome size. *Cell* **112**, 575–587 (2003).
- [69] J. Gopalakrishnan, V. Mennella, S. Blachon, B. Zhai, A. H. Smith, T. L. Megraw, D. Nicastro, S. P. Gygi, D. A. Agard, and T. Avidor-Reiss. Sas-4 provides a scaffold for cytoplasmic complexes and tethers them in a centrosome. *Nat. Commun.* **2**, 359–370 (2011).
- [70] J. Fu and D. M. Glover. Structured illumination of the interface between centriole and peri-centriolar material. *Open Biology* **2**, 120104 (2012).
- [71] E. O’Toole, G. Greenan, K. I. Lange, M. Srayko, and T. Müller-Reichert. The Role of γ -Tubulin in Centrosomal Microtubule Organization. *PLOS ONE* **7**, e29795 (2012).

- [72] S. Lawo, M. Hasegan, G. D. Gupta, and L. Pelletier. Subdiffraction imaging of centrosomes reveals higher-order organizational features of pericentriolar material. *Nat. Cell Biol.* **14**, 1148–1158 (2012).
- [73] V. Mennella, B. Keszthelyi, K. L. McDonald, B. Chhun, F. Kan, G. C. Rogers, B. Huang, and D. A. Agard. Subdiffraction-resolution fluorescence microscopy reveals a domain of the centrosome critical for pericentriolar material organization. *Nat. Cell Biol.* **14**, 1159–1168 (2012).
- [74] J. Lüders. The amorphous pericentriolar cloud takes shape. *Nat. Cell Biol.* **14**, 1126–1128 (2012).
- [75] D. Kellogg, M. Moritz, and B. Alberts. The centrosome and cellular organization. *Annu. Rev. Biochem.* **63**, 639–674 (1994).
- [76] R. Nogales-Cadenas, F. Abascal, J. Díez-Pérez, J. M. Carazo, and A. Pascual-Montano. CentrosomeDB: a human centrosomal proteins database. *Nucleic. Acids Res.* **37**, D175–D180 (2009).
- [77] K. Habermann and B. M. Lange. New insights into subcomplex assembly and modifications of centrosomal proteins. *Cell division* **7**, 1–21 (2012).
- [78] A. Kumar and R. Purohit. Computational centrosomics: An approach to understand the dynamic behaviour of centrosome. *Gene* **511**, 125–126 (2012).
- [79] M. Boxem, Z. Maliga, N. Klitgord, N. Li, I. Lemmens, M. Mana, L. d. Lichter-velde, J. D. Mul, D. v. d. Peut, M. Devos, N. Simonis, M. A. Yildirim, M. Cokol, H. Kao, A. d. Smet, H. Wang, A. Schlaitz, T. Hao, S. Milstein, C. Fan, M. Tipsworth, K. Drew, M. Galli, K. Rhrissorrakrai, D. N. Drechsel, D. Koller, F. P. Roth, L. M. Iakoucheva, A. K. Dunker, R. Bonneau, K. C. Gunsalus, D. E. Hill, F. Piano, J. Tavernier, S. Heuvel, A. A. Hyman, and M. Vidala. A protein domain-based interactome network for *C. elegans* early embryogenesis. *Cell* **134**, 534–545 (2008).
- [80] L. Pelletier, N. Özlü, E. Hannak, C. R. Cowan, B. Habermann, M. Ruer, T. Müller-Reichert, and A. A. Hyman. The *Caenorhabditis elegans* centrosomal protein SPD-2 is required for both pericentriolar material recruitment and centriole duplication. *Curr. Biol.* **14**, 863–873 (2004).
- [81] D. R. Hamill, A. F. Severson, J. C. Carter, and B. Bowerman. Centrosome maturation and mitotic spindle assembly in *C. elegans* require SPD-5, a protein with multiple coiled-coil domains. *Dev. Cell* **3**, 673–684 (2002).
- [82] E. Hannak, M. Kirkham, A. A. Hyman, and K. Oegema. Aurora-A kinase is required for centrosome maturation in *Caenorhabditis elegans*. *J. Cell Biol.* **155**, 1109–1115 (2001).

- [83] A. W. Bird and A. A. Hyman. Building a spindle of the correct length in human cells requires the interaction between TPX2 and Aurora A. *J. Cell Biol.* **182**, 289–300 (2008).
- [84] V. Joukov. Aurora kinases and spindle assembly: Variations on a common theme? *Cell Cycle* **10**, 895–903 (2011).
- [85] A. S. Nikonova, I. Astsaturov, I. G. Serebriiskii, R. L. Dunbrack, and E. A. Golemis. Aurora A kinase (AURKA) in normal and pathological cell division. *Cell. Mol. Life Sci.* **69**, 1–27 (2012).
- [86] R. Mahen, A. D. Jeyasekharan, N. P. Barry, and A. R. Venkitaraman. Continuous polo-like kinase 1 activity regulates diffusion to maintain centrosome self-organization during mitosis. *Proc. Natl. Acad. Sci. USA* **108**, 9310–9315 (2011).
- [87] A. Santamaria, B. Wang, S. Elowe, R. Malik, F. Zhang, M. Bauer, A. Schmidt, H. H. W. Sillje, R. Koerner, and E. A. Nigg. The Plk1-dependent Phosphoproteome of the Early Mitotic Spindle. *Mol. Cell. Proteomics* **10**, 1–18 (2011).
- [88] X. Zhang, Q. Chen, J. Feng, J. Hou, F. Yang, J. Liu, Q. Jiang, and C. Zhang. Sequential phosphorylation of Nedd1 by Cdk1 and Plk1 is required for targeting of the γ TuRC to the centrosome. *J. Cell Sci.* **122**, 2240–2251 (2009).
- [89] D. Chase, C. Serafinas, N. Ashcroft, and M. Kosinski. The polo-like kinase PLK-1 is required for nuclear envelope breakdown and the completion of meiosis in *Caenorhabditis elegans*. *Genesis* **26**, 26–41 (2000).
- [90] M. Srayko, A. Kaya, J. Stamford, and A. A. Hyman. Identification and characterization of factors required for microtubule growth and nucleation in the early *C-elegans* embryo. *Dev. Cell* **9**, 223–236 (2005).
- [91] J. M. Kollman, A. Merdes, L. Mourey, and D. A. Agard. Microtubule nucleation by γ -tubulin complexes. *Nat. Rev. Mol. Cell Bio.* **12**, 709–721 (2011).
- [92] W. C. Zimmerman, J. E. Sillibourne, J. Rosa, and S. J. Doxsey. Mitosis-specific anchoring of γ tubulin complexes by pericentrin controls spindle organization and mitotic entry. *Mol. Biol. Cell* **15**, 3642–3657 (2004).
- [93] D. Job, O. Valiron, and B. Oakley. Microtubule nucleation. *Curr. Opin. Cell Biol.* **15**, 111–117 (2003).
- [94] J. Dichtenberg and W. C. Zimmerman. Pericentrin and γ -tubulin form a protein complex and are organized into a novel lattice at the centrosome. *J. Cell Biol.* **141**, 163–174 (1998).
- [95] T. Stearns and M. Kirschner. In vitro reconstitution of centrosome assembly and function: the central role of gamma-tubulin. *Cell* **76**, 623–637 (1994).

- [96] T. Stearns, L. Evans, and M. Kirschner. γ -tubulin is a highly conserved component of the centrosome. *Cell* **65**, 825–836 (1991).
- [97] M. C. Alliegro, M. A. Alliegro, and R. E. Palazzo. Centrosome-associated RNA in surf clam oocytes. *Proc. Natl. Acad. Sci. USA* **103**, 9034–9038 (2006).
- [98] M. C. Alliegro. The implications of centrosomal RNA. *RNA Biol.* **5**, 198–200 (2008).
- [99] K. Chichinadze, A. Lazarashvili, and J. Tkemaladze. RNA in centrosomes: Structure and possible functions. In *Protoplasm, New ideas in cell biology*. Springer (2012).
- [100] S. C. Weber and C. P. Brangwynne. Getting RNA and protein in phase. *Cell* **149**, 1188–1191 (2012).
- [101] C. P. Brangwynne. Soft active aggregates: mechanics, dynamics and self-assembly of liquid-like intracellular protein bodies. *Soft Matter* **7**, 3052–3059 (2011).
- [102] C. P. Brangwynne, C. R. Eckmann, D. S. Courson, A. Rybarska, C. Hoege, J. Gharakhani, F. Jülicher, and A. A. Hyman. Germline P Granules Are Liquid Droplets That Localize by Controlled Dissolution/Condensation. *Science* **324**, 1729–1732 (2009).
- [103] J. Gharakhani. *Cell Cytoplasm Compartmentalization: Localization Through Gradients*. PhD thesis, Dresden University of Technology, (2013).
- [104] M. Dunder, M. D. Hebert, T. S. Karpova, D. Staněk, H. Xu, K. B. Shpargel, U. T. Meier, K. M. Neugebauer, A. G. Matera, and T. Misteli. In vivo kinetics of Cajal body components. *J. Cell Biol.* **164**, 831–842 (2004).
- [105] C. P. Brangwynne, T. J. Mitchison, and A. A. Hyman. Active liquid-like behavior of nucleoli determines their size and shape in *Xenopus laevis* oocytes. *Proc. Natl. Acad. Sci. USA* **108**, 4334–4339 (2011).
- [106] A. A. Hyman and C. P. Brangwynne. Beyond Stereospecificity: Liquids and Mesoscale Organization of Cytoplasm. *Dev. Cell* **21**, 14–16 (2011).
- [107] S. An, R. Kumar, E. D. Sheets, and S. J. Benkovic. Reversible compartmentalization of de novo purine biosynthetic complexes in living cells. *Science* **320**, 103–106 (2008).
- [108] R. Narayanaswamy, M. Levy, M. Tsechansky, G. M. Stovall, J. D. O’Connell, J. Mirrieles, A. D. Ellington, and E. M. Marcotte. Widespread reorganization of metabolic enzymes into reversible assemblies upon nutrient starvation. *Proc. Natl. Acad. Sci. USA* **106**, 10147–10152 (2009).
- [109] R. Garcia-Mata, Y. Gao, and E. Sztul. Hassles with taking out the garbage: aggravating aggresomes. *Traffic* **3**, 388–396 (2002).

- [110] J. Tyedmers, A. Mogk, and B. Bukau. Cellular strategies for controlling protein aggregation. *Nat. Rev. Mol. Cell Bio.* **11**, 777–788 (2010).
- [111] F. Chiti and C. M. Dobson. Protein misfolding, functional amyloid, and human disease. *Annu. Rev. Biochem.* **75**, 333–366 (2006).
- [112] A. C. Dumetz, A. M. Chockla, E. W. Kaler, and A. M. Lenhoff. Protein phase behavior in aqueous solutions: crystallization, liquid-liquid phase separation, gels, and aggregates. *Biophys. J.* **94**, 570–583 (2008).
- [113] P. M. Chaikin and T. C. Lubensky. *Principles of condensed matter physics*. Cambridge University Press, (2000).
- [114] T. Riste and D. Sherrington, editors. *Phase Transitions in Soft Condensed Matter*. Number 211 in NATO ASI Series B. Plenum Press, (1989).
- [115] P. K. Khabibullaev and A. A. Saidov. *Phase Separation in Soft Matter Physics*. Number 138 in Solid-state Sciences. Springer, (2003).
- [116] G. H. Pollack and W. Chin, editors. *Phase Transitions in Cell Biology*. Springer, October (2008).
- [117] Y. H. Choi, J. Spronsen, Y. Dai, M. Verberne, F. Hollmann, I. W. C. E. Arends, G. Witkamp, and R. Verpoorte. Are natural deep eutectic solvents the missing link in understanding cellular metabolism and physiology? *Plant Physiol.* **156**, 1701–1705 (2011).
- [118] F. J. Iborra. Can visco-elastic phase separation, macromolecular crowding and colloidal physics explain nuclear organisation? *Theor. Biol. Med. Model.* **4**, 1–11 (2007).
- [119] M. J. Karnovsky, A. M. Kleinfeld, R. L. Hoover, and R. D. Klausner. The concept of lipid domains in membranes. *J. Cell Biol.* **94**, 1–6 (1982).
- [120] K. Simons and E. Ikonen. Functional rafts in cell membranes. *Nature* **387**, 569–572 (1997).
- [121] D. Lingwood and K. Simons. Lipid rafts as a membrane-organizing principle. *Science* **327**, 46–50 (2010).
- [122] T. Schwarz-Romond, C. Merrifield, B. J. Nichols, and M. Bienz. The Wnt signalling effector Dishevelled forms dynamic protein assemblies rather than stable associations with cytoplasmic vesicles. *J. Cell Sci.* **118**, 5269–5277 (2005).
- [123] T. Schwarz-Romond, C. Metcalfe, and M. Bienz. Dynamic recruitment of axin by Dishevelled protein assemblies. *J. Cell Sci.* **120**, 2402–2412 (2007).
- [124] R. P. Sear. Dishevelled: a protein that functions in living cells by phase separating. *Soft Matter* **3**, 680–684 (2007).

- [125] R. P. Sear. Phase separation of equilibrium polymers of proteins in living cells. *Faraday Discuss.* **139**, 21–34 (2008).
- [126] E. R. Dufresne, H. Noh, V. Saranathan, S. G. J. Mochrie, H. Cao, and R. O. Prum. Self-assembly of amorphous biophotonic nanostructures by phase separation. *Soft Matter* **5**, 1792–1795 (2009).
- [127] S. A. Newman and W. D. Comper. 'Generic' physical mechanisms of morphogenesis and pattern formation. *Development* **110**, 1–18 (1990).
- [128] M. E. Cates, D. Marenduzzo, I. Pagonabarraga, and J. Tailleur. Arrested phase separation in reproducing bacteria creates a generic route to pattern formation. *Proc. Natl. Acad. Sci. USA* **107**, 11715–11720 (2010).
- [129] J. Tailleur and M. E. Cates. Lattice models of nonequilibrium bacterial dynamics. , P02029 (2011).
- [130] J. Toner, Y. Tu, and S. Ramaswamy. Hydrodynamics and phases of flocks. *Ann. Phys.* **318**, 170–244 (2005).
- [131] P. I. Flory. Thermodynamics of high polymer solutions. *J. Chem. Phys.* **10**, 51–61 (1942).
- [132] M. L. Huggins. Solutions of long chain compounds. *J. Chem. Phys.* **9**, 440–440 (1941).
- [133] J. W. Cahn. On spinodal decomposition. *Acta metallurgica* **9**, 795–801 (1961).
- [134] J. W. Cahn. Phase separation by spinodal decomposition in isotropic systems. *J. Chem. Phys.* **42**, 93–99 (1965).
- [135] L. Scriven. Equilibrium bicontinuous structure. *Nature* **263**, 123–125 (1976).
- [136] F. Frank. Radially symmetric phase growth controlled by diffusion. *Proc. R. Soc. Lon. A* **201**, 586–599 (1950).
- [137] A. Onuki. *Phase Transition Dynamics*. Cambridge University Press, (2002).
- [138] I. Lifshitz and V. Slyozov. The kinetics of precipitation from supersaturated solid solutions. *J. Phys. Chem. Solids* **19**, 35–50 (1961).
- [139] C. Wagner. Theorie der Alterung von Niederschlägen durch Umlösen (Ostwald-Reifung). *Z. Elektrochem.* **65**, 581–591 (1961).
- [140] M. Kahlweit. Ostwald ripening of precipitates. *Adv. Colloid Interface Sci.* **5**, 1–35 (1975).
- [141] Tétine. Vinaigrette #2 — olive oil, (2007). URL: <http://www.flickr.com/photos/83331954@N00/1374377040/>. Accessed: August 30, 2012.

-
- [142] S. W. Ip and J. M. Toguri. The Equivalency of Surface-Tension, Surface-Energy and Surface Free-Energy. *J. Mater. Sci.* **29**, 688–692 (1994).
- [143] P. Papon, J. Leblond, and P. H.E. Meijer. *The Physics of Phase Transitions*. Springer, 2nd edition, (2006).
- [144] J. Langer. Statistical theory of the decay of metastable states. *Ann. Phys.* **54**, 258–275 (1969).
- [145] J. C. Maxwell. On the dynamical evidence of the molecular constitution of bodies. *Nature* **11**, 357–359 (1875).
- [146] P. W. Voorhees. Ostwald ripening of two-phase mixtures. *Annu. Rev. Mater. Sci.* **22**, 197–215 (1992).
- [147] M. E. Cates. The physics of emulsions. In *Soft Interfaces*. École de Physique des Houches (to be published in 2013).
- [148] J. Brader and R. Evans. The fluid-fluid interface of a model colloid-polymer mixture. *Europhys. Lett.* **49**, 678–684 (2000).
- [149] D. G. A. L. Aarts. Direct Visual Observation of Thermal Capillary Waves. *Science* **304**, 847–850 (2004).
- [150] N. W. Goehring and A. A. Hyman. Organelle growth control through limiting pools of cytoplasmic components. *Curr. Biol.* **22**, R330–R339 (2012).
- [151] T. G. Mason, J. Wilking, K. Meleson, C. Chang, and S. Graves. Nanoemulsions: Formation, structure, and physical properties. *J. Phys.: Condens. Matter* **18**, R635–R666 (2006).
- [152] F. Leal-Calderon, J. Bibette, and V. Schmitt. *Emulsion Science*. Springer, (2007).
- [153] J. Yao and M. Laradji. Dynamics of Ostwald ripening in the presence of surfactants. *Phys. Rev. E* **47**, 2695–2701 (1993).
- [154] P. Stansell, K. Stratford, J. Desplat, R. Adhikari, and M. E. Cates. Nonequilibrium steady states in sheared binary fluids. *Phys. Rev. Lett.* **96**, 085701 (2006).
- [155] A. Webster and M. E. Cates. Stabilization of emulsions by trapped species. *Langmuir* **14**, 2068–2079 (1998).
- [156] M. M. Fryd and T. G. Mason. Advanced Nanoemulsions. *Annu. Rev. Phys. Chem.* **63**, 493–518 (2012).
- [157] Q. Tran-Cong, T. Nagaki, O. Yano, and T. Soen. Structure of polymer blends photo-cross-linked during the spinodal decomposition process. *Macromolecules* **24**, 1505–1510 (1991).

- [158] H. Yoon, Y. Feng, Y. Qiu, and C. C. Han. Structural stabilization of phase separating PC/polyester blends through interfacial modification by transesterification reaction. *J. Polym. Sci.* **32**, 1485–1492 (1994).
- [159] Q. Tran-Cong and A. Harada. Reaction-induced ordering phenomena in binary polymer mixtures. *Phys. Rev. Lett.* **76**, 1162–1165 (1996).
- [160] S. C. Glotzer, D. Stauffer, and N. Jan. Monte Carlo simulations of phase separation in chemically reactive binary mixtures. *Phys. Rev. Lett.* **72**, 4109–4112 (1994).
- [161] S. C. Glotzer, E. A. Di Marzio, and M. Muthukumar. Reaction-controlled morphology of phase-separating mixtures. *Phys. Rev. Lett.* **74**, 2034–2037 (1995).
- [162] M. Motoyama. Morphology of Binary Mixtures Which Undergo Phase Separation during Chemical Reactions. *J. Phys. Soc. Jpn.* **65**, 1894–1897 (1996).
- [163] K. Furtado and J. Yeomans. Lattice Boltzmann simulations of phase separation in chemically reactive binary fluids. *Phys. Rev. E* **73**, 066124 (2006).
- [164] C. Tong and Y. Yang. Phase-separation dynamics of a ternary mixture coupled with reversible chemical reaction. *J. Chem. Phys.* **116**, 1519–1529 (2002).
- [165] S. Puri and H. Frisch. Segregation dynamics of binary mixtures with simple chemical reactions. *J. Phys. A* **27**, 6027–6038 (1994).
- [166] M. Sabra, H. Gilhøj, and O. Mouritsen. Steady-state organization of binary mixtures by active impurities. *Phys. Rev. E* **58**, 3547–3551 (1998).
- [167] J. Christensen, K. Elder, and H. Fogedby. Phase segregation dynamics of a chemically reactive binary mixture. *Phys. Rev. E* **54**, R2212–R2215 (1996).
- [168] M. Motoyama and T. Ohta. Morphology of Phase-Separating Binary Mixtures with Chemical Reaction. *J. Phys. Soc. Jpn.* **66**, 2715–2725 (1997).
- [169] B. A. Huberman. Striations in chemical reactions. *J. Chem. Phys.* **65**, 2013–2019 (1976).
- [170] L. Leibler. Theory of microphase separation in block copolymers. *Macromolecules* **13**, 1602–1617 (1980).
- [171] T. Ohta and K. Kawasaki. Equilibrium morphology of block copolymer melts. *Macromolecules* **19**, 2621–2632 (1986).
- [172] F. Liu and N. Goldenfeld. Dynamics of phase separation in block copolymer melts. *Phys. Rev. A* **39**, 4805–4810 (1989).
- [173] S. C. Glotzer and A. Coniglio. Self-consistent solution of phase separation with competing interactions. *Phys. Rev. E* **50**, 4241–4244 (1994).

- [174] D. Carati and R. Lefever. Chemical freezing of phase separation in immiscible binary mixtures. *Phys. Rev. E* **56**, 3127–3136 (1997).
- [175] J. W. Cahn and J. E. Hilliard. Free Energy of a Nonuniform System. I. Interfacial Free Energy. *J. Chem. Phys.* **28**, 258–267 (1958).
- [176] R. Lefever, D. Carati, and N. Hassani. Comment on "Monte Carlo Simulations of Phase Separation in Chemically Reactive Binary Mixtures". *Phys. Rev. Lett.* **75**, 1674 (1995).
- [177] S. C. Glotzer, D. Stauffer, and N. Jan. Glotzer, Stauffer, and Jan Reply. *Phys. Rev. Lett.* **75**, 1675 (1995).
- [178] S. Camazine, J. Deneubourg, N. R. Franks, J. Sneyd, G. Theraulaz, and E. Bonabeau. *Self-Organization in Biological Systems*. Princeton University Press, (2001).
- [179] C. B. Muratov. Theory of domain patterns in systems with long-range interactions of Coulomb type. *Phys. Rev. E* **66**, 066108 (2002).
- [180] T. Boveri. *Zellen-Studien II: Die Befruchtung und Teilung des Eies von Ascaris megalocephala*. Jena, Gustav Fischer Verlag, (1888).
- [181] E. Schierenberg. Embryological variation during nematode development. In *Wormbook*. The C. elegans Research Community (2006). URL: <http://www.wormbook.org>. Accessed: February 21, 2013.
- [182] A. Carvalho, S. K. Olson, E. Gutierrez, K. Zhang, L. B. Noble, E. Zanin, A. Desai, A. Groisman, and K. Oegema. Acute drug treatment in the early C. elegans embryo. *PLOS ONE* **6**, e24656 (2011).
- [183] L. D. Landau and E. M. Lifshitz. *Fluid Mechanics*, volume 6 of *Course of Theoretical Physics*. Butterworth-Heinemann Ltd Oxford, 2nd edition, (1987).
- [184] S. Jaensch, M. Decker, A. A. Hyman, and E. W. Myers. Automated tracking and analysis of centrosomes in early Caenorhabditis elegans embryos. *Bioinformatics* **26**, i13–i20 (2010).
- [185] N. Le Bot, M. C. Tsai, R. K. Andrews, and J. Ahringer. TAC-1, a regulator of microtubule length in the C. elegans embryo. *Curr. Biol.* **13**, 1499–1505 (2003).
- [186] S. N. Hird and J. G. White. Cortical and Cytoplasmic Flow Polarity in Early Embryonic Cells of *Caenorhabditis elegans*. *J. Cell Biol.* **121**, 1343–1355 (1993).
- [187] H. H. Keating and J. G. White. Centrosome dynamics in early embryos of *Caenorhabditis elegans*. *J. Cell Sci.* **111**, 3027–3033 (1998).
- [188] P. Schuille. Molecular dynamics in living cells observed by fluorescence correlation spectroscopy with one- and two-photon excitation. *Biophys. J.* **77**, 2251–2265 (1999).

- [189] D. Banks and C. Fradin. Anomalous diffusion of proteins due to molecular crowding. *Biophys. J.* **89**, 2960–2971 (2005).
- [190] B. Daniels, B. Masi, and D. Wirtz. Probing Single-Cell Micromechanics in Vivo: The Microrheology of *C. elegans* Developing Embryos. *Biophys. J.* **90**, 4712–4719 (2006).
- [191] P. Li, S. Banjade, H. Cheng, S. Kim, B. Chen, L. Guo, M. Llaguno, J. V. Hollingsworth, D. S. King, S. F. Banani, P. S. Russo, Q. Jiang, B. T. Nixon, and M. K. Rosen. Phase transitions in the assembly of multivalent signalling proteins. *Nature* **483**, 336–340 (2012).
- [192] T. W. Han, M. Kato, S. Xie, L. C. Wu, H. Mirzaei, J. Pei, M. Chen, Y. Xie, J. Allen, G. Xiao, and S. L. McKnight. Cell-free Formation of RNA Granules: Bound RNAs Identify Features and Components of Cellular Assemblies. *Cell* **149**, 768–779 (2012).
- [193] C. Miller and L. Scriven. The oscillations of a fluid droplet immersed in another fluid. *J. Fluid Mech.* **32**, 417–435 (1968).
- [194] A. Bratz and I. Egry. Surface oscillations of electromagnetically levitated viscous metal droplets. *J. Fluid Mech.* **298**, 341–359 (1995).
- [195] K. Wantke, H. Fruhner, J. Fang, and K. Lunkenheimer. Measurements of the surface elasticity in medium frequency range using the oscillating bubble method. *J. Colloid Interf. Sci.* **208**, 34–48 (1998).
- [196] S. R. Derkach, J. Kraegel, and R. Miller. Methods of Measuring Rheological Properties of Interfacial Layers (Experimental Methods of 2D Rheology). *Colloid J.* **71**, 1–17 (2009).
- [197] L. Rayleigh. On theory of the capillary tube. *Proc. R. Soc. Lon. A* **92**, 184–195 (1916).
- [198] Y. Tian, R. Holt, and R. E. Apfel. Investigations of liquid surface rheology of surfactant solutions by droplet shape oscillations: Theory. *Phys. Fluids.* **7**, 2938–2949 (1995).
- [199] N. Bohr and J. Wheeler. The mechanism of nuclear fission. *Phys. Rev.* **56**, 426–450 (1939).
- [200] J. Crank. *Free and moving boundary problems*. Oxford University Press, USA, (1987).
- [201] E. Ott. *Chaos in dynamical systems*. Cambridge University Press, (1993).
- [202] G. Greenwood. The growth of dispersed precipitates in solutions. *Acta metallurgica* **4**, 243–248 (1956).

- [203] C. V. Rao, D. M. Wolf, and A. P. Arkin. Control, exploitation and tolerance of intracellular noise. *Nature* **420**, 231–237 (2002).
- [204] M. B. Elowitz, A. J. Levine, E. D. Siggia, and P. S. Swain. Stochastic gene expression in a single cell. *Science* **297**, 1183–1186 (2002).
- [205] A. Raj and A. Oudenaarden. Nature, nurture, or chance: stochastic gene expression and its consequences. *Cell* **135**, 216–226 (2008).
- [206] R. Milo, P. Jorgensen, U. Moran, G. Weber, and M. Springer. BioNumbers—the database of key numbers in molecular and cell biology. *Nucleic. Acids Res.* **38**, D750–D753 (2010).
- [207] N. G. van Kampen. *Stochastic processes in physics and chemistry*. Elsevier, 3rd edition, (2007).
- [208] E. M. Ozbudak, M. Thattai, I. Kurtser, A. D. Grossman, and A. Oudenaarden. Regulation of noise in the expression of a single gene. *Nat. Genet.* **31**, 69–73 (2002).
- [209] I. Golding, J. Paulsson, S. M. Zawilski, and E. C. Cox. Real-time kinetics of gene activity in individual bacteria. *Cell* **123**, 1025–1036 (2005).
- [210] J. S. Zon, M. Morelli, S. Tănase-Nicola, and P. R. Wolde. Diffusion of transcription factors can drastically enhance the noise in gene expression. *Biophys. J.* **91**, 4350–4367 (2006).
- [211] M. Springer and J. Paulsson. Harmonies from noise. *Nature* **439**, 27–28 (2006).
- [212] T. Tian. Effective Stochastic Simulation Methods for Chemical Reaction Systems. *J. Numerical Mathematics and Stochastics* **1**, 85–101 (2009).
- [213] D. Gillespie. Exact stochastic simulation of coupled chemical reactions. *J. Phys. Chem.* **81**, 2340–2361 (1977).
- [214] W. Woyczyński. *A first course in statistics for signal analysis*. Birkhauser, 2nd edition, (2011).
- [215] P. K. MacKeown. *Stochastic Simulation in Physics*. Springer, (1997).
- [216] E. Limpert, W. Stahel, and M. Abbt. Log-normal Distributions across the Sciences: Keys and Clues. *BioScience* **51**, 341–352 (2001).
- [217] S. Gangopadhyay, G. Hadjipanayis, B. Dale, C. Sorensen, K. Klabunde, V. Papaefthymiou, and A. Kostikas. Magnetic properties of ultrafine iron particles. *Phys. Rev. B* **45**, 9778–9787 (1992).
- [218] A. E. Magurran and P. A. Henderson. Explaining the excess of rare species in natural species abundance distributions. *Nature* **422**, 714–716 (2003).

- [219] S. Shen, H. Mo, S. White, M. Blanton, G. Kauffmann, W. Voges, J. Brinkmann, and I. Csabai. The size distribution of galaxies in the Sloan Digital Sky Survey. *Mon. Not. R. Astron. Soc.* **343**, 978–994 (2003).
- [220] S. Jaensch and M. Decker. Size of *C. elegans* cells measured from 3D reconstruction. Private communication. See Ref. [24] for details on the experimental procedure.
- [221] The centrosome size project, (2011). URL: <http://centsize.mpi-cbg.de>. Accessed: September 17, 2012.
- [222] M. Decker, S. Jaensch, and A. A. Hyman. Experimental data of centrosome volume versus time. Private communication. See Ref. [24] for details on the experimental procedure.
- [223] H. Walter and D. E. Brooks. Phase separation in cytoplasm, due to macromolecular crowding, is the basis for microcompartmentation. *FEBS Lett.* **361**, 135–139 (1995).
- [224] S. W. Grill, J. Howard, E. Schaffer, and E. H. K. Stelzer. The distribution of active force generators controls mitotic spindle position. *Science* **301**, 518–521 (2003).
- [225] S. W. Grill, K. Kruse, and F. Jülicher. Theory of Mitotic Spindle Oscillations. *Phys. Rev. Lett.* **94**, 108104 (2005).
- [226] M. C. Good, J. G. Zalatan, and W. A. Lim. Scaffold proteins: hubs for controlling the flow of cellular information. *Science* **332**, 680–686 (2011).
- [227] A. S. Mikhailov and G. Ertl. Nonequilibrium microstructures in reactive monolayers as soft matter systems. *ChemPhysChem* **10**, 86–100 (2009).
- [228] G. Nicolis and I. Prigogine. *Self-Organization in Nonequilibrium Systems*. Wiley, (1977).
- [229] A. Turing. The chemical basis of morphogenesis. *Phil. Trans. R. Soc. London* **237**, 37–72 (1952).
- [230] H. Meinhardt. Pattern formation in biology: a comparison of models and experiments. *Rep. Prog. Phys.* **55**, 797–849 (1992).
- [231] R. Gordon, N. S. Goel, M. S. Steinberg, and L. L. Wiseman. A rheological mechanism sufficient to explain the kinetics of cell sorting. *J. Theor. Biol.* **37**, 43–73 (1972).
- [232] K. Guevorkian, M. Colbert, M. Durth, S. Dufour, and F. Brochard-Wyart. Aspiration of biological viscoelastic drops. *Phys. Rev. Lett.* **104**, 218101 (2010).
- [233] J. Ranft, M. Basan, J. Elgeti, J. Joanny, J. Prost, and F. Jülicher. Fluidization of tissues by cell division and apoptosis. **107**, 20863–20868 (2010).

- [234] A. Burton. Rate of growth of solid tumours as a problem of diffusion. *Growth Develop. Aging* **30**, 157–176 (1966).
- [235] C. J. W. Breward, H. M. Byrne, and C. E. Lewis. The role of cell-cell interactions in a two-phase model for avascular tumour growth. *J. Math. Biol.* **45**, 125–152 (2002).
- [236] T. Roose, S. J. Chapman, and P. K. Maini. Mathematical models of avascular tumor growth. *Siam. Rev.* **49**, 179–208 (2007).
- [237] H. Greenspan. On the growth and stability of cell cultures and solid tumors. *J. Theor. Biol.* **56**, 229–242 (1976).
- [238] H. Tanaka. Viscoelastic phase separation. *J. Phys.: Condens. Matter* **12**, R207–R264 (2000).
- [239] H. Tanaka and Y. Nishikawa. Viscoelastic phase separation of protein solutions. *Phys. Rev. Lett.* **95**, 078103 (2005).
- [240] K. Danov, N. Denkov, D. Petsev, I. Ivanov, and R. Borwankar. Coalescence Dynamics of Deformable Brownian Emulsion Droplets. *Langmuir* **9**, 1731–1740 (1993).
- [241] H. Tanaka. A new coarsening mechanism of droplet spinodal decomposition. *J. Chem. Phys.* **103**, 2361–2364 (1995).
- [242] H. Tanaka. Coarsening mechanisms of droplet spinodal decomposition in binary fluid mixtures. *J. Chem. Phys.* **105**, 10099–10114 (1996).
- [243] V. Kumaran. Spontaneous motion of droplets during the demixing transition in binary fluids. *J. Chem. Phys.* **112**, 10984–10991 (2000).
- [244] E. Javierre, C. Vuik, F. Vermolen, and S. Zwaag. A comparison of numerical models for one-dimensional Stefan problems. *J. Comput. Appl. Math.* **192**, 445–459 (2006).
- [245] J. Crank. *The mathematics of diffusion*. Oxford University Press, (1979).
- [246] A. Tveito and R. Winther. *Introduction to partial differential equations: a computational approach*, volume 29. Springer, (1998).
- [247] A. Wachter and H. Hoerber. *Repetitorium Theoretische Physik*. Springer, 2nd edition, (2004).
- [248] M. Abramowitz and I. A. Stegun. *Handbook of mathematical functions with formulas, graphs, and mathematical tables*. Dover publications, (1972).
- [249] A. Einstein. Über die von der molekularkinetischen Theorie der Wärme geforderte Bewegung von in ruhenden Flüssigkeiten suspendierten Teilchen. *Ann. Phys.* **322**, 549–560 (1905).

- [250] D. Lemons and A. Gythiel. Paul Langevin’s 1908 paper “On the Theory of Brownian motion” [“Sur la théorie du mouvement brownien”, *C. R. Acad. Sci. (Paris)* **146**, 530-533 (1908)]. *Am. J. Phys* **65**, 1079–1080 (1997).
- [251] E. A. Peters and T. M. Barenbrug. Efficient Brownian dynamics simulation of particles near walls. I. Reflecting and absorbing walls. *Phys. Rev. E* **66**, 056701 (2002).

Eidesstattliche Erklärung

Hiermit versichere ich, dass ich die vorliegende Arbeit ohne unzulässige Hilfe Dritter und ohne Benutzung anderer als der angegebenen Hilfsmittel angefertigt habe. Die aus fremden Quellen direkt oder indirekt übernommenen Gedanken sind als solche kenntlich gemacht. Die Arbeit wurde bisher weder im Inland noch im Ausland in gleicher oder ähnlicher Form einer anderen Prüfungsbehörde vorgelegt. Die vorliegende Arbeit wurde am Max-Planck-Institut für Physik komplexer Systeme angefertigt und von Prof. Dr. Frank Jülicher betreut. Ich erkenne die Promotionsordnung der Fakultät Mathematik und Naturwissenschaften an.

Dresden, den 14. Mai 2013, David Zwicker